The effect of hadronization on the ϕ^* distribution of the Z boson in simulation compared to data from the CMS experiment at $\sqrt{s} = 8\,\mathrm{TeV}$

A DISSERTATION
SUBMITTED TO THE FACULTY OF THE GRADUATE SCHOOL
OF THE UNIVERSITY OF MINNESOTA
BY

Zachary John Lesko

IN PARTIAL FULFILLMENT OF THE REQUIREMENTS
FOR THE DEGREE OF
DOCTOR OF PHILOSOPHY

Jeremiah Mans

August, 2019

Acknowledgements

I would like to thank my parents, John Lesko and Amy Larson-Lesko. Without them this thesis would never have been possible. They helped me become the physicist and the person that I am today.

I would also like to thank the members of the Minnesota CMS group. They helped me both understand the physics as well the systems we used. A special thanks to Alex Gude, whose code became the basis for much of my research, as well as Nicole Ruckstuhl, who helped me get started in the group. They both were vital for my understanding of the analysis. I would also like to thank Peter Hansen, who helped me learn to code and create my own analysis. I would also like to thank Josh Hiltbrand and Michael Revering who looked through my thesis for errors in the organization as well as checks on the physics.

In addition I would like to thank my friends who helped proof my thesis. Dustin Passofaro, Scott Stapf, and D'Ann Barker. I know that I frustrated each of them and they are all breathing a sigh of relief that I will never pester them about this document again.

The collaborations that I was apart of were also vital to this thesis. The CMS, LHC, as well as CERN collaborations are made up of thousands of people who made this research possible.

And last I would like to thank my advisor, Jeremiah Mans. His help both allowed me to understand my research as well as how to be a better scientist.

Abstract

Measurements of the ϕ^* distribution of the Z boson decay are in disagreement with the theoretical distribution. This disagreement is of importance in its relationship to the transverse momentum of the Z boson (Q_{T}). This disagreement may be due to the hadronization step of the simulation, which attempts to describe QCD interactions involved in the event. If the hadronizer can be changed to remove this disagreement those changes can be applied to W simulations which would allow for the uncertainty of the W mass measurement to be decreased. This thesis presents normalized results of both ϕ^* measurements and rapidity measurements of the Z boson at a center-of-mass energy of 8 TeV along with multiple simulation results using changes to the hadronizer in an attempt to better match the data. The data used was collected by the CMS detector at the LHC in 2012. This data totaled 19.7 fb^{-1} of integrated luminosity. Although changes to the hadronizer had a major effect on the simulated results, it was found that none of the changes could fully resolve the disagreement between data and theory.

Contents

List of Tables

List of Figures

1

Introduction

"Science is what we have learned about how to keep from fooling ourselves."

– Richard Feynman

Particle physics is the study of the particles that make up the universe, as well as the forces that affect them. The most widely accepted model is known as the Standard Model(SM), and has been shown to accurately explain and predict many processes. However, despite this, the Standard Model is limited. For instance, it does not account for dark matter, dark energy or even gravity. Even some terms that are in Standard Model are not necessarily predictive, such as the mass and charge of some particles since those terms are related to free parameters. Another difficulty with the standard model is even if all the terms are known, sometimes the calculations are difficult if not impossible such as many interactions involving the strong force. For this reason many models do not use the Standard Model for predicting certain effects of the strong force.

An important concept when discussing the Standard Model is that although it doesn't predict the mass of particles directly, it does predict the relationship between some of the masses. For example by measuring the mass of the top quark and the Higgs Boson it is possible to predict the mass of the W. Figure 1.1 shows a relationship between the theoretical mass of the W and the top quark for 4 different masses of the Higgs boson. With the mass of the Higgs measured as 125 GeV it is possible to predict the mass of the W given the measured mass of the top quark. As can be seen the measured mass of the W is over one sigma away from the predicted mass. While tantalizing, the

significance of the disagreement is insufficient to currently demand the presence of new physics to explain it. The clearest way to resolve the disagreement would be to lower the error on the W boson's measured mass.

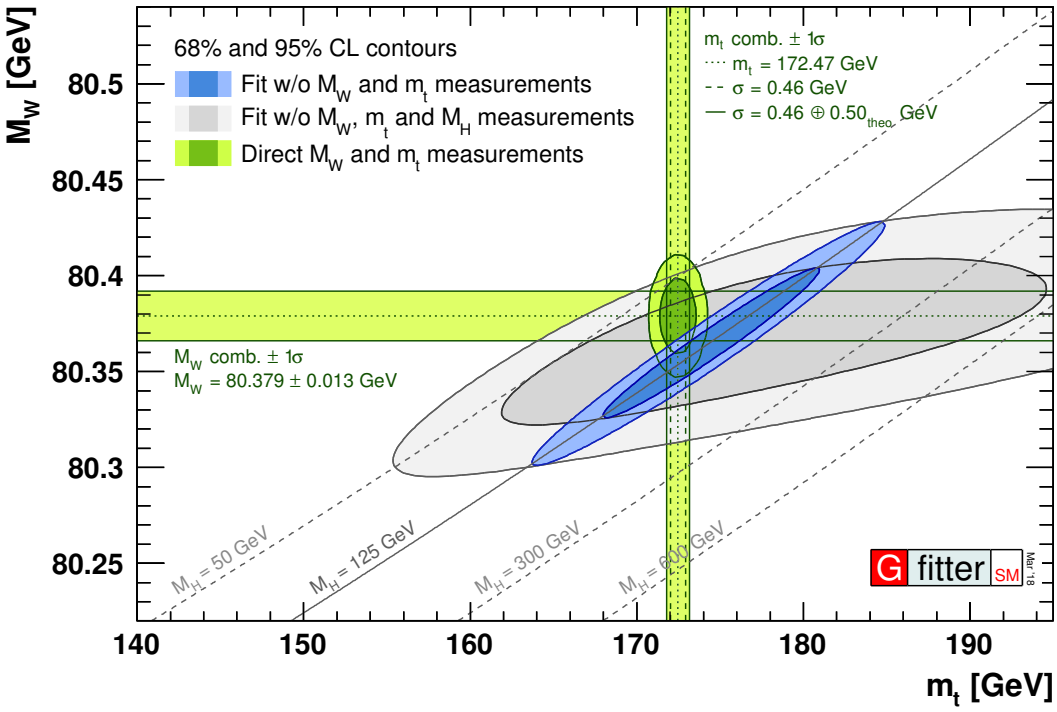

Figure 1.1: Current measured mass of the W boson and top quark using gfitter, compared to the theoretical values. With the current measured mass of the Higgs boson, 125 GeV, the theory does not match the experimentally measured masses of the W boson and the top quark.

Measuring the mass of the W is difficult to do with a hadron collider however, since it requires accurate predictions of the effect of low energy strong interactions. Instead of measuring the mass directly, the distribution of transverse momentum of the charged leptons that are produced through $W^{\pm} \rightarrow \nu\ell^{\pm}$ is measured. Unfortunately this distribution however is also sensitive to not only the mass of the W, but the transverse momentum of the W. This thesis attempts to test the effects of modifying the "hadronizer" which simulates the effects of low energy strong interactions. These effects are probed by measuring the leptons that result from a Z decay. Both the Z and

its decay products lack any direct interaction with the strong force. Therefore once the Z is produced, the strong force will have only a trivial effect on the measured value. Thus, by measuring the momentum of the leptons we can calculate the transverse momentum of the Z (Q_{T}) and can then infer information about the transverse momentum of the particles that produced it. In place of measuring the Q_{T} of the Z directly the novel variable ϕ^* is used[3]. This variable, while being highly correlated with Q_{T}, has a much smaller percentage uncertainty, allowing for more accurate tests of the transverse momentum of the parent particles of the Z.

The data used was collected using the Compact Muon Solenoid detector(CMS) at the Large Hadron Collider(LHC) in 2012. The data used contains $19.7\,\mathrm{fb}^{-1}$ of integrated luminosity at a center of mass energy of 8 TeV.

The final measured result compares normalized ϕ^* differential cross-sections that were collected at the CMS to different simulation programs. One of the simulation programs was used multiple times with different settings in an attempt to match the ϕ^* distribution of the data from CMS more effectively.

In Chapter 2 gives a general overview of the standard model including some basics of its history as well as how parts of it make predictions using perturbation theory impossible. The characteristics that can not be calculated with perturbation theory must be measured in order for them to be included in simulations. The possible effect of these errors is also discussed. In Chapter 3 a description of the detector used to collect the data analyzed in this thesis, the Compact Muon Solenoid, is given. This includes information on the methods of which the detector collects and processes events. Chapter 4 discuses how simulation samples are produced including the differences between specific simulation programs. An overview of the analysis method is given in Chap. 5, with the specifics of data collection and processing given in Chaps, 6 - 8. The direct results are given in Chap. 9, while the effects of changes to the simulation are shown in Chap. 10. Last the conclusion is shown in 11.

2

Physics of Z Transverse Momentum

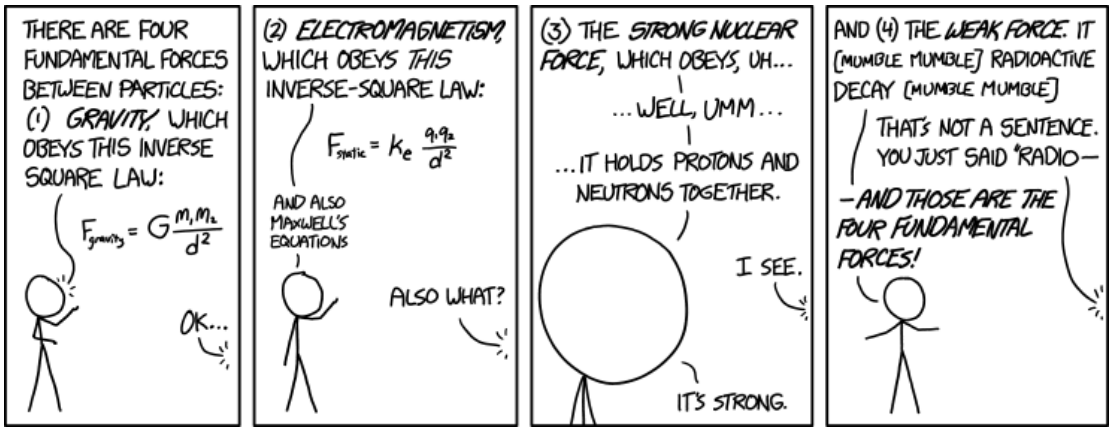

Figure 2.1: A `xkcd` comic explaining the four forces[4]

When discussing particle physics at a hadron collider it is useful to describe it in two major parts. The first part is the mathematical model that describes both the forces and the particles that make up the interactions. The second topic involves the interactions of hadrons, which can not be calculated using first principles, due to complications of the strong force. This section outlines both of these topics.

2.1 The Standard Model

Our current understanding of the fundamental constituents and forces of the physical world has developed through a continuous interplay between experimental observations and theoretical understanding. The theoretical framework which encapsulates this process is called the Standard Model(SM), and benefits from major contributions from Weinberg, Glashow, Salam, and Higgs, as well as many others[5, 6, 7, 8]. The model is a relativistically-correct quantum field theory(QFT) that separates particles into two categories: fermions, which includes all matter (the most well known being the electron); and bosons, which are force carriers (an example of which is the photon, the force carrier of the electromagnetic force). The experiments have ranged in complexity from very simple experiments, such as the Rutherford's gold foil experiment[9] which showed that atoms have nuclei, to giant collider experiments, such as CMS, which discovered the Higgs boson. Despite the amount of effort that has gone into the production of the SM, it still is incomplete, with the most obvious missing piece being that it does not include the force of gravity. Within a broad range of phenomena however, SM does an excellent job of describing particle physics as we are able to observe.

In particle physics, the definition of a force is different than the definition given to introductory physics students, $F = ma$. Instead, force is defined as something that allows the state of the particle to change. A change in momentum through attraction or repulsion is considered a force, but so too is a change in any other physical property, such as transforming into a different particle. When these forces are first explained to people the explanation tends to go like Fig 2.1.

The following subsections describe the the three commonly described forces in the standard model, both their history as well as the types of interactions they are involved in. Of these forces the one that is most important to this thesis is the strong force in Sec. 2.1.2.

2.1.1 The Electromagnetic Force

Unlike other forces, humans are able to directly detect the electromagnetic force using a specialized organ - our eyes - albeit in a very specific energy range. As a result, the nature of light has been a topic of debate for centuries. In the 17^{th} century, Gassendi and

Descartes put forward two competing and seemingly contradictory theories. Gassendi suggested that light was composed of beams of tiny particles, while Descartes argued that light was a wave, similar to those we see in water. Though both theories had supporters, Newton agreed with Gassendi that light was a particle. In part because of the weight of Newton's name, the majority of the scientific community followed the assumption that light was a particle for over a century. However, this opinion was challenged when later observations into diffraction were difficult to explain using the particle theory of light. One of these is the famous double slit experiment, wherein two slits are created on an opaque sheet and light is shone through it. When light passes through these slits, it creates a pattern of dark and light lines on a sheet behind it. This is in contrast to the expected result based on the particle theory, in which it would have created two bright spots. Later, Maxwell successfully described light as an electromagnetic wave, appearing to settle the debate in favor of the wave theory[10].

Near the beginning of the 20^{th} century Max Planck studied black body radiation from a theoretical point of view. When using Maxwell's equations, an object should emit more energy at smaller wavelengths, with the amount of energy emitted asymptotically approaching infinity as the wavelength approaches zero. This mathematical prediction has been dubbed the "Ultraviolet Catastrophe." To match the theory with the experimental data, Planck found that radiation had to be emitted in quantized bunches with the form

$$E = h\nu, \tag{2.1}$$

where E is the energy of the particle, ν is the frequency of the light and h is a constant now commonly given his name[11]. This put a minimum energy requirement on radiation in the high frequency range, rectifying the ultraviolet catastrophe. Einstein took this even further by stating that all light, not just light emitted from a black body, is quantized. This quantization became known as the photon.

The contradiction between light being both a particle and a wave was resolved by the development of Quantum Field Theory (QFT), and specifically Quantum Electrodynamics (QED). QED describes electromagnetic interactions through the exchange of photons. Some simple examples are shown in Fig. 2.2. Of these interactions, Fig. 2.2a illustrates the most common: charged particles exchanging momentum via a photon,

specifically two electrons repelling each other. Fig. 2.2b, on the other hand, represents a way of particles changing at a more intrinsic level. As mentioned earlier, fundamental forces allow a particle to change state; in the case of the electromagnetic force when a charged particle meets its antiparticle it is possible for them to become a new type of particle/antiparticle pair. This example is an electron and an antielectron changing into a muon/antimuon pair. A muon is a Standard Model particle, similar to the electron but with around 200 times more mass[1]. Figure 2.2c shows pair annihilation, which can result when a charged particle meets its antiparticle; rather than becoming a new pair, they can become two high energy photons, with all the mass of the system converting to energy.

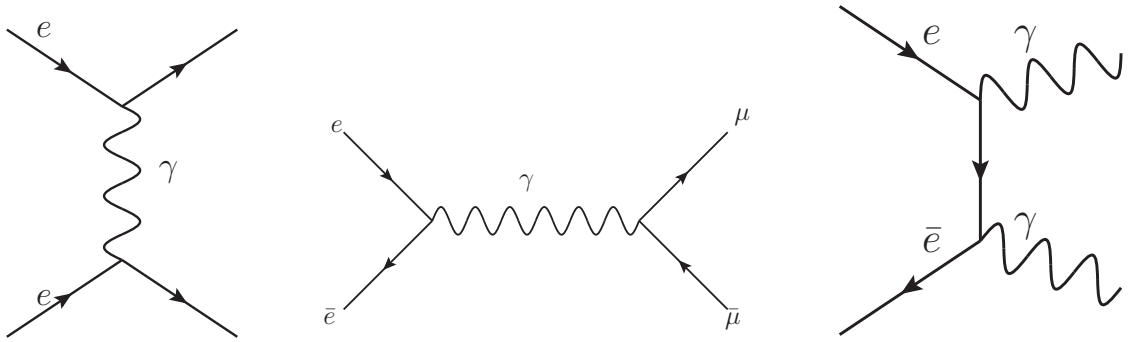

Figure 2.2: Examples of interactions involving the photon. The left figure shows scatter, with two electrons repelling each other. The center demonstrates fusion, with electron/antielectron forming into a photon, which in turn becomes a muon/antimuon pair. The right figure is annihilation, where a electron/antielectron change into a pair of photons.

2.1.2 The Strong Force

On the scale of an atom, the electromagnetic force can explain many properties of the universe, but it is incapable of explaining the structure of atomic nuclei. Neutrons, being uncharged, should not be bound in the positively charged nucleus; protons, being positively charged, should repel other protons. Thus, if only the electromagnetic force

[1]There exists one other particle that shares almost all properties with the electron and the muon, which is called a tau, with more mass than either of the other two.

existed, and assuming that the proton was a fundamental particle, the universe would consist solely of hydrogen atoms, i.e. atoms with only one proton. The force responsible for allowing complex nuclei to form is called the strong nuclear force, more simply referred to as just the "strong force." However, binding nuclei together is merely a residual effect of the strong force; its main function is to bind together the constituent particles that make up neutrons and protons. These particles are called quarks, with protons and neutrons being made of "up" quarks and "down" quarks. The proton consists of two up quarks and a down quark, while the neutron is made of two down quarks and an up quark. Similar to electrons, there are two heavier versions of both the up and the down quark, shown in Figure 2.5. Both the proton and the neutron fall in the overarching classification of a "hadron," which are particles made up of quarks.

The strong nuclear force operates by the exchange of "gluons" between individual quarks, working similarly to the way the exchange of photons cause the electromagnetic force to function. Even so, there are major differences between the two forces. Unlike the electromagnetic force, wherein a particle can have either positive or negative electric charge, the strong force interacts with "color" charge. This color charge has no relationship to the colors of the electromagnetic spectrum, but rather reflects our familiarity with the term. The color charge can either be red, blue, or green, and in the case of antiquarks, antired, antiblue, or antigreen. This naming convention was chosen due to the fact that stable combinations of quarks exist in sets such that the "color" of the set is either "white" or "black". This can either be done by having a set of three quarks, with the colors, red, blue and green, creating a white state or a quark/antiquark pair of opposite colors such as blue and antiblue creating a black state. Gluons also carry color charges, allowing them to self-couple; this is unlike a photon, which does not carry electric charge and therefore can not directly interact with other photons.

Although quarks need to be bound to other quarks to stay in a white or black state, if energy is added to a hadron this energy can be used to create new quark/antiquark pairs. This allows for two quarks to separate while staying in a "white" or "black" state, since they now have a new quarks to bind to that maintain color neutrality. If enough energy was added this can happen multiple times leading to two "jets" of hadrons going in the direction of the initial quarks. An example is shown in Fig. 2.3.

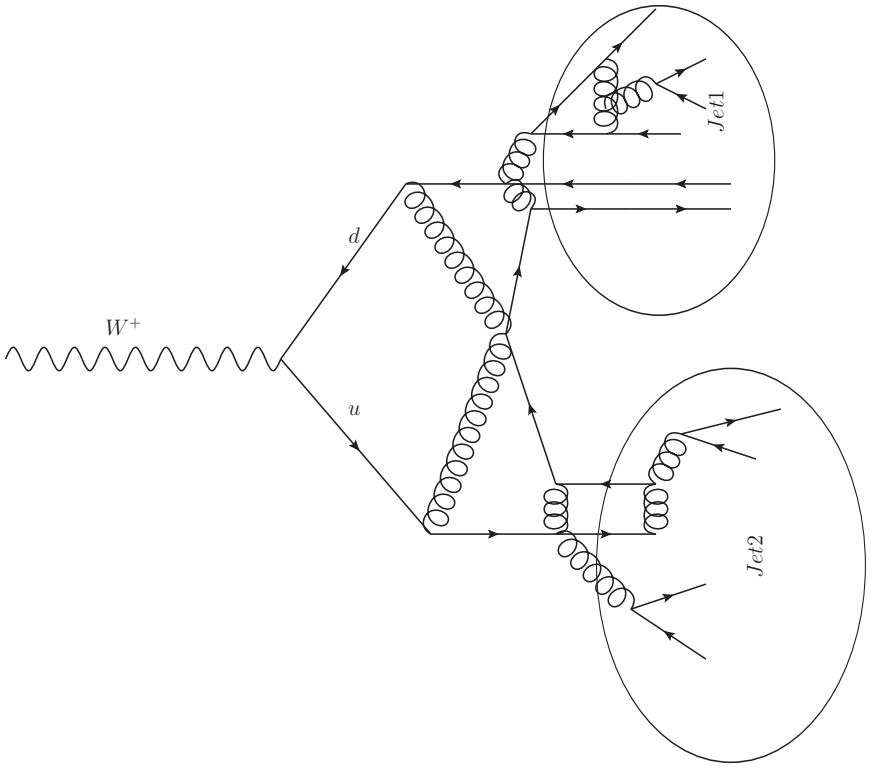

Figure 2.3: A W boson decaying to a quark antiquark pair. Due to the excess of energy this leads to the production of multiple new quarks, creating two jets of quarks moving in the direction of the initial proton

2.1.3 The Weak Force

The weak force interacts with almost all known particles (the exception being the gluon and the photon). However, the relative weakness of the force means that these interactions happen at a very low rate. The low rate is primarily due to the fact that all the carriers of the weak force, the two charged bosons W^+, W^- and the neutral Z, have mass, unlike the other two forces. This mass is extremely large compared to the fermions that make up stable matter, being around twenty thousand times heavier than an up or down quark, and two hundred thousand times heavier than a electron. Thus, the rate is so low at usual energy scales experienced on earth, that when compared to other exchanges, such as those that use the photon like in Fig 2.2a, momentum changes due to the weak force interactions are negligible. The exception is in cases where only the weak force is involved, such as neutrino interactions.

Instead, the weak force is known for allowing fundamental particles to decay. Unlike both the strong and the electromagnetic forces, which allow a particle/antiparticle pair to change into a different pair, the weak force allows a fundamental particle to change identity. The typical example given is beta decay as shown in Fig. 2.4, where a down quark inside a neutron decays to an up quark, leaving a final state of a proton, an electron, and an antielectron neutrino. Without this property fundamental particles such as taus and muons would not decay and would only be destroyed when they eventually interact with their respective antiparticles. By contrast, particles like taus and muons do decay on their own, and we only see instances of these particles very shortly after their creation.

The weak force also shows a major difference to the other two forces in that it does not respect parity. One of the first examples given to physics students is the beta decay of cobalt-60, whose decay results in the emission of an electron. This electron tends to be emitted in the opposite direction of the spin of the atom. With a parity-conserving force, this type of decay would happen in both the direction of spin and the opposite with equal probability. The reason for this disparity is that the force carriers of the weak force do not interact with particles of different handedness with equal strength. The handedness of a particle is related to how spin is correlated to its momentum. At high velocity, a particle is right-handed if the momentum matches the direction of its spin, while it would be left-handed if the spin was the opposite of its momentum. In

the case of the two W bosons, they only interact with left-handed particles and right-handed antiparticles, while the Z boson can also interact with right-handed particles and left-handed antiparticles, but not at the same rate.

The weak force is also the only force that can interact with neutrinos. These particles were first predicted when studying beta decay. When an atom underwent beta decay, the energy of the emitted electron was not a set value. According to the conservation of energy, the energy of the electron should be the mass lost during the decay, which is constant for each decay. Experiments, however, saw that the energy was a continuous distribution. Therefore, it was hypothesized that the energy was being carried off by an invisible neutral particle. This particle, being neutral in both electric charge as well as color charge, did not interact with either the electromagnetic force or the strong force, which made it invisible to detectors at the time. This particle was dubbed the neutrino which has subsequently been observed and subject to much experimental effort.

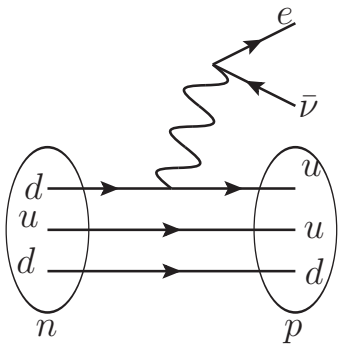

Figure 2.4: Neutron decay in which a down quark changes to an up quark, as well as an electron and antineutrino.

2.2 Colliders

The mass of the W is quite large (eighty times the mass of a proton), so powerful accelerators are necessary to create the energy to produce them. One type of collider is a lepton collider, such as the Large Electron Positron collider (LEP). Electron colliders are valuable since they produce very clean signals, due to the lack of beam remnants. They are restricted, however, by the synchrotron radiation which limits the energy that

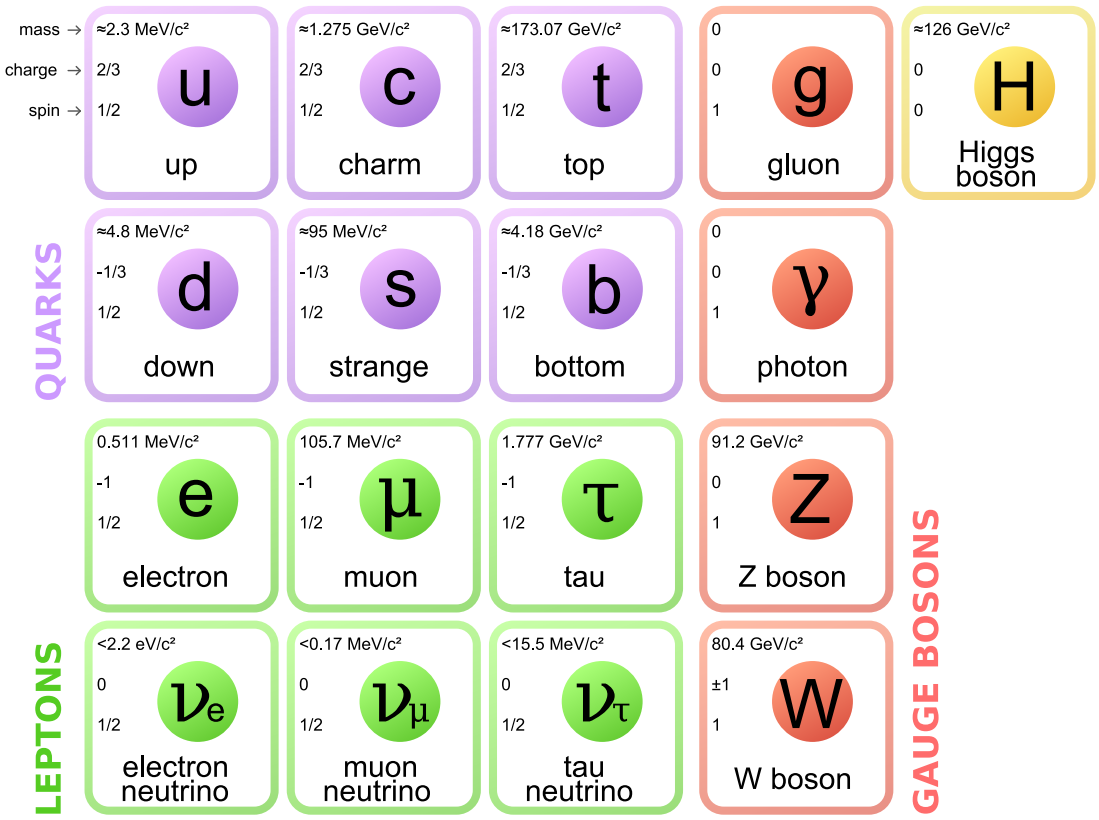

Figure 2.5: The particles of the Standard Model.

can be practically achieved. Thus, despite the clarity of the signals, lepton colliders have only discovered the gluon and the tau, as well as helping with the discovery of the charm[12][13].

Hadron colliders, which come in many types, have been instrumental in discovering many particles and confirming many theories. It is possible to reach higher energies than it would be with a similarly sized lepton collider, due to the larger mass of the hadrons which leads to lower energy loss due to synchrotron radiation, which aids the discovery of very massive particles. There are two main ways of colliding the particles, a two-beam setup and a fixed targetAlthough referring to a fixed target collider as a hadron collider is accurate, it is an uncommon to do so. The simplest type is a fixed target. Having a fixed target lowers the possible energies of the interaction, but it drastically increases the luminosity, versus experiments that collide two beams. This is due to the large density of a solid object compared to the density of a second beam. This type of accelerator was used in the discovery of the bottom quark, and tau neutrino[14]. The other type of hadron colliders collide two beams. These greatly increase the energy of the interaction point. One example is a Proton/Antiproton collider such as the Tevatron and the CERN's Proton-Antiproton Collider. These types of experiments have been used to great success in finding particles of the Standard Model such as the W and the Z bosons, as well as the top quark[15][16][17][18]. Another example of a two beam collider is a proton/proton collider. This includes the LHC, which is currently the largest collider in the world. In 2012 the LHC was used to discover the Higgs boson [19] which had been sought unsuccessfully with the Tevatron, among others. Hadron colliders do have a major drawback when compared to lepton colliders, in that collisions always involve beam remnants, leftover pieces of the proton, that complicate analysis of the interactions.

At the LHC, one of the main modes of proton/proton interactions producing a W ($pp \rightarrow W+X$) is shown in Fig 2.6. The resulting decay process of the W includes a neutrino, which is undetectable by the detector, complicating the mass measurement of the W. In order to directly measure the mass of a particle that decays practically instantaneously, the properties of the decay products must be known, either through direct measurement or by other means. It would be possible to reconstruct the energy of the neutrino by measuring the missing momentum, however the momentum of all other

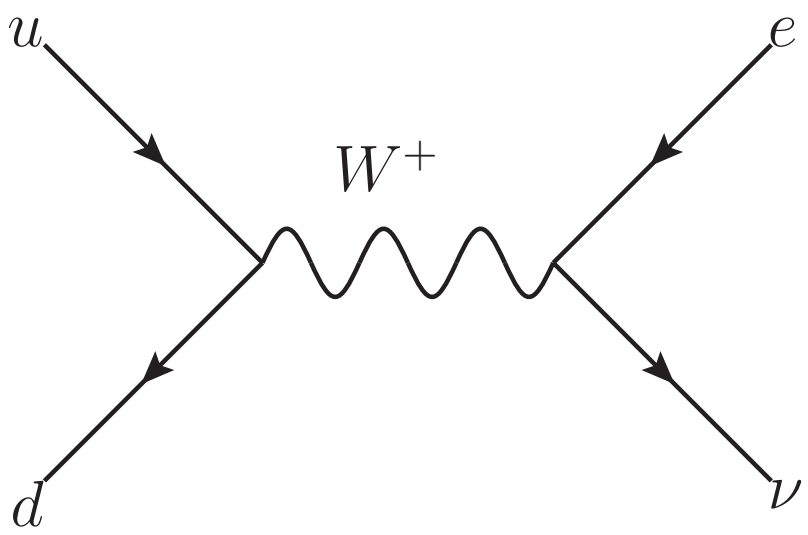

Figure 2.6: This is an example of a W^+ production in a pp collision.

particles in the interaction must be known. Although the momentum of the protons are well known, each quark carries only a fraction of it, and not a constant fraction as the quarks are in constant motion inside the proton. This is further complicated since the leftover quarks, ones not involved in creating the W, are capable of going down the beam pipe, and not interacting with the detector, therefore it is impossible to measure their momentum.

In addition to the momentum carried by the real quarks, momentum is carried by the gluons, which hold the quarks together. These gluons are capable of producing new $q\bar{q}$ pairs, which is of particular importance in the production of the W. As was mentioned earlier, protons are described as being made of three quarks. In order to create a W, a source of antiquarks is required, in this case gluons. This adds further complications to predicting the momentum of the initial particles, removing the possibility of measuring the W mass directly. Instead, in order to calculate the mass of the W, measured events are compared with an array of simulations that contain different masses. This requires all other aspects of the simulation to be accurately modeled. The uncertainty of many of the components of these simulations, such as the motion of the quarks within the

proton, leads to a large uncertainty in the calculated mass of the W which needs to be minimized.

2.2.1 Parton Distribution function

As mentioned in the previous section, quarks within a proton do not carry a constant fraction of the momentum of the proton. The momentum fraction is described using a probability distribution $f_i(x_i; Q^2)$ with Q^2 being the energy scale of the interaction, and x_i being equal to the fraction of the proton's momentum carried by the particular parton(quarks and gluons that make up the proton). Rather than the intuitive limit

$$\lim_{Q^2 \to \infty} f_i(x_i; Q^2) \approx \delta(x_i - 1/3) \tag{2.2}$$

that one would expect at high energies, with each real quark containing 1/3 of the proton's momentum, as the quark's motion in the proton becomes small compared to the proton's motion in the accelerator. The strong force allows the quarks to drastically change their momentum with respect to each other while staying confined by the exchange of gluons, which also carry momentum. This is further complicated by the gluons splitting into virtual $q\bar{q}$ pairs(referred to as sea quarks) which also carry momentum. Unfortunately, the amount of momentum each quark and gluon carries is dependent on the strong force's interaction constant, α_s, which varies with Q as can be seen in Fig 2.7. As can be seen, α_s is larger then one for small values of Q, which makes it impossible to use perturbation theory to calculate $f_i(x_i; Q^2)$ using first principles.

Instead $f_i(x_i; Q^2)$ is calculated based on measurements made at specific values of Q^2. This function is called the Parton Distribution Function (PDF). Fortunately, although it is not possible to predict PDFs from first principles, it is possible to calculate a PDF at a new Q^2 based on a previous measured PDF using the Dokshitzer-Gribov-Lipatov-Altarelli-Parisi(DGLAP) equation [20][21][22][23]. Two example PDFs are shown in figure 2.8. In the left plot, the up and down quarks carry the majority of the momentum, as expected, since the proton contains two real up quarks and a down quark. However, as can be seen on the right plot, at higher Q^2 more of the proton's momentum is being carried by all the other types of quarks and gluons.

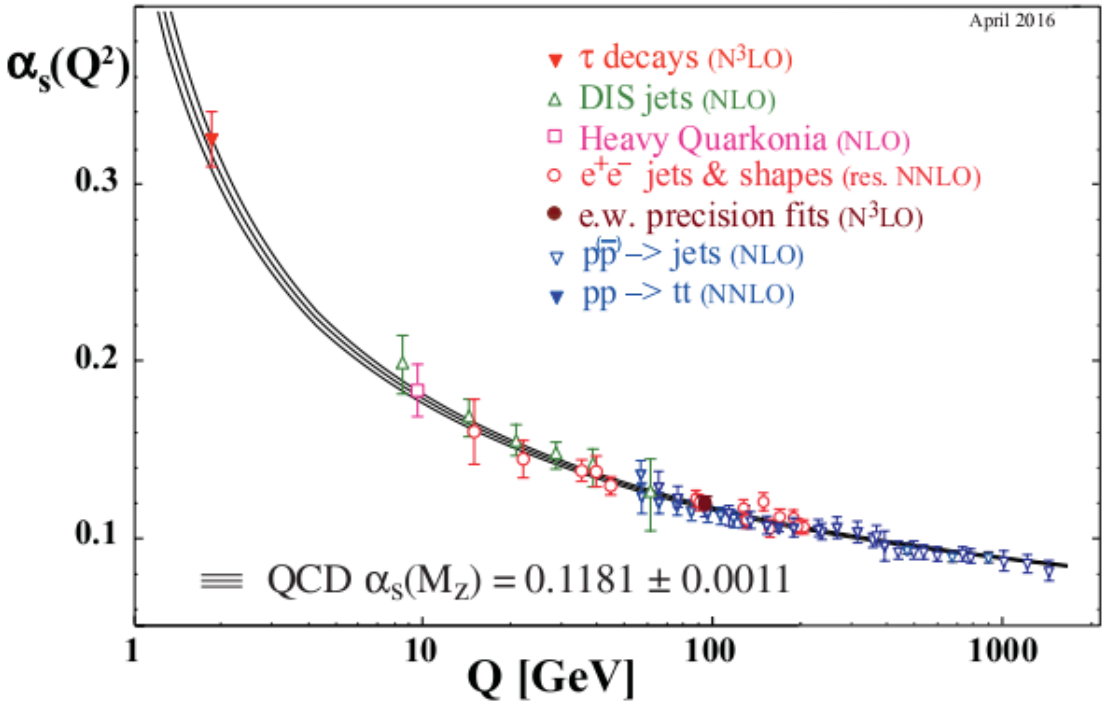

Figure 2.7: Strong coupling constant α_s as a function of Q. As can be seen as Q decreases α_s increases, being in the order of 1 for $1\,\text{GeV} < Q < 10\,\text{GeV}$.

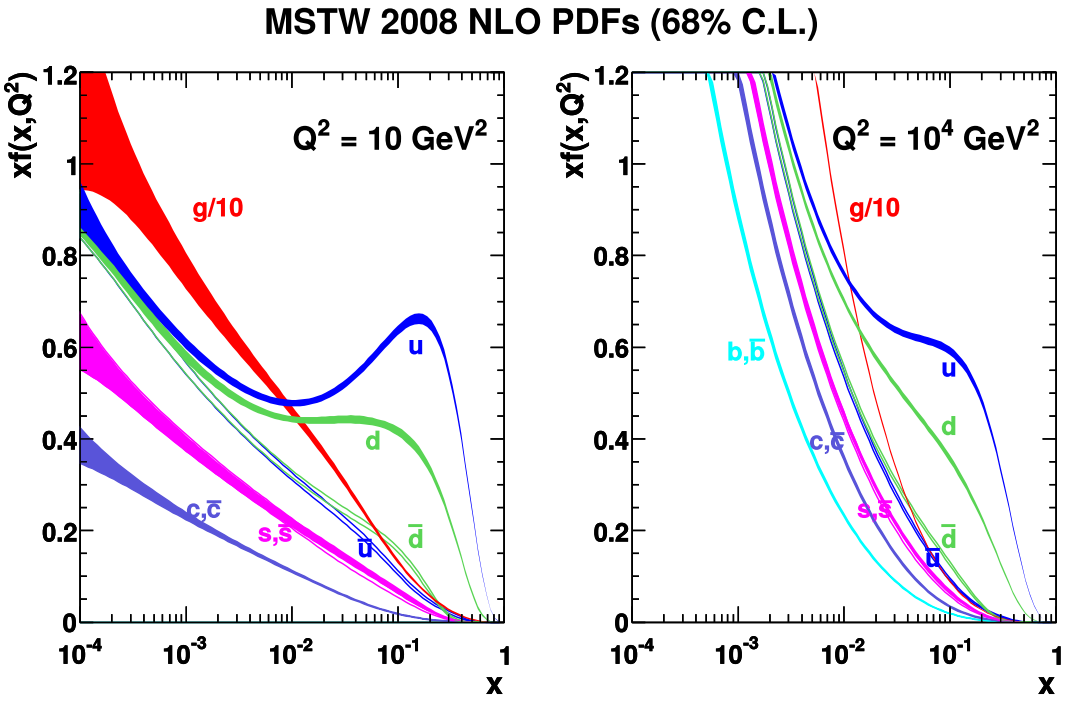

Figure 2.8: PDF examples for two different Q^2 from the MSTW collaboration including confidence levels [24]. The thickness of the line shows the uncertainty of the PDF.

2.2.2 Kinematics of LHC collisions

At the LHC the center-of-momentum frame for a particle produced from parton interaction(such as a Z produced from $q\overline{q} \rightarrow Z$) is not the same as the rest frame for the detector. Although normally the particle has very little momentum perpendicular to the beam direction, it often carries a large amount of momentum in the direction of the beam. Because of this, it is traditional to use measurements that are Lorentz invariant to a boost along the beam line. These include invariant mass (M) and momentum perpendicular to the beam line, otherwise known as transverse momentum (p_{T}). Also useful is rapidity, which is based on the energy of the particle(E), and its P_z:

$$y = \frac{1}{2} \ln \left(\frac{E + P_z}{E - P_z} \right). \tag{2.3}$$

Although y is not Lorentz invariant, it is still useful because the difference between two rapidities is Lorentz invariant. Although, as mentioned in the previous section, each parton in a proton can have wildly different momenta, it is highly unlikely for them to have a large transverse momentum (p_{T}). Using the assumption that they have neither mass nor transverse momentum, the 4-momenta of the two interacting partons can be described as a function of the center of mass energy of the two protons ($\sqrt{s}$) and the fraction of the momentum carried by the particular partons (x_1 and x_2):

$$p_1 = \frac{\sqrt{s}}{2}(x_1, 0, 0, x_1), \tag{2.4}$$

$$p_2 = \frac{\sqrt{s}}{2}(x_2, 0, 0, -x_2). \tag{2.5}$$

Using these two four-vectors it is possible to write equation 2.3 in terms of x_1 and x_2.

$$y = \ln \left(\frac{x_1}{x_2} \right). \tag{2.6}$$

It is then possible to describe x_1 and x_2 in terms of y, M, and s as

$$x_{1,2} = \frac{M}{\sqrt{s}} e^{\pm y}. \tag{2.7}$$

This is useful because, although we cannot measure the momentum of the partons, we

are able to use measurable quantities of the interaction (in this case the mass and the rapidity) to calculate the momentum of the initial particles.

2.3 Understanding the initial conditions in hadron collisions

Understanding the quarks that are involved in the production of particles of interest in hadron collisions is vital for tests of the Standard Model that use them. Although it is possible to calculate many different hard interactions for different energies of quarks, this calculation can not predict final results without knowledge of the quarks properties(such as their energy, momentum, as well as type). Therefore, studying these initial conditions of a proton are necessary to do analysis that use proton collisions.

2.3.1 Importance of probing QCD for measuring mass of the W Boson

As outlined above, measuring the mass of the W boson (M_W) accurately is difficult to do in hadron colliders. Without improving this measurement it is not possible to tell if there is a disagreement between SM and the measured data. The W's most common decay, $W \rightarrow q\bar{q}$ creates two jets (Fig. 2.3). In hadron colliders, the strong force produces jets at high enough rates that it is not practical to attempt use them to measure electroweak physics which is discussed in more detail in Sec. 3.3.2. Therefore the best decay channel for measuring M_W is $W \rightarrow l\nu$. In this technique the p_{T} of the lepton is compared to simulations, with an example shown in Fig 2.9. The technique, however, requires that the p_{T} of the W itself is accurately modeled. It is difficult since QCD interactions that boost the W by relevant amounts must be accurately modeled, but are impossible to predict using the SM because α_{s} is greater than one for low energy interactions. Since this model is not based on a calculable theory but rather attempts to fit data, it inherently can bring uncertainty into the system if the area being probed is not near where the model was based.

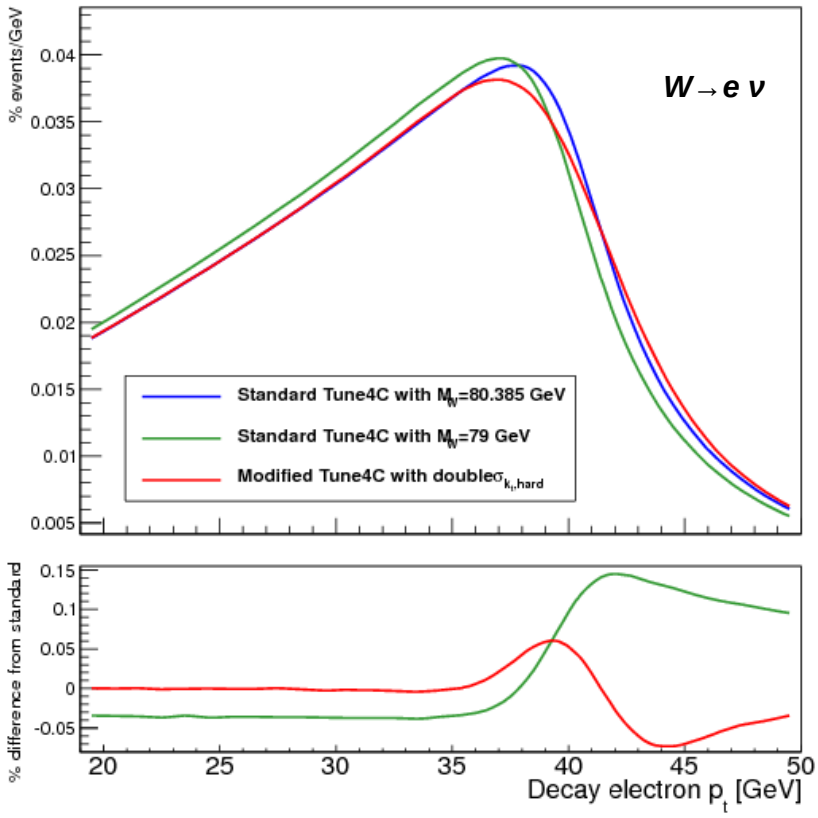

Figure 2.9: W boson lepton p_{T} of multiple simulated W bosons with changes to the W mass as well as other simulation settings.

2.3.2 Next-to-leading order production

Although, as can be seen in Fig 2.7, α_s is smaller than unity at energies that produce a weak vector boson, allowing for a solution to be solved perturbatively, this is not practically feasible. This is due to the large value of α_s at energies near the mass of the W boson with $\alpha_s \approx 0.3$, which would require at least 8th-order effects to be calculated to get the required accuracy. This is not practical with current technology since the time taken to compute an event increases at a rate faster than exponential as a function of its order. Instead, the current simulation makes next-to-leading order (NLO) corrections to the cross-section that come with the strong-coupling directly involving single gluon loops, and a hadronizer simulates the higher order effects. These higher order effects include situations that have extra terms in the final state as well as extra gluon loops. The emission of a parton during the process is of particular importance in the calculation of transverse momentum since they can boost the quarks that produce the boson in the transverse direction. For example one possible emission is a single gluon, as is shown in Fig. 2.10a. This emission can give the quark a transverse momentum. Because α_s increases at low energies, these gluons tend to have small momenta, so usually contribute small amounts of momentum to the boson. Thus, it is quite important to accurately model when comparing the low momentum vector bosons in data. Figure 2.10b shows a quark emitting a vector boson and interacting with a gluon. Unlike the case when the gluon is emitted, the quark can have a large momentum and generate a vector boson with a larger transverse momentum. Such an interaction can be accurately predicted by perturbation QCD calculations.

2.3.3 Using the Z Boson to more accurately measure QCD interactions

The Drell-Yan (DY) process produces a pair of leptons from the annihilation of a quark-antiquark pair in a hadron-hadron collision - a process that is almost exactly the same as W production in Fig 2.11. However, the Drell-Yan process differs in that both its final products are detectable which allows for direct measurements of the Z unlike the W. This allows all aspects of the prediction, such as the Q_T, to be compared to data with more precision than can be achieved using measurements of the W. By improving the accuracy of the Z simulation, the accuracy of the W can also be improved.

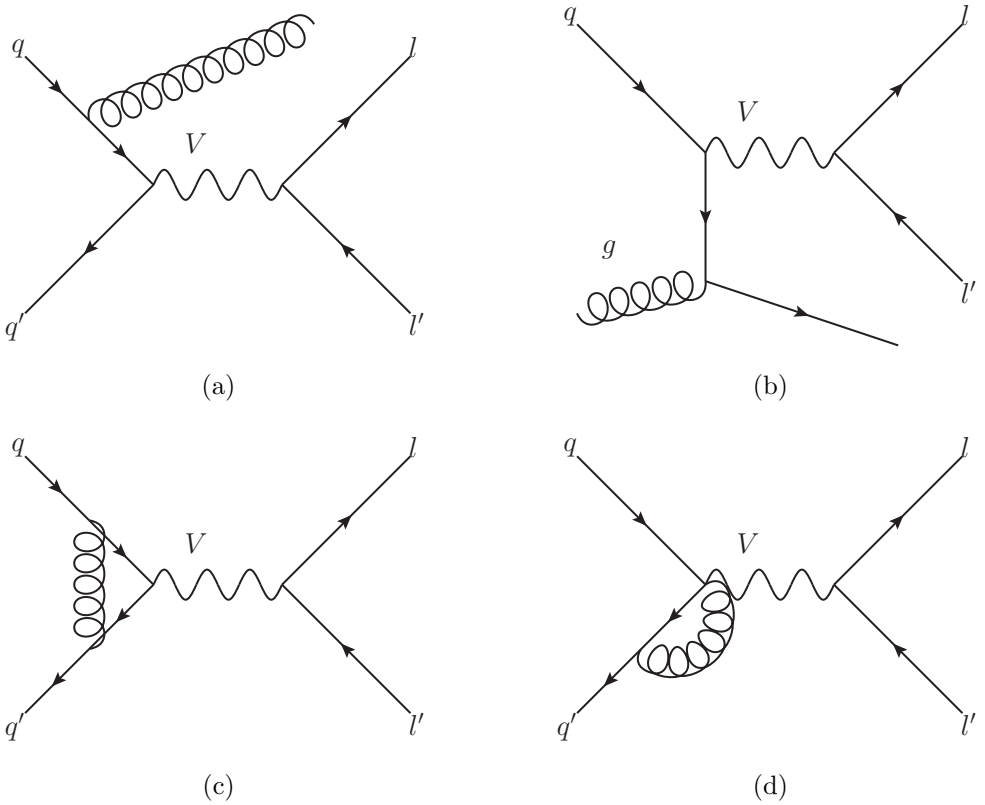

Figure 2.10: Higher order DY Feynman diagrams. a is an example of when an incoming quark radiates a gluon. In b the quark radiates a Z before interacting with a gluon. In both c and d the gluons interact with the quarks but are not radiated.

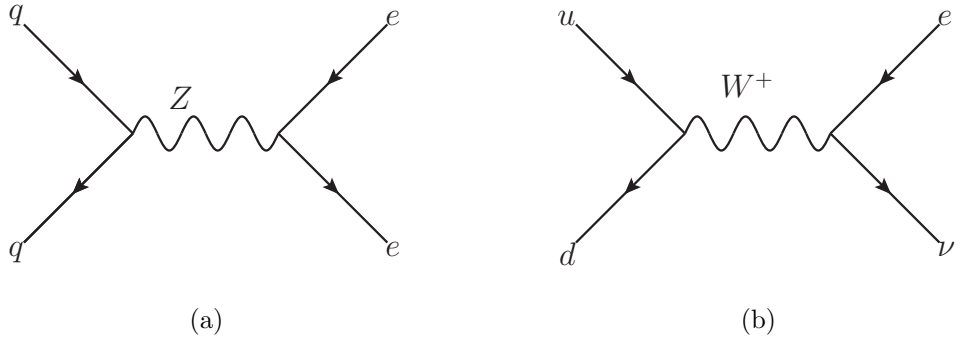

Figure 2.11: Fenymen diagrams showing quarks going to leptons. The left plot shows a quark pair going to a charged pair of leptons while the right plot shows a pair of quarks using a W to become a positron and an antineutrino.

2.3.4 Photon Emission

Despite the fact that the photon does not couple directly with the Z boson, it can either affect the measurement of the Z or the production of the Z itself. The most obvious examples are the case of Initial State Radiation(ISR) and Final State Radiation(FSR), both of which are shown in Fig 2.12. FSR is of particular importance for this study since the photon carries off some of the energy of the leptons. This can cause inaccurate measurements of the vector bosons Q_{T} since the decay products are used to calculate the properties of the vector boson. Happily, existing perturbation techniques are well-adapted to the necessary precision in this case.

2.3.5 Indirect measurements of Q_{T} using ϕ^*

With the current detector measurements, the energy of the electron has uncertainties of the order 1% due to systematics, as well as detector resolution. This leads to measurements of the Z having resolutions on the order of a GeV. As mentioned in Sec. 2.3.2, QCD radiation can give the vector boson a small boost in the transverse direction. For this reason, it is useful to compare the models to the data in the low Q_T region. However, the uncertainty of the measurements are of the order of the measurements themselves. Rather then measuring the Q_{T} directly, theorists have proposed using a variable named ϕ^* [3]. The variable ϕ^* is correlated with Q_{T} as can be seen in Fig 2.13. In this figure events tend to fall into bins that are in the diagonal with fewer events as you get farther from it. This demonstrates a high, simple correlation between the two variables with high Q_{T} implying a high ϕ^* and more importantly a low Q_{T} implying a Z with a low ϕ^*. The definition of ϕ^* is

$$\phi^* = \cot \frac{\Delta\phi}{2} \operatorname{sech} \frac{\Delta\eta}{2}, \tag{2.8}$$

where $\Delta\phi$ is the azimuthal opening angle between the leptons, and $\Delta\eta$ is the angle of the leptons with respect to the beam line in the rest frame of the dilepton pair. The variable ϕ^* can be measured precisely when compared to Q_{T} because the precision of the measurements of position and direction inside the CMS detector are, in general, more accurate than the measurements of energy. As can be seen from Fig 2.14, the relative error in reconstruction of Q_T to the simulated Z boson's generated value is much larger

than in the case of ϕ^*, with the majority of events of ϕ^* having errors below 5%.

This variable has been measured by different groups at different center of mass energies. This includes two measurements at the LHC: one by CMS at center-of-mass energy of 8 TeV[25], as well as one by ATLAS (another experiment at the LHC), which measured ϕ^* at center-of-mass energy of 7 TeV [26]. D0 also measured ϕ^* at the Tevatron at center-of-mass of 1.96 GeV [27][28]. However, each of these shows a difference between simulations and data that can not be explained by systematic errors. This thesis presents an attempt to tune the simulation to match the 8 TeV CMS data.

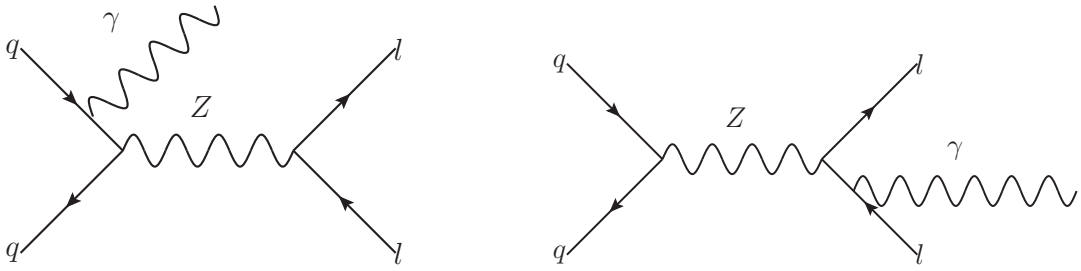

Figure 2.12: On the left is an example ISR in which one of the initial quarks produces a photon before fusing into a Z. The right plot shows a FSR example in which one of the leptons produced emits a photon.

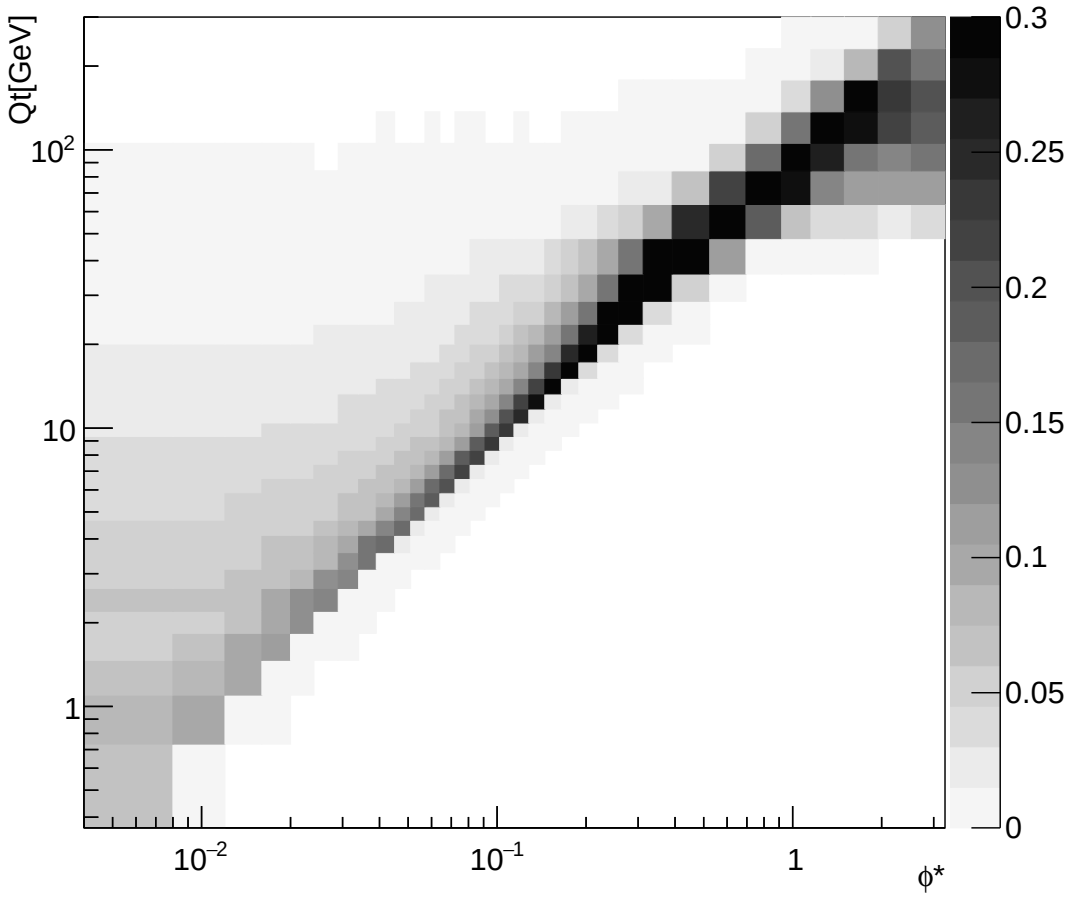

Figure 2.13: Two dimensional plot showing the correlation between ϕ^* and Q_{T} of the Z. A relationship between the two is clear with a strong diagonal line down the two dimensional histogram showing a high degree of corrilation between the two variables

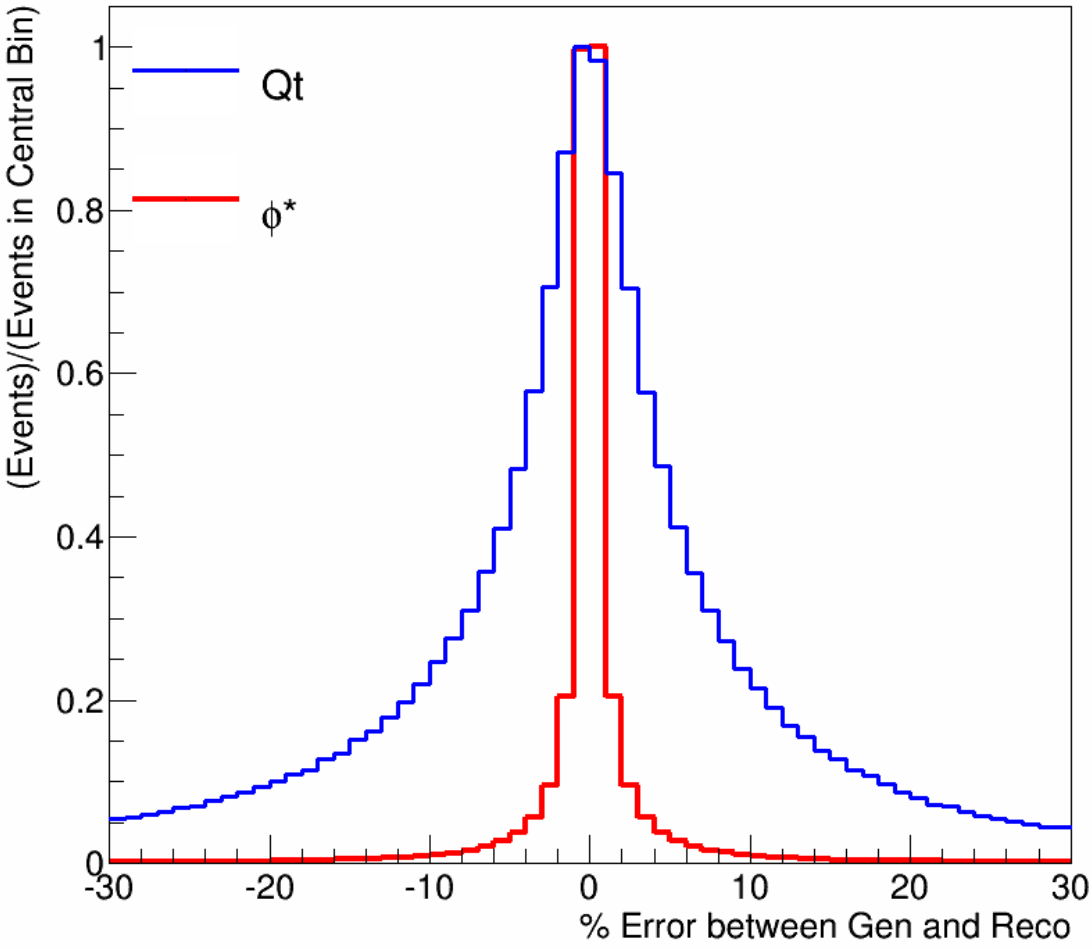

Figure 2.14: Relative error in ϕ^* and Q_T measurements of a simulated sample. The measurement of ϕ^* tends to have a relative error between the reconstructed and the generated value of a couple percentage points while the Q_{T} has an appreciable percentage of events over 20%.

3

The CMS Experiment

"When I read that, I was reminded of the medieval cathedral builders the architects who embarked on these grand projects knowing, or so the story goes, that they wouldn'tt see them to completion in their own lifetime. This selfless labor produced some magnificent architecture but while I admire the beauty of great cathedrals, ultimately theyre sterile; they produce nothing of tangible benefit to humanity. But the same is not true of the great modern scientific experiments, the cathedrals of our time. These grand projects, while built on the same soaring scale and evoking the same reactions of awe and wonder, prove their worth by producing knowledge that expands our vision of the cosmos and humanitys own place in it."

– Adam Lee, writing about the LHC[29]

Particle physics shares an odd relationship with size. It requires the largest machines ever made to look at the smallest things in the universe. This chapter discusses the pieces of the detector that were used to collect the data analyzed in this thesis. Although this thesis focuses on electrons produced by Z decays, which are measured by the two innermost subdetectors of the Compact Muon Solenoid, the other parts of CMS are still discussed due to their use in removing hadron backgrounds as well as identifying muons.

3.1 The Large Hadron Collider

The Large Hadron Collider (LHC) is a circular proton-proton accelerator that lies on the border between France and Switzerland [30]. The ring has a circumference of 27 km and is designed to accelerate two beams of protons to a center of mass energy up to 14 TeV in order to allow the study of interactions that require a high energy scale. The LHC was commissioned in 2008, and first produced proton-proton collisions in 2009. Initially, the collider was limited to a center of mass energy of 7 TeV due to concerns over magnet stability. Over time the beam energy has been increased - first to 8 TeV in 2012, from which this data is taken, followed by 13 TeV in 2015. Luminosity has also been increasing, as can be seen in Fig 3.1, which increases the rate of production of all interactions. The LHC is currently the highest energy accelerator in existence.

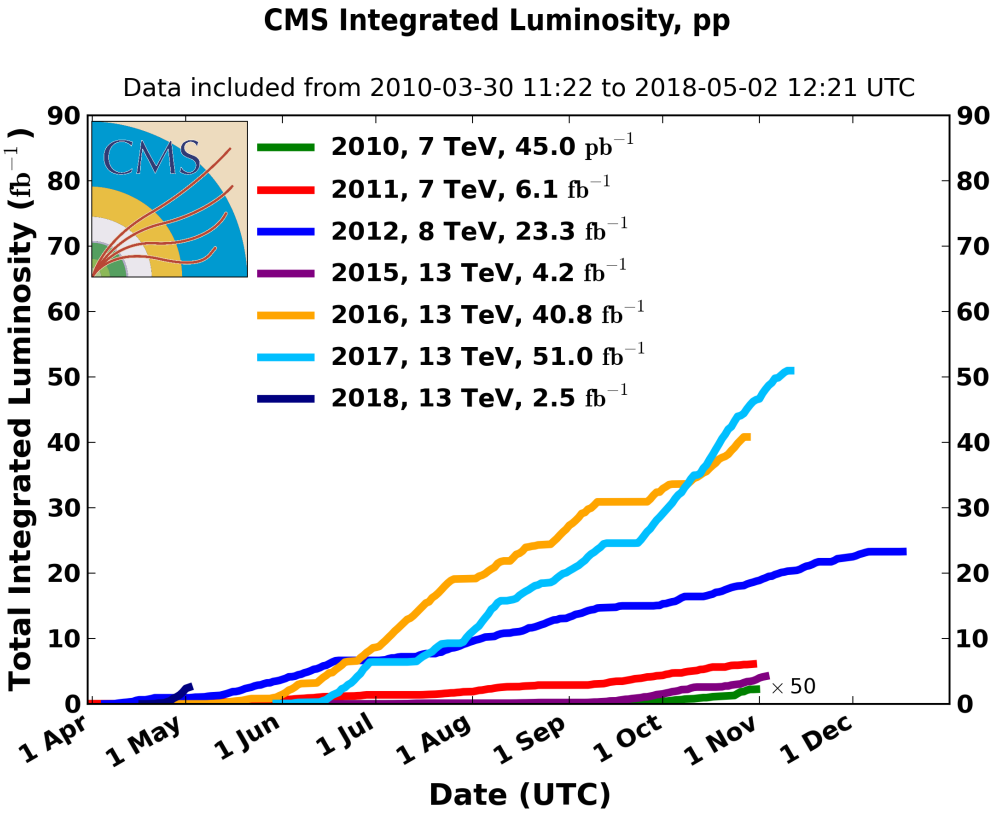

Figure 3.1: Comparison of luminosity of the detector. The luminosity has increased dramatically over the years.

3.2 The Compact Muon Solenoid

The Compact Muon Solenoid(CMS) detector is one of two general-purpose detectors at the LHC, and was designed to make precise measurements of the Standard Model and search for new physics. In order to accomplish this goal, CMS was built to get accurate and precise measurements of interactions by identifying and measuring the particles produced in collisions. These measurements allow the separation of events by the type of interaction which occurred, and then each data analysis selects a particular type of interaction as 'signal' and the others as 'background.' The CMS detector is made of four major sub-detectors(the tracker, the electron calorimeter, the hadron calorimeter, and the muon chambers) arranged inside or around the large solenoid for which CMS was named. This solenoid creates a magnetic field of over 3.8T, requiring a current of 20,000 A. The energy of the field is the same as half a tonne of TNT. This large field is required to get accurate measurements of charged particles momentum using the tracker. The entire detector weighs 14,000-tonne, or as much as 80 full-grown blue whales. A cut out view of the CMS detector as well as a person for scale is shown Fig 3.2 In hadron collider experiments, the angular coordinate from the beam axis, which would be labeled as θ in standard polar coordinates, is instead measured using pseudodity η. Pseudorapidity is defined as:

$$\eta = -\ln\left(\tan\left(\frac{\theta}{2}\right)\right). \tag{3.1}$$

Figure 3.3 shows a number of different pseudorapidity values and how they relate to the beam angle. The use of η is motivated by its relationship with rapidity(y), with $\eta \approx y$ for highly relativistic particles. Due to the kinematics of hadron colliders where the z-momentum of the collision is not fixed, many processes have a uniform rate over a significant range of y. Examples include particles in soft collisions, Fig 3.4a, as well as Z boson production, Fig 3.4b. As can be seen for the figures pions are produced at a nearly constant rate in the range, $|\eta| < 2.5$ and the Z boson is produced at a near constant rate in the range $|y| < 2$.

3.2.1 Tracker

The silicon tracker is the subdetector that lies closest to the interaction point and is used to measure and identify charged particles such as electrons. It is shown in green in

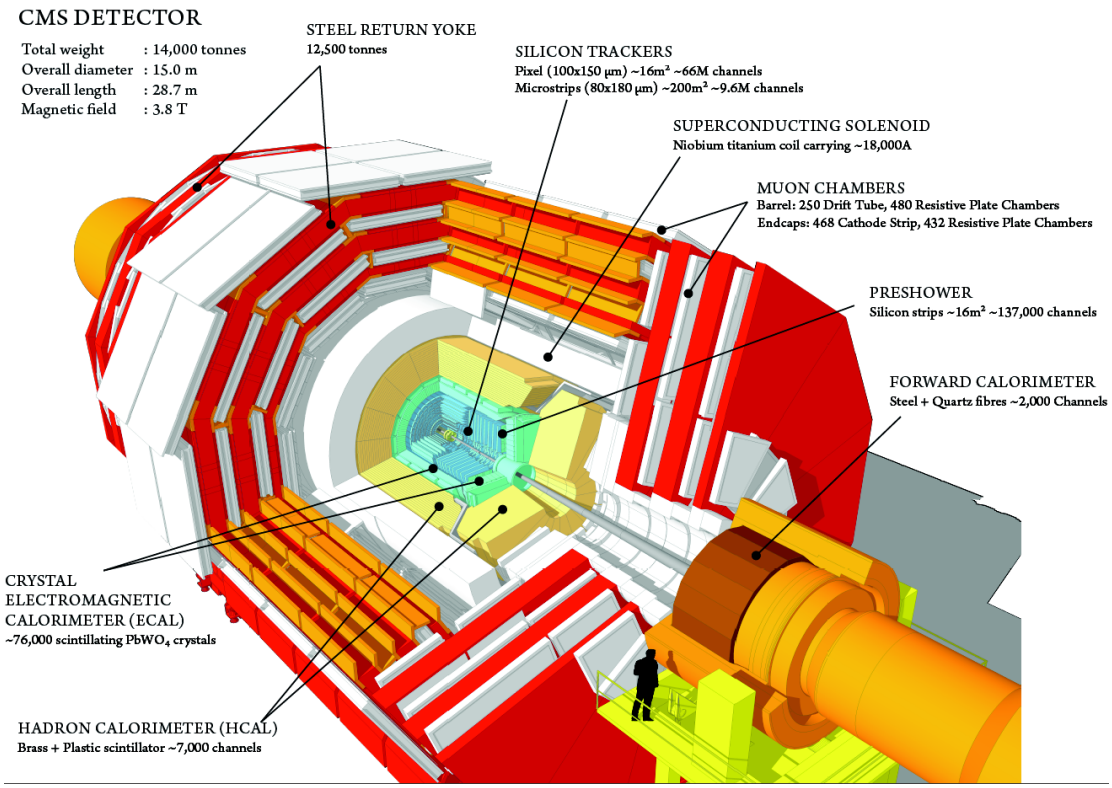

Figure 3.2: A view of the CMS detector with a person shown for scale. All major components, including subdetectors are shown.

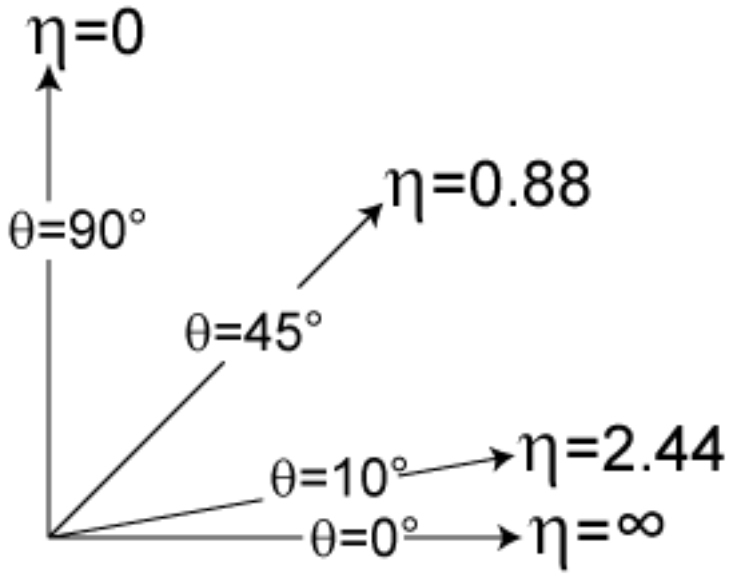

Figure 3.3: Pseudorapidity relationship to θ. As can be seen, although η approaches infinity at $\theta = 0$, $|\eta| < 2.44$ contains the vast majority of the phase space for a spherically-uniform interaction.

Fig. 3.2. It makes measurements of charged particles position over the range of $|\eta| < 2.4$ [33, 34]. The tracker is made up of silicon sensors that detect charged particles when they create ions in the sensors. The location of the charge deposition allows for the track of the charged particle to be reconstructed. Because the particles travel through a magnetic field, they curve in a predictable way related to their p_{T}. This allows the charged particle's momentum to be calculated based on its path.

The tracker is made up of two main types of sensors: pixels and strips. The layout of these is shown in Fig. 3.5. The pixels are used for the three layers closest to the interaction point. This is where the density of particles is highest, so a high granularity is required. Each of these pixels have dimensions of $100 \times 150\,\mu\mathrm{m}^2$, though the hit resolution is better due to charge sharing between adjacent pixels, which is itself dependant on the angle that the charged particle passes through the sensor.

As the distance from the center of the detector increases, the area that needs to be covered also increases, while the density of particles falls off. For this reason, it is not practical from a cost perspective to use pixels for the outer layers of the tracker.

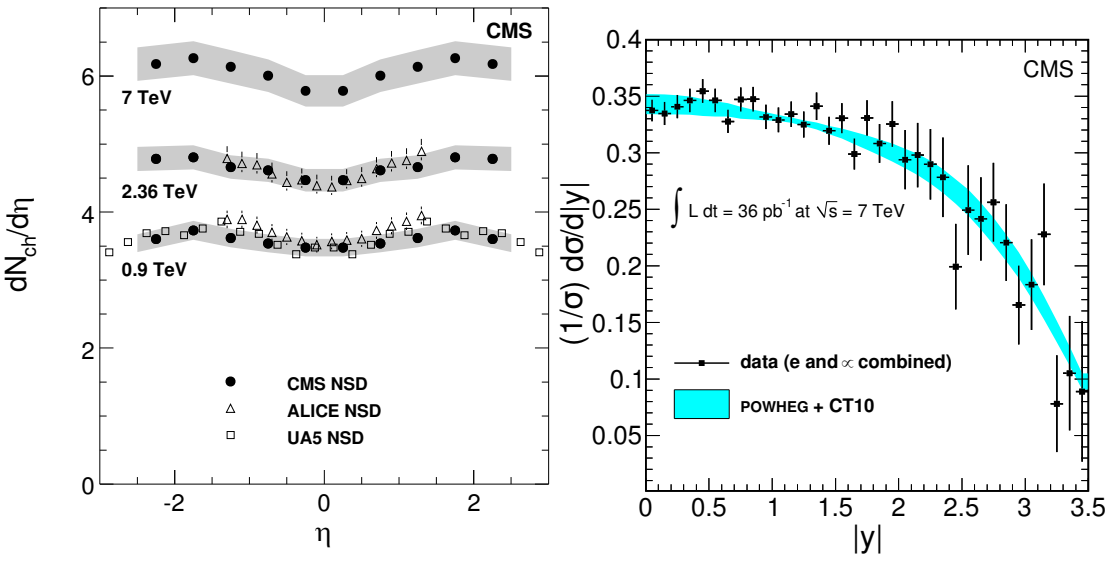

(a) (b)

Figure 3.4: The left plot shows the distribution of pseudorapidity for charged hadrons in underlying events at multiple center of mass energies [31]. The right plot shows the rapidity distribution of Z bosons at CMS at 7 TeV [32]. As can be seen from the plots both particle rates are relatively constant over a wide range of y and η with a cutoff inversely related to mass of the particle, with the cutoff for the Z being smaller than for the pions.

Instead, silicon strips, which are 220cm long in one dimension, are used. These can be separated into four regions: Tracker Inner Barrel, Tracker Outer Barrel, Tracker Inner Disk, and Tracker End Cap. These strips, unlike the pixels, individually give accurate measurements in 2D. In order to measure the third dimension accurately, there exist pairs of strips called stereo modules. These pairs of strips are offset by an angle of 100 mrad between the two layers. The Tracker Inner Barrel and the Tracker Outer Barrel are created out of strips that run parallel to the beam. This gives an accurate $r - \phi$ measurement which is necessary for p_{T} calculations. The Tracker Inner Disk and Tracker End Cap are made of strips that are perpendicular to the beam line, appropriate for particles moving in the forward direction(Fig.3.5). The tracker is the first step in a two-step system for both identifying and measuring electron properties, such as charge and momentum.

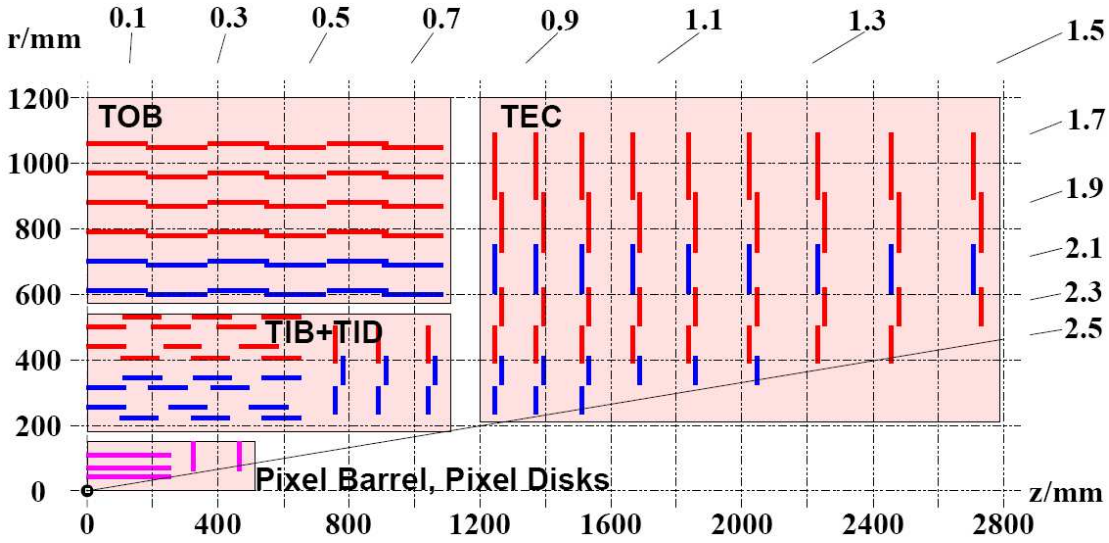

Figure 3.5: A quarter view of the CMS tracker. The blue lines represent strips sets of two strips that are slightly off parallel from each other.

3.2.2 Electromagnetic Calorimeter

The Electromagnetic Calorimeter(ECAL) is located directly outside of the tracker(Fig 3.2) and is vital for measuring the energy of electrons. It is made of lead tungstate ($PbWO_4$) scintillating crystals. When an electron or a photon enters a crystal they

create a shower of particles, through processes of bremsstrahlung and pair production. These particles excite atoms that make up the crystal, which in turn emit photons. By counting the number of visible photons produced, the energy that was deposited in the crystal can be calculated. Electrons and photons that make it to ECAL deposit almost all their energy into the crystals, allowing the subdetector to accurately measure their energy. However, used by itself, it is difficult to differentiate between the two. To resolve the ambiguity, the tracker is used since electrons, unlike photons, leave a track.

ECAL was created with the specification that it would be able to detect and accurately measure H$\rightarrow \gamma\gamma$, which set a tight requirement on the energy resolution. The other requirements on ECAL come from the size of the solenoid, since the ECAL must fit inside, as well as the high radiation environment. The closely-spaced bunches of the LHC require the ECAL to have a fast response (<25 ns). Lead tungstate crystals fulfill these requirements. It has a radiation length of $X_0 = 0.89$ cm which allows the crystals to be short, while having both the particles deposit most of their energy with a length of $\approx 25X_0$. It also has a Moliere radius(a measurement of how much the shower spreads out perpendicularly to the incoming particle) of 22.2 cm which allows for high granularity and a smaller chance of multiple particles showering into the same crystal even at higher luminosities. $PbWO_4$ produces 80% of its light in 25 ns, with the trade off of only producing 20 photons/MeV.

ECAL is made up of two main parts, the Electromagnetic Calorimeter Barrel , and the Electromagnetic Calorimeter Endcap as shown in Fig 3.6. The Electromagnetic Calorimeter Barrel covers the pseuodorapidity range $\eta < 1.479$. In order to measure the light produced by scintillation and Cherenkov radiation it uses avalanche photodiodes. The Electromagnetic Calorimeter Endcap covers the range $1.479 < |\eta| < 3.0$ and uses vacuum phototriodes. Both of these are sections created with crystals that are aimed almost directly at the interaction point. They have a slight tilt so that photons do not travel in the gap between crystals and become lost.

3.2.3 Hadron Calorimeter

The Hadron Calorimeter(HCAL), whose layout is shown in Fig. 3.7, is built around ECAL and was created to measure the energy of hadrons. Although this study does not use hadrons, HCAL is important in removing fake electrons. HCAL was built

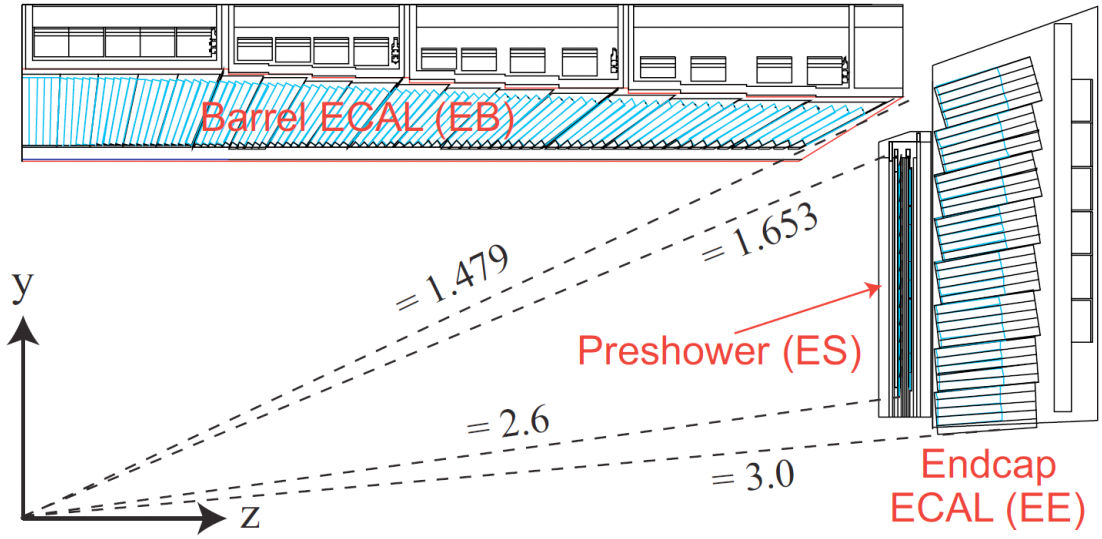

Figure 3.6: The layout of the Electron Calorimeters of CMS, showing the relationship of the barrel and endcap subdetectors.

with three major requirements. HCAL was required to be compact so that it could fit inside the solenoid, as well as being inexpensive, since the lead tungstate crystals that made up ECAL were so expensive. The last requirement was to measure energy in the entire detector so that E_T^{miss} can be calculated, which requires good energy resolution, as well as having no gaps that energy could be lost in. This is vital to finding the energy of non-interacting particles, such as neutrinos, as well as other non-standard model particles such as dark matter. In order accomplish these tasks, HCAL was constructed as a sampling calorimeter, which measures showers that are created by particles interactions with an absorber. The barrel and endcap, Hadron Barrel and Hadron Endcap respectively, of HCAL cover the pseudorapidity range $|\eta| < 3.0$. They are made of alternating layers of absorbers and scintillators. The absorber is made of brass, which was chosen due to its being non-magnetic, having a short interaction length, and low cost. The measurements of the energy are done with plastic scintillators that are sandwiched between the layers of absorbers. The light created by the scintillation is transported to hybrid photodiodes by way of wavelength-shifting fibers.

The Hadron Outer Calorimeter, exists as a single layer outside of the solenoid. Because hadrons have such a large interaction length, some of the hadrons are not

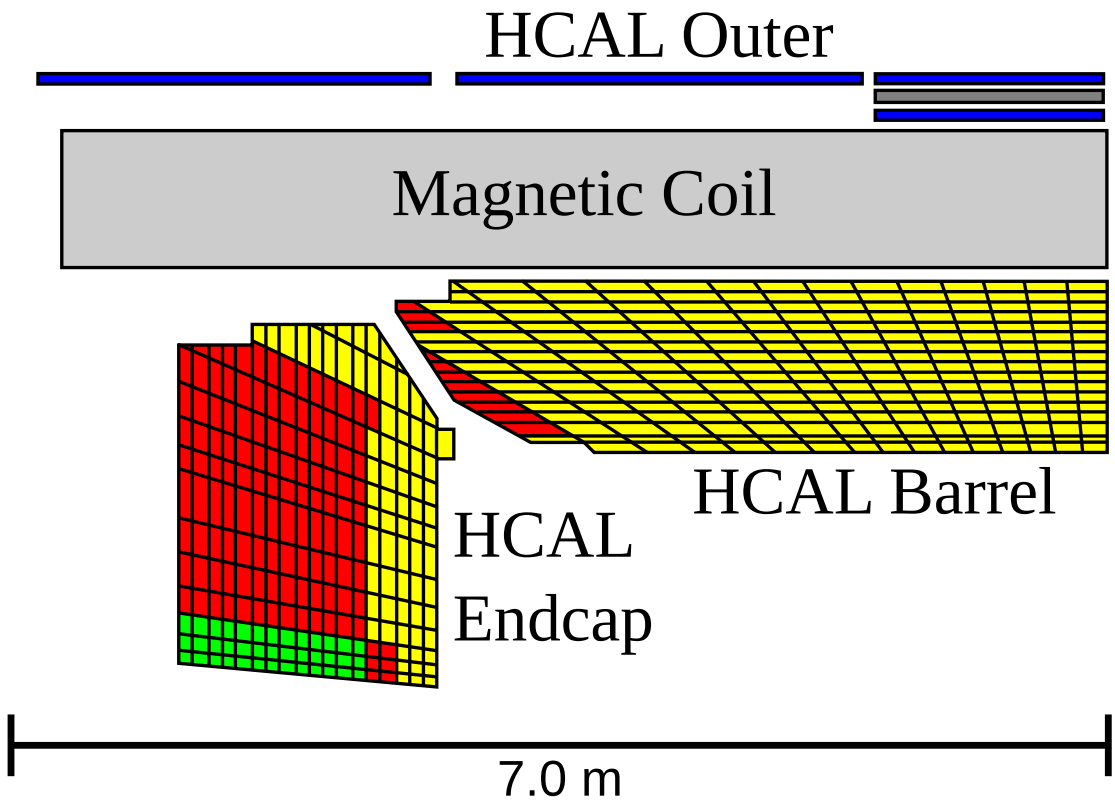

Figure 3.7: The Hadron Calorimeter layout of CMS. It lies directly outside of ECAL, and, therefore, only measures hadrons as well as the rare muon.

completely stopped by the end of HCAL, and can even go through the solenoid. This is more common at very low pseudorapidity since this region has the least amount of material to transverse. The Hadron Outer Calorimeter then can help catch the tail end of these showers.

The forward calorimeter covers the pseudorapidity range $3 < |\eta| < 5$. This subdetector is included for completeness since this study does not look at particles in this range of η. The high rapidity range means that this sub detector receives a higher rate of radiation, since the majority of particles produced in a hadron collision only gain a slight amount of transverse momentum leading to a high pseudorapidity. This then requires it to be more radiation hard then the rest of HCAL. It is made out of a bulk steel absorber with quartz fibers running through it pointed towards the interaction point. These quartz fibers do not scintillate; instead, the calorimeter detects Cherenkov radiation that charged particles emit when traveling through the quartz fibers. There are two different types of these fibers - short and long, with the long fibers capable of detecting particles throughout the entire sub-detector while the short fibers start 22 cm from the inner face of the steel absorber allowing for information of the depth of the shower to be measured.

3.2.4 Muon Chambers

The muon chambers surround the rest of the detector, including the solenoid itself(3.2). At this position almost all other observable particles produced have been absorbed, making the identification of muons much easier. The muon system measures muons' energy similar to the tracker, in that it measures the curve of the muon in the magnetic field. However, since the muon chambers cover a much larger volume than the tracker, it is not practical to use the same silicon sensors. Instead, gaseous detectors are used. These come in three types: drift tube chambers, resistive plate chambers, and cathode strip chambers.

Drift Tube Chambers

The drift tube chambers are used in the barrel region of the muon chamber, which covers the range of $|\eta| < 1.2$. They consist of a gas filled tube with a wire strung through the center that is kept at a high positive voltage(Fig. 3.8). When a muon travels through

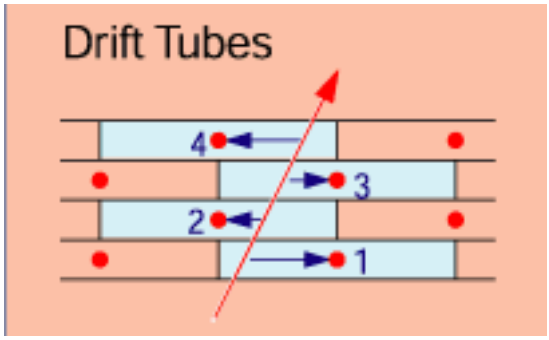

Figure 3.8: A diagram showing the cross section of a collection of drift tubes including the wire which collects the charge. The red line represents a muon traveling through them. the blue lines represent the charge that cascades onto the wires which are the red dots.

the chamber it ionizes the gas, leading to an avalanche of electrons to deposit charge on the wire. By measuring the timing of when this signal reaches both ends of the wire it is possible to calculate the position of the muon.

Resistive Plate Chambers

The resistive plate chambers are made of charged parallel plates that cover $|\eta| < 2.1$ (Fig 3.9). The positively charged plate is separated into strips, so that when an avalanche is created the muon's position can be measured. The resistive plate chambers have a worse position resolution then the drift tube chambers but a better timing measurement, aiding in crosschecks in the barrel region.

Cathode Strip Chambers

The Cathode Strip Chambers are used in the endcap, which covers $1.2 < |\eta| < 2.4$(Fig 3.10. Rather then having a single anode in each chamber as the Drift Tubes does, it is made up of chambers with positively charged wires and negatively charged copper strips, with the strips parallel to the radial direction, and the wires parallel to the ϕ direction. The electron avalanche deposits charge on a wire giving a radial measurement, while an image charge forms over multiple strips allowing for an accurate ϕ measurement to be made. This is done due to the higher η, which leads to higher background levels, as well as a less uniform magnetic field, both of which require more precise measurements.

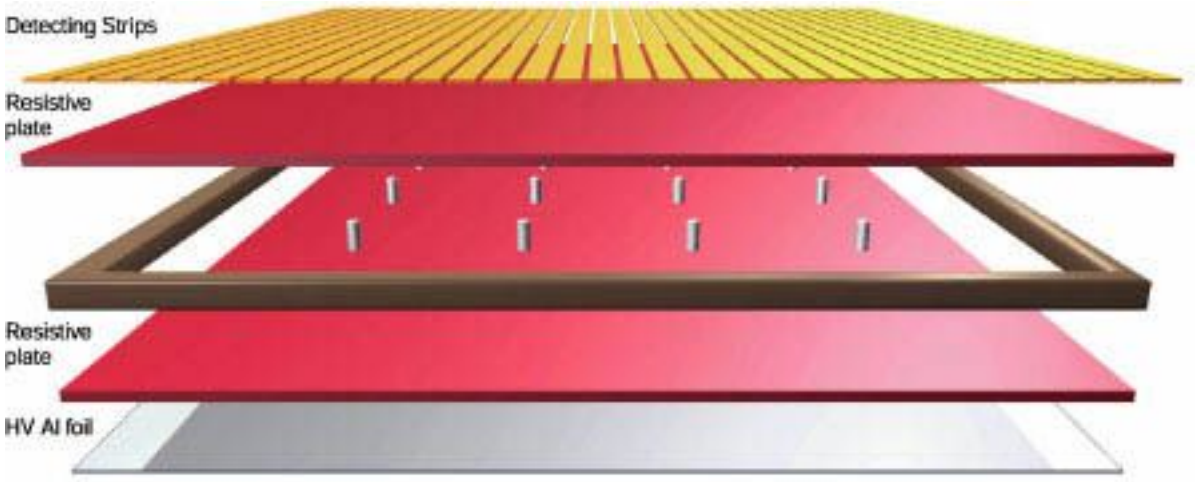

Figure 3.9: A diagram showing the make up of the Resistive Plate Chambers with layer labeled.

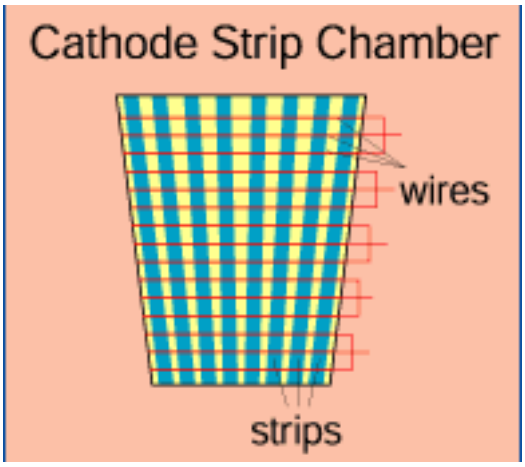

Figure 3.10: In this diagram the strips are all set up radially to the beam pipe. The red lines are the wires while the blue lines are the strips.

3.3 Data Storage and Triggering

Although creating a detector that is capable of working with the speed, and precision required while being radiation hard was perhaps the most obvious engineering issue in the creation of CMS, it was in no way the only one. Another obstacle is the sheer scale of the data produced. In 2012, bunches collided every 50 ns. Therefore it is impractical to save every event. Fortunately it is also not necessary, because the vast majority of events do not contain interesting interactions and do not need to be saved. Consider Fig 3.11, which shows the cross-sections (or rates) for a range of processes at the LHC. While the soft collisions may occur at nearly one GHz, interesting events such as Z boson occur at a few tens of Hz and $H \rightarrow \gamma\gamma$ at less than one per a hour.

3.3.1 Pileup and QCD Background

One of the important factors in triggering and data volume is pileup. Pileup occurs when multiple interactions happen in the same event. Because of the strength of the strong force, the vast majority of pileup events are QCD interactions. For each bunch crossing roughly 20 sets of protons interact, leading to large sprays of hadrons, the majority being pions. This pileup complicates measurements since it tends to deposit energy in multiple different parts of both HCAL and ECAL that must be compensated for. A second issue comes from jets produced from non-interesting interactions. As can be seen from Fig 3.11, jets, while not produced in every event, are still produced in a large fraction of events. Because so many events contain QCD-based jets it is difficult to have the trigger save events based on jets such as $W \rightarrow q\overline{q}$.

3.3.2 Trigger

Although beam crossing at the LHC happens at a rate of 40 MHz, data itself is only saved at, on average, a rate of around 400Hz. In order to decide which events to save, a two-stage trigger is used. The first stage, called the Level 1 trigger removes 99.75% of events, lowering the rate to 100KHz. It does this through customized hardware. Because the L1 trigger is required to make decisions at a high rate to keep up with bunch crossings, this hardware must be very quick. In order to accomplish this, L1 trigger looks at a very simplified version of the CMS detector. For example it does not

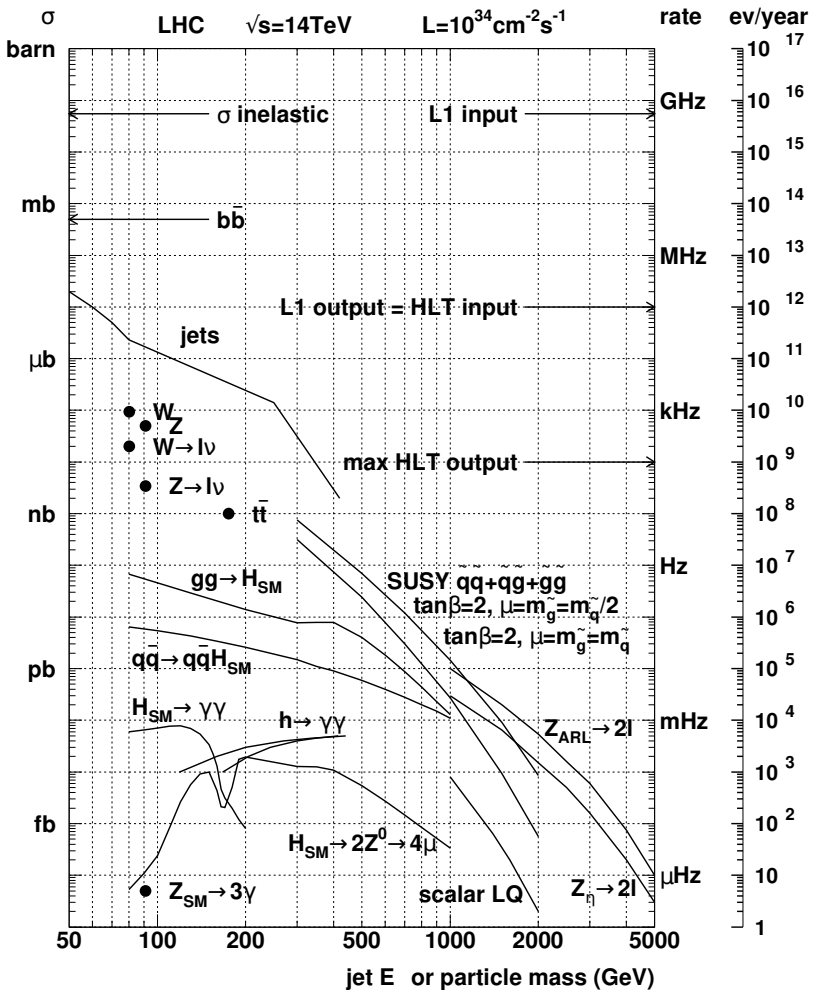

Figure 3.11: This shows the relative cross sections as well as rates for multiple different interactions in CMS. Theoretical particles cross sections are shown as a a function of their mass. As can be seen the Z to two leptons happens at a rate of less than one hundred Hz.

look at individual crystals of ECAL but clusters of them, as well as not looking at the depth information from HCAL.

The second trigger system is known as the High Level Trigger. Because the High Level Trigger only receives 0.25% of the events the L1 trigger receives, it can spend over 100 times longer making decisions, allowing it to use more sophisticated methods. This increase in time allows the High Level Trigger to make decisions based on the detector as a whole, as well as use more complex algorithms to make the decision. An example would be when attempting to trigger on electrons, the High Level Trigger could look for a charged track in the tracker that leads to a deposit of energy in ECAL, with little energy deposited in the corresponding section of HCAL. In order to be able to accomplish these tasks, the High Level Trigger uses and uses more standard computer hardware than the L1 trigger in the form of a computer farm. The High Level Trigger is able to remove 99.6% of bunch crossings that pass the L1 trigger.

3.4 Electron Reconstruction

The process of reconstructing the energy and momentum of an electron is an excellent example of the complementarity of the CMS subdetectors. At the limit of very low energy, the electron path is highly curved, allowing the tracker to very accurately measure its momentum, whereas at high energies the path becomes so straight that it is hard to measure its energy using the tracker. However at high energies ECAL becomes more accurate. By comparing the measurements of both the tracker and ECAL, particles can be measured over a wide range of different energies.

The two subdetectors also allow for the rejection of other charged particles, such as pions. This is done by comparing the energy measured by the tracker to the energy deposited by the particle into ECAL. Since pions tend to not deposit all their energy into ECAL, a mismatch between the two subdetectors is a sign that the particle is not an electron. This can also be used to remove photons, since they leave no track at all, so a crystal that has energy deposited in it with no corresponding track would be reconstructed as a photon. Even photons that happen to line up with a track can be rejected if the track's energy does not match the energy deposited in the crystal.

In practice, the energy deposited in a single crystal of ECAL can not be directly

compared to the energy of a track since the passage of an electron through the CMS tracker often involves significant scattering and emission of bremsstrahlung photons. These photons are not affected by the magnetic field of the detector so they travel in a straight line unlike the electron. When the electron does hit a crystal, the shower it creates bleeds into other crystals. In order to reconstruct the original energy of the electron, it is necessary to include these energies by measuring the energy deposited in a cluster of crystals near the central crystal. Super-clusters are then created to take into account the photons that were emitted due to Bremsstrahlung radiation. Because the magnetic field causes the electron to bend primarily in the ϕ direction, the super-clusters are not circularly symmetric, but extend further in the ϕ direction than in η. The super-cluster is then matched to a track from the tracker. The algorithm constructs an electron track using a Gaussian Sum Filter (GSF)[35]. This is a modified version of the standard Kalman filter[36] used for muons and hadrons, and was created to handle the large energy loss and corresponding large change in path of the electron when traveling through the tracker. The final η and ϕ measurement for electrons uses data from the tracker, while the energy measurement optimally combines ECAL and tracker measurements as a function of energy, putting more weight on ECAL as the momentum rises.

3.4.1 Corrections to the Electron

In order to increase the accuracy of the reconstructed electron, two sets of corrections are applied to the data as well as the reconstructed electrons in the simulation. These corrections affect the reconstructed momentum of the electrons. In general, the impact of these corrections is limited for the analysis described here, as the angle measurement of the lepton is more critical than the energy. However, because the acceptance sets a requirement on energy, the energy corrections do have some effect.

3.4.2 Regression

In order to improve the reconstructed energy of ECAL, a regression technique was used. This is necessary since the measurement of energy in the ECAL is affected by a large number of additional effects, primarily the loss of a portion of the energy of the electron

in cracks and dead materials. It is difficult to write an analytic correction for these effects but they are well represented by the simulation of CMS. To provide a correction, we categorize aspects such as shower shape, and the location in ECAL, as well as 39 other variables in an automated technique through a boosted decision tree. This is trained on $Z \rightarrow e^+e^-$ and $H \rightarrow ZZ$ simulation[37]. The regression was trained separately for both the Electron Barrel and Electron Endcap. Half of the sample was used to train the regression, while the other half was used for validation. Electrons used are required to have $p_T > 7\,\text{GeV}$, as well as have emitted less than 1% of its initial energy in the form of FSR. An example showing the effects of this regression are shown in Fig. 3.12. This example was picked due to how visibly the regression improved the measured value of the electron's energy. The reason for the vast improvement is this region includes electrons that are near the separation between the barrel and the endcap of ECAL, which exaggerates the impact compared with more uniform regions of the detector.

3.4.3 Energy Scale and Resolution

Energy scale and resolution effects were further corrected using two methods based on a $Z \rightarrow e^+e^-$ sample[38]. The purpose of this was to create better agreement between the simulation and the data for parts in which the simulation less accurately represents the detector.

In the first method, the data and simulations were fit with a convolution of a Breit-Wigner with a Crystal Ball function. The Crystal Ball function gets its name from an early spherical crystal calorimeter and the collaboration which developed the function to reproduce the characteristic response of a segmented total absorption calorimeter[39]. The Crystal Ball function is a power-law below a threshold value, and a Gaussian above the threshold. The Crystal Ball is used for modeling the detector resolution as well as losses in the tracker due to the bremsstrahlung. The Breit-Wigner distribution is used to model the resonance of the Z itself, and uses the nominal values from the Particle Data Group with a nominal mass of $M_Z = 91.1876 \pm 0.0021\,\text{GeV}$ and a width of $\Gamma_Z = 2.4952 \pm 0.0023\,\text{GeV}$[40]. Because the state of the detector changes over time, there is a time dependence of the scale correction, as well as an inherent pseudorapidity dependence. The fit was done for four different pseudorapidity bins as well as various run ranges. The scale correction, ΔP, was then taken to be the difference between the

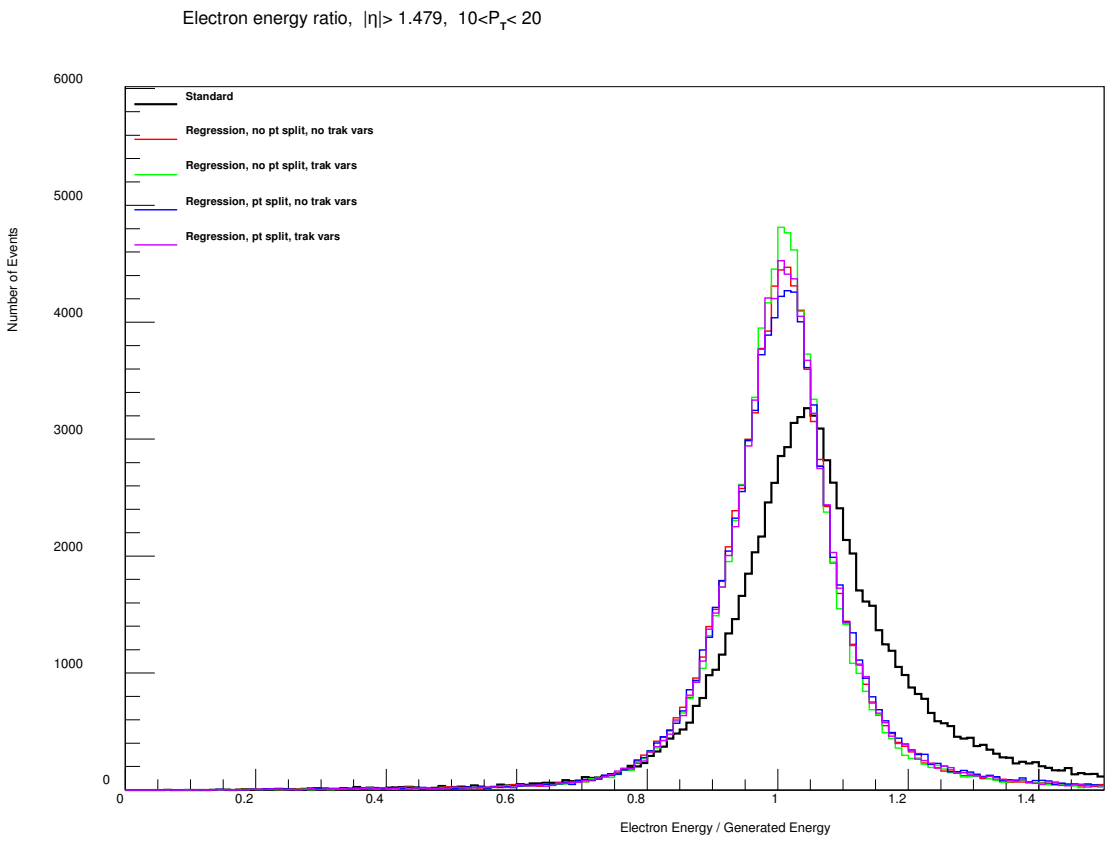

Figure 3.12: An example simulation showing the effects of the regression method on a specific subset of electrons. The ratio of generated energy of an electron to the reconstructed energy is on average closer to one after the regression

peak of the Crystal Ball function of both data and signal and is calculated using

$$\Delta P = \frac{\Delta m_{\mathrm{Data}} - \Delta m_{\mathrm{MC}}}{M_{\mathrm{Z}}}. \tag{3.2}$$

The second method further separates electrons based on the parameter R_9. This variable is defined as the energy in the 3×3 set of crystals around the peak of the shower over the super-cluster as a whole. Therefore, larger showers give smaller R_9 values. Showering electrons are defined as $R_9 < 0.94$, and non-showering are defined as $R_9 > 0.94$. A probability distribution function of the mass of the Z based on simulation is created in which the energy of each super-cluster in the simulation is multiplied by a Gaussian factor centered at ΔP with a standard deviation of $\Delta\sigma$. The $\Delta\sigma$ is calculated separately for both types of electrons, the four rapidity bins, and the different runs using likelihood maximization. In electron barrel, due to a large amount of statistics, it was also possible to further subdivide in terms of E_{T}, allowing for corrections to be created based on E_{T}.

4

Monte Carlo Generation

"Maybe the only significant difference between a really smart simulation and a human being was the noise they made when you punched them."

– Terry Pratchett, *The Long Earth*

Many theoretical models of the fundamental forces have been produced by physicists. Such models can predict the total rate or cross-section for interactions as well as, ideally, differential cross-sections as a function of an interesting variable (such as ϕ^*), allowing them to be tested by comparing them to measured results. However, some of these properties can not be calculated and some properties can not be measured directly due to limitations in experiments. These limitations include insufficient precision in measurement as well as cases where a fraction of events can not be observed by the experiment, such as when an electron is curved by the magnetic field and never reaches the detector, or cases where it travels parallel to the beam line. In these cases, applying the full theoretical calculations would require phase-space constraints and marginalizing over resolution variables in a highly complex manner. Rather than calculating continuous distributions, the Monte Carlo method is used to generate simulated events using physics and random numbers. These numbers are drawn from distributions that are either based on theory or measured results, and are used to create a simulated event. Simulated events can be subjected to detector simulation to model imperfections and can be processed identically to detector events. This chapter concerns the specifics of how these simulated events are created.

4.1 A simple simulation example

Here is a simple example of a simulation and the distributions used for $e^+e^- \to Z \to \mu^+\mu^-$. The differential cross section, assuming no higher order effects, is

$$\frac{d\sigma_0(s)}{d\Omega_{\mu^-}} = \frac{g_Z^4 s}{1024\pi^2} \frac{[(c_V^e)^2 + (c_A^e)^2][(c_V^\mu)^2 + (c_A^\mu)^2](1+\cos^2\theta) + 8c_V^e c_A^e c_V^\mu c_A^\mu}{(s-m_Z^2)^2 + m_Z^2\Gamma_Z^2}, \tag{4.1}$$

where c_V and c_A are the vector and axial coupling factors respectively, with $c_A^e = c_A^\mu = -0.5$ and $c_V^e = c_V^\mu = c_V \approx -0.04$, such that

$$\frac{d\sigma_0(s)}{d\Omega_{\mu^-}} = \frac{g_Z^4 s}{1024\pi^2} \left[\frac{\left(c_V^2 + \frac{1}{4}\right)^2 (1+\cos^2\theta) + 2c_V^2}{(s-m_Z^2)^2 + m_Z^2\Gamma_Z^2} \right]. \tag{4.2}$$

The variable Ω_{μ^-} is the angular phase space of the muon. In this case, the center of mass energy for each event ($\sqrt{s}$) could be held at the accelerator-defined value, leaving only two random variables: the azimuthal angle ϕ and the polar angle θ of one of the resulting muons, as they have equal and opposite momenta. The ϕ could be chosen from a flat distribution and θ would be taken from the differential cross section distribution. As can be seen in Fig 4.1, even after 100 events, the distribution of θ produced through the Monte Carlo method approaches the nominal distribution quickly.

In order to improve the accuracy of the simulation, Initial State Radiation (ISR) can be included, in which one the initial particles emits a photon ($e^+e^- \to Z\gamma \to \mu^+\mu^-\gamma$). This leads to a more complicated cross section as can be seen in Ref. [41] where it occupies three pages of text. This example is the simplest example with one photon, and ignores situations such as when the photon is absorbed by the other electron. As additional photons are added, the complexity would increases geometrically making it impractical to directly calculate even relatively simple interactions.

4.2 Structure of a Hadron Collision Simulation

Due to the composite nature of the projectiles in a hadron collider, simulations typically have two major pieces. The first step simulates the specific interaction using first

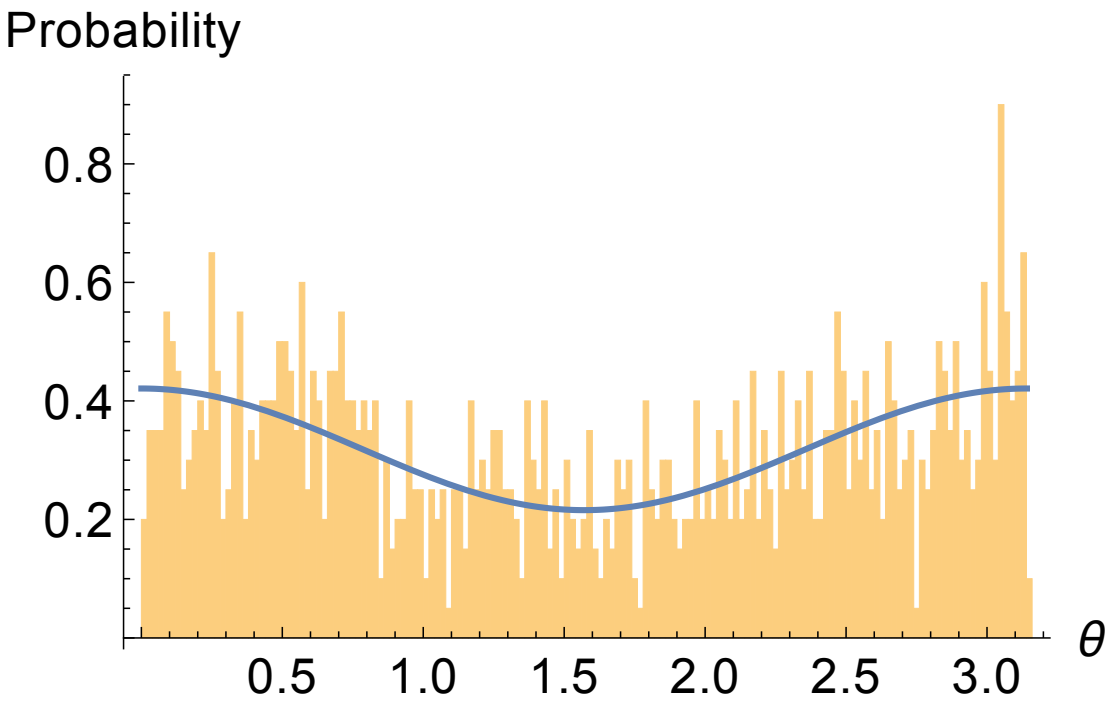

Figure 4.1: The probability distribution expected for the θ measurement of a μ produced by a Z based on Eq. 4.2 compared to a distribution created using 1000 randomly produced events using Eq. 4.2.

principles with a "generator." For the leading order (LO) case, this would mean simulating just the quarks directly creating a Z as can be seen in Fig 4.2. However, this is a non-physical event in that it has two quarks colliding directly rather than two protons, which contain multiple quarks as well as gluons. To complete the event, "hadronizers" are used. These pieces of software work backwards from the quarks to describe the proton they came from and the fate of the other partons of each proton, by describing QCD interactions. The hadronizer is also responsible for describing the process by which any final state quark or gluon eventually produces a collection of observable hadrons. Such collections, whether produced in the final state of the hard scatter or the initial proton fragmentation, are called **jets**.

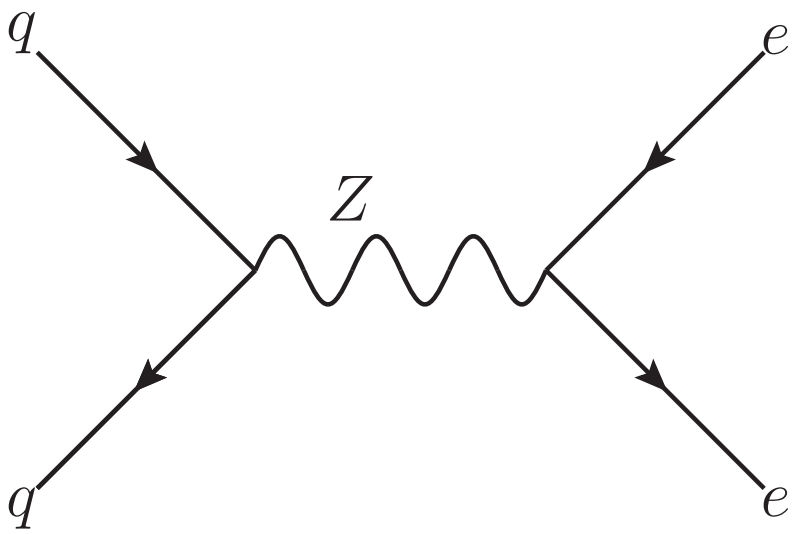

Figure 4.2: Simple $q\bar{q} \rightarrow Z \rightarrow e^+e^-$

Jets can be created when a large amount of energy is added to partons making up a hadron. As mentioned in Sec. 2.1.2, partons must exist in a colorless state. Normally the quarks and gluons that make up a hadron such as a proton are unable to separate. However, when enough energy is added to the partons, it is possible for new quark antiquark pairs to be created, allowing quarks to leave the confines of the hadron. An example is shown in Fig. 4.3, in which a photon is absorbed by a proton, which then

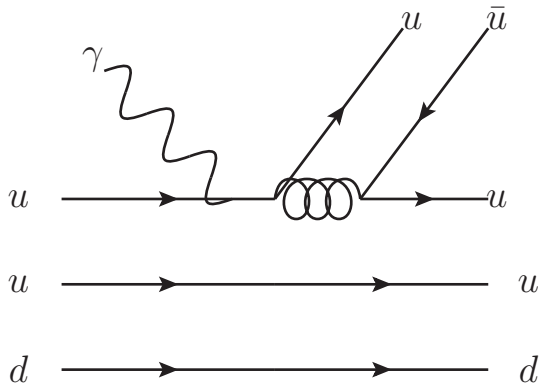

Figure 4.3: A simple example showing how energy added to a parton can produce an additional hadron

produces a $u\bar{u}$ pair. If enough energy is added to the system, the new particle can also create additional new particles, and so on, until all the new particles are near their ground state, leading to a collection of hadrons traveling in roughly the same direction.

When the hadronizer adds new particles to the simulation they are not added completely independent of the particles created by the generator. The new quarks and gluons can interact with the particles created by the generator, such as exchanging gluons or even by having the "generator" quarks produce gluons such as in the example shown in Fig 4.4. The initial quarks, labeled 0, are produced by a different generator such as POWHEG. The hadronizer then produces the particles in the order labeled. The choice of what particle to add and its momenta is influenced by the particular PDF that the hadronizer uses, with the PDF being called for each new particle added. These new interaction vertices are created in decreasing order of hardness, with the quark labeled 2 having the largest energy, followed by gluon 4 and so on. This is intuitive as virtual particles are only capable of existing for a very short time. When these quarks emit a gluon, they become more and more virtual, and therefore can only emit large energy particles right before they have their final interaction. These emitted gluons are capable of splitting into a $q\bar{q}$ pair and becoming a jet. The scale of these emissions are of the order of a few GeV.

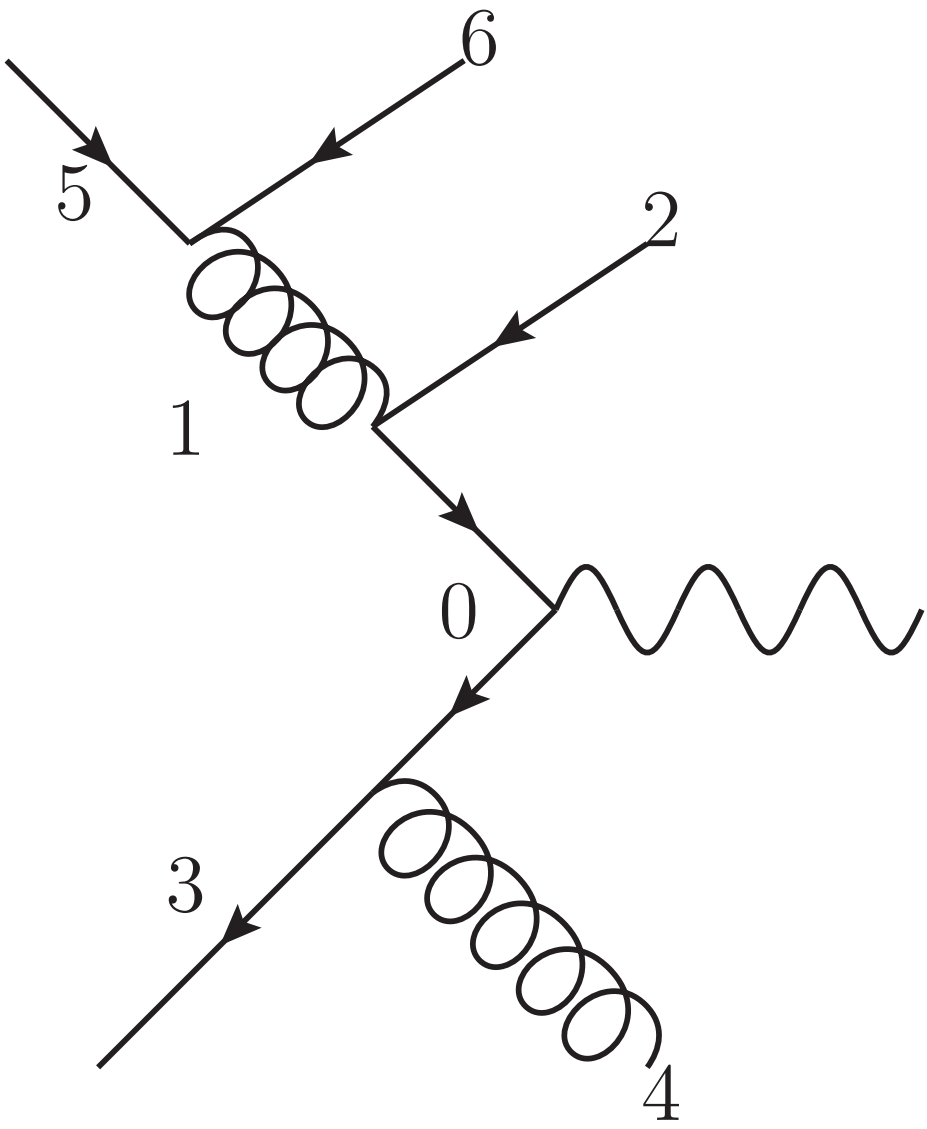

Figure 4.4: An example showing the order of creation of particles by PYTHIA. The 0 indexed quarks are the inputs to the system and are created by the generator, such as POWHEG.

4.2.1 PDFs and Simulations

As mentioned before, PDFs can not be calculated from first principles. Therefore, simulation software is fed premade PDFs. Although not uncorrelated, the generator and the hadronizer do not use the same PDFs. This is partially due to the fact the PDFs are related to the energy of the interaction, and the generator and the hadronizer are inherently focused on different energy scales. Despite this, each PDF can not be chosen completely independently from the other, due to overlaps in the phase spaces of their interactions. The choice of PDF can affect the final distribution as much as changing other aspects of the simulation.

An example of the effect these parameters have is shown in Fig 4.5, which compares the default Z rapidity distribution changing either the PDF of the hadronizer or the generator. As can be seen in the plot, the changes to the hadronizer do not change the rapidity distribution of the Z in a statistically significant way. However, changing the PDF of the generator creates a very noticeable change in the rapidity distribution. This is intuitive due to the difference in energy scales between the generator and the hadronizer. From Eq. 2.6, changing the PDF of the generator must change the rapidity distribution. In contrast, the hadronizer, which changes the quarks momentum and therefore the Z's momentum by only a few GeV, has a minor effect on the rapidity distribution. For energies on the order of the Z mass, the rapidity of any Z only changes on the order of 1% due to hadronizer effects. However the effect on the Z p_{T} can be larger as we will observe later.

4.2.2 Higher Order simulations

In order to increase the accuracy of the simulations, higher order generators are used. These include effects from extra gluons such as loops as shown in Fig 4.6. The increase in accuracy comes at a cost of increased complexity. In the case of next-to-leading order (NLO) simulation, one of the most important issues involves overlap of phase-space for produced gluons of both the generator and the hadronizer. As mentioned earlier, the value of α_{s} increases at lower energies, which limits the ability for generators to include low energy gluons. However, this lower limit is not well-defined; as α_{s} approaches unity the higher order terms have larger and larger effects on the output, but do not have an

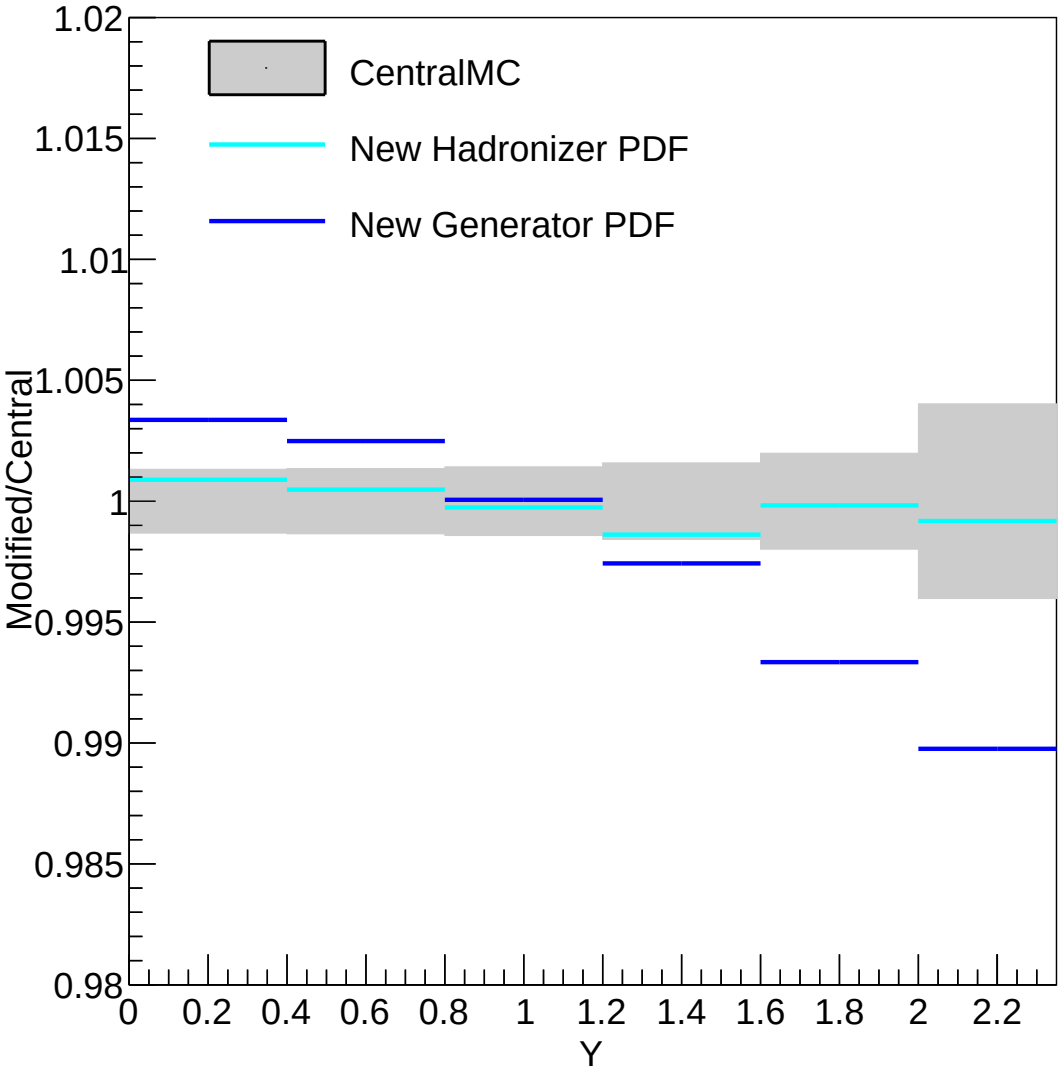

Figure 4.5: This plot shows the rapididty distribution of a Z boson produced by using POWHEG +PYTHIA8 after changing either the PDF of POWHEG or the PDF used by PYTHIA8

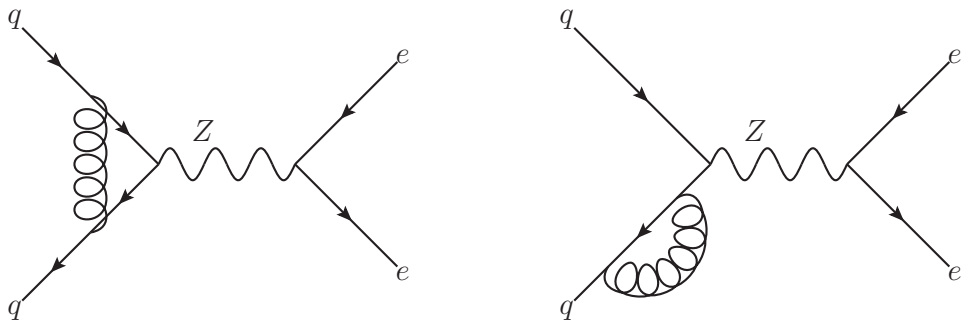

Figure 4.6: Higher order terms of the production of a Z. These include extra gluons that are involved in the production.

obvious cutoff. This causes issues in the case of gluon ISR with an example shown in Fig 4.7. For high energy, this gluon would be produced by the generator while for low energy this gluon is produced by the hadronizer. Intrinsically there exists an area where both phases spaces overlap, leading to a nonphysical excess of these types of events.

Multiple methods exist to correct for this overlap effect. One method has the generator create events with negative weights to cancel out this overlapping phase space. This requires knowledge of which hadronizer will be used with the output, as well as increasing the statistical uncertainty. Another method to avoid these negative weights and increase the flexibility of the hadronizers used is the Positive Weight Hardest Emission Generator (POWHEG). Using this method, a single jet is always created with the process of interest by the generator, and is defined as the highest p_{T} jet in the interaction. The NLO events thus produced can then be hadronized by any hadronizer that is p_{T}-ordered. Such p_{T}-ordered hadronizers create objects so that each new object has a smaller p_{T} than the other objects in the event, leading to $p_{\mathrm{T}1} > p_{\mathrm{T}2} > p_{\mathrm{T}3} > p_{\mathrm{T}4}$... Such a hadronizer can be combined very easily with POWHEG since POWHEG's jet's $p_{\mathrm{T}} = p_{\mathrm{T}1}$ by definition.

4.2.3 Initial State Parameters

The PYTHIA hadronizer is the most widely used software package for this task in HEP. Hadronizers use many parameters to calculate the final state of an interaction that were

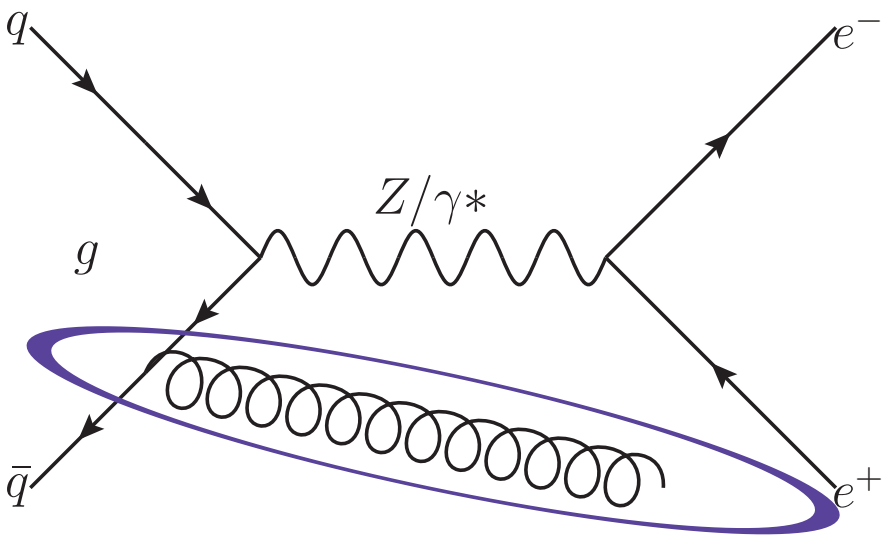

Figure 4.7: A gluon is being emitted from one of the initial quarks. This gluon can be produced by either the generator or the hadronizer tuning.

created in an attempt to match data. These are referred to as "tunes". By changing some of the values of these parameters, it is possible to attempt to better match the simulation to the data.

The quarks that make up a proton are in constant motion inside of it. This motion means that even when the proton is at rest, the partons that make up the proton all have some p_{T}. The p_{x} and p_{y}[1] of these particles is individually chosen from a Gaussian distribution. The width of this Gaussian distribution for each parton is defined as:

$$\sigma_{\mathrm{B}}(Q, m, y_{\mathrm{damp}}; \sigma_{\mathrm{soft}}, \sigma_{\mathrm{hard}}, m_{\mathrm{half}}) = \frac{(\sigma_{\mathrm{soft}} * Q_{\mathrm{Half}} + \sigma_{\mathrm{hard}} * Q)}{Q_{\mathrm{Half}} + Q} * \frac{m}{m + m_{\mathrm{half}} * y_{\mathrm{damp}}}. \tag{4.3}$$

This contains three variables that are event dependant, Q, m, and y_{damp}. Q is the hard process renormalization, which is dependant on the individual parton interactions, m the mass of the system, and y_{damp} is a variable that was created to damp the production of high p_{T} at high rapidity regions. Because of limits to our detector, this study does not contain many Z bosons of high rapidity, therefore y_{damp}, which was created

[1] As was mentioned in Chapter 3 the x coordinate points directly towards the centre of the LHC ring, and the y coordinate points directly up, and they make up the transverse plane.

to limit effects in the high rapidity region, is small. The other four components of this equation, σ_{soft}, σ_{hard}, Q_{Half}, and m_{half}, are set by the user and constant for each data set. Q_{Half} is the halfway point between hard and soft interactions, and m_{half} is the halfway point between low mass and high mass subsystem. The last two tuning parameters are σ_{soft} and σ_{hard}, the widths in the soft and hard interaction limits respectively. For the limiting cases, if the interaction is very hard($Q \gg Q_{\text{Half}}$) then $\sigma_{\text{B}} \approx \sigma_{\text{hard}}$, while for very soft interactions($Q \ll Q_{\text{Half}}$) $\sigma_{\text{B}} \approx \sigma_{\text{soft}}$. By changing these variables the distribution of the p_{T} of these initial particles will change, which can effect the momentum of the Z. In the example shown in Fig 4.4, each vertex will have a different σ_{B} that will be used to calculate the momentum of the ISR particles, 6, 2, and 4.

4.3 Specific production software

This analysis compared unfolded data to a total of five samples.

- MadGraph (v1.3.30)[42]+Pythia6 (v6.4.24)[43]. This sample was also used to both unfold the data as well as estimate the efficiency. The MadGraph generator used the PDF set CTEQ6L1 [44]. A k_T-MLM matching scheme was used [45], along with a Z* tune [46, 47] for the underlying event.

- MadGraph5_aMC@NLO+Pythia8 (v8.2). MadGraph5_aMC@NLO, commonly referred to as aMC@NLO. This new version of MadGraph is capable of creating events that are NLO accurate [48]. Pythia8 used the CUETP8M1 tune [47] using NNPDF2.3 LO PDF [49, 50].

- powheg +Pythia6. The powheg sample[51, 52, 53, 54] used a CT10NLO PDF[55]. It was then hadronized using Pythia6 with the Z* tune, as was used with MadGraph +Pythia6.

- powheg +Pythia8 (v8.2). The same powheg sample was also used for the powheg +Pythia6 was hadronized with Pythia8. The settings for Pythia8 were the same as for MadGraph5_aMC@NLO+Pythia8 (v8.2).

- ResBos [56, 57, 58] with CT10NLO

4.3.1 MadGraph and aMC@nlo

MadGraph is a very commonly used generator. It is very flexible, in that it can be given a theoretical model and produce samples based on it. It does this by calculating every possible Feynman diagram for the process of interest, to LO, or in the case of aMC@NLO, NLO level. These are then used to create the matrix elements. This LO matrix element generator can include up to 4 extra partons in its calculation. When creating events at NLO however, aMC@NLO does create negative weights as was mentioned in Sec 4.2.2.

4.3.2 POWHEG

The powheg generator is a NLO calculator. However unlike MadGraph, it always produces one and only one extra parton that becomes the hardest jet in the interaction. For this reason it tends to be more inaccurate in producing Z bosons with high p_{T}. This is because it limits the boost that the Z can get from partons since it is not possible to have multiple high energy jets going in the same direction that would boost the Z in the opposite direction. This leads to a deficit of high p_{T} Z events.

4.3.3 RESBOS

Unlike the other generators used, this generator does not require a hadronizer. In fact this generator does not produce single gluons but instead calculates the overall effect of all orders of gluon loops on the final product [56, 57, 58]. As mentioned earlier $\alpha_{\mathrm{s}} > 1$ for low energy interactions, making it impossible to just consider interactions with a finite number of gluons. However, this method's weakness is that it does not have individual gluons to make jets, and in fact does not have individual particles in an event. Rather it just outputs the value of interest, in our case ϕ^*.

4.4 Pileup Simulation

On top of the complexities of producing the interaction of interest, the simulation must predict what the detector would have seen. This is normally done with Geant4 [59] which predicts detector responses. This, however, only simulates a single pp collision.

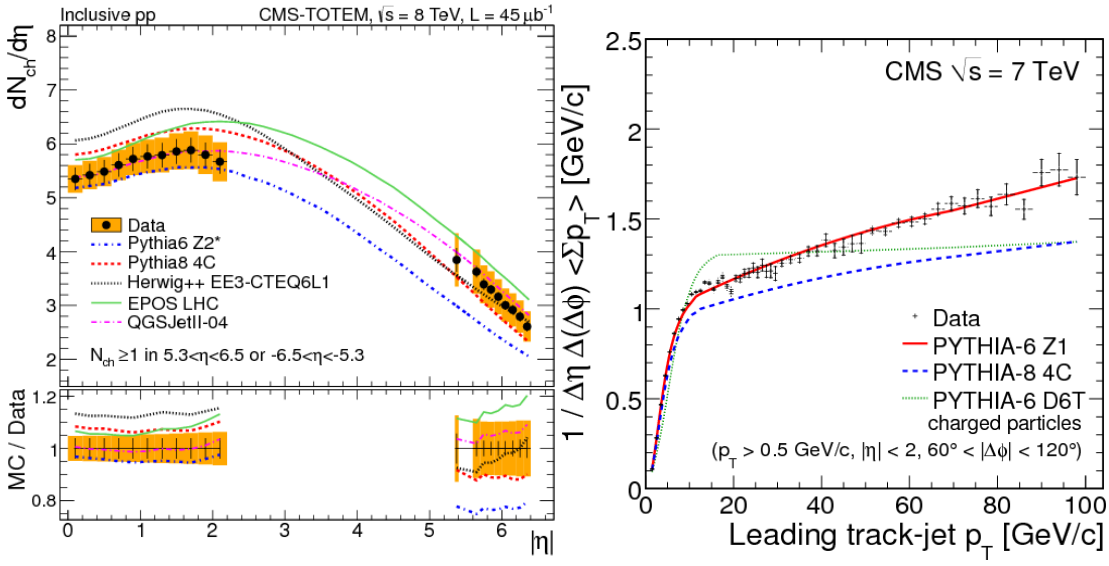

(a) (b)

Figure 4.8: The left figure shows the density of charged particles produced from a pp collision in a normal minbias event [1]. The right plot shows the average transverse energy emitted perpendicular to the largest jet of an interaction as a function of the largest jet p_{T}.[2]

As mentioned in section 3.3.1, in most events multiple protons interact, around 20 pairs for this data-set. These interactions can lead to the production of a large number of charged particles that can contaminate signal and lower its probability to be accurately reconstructed.

In order to simulate an event accurately, simulated pileup events are added to the event. This is done using PYTHIA to create collections of soft interactions, in which two protons hit and produce large collections of low energy particles, mostly pions. The number of these interactions that are added to an event is taken from a distribution that was created before the data was taken. For this reason the pileup distribution does not perfectly match the measured pileup distribution. An example of this is shown in Fig 4.9. As can be seen, both the position and shape of the distributions are different. This does not mean that on an event-by-event basis anything is wrong, rather that the rate of these events is incorrect. To more accurately reflect the pileup distribution taken from data, events are re-weighted, with the weight being the ratio of the data events over the

number of Monte Carlo events in a particular bin. The data distribution was calculated using the instantaneous luminosity and the inelastic proton-proton cross-section, with the weight being the data pileup distribution over the Monte Carlo pileup distribution.

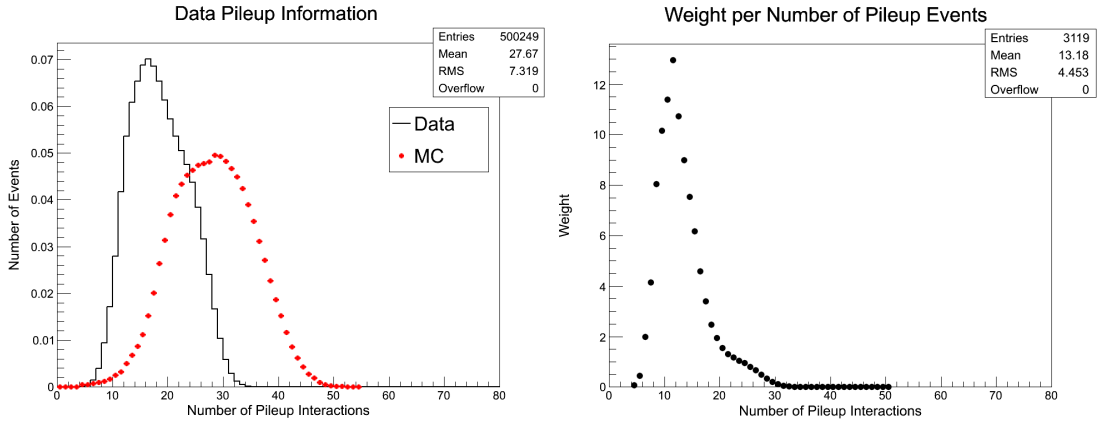

(a) (b)

Figure 4.9: The left plot compares the number of vertices per an event for Monte Carlo compared to data, while the right plot shows the resulting weights.

5

Data Analysis Strategy

"Would it save you a lot of time if I just gave up and went mad now?"

– Douglas Adams, *The Hitchhiker's Guide to the Galaxy*

We are measuring the Z boson differential cross section in ϕ^* and y. At its simplest, the observed differential cross section can be calculated as

$$\left[\frac{\mathrm{d}\sigma}{\mathrm{d}\phi^*}\right]_i^{\mathrm{obs}} = \frac{N_i - B_i}{\mathcal{L}\epsilon_i \Delta\phi_i^*}, \tag{5.1}$$

where integrated luminosity is $\mathcal{L}$, ϵ_i is the efficiency for reconstructing a Z in the bin given one was produced within the acceptance criteria, $\Delta\phi_i^*$ is the bin width, and N_i and B_i are the total number of Z candidates observed and the estimated background in the ith bin respectively. Although the actual value of B_i is unknown, since if we were able to count background events they would not be background, it can be estimated using simulation and data samples.

Equation 5.1 ignores bin migration, which happens when the kinematic properties of a lepton are reconstructed incorrectly which causes a event to be placed in the wrong ϕ^* bin. In the electron data set, this occurs for approximately 9.8% of events. In order to find the "true" ϕ^* distribution,[1] the measured distribution is corrected for bin migration or "unfolded". This allows the data measurement to be compared to simulation which has a true, theoretical ϕ^* distribution. Because the simulation sample

[1]The ϕ^* distribution of the actual particles rather than the reconstructed ones

has both reconstructed events as well as generator level events the relationship between the two can be used to create a matrix M_{ij} that allows for the true ϕ^* distribution of the data to be calculated based on the reconstructed values. This term can be used to create the final equation

$$\left[\frac{\mathrm{d}\sigma}{\mathrm{d}\phi^*}\right]_i^{\text{unfold}} = \sum_j M_{ij} \frac{N_j - B_j}{\mathcal{L}\epsilon_j \Delta\phi_j^*}. \tag{5.2}$$

5.1 Binning

Due to a large change in differential cross-section of ϕ^*, it was chosen to not have uniform bin widths. Instead bin widths were chosen to have roughly the same number of events in each bin, except for the very high ϕ^* range. The boundaries of theses bins are given in Table 5.1

Table 5.1: The range of ϕ^* bins.

Bin #	ϕ^* Range	Bin #	ϕ^* Range
1	0.000-0.004	17	0.102-0.114
2	0.004-0.008	18	0.114-0.145
3	0.008-0.012	19	0.145-0.165
4	0.012-0.016	20	0.165-0.189
5	0.016-0.020	21	0.189-0.219
6	0.020-0.024	22	0.219-0.258
7	0.024-0.029	23	0.258-0.312
8	0.029-0.034	24	0.312-0.391
9	0.034-0.039	25	0.391-0.524
10	0.039-0.045	26	0.524-0.695
11	0.045-0.052	27	0.695-0.918
12	0.045-0.052	28	0.918-1.153
13	0.052-0.057	29	1.153-1.496
14	0.057-0.064	30	1.496-1.947
15	0.081-0.091	31	1.947-2.522
16	0.091-0.102	32	2.522-3.277

The boundaries for the rapidity bin were chosen to all be equal size of 0.4 and are shown in Table 5.2.

Table 5.2: The range of y bins.

Bin #	y range
1	0.0-0.4
2	0.4-0.8
3	0.8-1.2
4	1.2-1.6
5	1.6-2.0
6	2.0-2.4

5.2 Acceptance

A measurement such as ϕ^* is subject to the limitation that not all electrons produced by $pp \to Z + X \to \mathrm{e}^+\mathrm{e}^- + X$ can be observed or triggered on by the CMS detector. As a result, the measurement can be reported in one of two ways. In the first option, we establish clear selections in simple kinematic variables. These selections are applied to both the data and the simulation samples before they are compared. The second method uses other simulation samples to attempt to calculate the full distribution of data based on the components that we are able to observe. This is then compared to the full distribution of a simulation sample. A disadvantage of the second method is that it is highly dependent on the simulation sample used and introduces additional sources of uncertainty. For this reason, the former method was chosen for this analysis.

Two acceptance selections required due to limitations of the detector, are selections on p_T and η of the leptons. It is required that one lepton have $p_\mathrm{T} > 30\,\mathrm{GeV}$ and $|\eta| < 2.1$, while the second lepton has looser requirements with $p_\mathrm{T} > 20\,\mathrm{GeV}$ and $|\eta| < 2.4$. The η requirements were chosen to allow the use of the high-efficiency single-lepton triggers. Also, such events will be covered by both the ECAL and the tracker, allowing for a more precise angular measurement. The p_T bounds were chosen such that the leptons were not near the edge of the turn-on curve of the trigger.

Another acceptance selection that is required is on the invariant mass of the lepton pair. As can be seen in Fig 5.1, many mesons are capable of producing a lepton pair, and there is a continuum distribution from virtual photons. To allow a precise interpretation of events arising from the initial hard-scatter, an acceptance selection on the mass is used

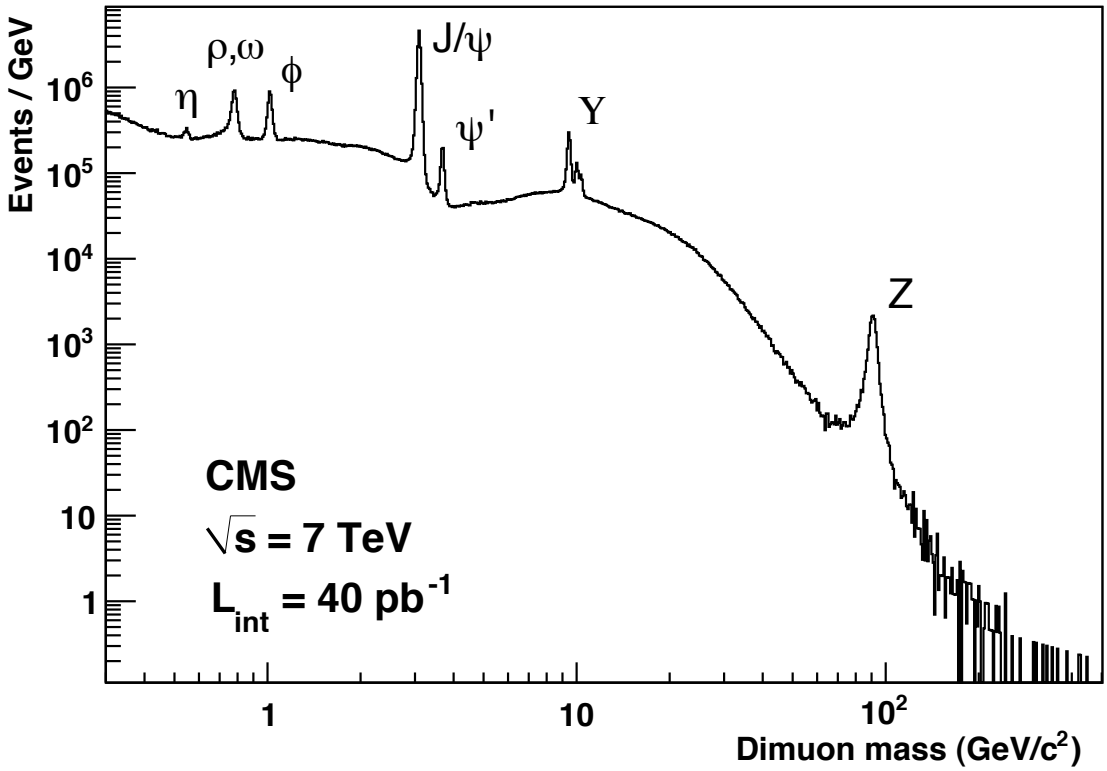

Figure 5.1: A distribution of the invariant mass of dimuon events at CMS 2010. Although many processes are capable of produce dileptons, almost all of them are produced with a invariant mass an order of magnitude smaller then the Z.

to remove objects that decay to dileptons that were not a Z by requiring $60 < m_{\ell\ell} < 120$ GeV.

The effect of the p_{T} and η selections on the distribution of leptons can be seen in Fig 5.2, while the effects on the Z mass and the Z rapidity distributions can be seen in Fig 5.3. All these distributions include the mass selection since further from the Z peak the photon component of the wave function becomes large compared to the Z component.

5.3 Efficiency, Background, and Unfolding

The parameters, ϵ_i and B_i, which correspond to the efficiency and the background used in equations 5.2, are explored in depth in Chapters 6 and 7 respectively. The efficiency is the probability of a Z, whose properties pass acceptance, being reconstructed. The backgrounds are events that can look like a $\mathrm{Z} \to \mathrm{e}^+\mathrm{e}^-$ decay in our detector, and the unfolding is the matrix that corrects for bin migration.

5.4 Unfolding

Processing the data is pointless if there is nothing to compare it to. In theory we should be able to directly compare the data to a simulation sample. However due to detector effects, particles are never perfectly reconstructed, therefore the measured value of ϕ^* can fall in a different bin from the real value. This is called bin migration. Fortunately, this bin migration is well modeled, since it is possible to simulate these detector effects and create a sample of reconstructed particles using the true particles. As can be seen in Fig 5.4, which uses a MadGraph sample, the majority of events' reconstructed and generated ϕ^* values fall in the same bin, however a non-trivial amount–about 9.8%–fall in separate bins. Using this matrix it is possible to calculate the true distribution of the data using the reconstructed data, as well as the matrix shown in Fig 5.4.

5.4.1 Two Dimensional Unfolding

Although bin migration is relatively easy to represent for single measurements it becomes harder to represent when multiple measurements are done for each event. An example is a dual measurement of our Z samples where a measurement of both ϕ^* as well as the

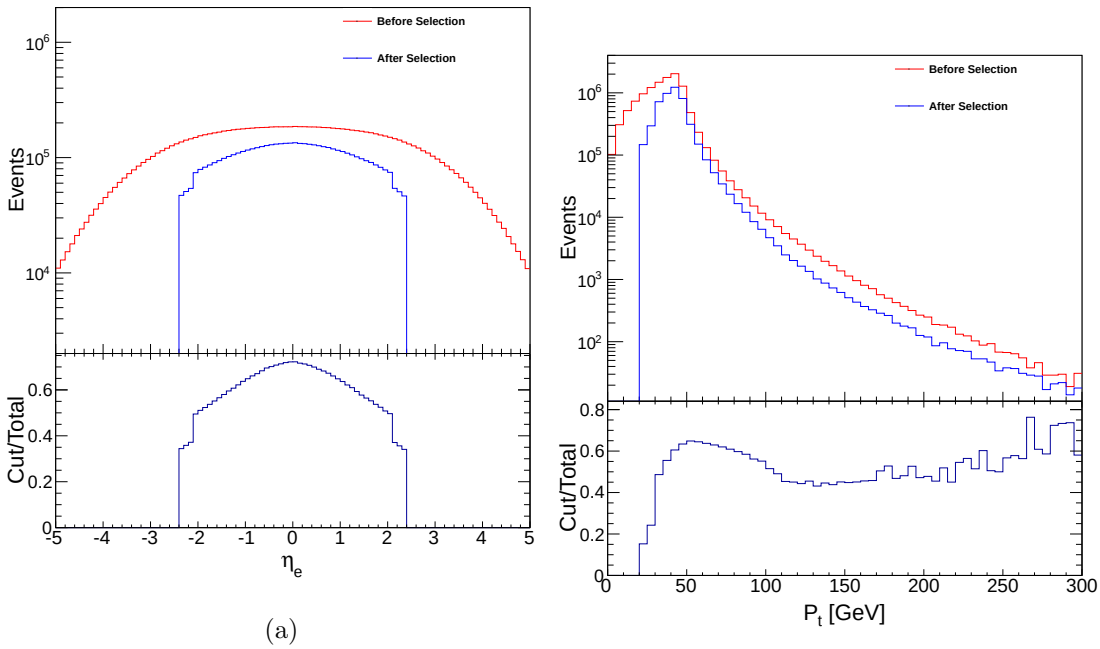

(a)

Figure 5.2: These plots show the p_{T} and η distribution of electrons that are produced from a Z decay. These results are from a simulated sample, showing the results of p_{T} and η selections on the distribution. A invariant mass requirement of $60\,\mathrm{GeV} < m_{\mathrm{ee}} < 120\,\mathrm{GeV}$ was included with both distributions. Since different η and p_{T} selections are used for the leading electron compared to the subleading electron a jump in the number of events can be seen in the after selections plots at $\eta = 2.1$ and $p_{\mathrm{T}} = 30$.

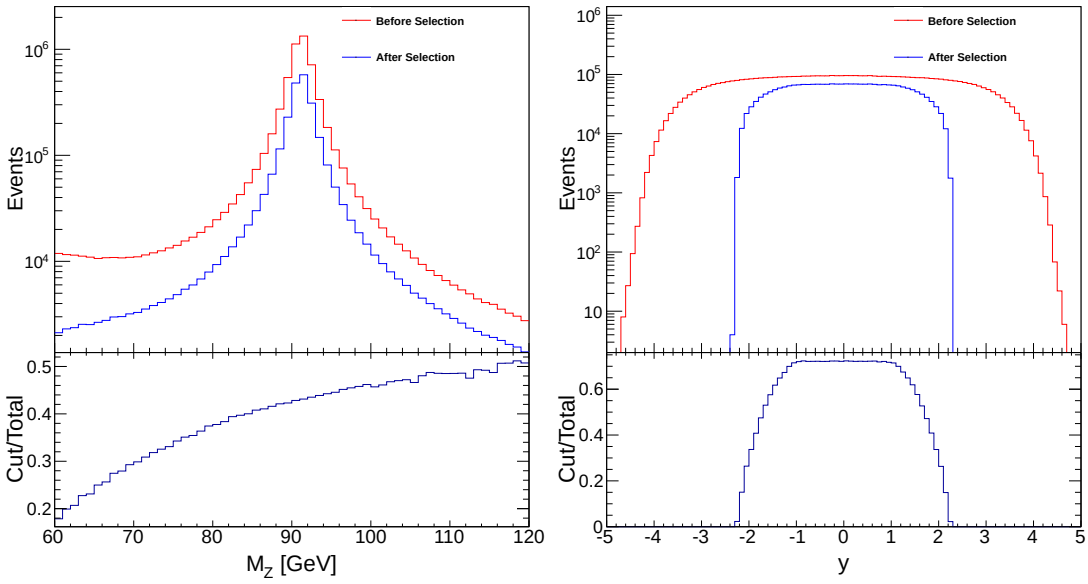

(a) (b)

Figure 5.3: These plots show distribution of the mass of the Z and its rapidity. These results are from a simulated sample, showing the results of p_{T} and η selections on the distribution. Due to the p_{T} requirements on the electron, more massive Z bosons are likely to be kept, leading to an upward slope in the selection/total M_{Z} plot. The rapidity plot however is extremely flat up to where it quickly drops off at around $y = 1$

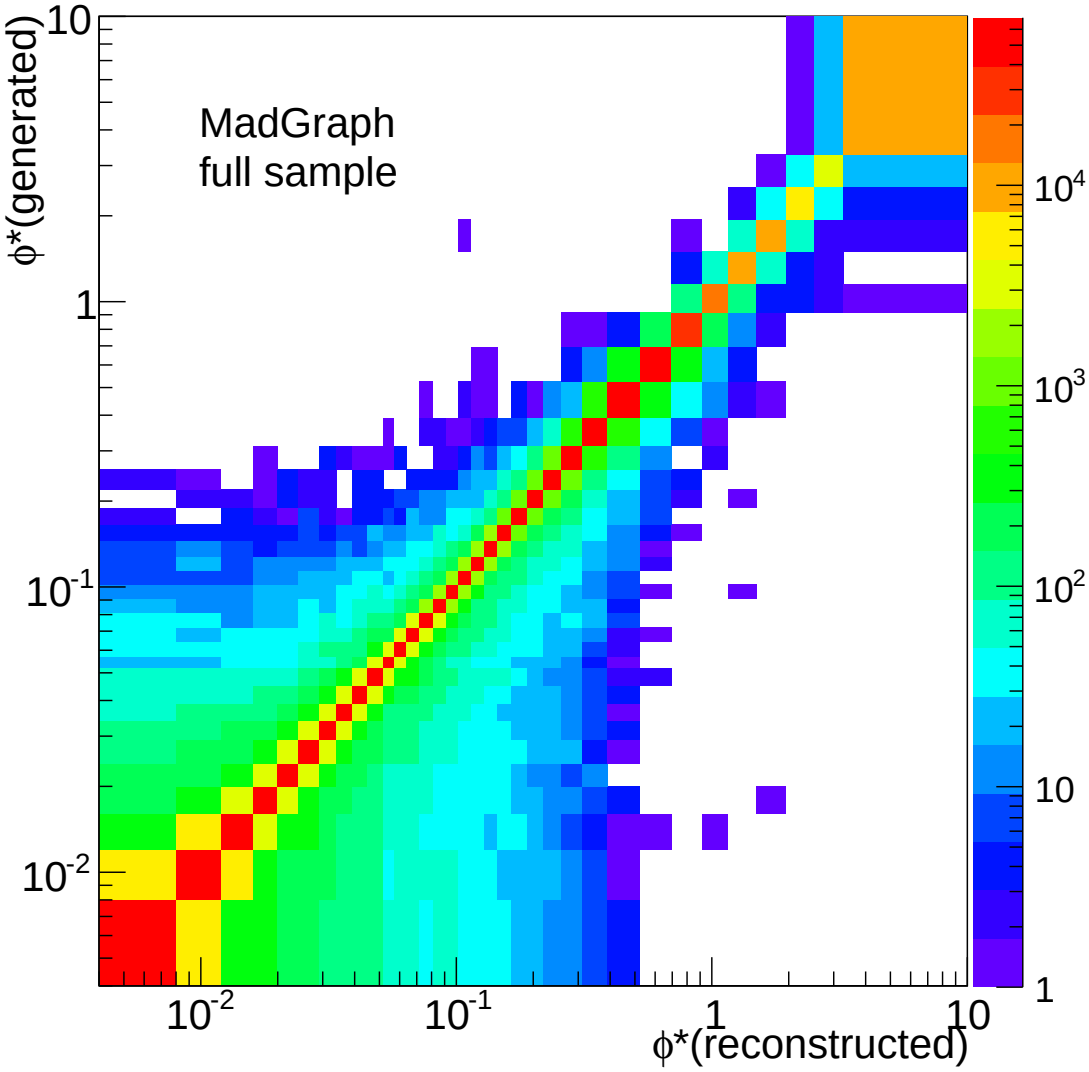

Figure 5.4: A comparison of the Born vs reconstructed measured values.

rapidity is made. Intuitively this would require a four-dimensional histogram, with two dimensions for both the generator and reconstructed values. This issue can be solved by representing higher dimensional studies as a larger 1D study. For the ϕ^* y study, this is done by having the first 36 bins represent all of ϕ^* measurement in which the rapidity of the Z is $|y| < 0.4$, the next 36 bins represent all of ϕ^* measurement in which the rapidity of the Z is $0.4 < |y| < 0.8$ and so on. These bins are shown in tables 5.3 and 5.4. Using this method it is possible to represent two dimensions as a single axis. This allows us to represent the generated to reconstructed measurements in a single 2D matrix shown in Fig. 5.5.

Bin #	ϕ^* Range	η range	Bin #	ϕ^* Range	η range	Bin #	ϕ^* Range	η range
1	0.000-0.004	0.0-0.4	33	0.000-0.004	0.4-0.8	65	0.000-0.004	0.8-1.2
2	0.004-0.008	0.0-0.4	34	0.004-0.008	0.4-0.8	66	0.004-0.008	0.8-1.2
3	0.008-0.012	0.0-0.4	35	0.008-0.012	0.4-0.8	67	0.008-0.012	0.8-1.2
4	0.012-0.016	0.0-0.4	36	0.012-0.016	0.4-0.8	68	0.012-0.016	0.8-1.2
5	0.016-0.020	0.0-0.4	37	0.016-0.020	0.4-0.8	69	0.016-0.020	0.8-1.2
6	0.020-0.024	0.0-0.4	38	0.020-0.024	0.4-0.8	70	0.020-0.024	0.8-1.2
7	0.024-0.029	0.0-0.4	39	0.024-0.029	0.4-0.8	71	0.024-0.029	0.8-1.2
8	0.029-0.034	0.0-0.4	40	0.029-0.034	0.4-0.8	72	0.029-0.034	0.8-1.2
9	0.034-0.039	0.0-0.4	41	0.034-0.039	0.4-0.8	73	0.034-0.039	0.8-1.2
10	0.039-0.045	0.0-0.4	42	0.039-0.045	0.4-0.8	74	0.039-0.045	0.8-1.2
11	0.045-0.052	0.0-0.4	43	0.045-0.052	0.4-0.8	75	0.045-0.052	0.8-1.2
12	0.045-0.052	0.0-0.4	44	0.045-0.052	0.4-0.8	76	0.045-0.052	0.8-1.2
13	0.052-0.057	0.0-0.4	45	0.052-0.057	0.4-0.8	77	0.052-0.057	0.8-1.2
14	0.057-0.064	0.0-0.4	46	0.057-0.064	0.4-0.8	78	0.057-0.064	0.8-1.2
15	0.081-0.091	0.0-0.4	47	0.081-0.091	0.4-0.8	79	0.081-0.091	0.8-1.2
16	0.091-0.102	0.0-0.4	48	0.091-0.102	0.4-0.8	80	0.091-0.102	0.8-1.2
17	0.102-0.114	0.0-0.4	49	0.102-0.114	0.4-0.8	81	0.102-0.114	0.8-1.2
18	0.114-0.145	0.0-0.4	50	0.114-0.145	0.4-0.8	82	0.114-0.145	0.8-1.2
19	0.145-0.165	0.0-0.4	51	0.145-0.165	0.4-0.8	83	0.145-0.165	0.8-1.2
20	0.165-0.189	0.0-0.4	52	0.165-0.189	0.4-0.8	84	0.165-0.189	0.8-1.2
21	0.189-0.219	0.0-0.4	53	0.189-0.219	0.4-0.8	85	0.189-0.219	0.8-1.2
22	0.219-0.258	0.0-0.4	54	0.219-0.258	0.4-0.8	86	0.219-0.258	0.8-1.2
23	0.258-0.312	0.0-0.4	55	0.258-0.312	0.4-0.8	87	0.258-0.312	0.8-1.2
24	0.312-0.391	0.0-0.4	56	0.312-0.391	0.4-0.8	88	0.312-0.391	0.8-1.2
25	0.391-0.524	0.0-0.4	57	0.391-0.524	0.4-0.8	89	0.391-0.524	0.8-1.2
26	0.524-0.695	0.0-0.4	58	0.524-0.695	0.4-0.8	90	0.524-0.695	0.8-1.2
27	0.695-0.918	0.0-0.4	59	0.695-0.918	0.4-0.8	91	0.695-0.918	0.8-1.2
28	0.918-1.153	0.0-0.4	60	0.918-1.153	0.4-0.8	92	0.918-1.153	0.8-1.2
29	1.153-1.496	0.0-0.4	61	1.153-1.496	0.4-0.8	93	1.153-1.496	0.8-1.2
30	1.496-1.947	0.0-0.4	62	1.496-1.947	0.4-0.8	94	1.496-1.947	0.8-1.2
31	1.947-2.522	0.0-0.4	63	1.947-2.522	0.4-0.8	95	1.947-2.522	0.8-1.2
32	2.522-3.277	0.0-0.4	64	2.522-3.277	0.4-0.8	96	2.522-3.277	0.8-1.2

Table 5.3: The full list of unrolled ϕ^*,y bins for the double differential measurement.

Bin #	ϕ^* Range	η range	Bin #	ϕ^* Range	η range	Bin #	ϕ^* Range	η range
97	0.000-0.004	1.2-1.6	129	0.000-0.004	1.6-2.0	161	0.000-0.004	2.0-2.4
98	0.004-0.008	1.2-1.6	130	0.004-0.008	1.6-2.0	162	0.004-0.008	2.0-2.4
99	0.008-0.012	1.2-1.6	131	0.008-0.012	1.6-2.0	163	0.008-0.012	2.0-2.4
100	0.012-0.016	1.2-1.6	132	0.012-0.016	1.6-2.0	164	0.012-0.016	2.0-2.4
101	0.016-0.020	1.2-1.6	133	0.016-0.020	1.6-2.0	165	0.016-0.020	2.0-2.4
102	0.020-0.024	1.2-1.6	134	0.020-0.024	1.6-2.0	166	0.020-0.024	2.0-2.4
103	0.024-0.029	1.2-1.6	135	0.024-0.029	1.6-2.0	167	0.024-0.029	2.0-2.4
104	0.029-0.034	1.2-1.6	136	0.029-0.034	1.6-2.0	168	0.029-0.034	2.0-2.4
105	0.034-0.039	1.2-1.6	137	0.034-0.039	1.6-2.0	169	0.034-0.039	2.0-2.4
106	0.039-0.045	1.2-1.6	138	0.039-0.045	1.6-2.0	170	0.039-0.045	2.0-2.4
107	0.045-0.052	1.2-1.6	139	0.045-0.052	1.6-2.0	171	0.045-0.052	2.0-2.4
108	0.045-0.052	1.2-1.6	140	0.045-0.052	1.6-2.0	172	0.045-0.052	2.0-2.4
109	0.052-0.057	1.2-1.6	141	0.052-0.057	1.6-2.0	173	0.052-0.057	2.0-2.4
110	0.057-0.064	1.2-1.6	142	0.057-0.064	1.6-2.0	174	0.057-0.064	2.0-2.4
111	0.081-0.091	1.2-1.6	143	0.081-0.091	1.6-2.0	175	0.081-0.091	2.0-2.4
112	0.091-0.102	1.2-1.6	144	0.091-0.102	1.6-2.0	176	0.091-0.102	2.0-2.4
113	0.102-0.114	1.2-1.6	145	0.102-0.114	1.6-2.0	177	0.102-0.114	2.0-2.4
114	0.114-0.145	1.2-1.6	146	0.114-0.145	1.6-2.0	178	0.114-0.145	2.0-2.4
115	0.145-0.165	1.2-1.6	147	0.145-0.165	1.6-2.0	179	0.145-0.165	2.0-2.4
116	0.165-0.189	1.2-1.6	148	0.165-0.189	1.6-2.0	180	0.165-0.189	2.0-2.4
117	0.189-0.219	1.2-1.6	149	0.189-0.219	1.6-2.0	181	0.189-0.219	2.0-2.4
118	0.219-0.258	1.2-1.6	150	0.219-0.258	1.6-2.0	182	0.219-0.258	2.0-2.4
119	0.258-0.312	1.2-1.6	151	0.258-0.312	1.6-2.0	183	0.258-0.312	2.0-2.4
120	0.312-0.391	1.2-1.6	152	0.312-0.391	1.6-2.0	184	0.312-0.391	2.0-2.4
121	0.391-0.524	1.2-1.6	153	0.391-0.524	1.6-2.0	185	0.391-0.524	2.0-2.4
122	0.524-0.695	1.2-1.6	154	0.524-0.695	1.6-2.0	186	0.524-0.695	2.0-2.4
123	0.695-0.918	1.2-1.6	155	0.695-0.918	1.6-2.0	187	0.695-0.918	2.0-2.4
124	0.918-1.153	1.2-1.6	156	0.918-1.153	1.6-2.0	188	0.918-1.153	2.0-2.4
125	1.153-1.496	1.2-1.6	157	1.153-1.496	1.6-2.0	189	1.153-1.496	2.0-2.4
126	1.496-1.947	1.2-1.6	158	1.496-1.947	1.6-2.0	190	1.496-1.947	2.0-2.4
127	1.947-2.522	1.2-1.6	159	1.947-2.522	1.6-2.0	191	1.947-2.522	2.0-2.4
128	2.522-3.277	1.2-1.6	160	2.522-3.277	1.6-2.0	192	2.522-3.277	2.0-2.4

Table 5.4: The full list of unrolled ϕ^*,y bins for the double differential measurement. (continued)

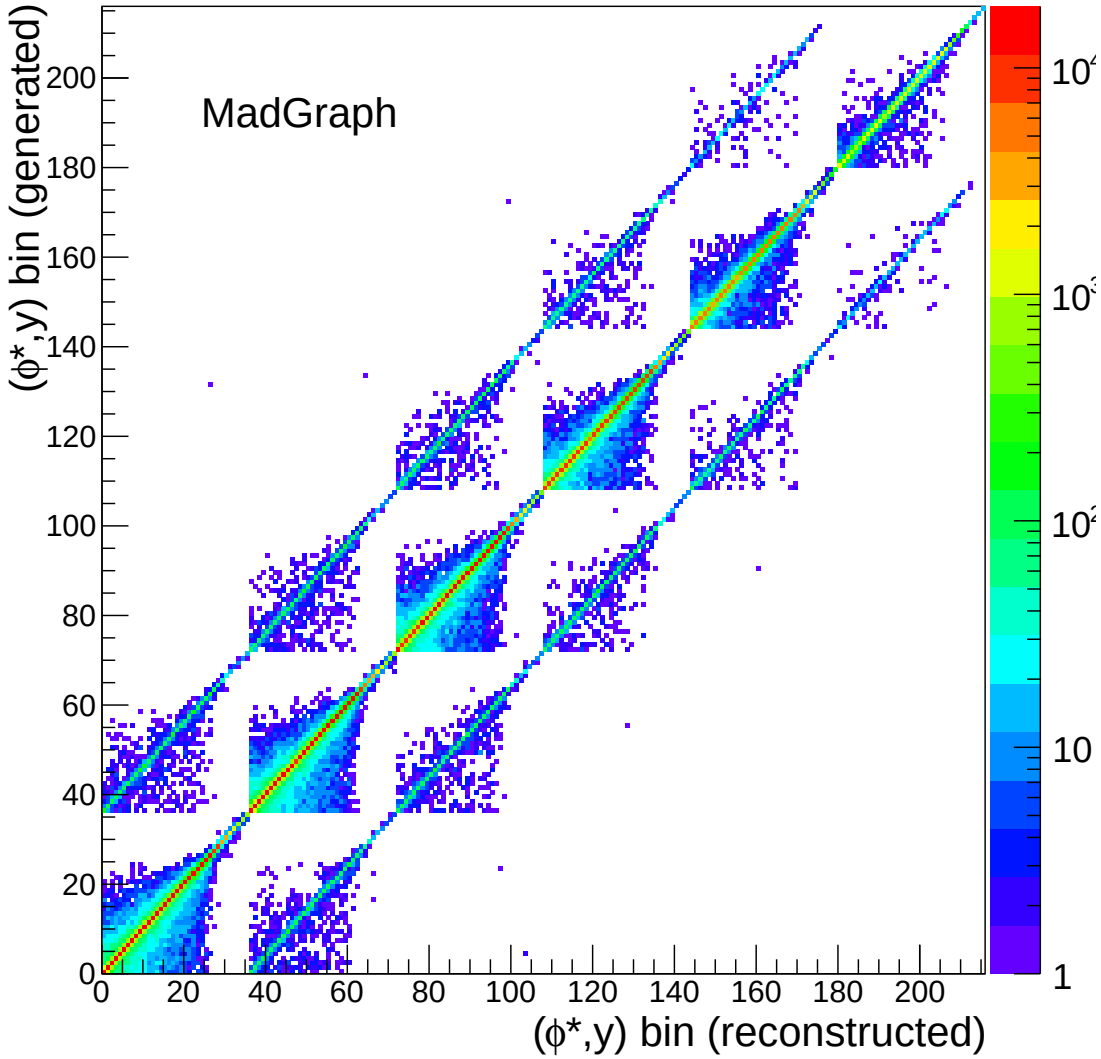

Figure 5.5: A comparison of Generated VS Reconstructed values for double differential measurement. As expected , migreation is largest for adjacent bins in ϕ^* or y, which may not be adjacent in the matrix which produces the observed pattern.

6

Requirements and Efficiency

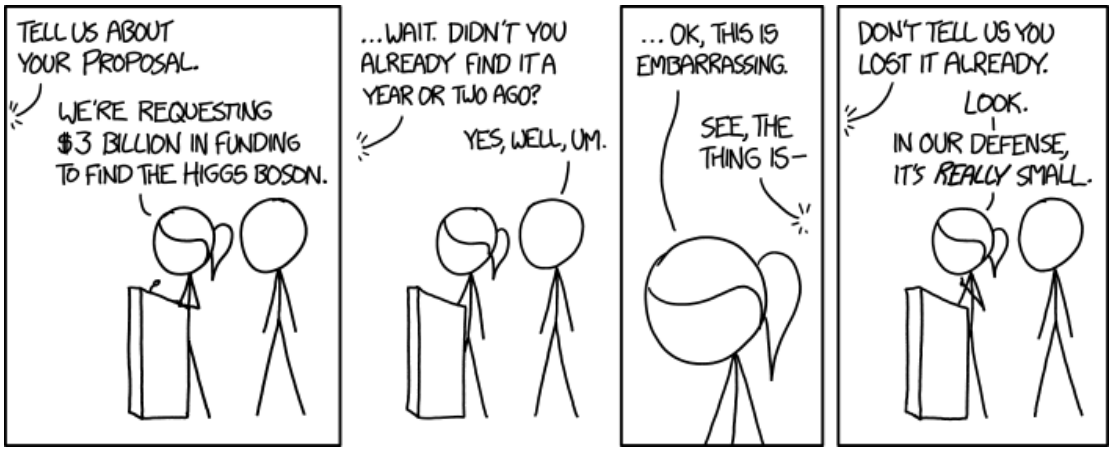

Figure 6.1: Although few events are required to prove a particle's existence, in order to study the particle, samples must be created with both large numbers of the particle in question, while having a relatively low number of fakes.[4]

In Sec. 5.2, the acceptance requirements for the Z boson decays to be considered for this analysis were established as having at least one electron with $p_{\mathrm{T}} > 30\,\mathrm{GeV}$ and $|\eta| < 2.1$, having a second electron with $p_{\mathrm{T}} > 20\,\mathrm{GeV}$ and $|\eta| < 2.4$, and finally requiring the pair to have $60\,\mathrm{GeV} < m_{\mathrm{ee}} < 120\,\mathrm{GeV}$. However, not every event which met those requirements when produced in the collider will be properly measured and reconstructed, and will be "lost."

We use efficiency to describe the number of correct events lost for one reason or

another. The efficiency is defined as the number of Z events that decay to leptons with kinematic properties that have passed the acceptance requirements, divided by the number of events that should have passed all requirements ($\epsilon = \mathrm{n}^{\mathrm{obs.}}_{\mathrm{pass}}/\mathrm{n}^{\mathrm{obs}}_{\mathrm{total}}$). In order to accurately calculate the true distribution of ϕ^*, ϵ must be accurately calculated and applied.

There are many reasons that an "acceptable" electron may be rejected. Even if the true parameters of the electron are within the window, if the measured values fall outside the acceptance window the event will be thrown out, such as if the true p_{T} of the electron was 21 GeV but the measurement yields 19 GeV. Unfolding the distribution makes it possible to compensate for these effects. A second way for an electron to not be included is if for some reason the electron is not reconstructed. This can happen if the electron does not deposit energy in ECAL by falling into a crack between crystals or depositing all its energy in the tracker. An electron could also be rejected due to spatial overlap with other particles in the same event. For example, if a photon happens to deposit energy in the same crystal as the electron, the electron's energy measured by ECAL and the electron's momentum measured by the tracker will be incompatible. Due to this incompatibility, the reconstruction algorithm may reject the electron.

6.1 Requirements

The efficiency is often lowered due to requirements to remove reconstructed electrons that are not produced from Z decay. These background events can include photons that pair produce ($\gamma \to e^+e^-$) inside the tracker, and events that do not include an electron, such as a charged pion that interacts inside the ECAL depositing all its energy in a crystal. There can also be coincidence events, in which a charged particle leaves a track to a cluster that had a photon deposit energy.

Rather than have each analysis team pick every requirement completely independently, requirements are grouped into sets by the CMS Collaboration and studied centrally. These groups of requirements are designed to remove fake or unimportant electrons, such as electrons that are produced by a high energy particle interaction with the tracker, while keeping interesting electrons. The severity of these requirements is chosen depending on how important it is to remove backgrounds compared to how vital

it is to not remove real electrons. This analysis uses two different sets of requirements, referred to as `Tight` and `Medium`, with the more severe requirement being the `Tight`. The specific requirements of `Tight` and `Medium` are shown in Table 6.1.

Variable	`Tight`		`Medium`	
	EB	EE	EB	EE
$\Delta\eta_{\text{in}} <$	0.004	0.005	0.004	0.007
$\Delta\phi_{\text{in}} <$	0.03	0.02	0.06	0.03
$\sigma_{i\eta i\eta} <$	0.01	0.03	0.01	0.03
H/E $<$	0.12	0.10	0.12	0.10
d0 $<$	0.02	0.02	0.02	0.02
dz $<$	0.1	0.1	0.1	0.1
$\lvert\,(1/E - 1/p)\,\rvert <$	0.05	0.05	0.05	0.05
$\text{P}_{\text{vtx}} <$	10^{-6}	10^{-6}	10^{-6}	10^{-6}
$\text{N}_{\text{miss}} \leq$	0	0	1	1
$\text{Iso}_{\text{PF}} <$	0.10	0.10	0.15	0.15

Table 6.1: Identification and isolation requirements for `Tight` and `Medium` requirements in the ECAL barrel (EB) and ECAL endcap (EE).

6.1.1 Fake Electrons

Many methods are used to lower the rate at which fake electrons are reconstructed. As mentioned, these fake electrons can have multiple sources, such as photons, pions, or even protons. One method to reduce the level of hadronic events being mislabeled as an electron is to use the ratio of the energy read out of HCAL in the area around where the hit was in ECAL, H/E. As mentioned earlier, electrons tend to deposit all their energy in ECAL, leading to a small value of H/E. In comparison, hadrons tend to travel through ECAL, keeping some of their energy until they get to HCAL, leading to a larger H/E value. This is shown in Fig. 6.2.

If a hadron deposits all of its energy in ECAL, H/E discrimination will not work. A

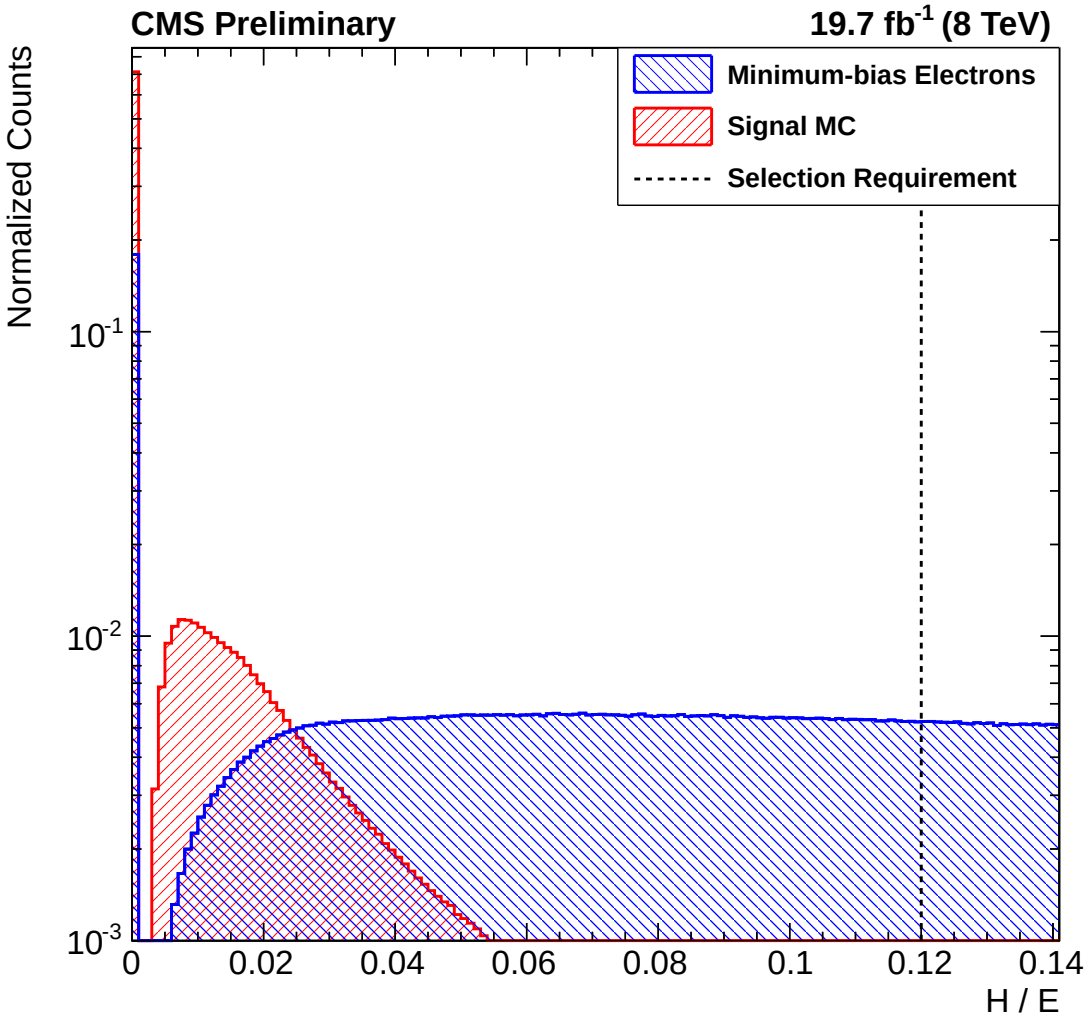

Figure 6.2: The H/E ratio of reconstructed electrons in a minimum bias sample compared to a MadGraph $Z \to e^+e^-$ sample. These electrons were required to be in the acceptance region, with $p_T > 20\,\text{GeV}$ and $|\eta| < 2.4$. Electrons from the Z decay tend to not deposit much energy in the hadron calorimeter, with no events having a H/E above 6%. In contrast the reconstructed electrons from the minumum bias sample have a relatively uniform distribution.

common cause of this is when a positively charged pion interacts with a neutron:

$$\pi^+ + \mathrm{n} \rightarrow \pi^0 + \mathrm{p} \rightarrow 2\gamma + \mathrm{p}. \tag{6.1}$$

This is referred to as charge exchange. Because of the short lifetime of the π^0, almost all of its energy is deposited in the crystal as two photons. This tends to lead to a larger shower than a single electron. Because of this, and the fact that hadron showers in general are larger than electron showers, it is possible for shower size requirements to effectively help differentiate the two. The shower width in the $\eta(\sigma_{i\eta i\eta})$ is used since the curvature of the electron in the magnetic field can widen its shower in the ϕ direction, but will not effect the shower shape in the η direction.

Checking the consistency of the tracked particle's measured momentum value (p) vs the energy deposited in the cluster (E) can also be a useful measurement in removing fake electrons. Due to the tracker's increasing fractional uncertainty of p at high momenta, these comparisons are done with their inverse, $(1/E - 1/p)$. For electrons this should be close to 0, while for hadrons that do not deposit all their energy in ECAL, this will be positive, and events caused by a coincidence can be either positive or negative values. Therefore both sets of selections, `Tight` and `Medium`, include the requirement $|1/E - 1/p| < 0.05\,\mathrm{GeV}^{-1}$. A plot comparing the $1/E - 1/p$ of reconstructed electrons from a $\mathrm{Z} \rightarrow \mathrm{e}^+\mathrm{e}^-$ simulated sample to a minimum bias sample is shown in Fig 6.3

6.1.2 Electrons from other sources

Many processes other than Z decay are capable of producing electrons. These electrons can also be suppressed by selection requirements, each of which may introduce an inefficiency.

Electrons from Pair productions

Pair production happens when a high energy photon interacts with a nucleus, creating an electron-positron pair, $\gamma \rightarrow \mathrm{e}^+\mathrm{e}^-$. Due to the need for a nucleus, pair production tends to happen in the tracker, leading to two simple ways of rejecting these types of events.

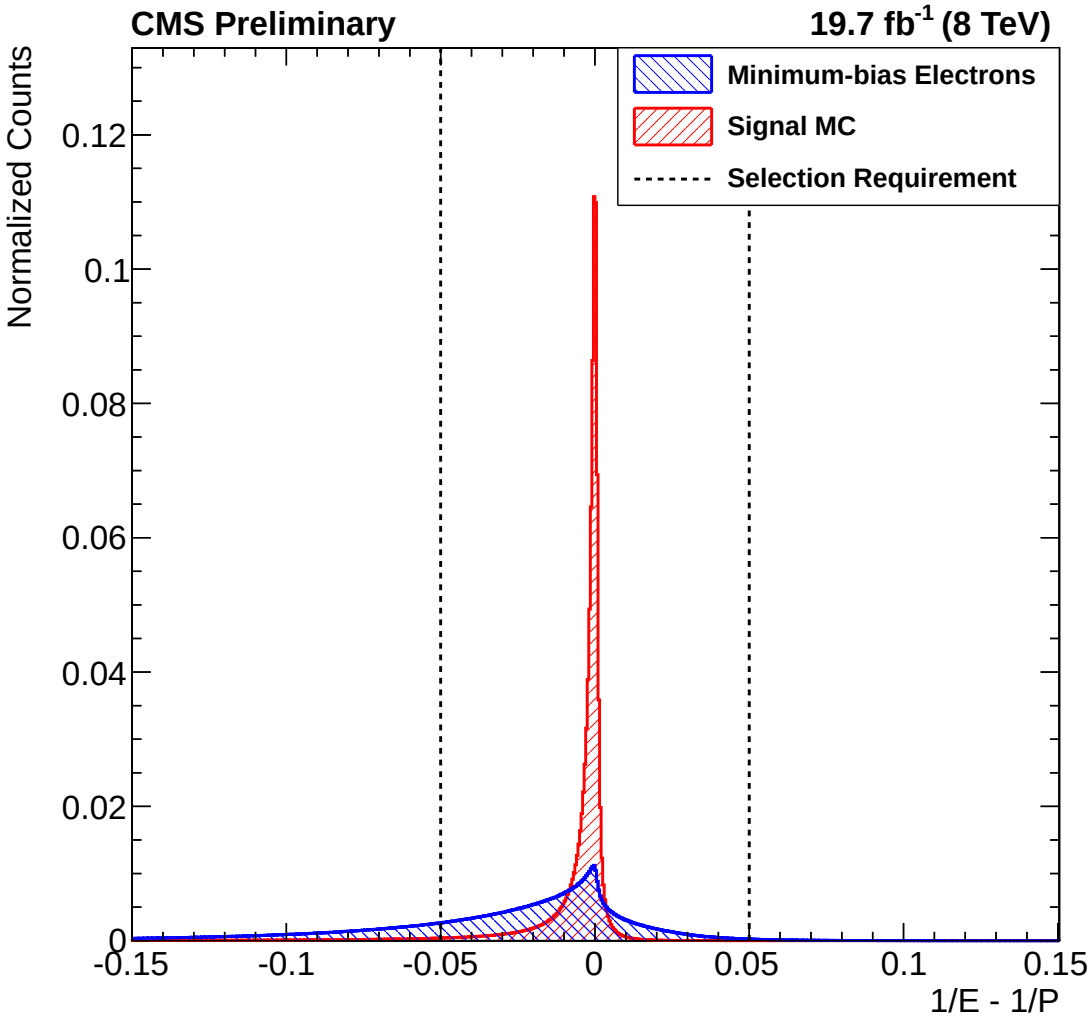

Figure 6.3: The $1/E - 1/p$ of reconstructed electrons in a minimum bias sample compared to a MadGraph $Z \to e^+e^-$ sample. These electrons were required to be in the acceptance region, with $p_T > 20\,\text{GeV}$ and $|\eta| < 2.4$. For the signal sample almost all events are within 0.01 GeV^{-1} of 0, while the minimum bias tail continues in both the negative and positive direction.

The first way is by looking at the position of the electron's production vertex compared to the collision point. The second way is by looking at the track and how many layers it was detected in. Since on average, pair production happens after the photon travels through several layers, there will be many layers of the track in which the tracker does not see the electron.

Electrons from Jets

During the production of a jet, it is possible for electrons to be produced through the decay of hadrons. These electrons are usually surrounded by other particles of all types. These other particles then deposit energy in ECAL and HCAL allowing the embedded electrons to be rejected by observing the area around the electron. For electrons produced by Z decay, not much energy is deposited around the electron. In contrast, jet produced electrons are accompanied by energy deposits over a wide range of space from the rest of the jet.

Isolation is defined as a ratio of the electron energy to all other energy around the electron event. Mathematically, in ECAL and HCAL, the isolation is defined as

$$\mathrm{Iso}_{\mathrm{ECAL}} = \frac{\sum_{\Delta \mathrm{R}<0.3} E^{\mathrm{ECAL}} - E^{\mathrm{SC}}}{E_{\mathrm{T}}^{\mathrm{Electron}}}, \tag{6.2}$$

$$\mathrm{Iso}_{\mathrm{HCAL}} = \frac{\sum_{\Delta \mathrm{R}<0.3} E^{\mathrm{HCAL}}}{E_{\mathrm{T}}^{\mathrm{Electron}}}. \tag{6.3}$$

These variables attempt to find how much energy is deposited within a certain ΔR around the central crystal: $\Delta \mathrm{R} = \sqrt{\Delta\eta^2 + \Delta\phi^2}$, where $\Delta\eta$ is the distance in η from the central crystal, and $\Delta\phi$ is the distance in ϕ. By subtracting E^{SC}, the energy in the super-cluster, in the calculation of $\mathrm{Iso}_{\mathrm{ECAL}}$, the contribution of the electron itself is removed from the isolation calculation. Because almost none of the energy from the electron is deposited in HCAL, no subtraction is required for $\mathrm{Iso}_{\mathrm{HCAL}}$. The last type of isolation used is the particle flow isolation, defined as

$$\mathrm{Iso}_{\mathrm{PF}} = \frac{\sum_{\Delta \mathrm{R}<0.3} (p_{\mathrm{T}}^{\mathrm{Track}} + E^{\mathrm{HCAL}} + E^{\mathrm{ECAL}} - E^{\mathrm{SC}} - p_{\mathrm{T}}^{\mathrm{Electron}} - 0.3^2\pi\rho)}{p_{\mathrm{T}}^{\mathrm{Electron}}}. \tag{6.4}$$

This isolation variable includes two new variables: $p_{\mathrm{T}}^{\mathrm{Track}}$, the measured p_{T} of the tracks surrounding the central crystal, and ρ, a variable that helps compensate for pileup. Each time a bunch crosses, multiple protons interact. Most of these interactions do not produce any heavy particles, but they do cause a spray of low energy light particles leading to a deposit of energy all over the detector. The ρ is calculated for each event by counting the particles that did not end up in a jet.

6.2 Measuring Efficiency using Data

The efficiency of requirements, such as `Tight` and `Medium`, can be calculated based on simulated samples because the simulation has access to both the generator level electrons as well as the reconstructed level. However, there are differences between reconstructed particles in the simulation and reality that must be compensated for. This requires knowledge of the data efficiency, which is tricky to do since it requires a sample of pure electrons that we are interested in. Because the selections are to remove the background, a different method is required to remove the background from the sample in order to find the efficiency of the selections on data. The popular method to do this is the tag-and-probe method. The tag-and-probe method requires an event to have one reconstructed electron that passes very stringent requirements. This electron is known as the tag. This tag electron is then matched to another possible electron object. If the pair has an invariant mass close to the Z mass it is very likely that this was an electron produced from a Z decay. The electron matched to the tag electron is called the probe. These probes are used to calculate the efficiency of the selections on data. This is necessary due to differences between the simulated detector and the real detector, leading to different efficiencies for the data and the simulation. A scale factor, which is used to compensate for these differences, is defined as:

$$SF = \frac{\epsilon_{Data}}{\epsilon_{simulation}}. \tag{6.5}$$

6.2.1 Tag-and-probe requirements

Single Electron Trigger

The electron data set that was used in this analysis was created with a "single electron trigger," `HLT_Ele27_WP80`, and was taken from 2012 CMS data. This trigger was created to save events that contain at least one electron with $p_{\mathrm{T}} > 27\,\mathrm{GeV}$. This trigger was chosen due to its similarity to the single muon trigger, allowing direct comparisons to be made between $\mathrm{Z} \to \mathrm{e}^{+}\mathrm{e}^{-}$ and $\mathrm{Z} \to \mu^{+}\mu^{-}$ data sets.

The efficiency of the trigger that was used to create the `HLT_Ele27_WP80` was measured using the tag-and-probe method on the data set itself. In order to be considered, an event must pass four requirements:

- Two electrons with $p_{\mathrm{T}} > 30\,\mathrm{GeV}$ and $|\eta| < 2.1$
- Both Electrons must pass the `Tight` requirement
- The invariant mass of the system falls in the range of $60\,\mathrm{GeV} < m_{\mathrm{ee}} < 120\,\mathrm{GeV}$
- The tag electron is required to be close to an HLT trigger object with $\Delta R < 0.3$.

If an event has more then two electrons satisfying these requirements it is not considered. A probe is considered passing if it matches with an HLT trigger object with $\Delta R < 0.3$. Because of the similar requirements on the tag and the probe, if the probe passes, then it can also be the tag, causing these events to be counted as two passes, while an event that the probe fails is counted as one fail. The efficiency for simulation and data is shown in Tables 6.2 and 6.3.

Since the single electron trigger only needs one electron to trigger it, there are not two scale factors for each electron, but rather one scale factor based on whether either the leading(ϵ_{L}) or trailing(ϵ_{T}) electron triggers the HLT:

$$SF_{\mathrm{L\ or\ T}} = \frac{1 - (1 - \epsilon_{\mathrm{L}}^{\mathrm{Data}})(1 - \epsilon_{\mathrm{T}}^{\mathrm{Data}})}{1 - (1 - \epsilon_{\mathrm{L}}^{\mathrm{simulation}})(1 - \epsilon_{\mathrm{T}}^{\mathrm{simulation}})}. \tag{6.6}$$

In the case where the trailing electron either has $p_{\mathrm{T}} < 30\,\mathrm{GeV}$ or $|\eta| > 2.1$ then $\epsilon_{\mathrm{T}}^{\mathrm{Data}} = \epsilon_{\mathrm{T}}^{\mathrm{simulation}} = 0$.

η	30–40 GeV	40–50 GeV	50–70 GeV	70–250 GeV
-2.1 to -2	$0.741^{+0.003}_{-0.003}$	$0.773^{+0.003}_{-0.003}$	$0.780^{+0.005}_{-0.005}$	$0.79^{+0.01}_{-0.01}$
-2 to -1.556	$0.734^{+0.001}_{-0.001}$	$0.772^{+0.001}_{-0.001}$	$0.786^{+0.002}_{-0.002}$	$0.792^{+0.005}_{-0.005}$
-1.556 to -1.442	$0.725^{+0.003}_{-0.003}$	$0.821^{+0.002}_{-0.002}$	$0.809^{+0.004}_{-0.004}$	$0.848^{+0.010}_{-0.010}$
-1.442 to -0.8	$0.8930^{+0.0005}_{-0.0005}$	$0.9396^{+0.0003}_{-0.0004}$	$0.9509^{+0.0006}_{-0.0006}$	$0.966^{+0.001}_{-0.001}$
-0.8 to 0	$0.9213^{+0.0004}_{-0.0004}$	$0.9528^{+0.0002}_{-0.0002}$	$0.9601^{+0.0004}_{-0.0004}$	$0.9692^{+0.0010}_{-0.0010}$
0 to 0.8	$0.9174^{+0.0004}_{-0.0004}$	$0.9473^{+0.0003}_{-0.0003}$	$0.9561^{+0.0004}_{-0.0004}$	$0.963^{+0.001}_{-0.001}$
0.8 to 1.442	$0.8964^{+0.0005}_{-0.0005}$	$0.9424^{+0.0003}_{-0.0003}$	$0.9533^{+0.0006}_{-0.0006}$	$0.966^{+0.001}_{-0.001}$
1.442 to 1.556	$0.714^{+0.003}_{-0.003}$	$0.823^{+0.002}_{-0.002}$	$0.827^{+0.004}_{-0.004}$	$0.861^{+0.009}_{-0.010}$
1.556 to 2	$0.758^{+0.001}_{-0.001}$	$0.800^{+0.001}_{-0.001}$	$0.811^{+0.002}_{-0.002}$	$0.823^{+0.005}_{-0.005}$
2 to 2.1	$0.764^{+0.003}_{-0.003}$	$0.792^{+0.002}_{-0.002}$	$0.797^{+0.005}_{-0.005}$	$0.82^{+0.01}_{-0.01}$

Table 6.2: The electron trigger efficiency in data.

Electron Reconstruction Efficiency

The electron GSF reconstruction scale factors are centrally produced [60]. In order for an electron to be reconstructed, a track must be matched to a super cluster in ECAL. If the electron's energy is either not deposited in the crystal or deposited in dead crystals in the detector, the electron will not be seen with ECAL. Since this method lacks an energy deposit, there is nothing to match to the tag electron to act as the probe. For this reason, the loss of efficiency due to super clusters failing to form is calculated from simulation. The efficiency and scale factor that come from matching super clusters to tracks is done using a data sample that was created with a special tag-and-probe trigger, `HLT_Ele20_CaloIdVT_CaloIsoVT_TrkIdT_TrkIsoVT_SC4_Mass50`. This trigger requires one electron with $p_{\mathrm{T}} > 20\,\mathrm{GeV}$, passing very tight ID and isolation requirements. By requiring $m_{\mathrm{ee}} > 50\,\mathrm{GeV}$ a very lax requirement can be placed on the other electron's transverse energy ($E_{\mathrm{T}} > 4\,\mathrm{GeV}$). In order to reject events that are poorly reconstructed, good events are required to have all the reconstructed particles be well-balanced transversely, with the particle flow missing transverse energy being

η	30–40 GeV	40–50 GeV	50–70 GeV	70–250 GeV
-2.1 to -2	$0.734^{+0.004}_{-0.004}$	$0.769^{+0.004}_{-0.004}$	$0.771^{+0.008}_{-0.008}$	$0.76^{+0.02}_{-0.02}$
-2 to -1.556	$0.736^{+0.002}_{-0.002}$	$0.768^{+0.002}_{-0.002}$	$0.779^{+0.003}_{-0.003}$	$0.789^{+0.008}_{-0.008}$
-1.556 to -1.442	$0.791^{+0.004}_{-0.004}$	$0.847^{+0.003}_{-0.003}$	$0.850^{+0.006}_{-0.006}$	$0.87^{+0.01}_{-0.02}$
-1.442 to -0.8	$0.9395^{+0.0006}_{-0.0006}$	$0.9612^{+0.0004}_{-0.0004}$	$0.9690^{+0.0007}_{-0.0008}$	$0.980^{+0.002}_{-0.002}$
-0.8 to 0	$0.9469^{+0.0005}_{-0.0005}$	$0.9670^{+0.0003}_{-0.0003}$	$0.9745^{+0.0005}_{-0.0005}$	$0.982^{+0.001}_{-0.001}$
0 to 0.8	$0.9466^{+0.0005}_{-0.0005}$	$0.9665^{+0.0003}_{-0.0003}$	$0.9739^{+0.0005}_{-0.0006}$	$0.982^{+0.001}_{-0.001}$
0.8 to 1.442	$0.9364^{+0.0007}_{-0.0007}$	$0.9597^{+0.0004}_{-0.0004}$	$0.9668^{+0.0008}_{-0.0008}$	$0.979^{+0.002}_{-0.002}$
1.442 to 1.556	$0.779^{+0.004}_{-0.005}$	$0.841^{+0.003}_{-0.003}$	$0.842^{+0.006}_{-0.006}$	$0.86^{+0.02}_{-0.02}$
1.556 to 2	$0.749^{+0.002}_{-0.002}$	$0.786^{+0.002}_{-0.002}$	$0.798^{+0.003}_{-0.003}$	$0.810^{+0.008}_{-0.008}$
2 to 2.1	$0.737^{+0.004}_{-0.004}$	$0.769^{+0.004}_{-0.004}$	$0.779^{+0.007}_{-0.008}$	$0.82^{+0.02}_{-0.02}$

Table 6.3: The electron trigger efficiency in MadGraph simulation.

less than 20 GeV. Reconstructed tag electrons are required to match spatially to the `Tight` trigger electron. This reconstructed electron is then required to pass `Tight`, as well as $p_{\mathrm{T}} > 25\,\mathrm{GeV}$ and $\eta < 2.5$. Electrons that fall in the gap between the ECAL barrel and endcap, $1.4442 < |\eta| < 1.566$, are rejected. The super-cluster is required to have a tracker isolation of < 0.15. The simulation requires that the reconstructed tag electron matches with a generated electron, with $\Delta\mathrm{R} < 0.2$. For simulation, $\mathrm{n}^{\mathrm{obs.}}_{\mathrm{pass}}$ and $\mathrm{n}^{\mathrm{obs}}_{\mathrm{total}}$ are the counts of the probe that pass and total probes, respectively. For data, the background is compensated for by first separating events by the probe p_{T} and η, and creating a distribution of the dielectron invariant mass. This distribution is then fit with a Gaussian-smeared $\mathrm{Z} \to \mathrm{e}^{+}\mathrm{e}^{-}$ simulation sample added to an exponential that represents the background. These fits were used to calculate the $\mathrm{n}^{\mathrm{obs.}}_{\mathrm{pass}}$ and $\mathrm{n}^{\mathrm{obs}}_{\mathrm{total}}$ that were used to calculate the efficiency of the data and the scale factors shown in Table 6.4.

$\lvert\eta\rvert$	20–30 GeV	30–40 GeV	40–50 GeV	$>$ 50 GeV
0.0 to 0.8	$0.982^{\pm0.003}_{\pm0.012}$	$0.988^{\pm0.001}_{\pm0.008}$	$0.990^{\pm0.001}_{\pm0.004}$	$0.990^{\pm0.001}_{\pm0.004}$
0.8 to 1.4442	$0.993^{\pm0.002}_{\pm0.012}$	$0.993^{\pm0.001}_{\pm0.008}$	$0.993^{\pm0.001}_{\pm0.004}$	$0.991^{\pm0.001}_{\pm0.004}$
1.4442 to 1.566	$1.016^{\pm0.012}_{\pm0.020}$	$0.985^{\pm0.004}_{\pm0.009}$	$0.987^{\pm0.004}_{\pm0.004}$	$0.974^{\pm0.009}_{\pm0.006}$
1.566 to 2.0	$0.988^{\pm0.003}_{\pm0.012}$	$0.993^{\pm0.002}_{\pm0.008}$	$0.992^{\pm0.001}_{\pm0.004}$	$0.990^{\pm0.003}_{\pm0.004}$
2.0 to 2.5	$1.002^{\pm0.004}_{\pm0.012}$	$1.004^{\pm0.002}_{\pm0.008}$	$1.005^{\pm0.002}_{\pm0.004}$	$0.998^{\pm0.004}_{\pm0.004}$

Table 6.4: Scale factors for GSF electron reconstruction. The upper uncertainty listed is statistical, the lower is systematic.

6.2.2 ϕ^* efficiency

The overall efficiency for the signal events in data can be calculated using a simulated sample by taking the previously calculated scale factors into account:

$$\epsilon_i = \frac{\sum_{obs} SF(l_1, l_2)}{n_i^{total}} \tag{6.7}$$

Here, rather then using the number of observed events in the simulation directly, n_i^{obs}, each observed event uses $SF(l_1, l_2)$, which is the product of all applicable scale factors, and used as a weight to calculate the ϵ_i of data from simulated samples.

7

Background Samples

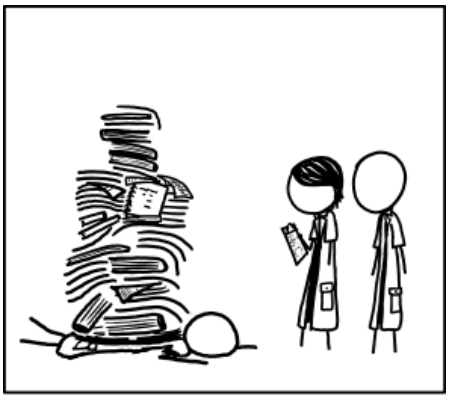

Figure 7.1: fortunately for us, we do not need to make paper copies of all the simulated events we have. [4]

Studies of $Z \to \ell^+\ell^-$, such as ϕ^*, are useful due to the clarity of the signal, with over 99.5% of the data being signal events($Z \to e^+e^-$) after selection has been applied. The majority of background events involve a Z, such as ZZ, WZ, as well as $Z \to \tau^+\tau^-$. These along with the other backgrounds that do not contain a Z are used are shown in Table 7.1.

All analyzed backgrounds were predicted via simulation with the exception of QCD Multi-jet and $W^{\pm}$ + jets. A distribution of the m_{ee} of the backgrounds is shown in Fig 7.2. Around 50% of background events are within 10 GeV of the Z mass due to the

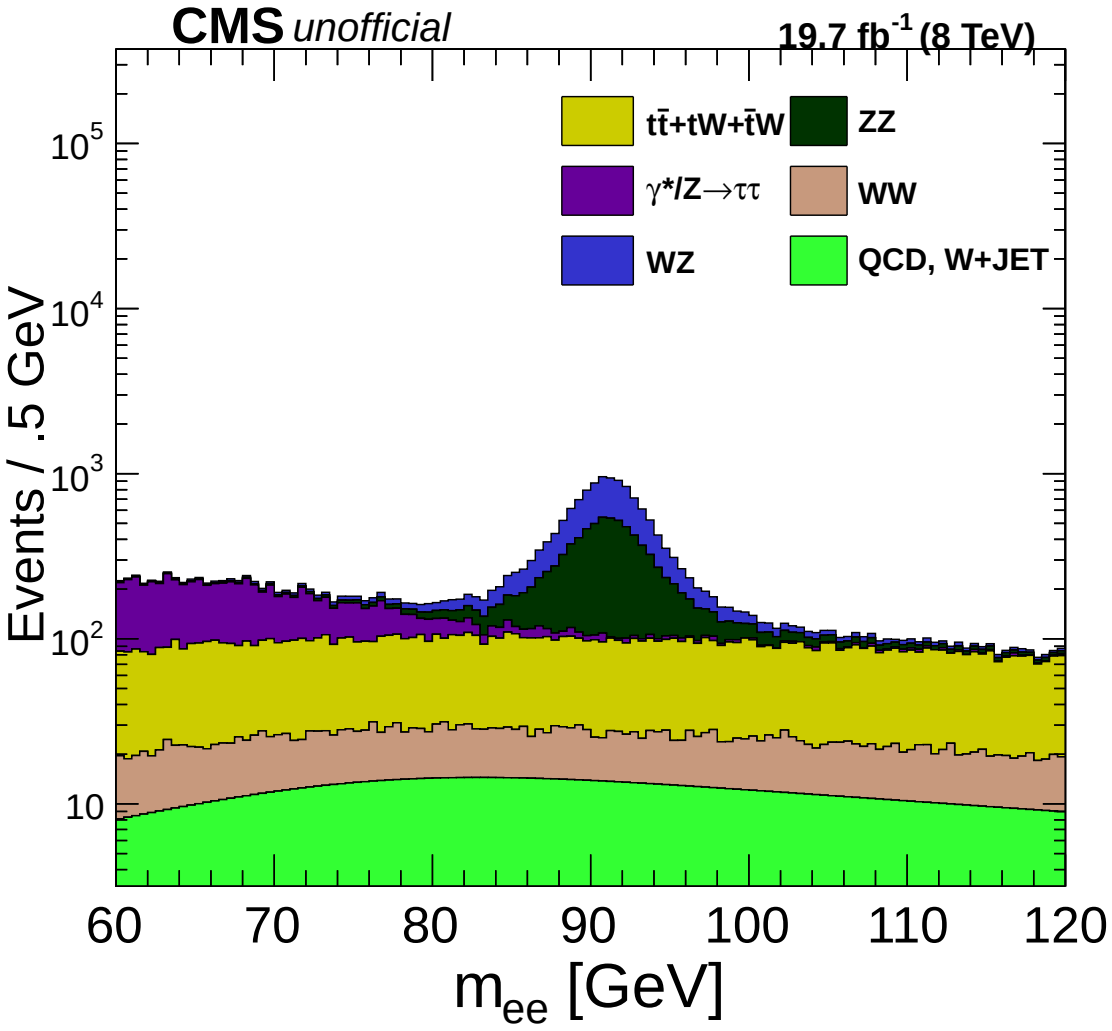

Figure 7.2: A plot of the center of mass values of all the backgrounds stacked. With the exception of the ZZ and WZ all the Backgrounds have a relatively flat distribution.

Table 7.1: Data sample composition as a percentage of the total and as a percentage of just the backgrounds. These represent the samples that were used for unfolding

Process	Generator	σ (pb)	ratio to signal	% background
$t\bar{t}$	Madgraph	23.64	0.0017	27.7
ZZ	Pythia6	17.7	0.0012	19.9
$W^{\pm}Z$	Pythia6	33.21	0.0012	19.7
$Z \rightarrow \tau^{+}\tau^{-}$	Powheg	1966.7	0.0009	14.9
QCD Multi-jet & $W^{\pm}+$jets	N.A.	N.A.	0.0006	10.0
$W^{+}W^{-}$	Pythia6	54.84	0.0003	5.2
$tW^{-}\&\bar{t}W^{+}$	Powheg	22.1	0.0002	2.7

WZ and ZZ backgrounds. Most of the other backgrounds produce a relatively flat m_{ee} distribution, with the exception being $\mathrm{Z} \rightarrow \tau^{+}\tau^{-}$ which continuously decreases. When comparing the ratio of background to data of ϕ^{*}, as is shown in Fig. 7.3, for all bins that $\phi^{*} < 0.1$ the backgrounds are at a level of approximately 0.2%, while in the highest bins the background is nearly 5% of the data. This is relatively intuitive since many of the backgrounds come from electrons that were not produced in pairs, which means the angles of the electrons from the background are uncorrelated and can easily produce a high ϕ^{*} event, while Z events tend to produce low ϕ^{*} values, since the ϕ^{*} measurement of the Z is correlated with Q_{T}, and the Z is rarely highly boosted.

7.1 QCD Multi-jet and $W^{\pm}+$ jets

QCD events are extremely common, happening at a rate of roughly 10 million times that of $\mathrm{Z} \rightarrow \mathrm{e}^{+}\mathrm{e}^{-}$. Although QCD can not produce electrons directly, because electrons lack color charge, it does produce hadrons that can then produce electrons when the hadrons decay such as $\mathrm{b} \rightarrow \mathrm{c} + \mathrm{W}^{-} \rightarrow \mathrm{c}+\mathrm{e}^{-} + \bar{\nu}$. Therefore QCD can produce them at a large rate. However, the selections made on electrons, described in the previous chapter, remove the vast majority of these QCD events leaving roughly only 1 in 10 billion making it into the final data sample. To successfully estimate the background rate due to these QCD events an impractically-large simulation sample for this analysis would be required. Thus a data-driven method is used to approximate the rate of QCD events for each ϕ^{*} bin individually.

The data-driven method that is used takes advantage of the fact that QCD events

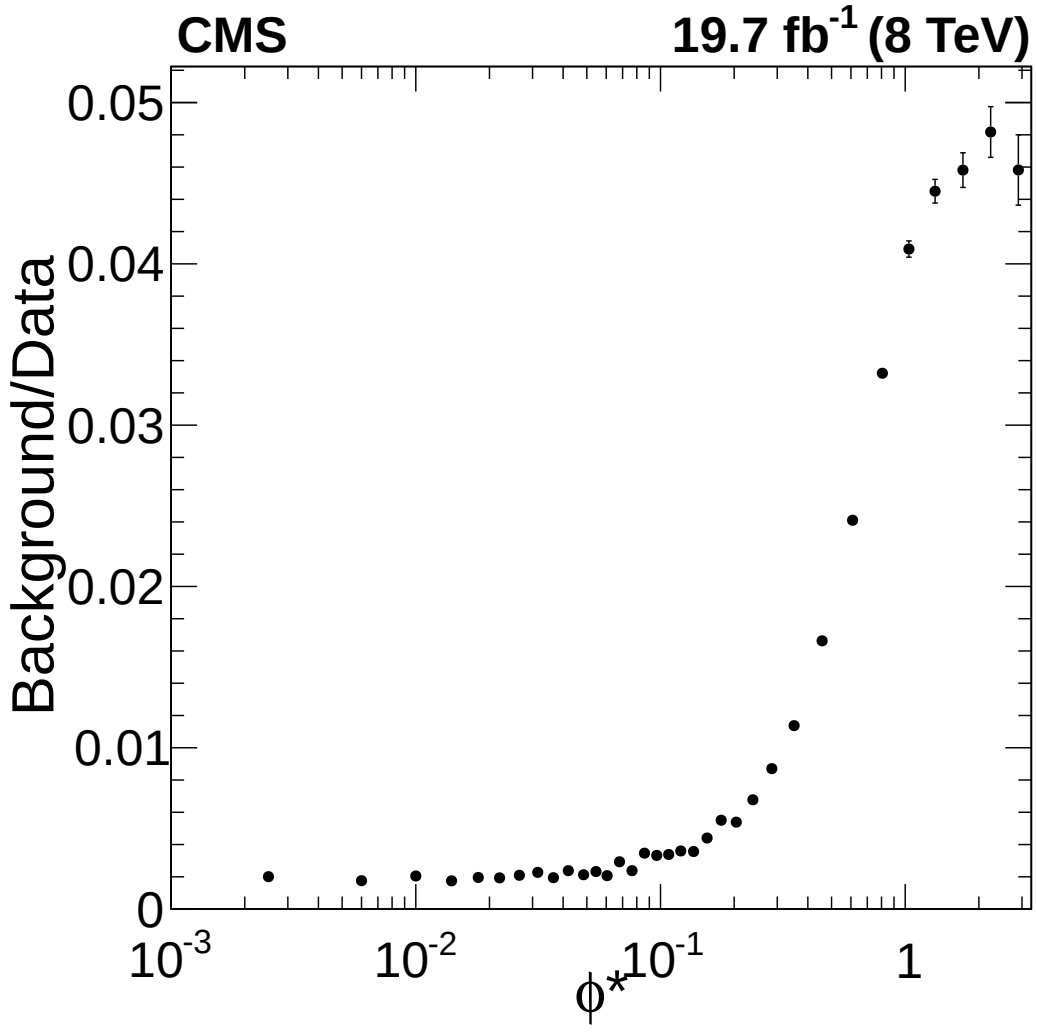

Figure 7.3: Ratio of the background to data. This ratio grows by over a factory of 20 from low to high ϕ^*

generate electrons independently of each other. Therefore it is possible to do a study on events that produce either e^-e^- or e^+e^+, which are referred to as same sign events. These events happen at the same rate as e^+e^-. Consequently, by calculating the rate of same sign events, the rate of opposite sign events is known.

A collection of events was created from data using reconstructed electrons with the same sign, and passing all the same requirements used in the main analysis, except for m_{ee}, as outlined in Chapter 6. The same requirements were placed on each simulation, as well as weighting them to the proper luminosity. The simulations used were the same as those that were used for the analysis itself. By requiring same sign events, most background and signal events in the simulation could be discarded, though some of the backgrounds were capable of creating a same sign pair that pass the requirements. These include ZZ, $W^{\pm}Z$, and even $t\bar{t}$ which could produce an electron from a jet. Other events, such as signal events could be kept if one of the two charges of the electron pair was misidentified. In fact because the Z cross-section is so large compared to the others, even though the vast majority of Z events were removed, there is still a noticeable amount of Z events in the final selection. These weighted events are then separated into their respective ϕ^* bin and a m_{ee} plot is created. The following function is then fit to the data:

$$\alpha\, T_{\mathrm{MC}} + \beta\, F_{\mathrm{BG}}(x;\gamma,\delta,\varepsilon). \tag{7.1}$$

Where T_{MC} comes directly from the simulations and F_{BG} is a function that represents the QCD rate. The QCD function used in this analysis is:

$$F_{\mathrm{BG}}(x;\gamma,\delta,\varepsilon) = e^{-\gamma x}\,\mathrm{erfc}\left(\frac{\varepsilon - x}{\delta}\right). \tag{7.2}$$

The free fit parameters are α, β, γ, ε, and δ. The resulting function is then integrated over the mass range of the analysis($60\,\mathrm{GeV} < m_{\mathrm{ee}} < 120\,\mathrm{GeV}$) and multiplied by two to compensate for the lack of charge requirements in the main analysis. However, due to a limited number of events in the bins and a high uncertainty for the fit, there are large jumps in the QCD values for each ϕ^* bin that are not physical. Therefore, the total distribution is smoothed by averaging each bin with its neighbors. The final uncertainty of this distribution is set to 100%. Two examples fits are shown in Fig. 7.4.

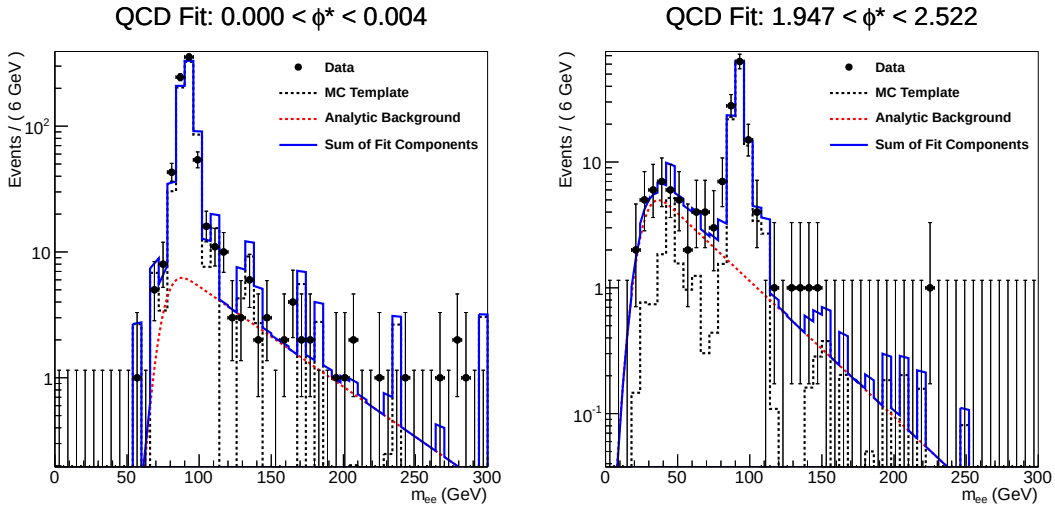

(a) (b)

Figure 7.4: QCD Fit examples from the first and final ϕ^* bins. As can be seen from the plot there still exist a Z peak due to misidentification of charge for some $Z \rightarrow e^+e^-$ events. The QCD is taken as the integral of the fitting function from 60 to 120 GeV.

8

ϕ^* Uncertainties

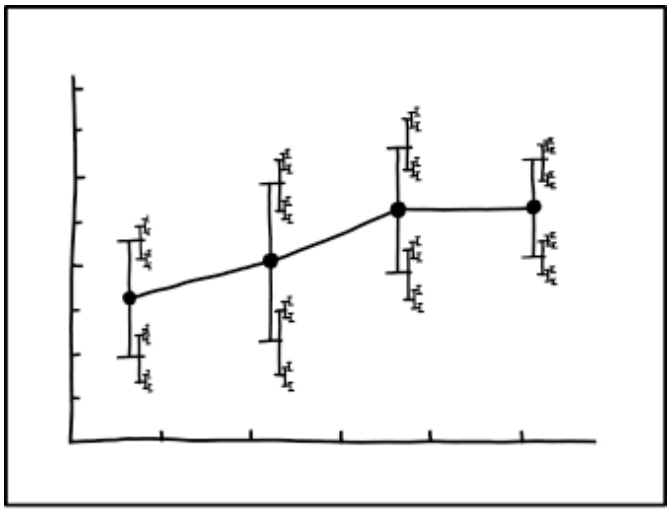

Figure 8.1: The propagation of uncertainty can be complicated, as this `xkcd`[4] alludes,

The uncertainty of a measurement is as important as the measurement itself. Without knowing the uncertainty, it is not possible to quantify the theory's agreement with data. This chapter describes how these uncertainties are included in both data and simulation.

8.1 Propagation of Statistical Uncertainty

The statistical uncertainty of a measured number of events, N_i, is trivially defined by $\sqrt{N_i}$. However, the measured ϕ^* distribution is not directly comparable to simulation. Rather, the measured ϕ^* distribution is unfolded first, which leads to the need to propagate the statistical uncertainty into the unfolded results. This calculation is performed by RooUnfold which propagates the statistical uncertainty of the data through the unfolding matrix and outputs a covariance matrix. Due to the small amount of bin migration it was decided to just use the diagonal of the covariance matrix as the unfolded statistical uncertainty. Two tests were preformed to validate this assumption.

8.1.1 Validation of the Statistical Approach

A test was preformed to prove the triviality of the off diagonal terms of the statistical covariance matrix. This test used simple "toy" Monte Carlo samples that were created using a central MadGraph ϕ^* distribution to create new Monte Carlo distributions. Each new toy Monte Carlo distribution was generated by taking each bin of the original MadGraph distribution and varying it randomly using a Gaussian distribution, centered at the bin's original value, and using the bin's uncertainty as the width of the Gaussian distribution. This method was used to create 500 new distributions with each distribution unfolded using the powheg distribution. The resulting bin values along with their deviation is compared to the central result whose deviation comes directly from the diagonal of the covariance matrix for the statistical data. With the results shown in Fig 8.2, the correlation between bins due to statistical fluctuations in the unfolded sample have minor effects on the uncertainty of each bin.

8.1.2 Cross Check of Simulation Statistics

This test was done to prove that the output statistical uncertainty of RooUnfold does not include and is not affected by the statistics of the simulation used to unfold the sample. This was done twice, once with 5000 randomly chosen powheg events, and a second time with 50000 randomly chosen events. As was done with the first test, 500 toy samples were created and unfolded using these two subsamples, with the results shown in Fig 8.3. By observing both figures it can be seen that there is a larger fluctuation in

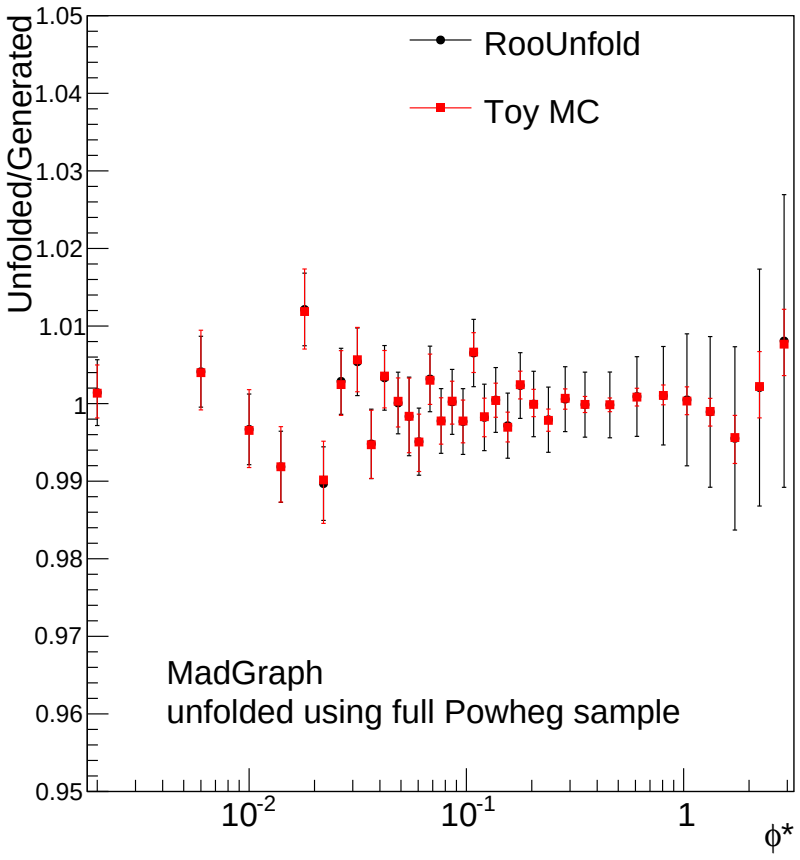

Figure 8.2: A MadGraph sample unfolded using POWHEG. The black shows the results from RooUnfold with the uncertainty taken from the Diagonal of the covariance matrix that RooUnfold produces. The red is the average position of the result from unfolding using the Toy samples, where the red line defines one standard deviation, defined as the spread of the central 68.2% of the values in that bin.

the data when a smaller Monte Carlo sample is used to unfold the data, however the error bars on the unfolded data are still on the order of 1% because they only include the propagated uncertainty of the unfolded results. The red error bars, however, show the standard deviation of the unfolded toy Monte Carlo samples, which is sensitive to the lack of statistics in the sample used for the unfolding.

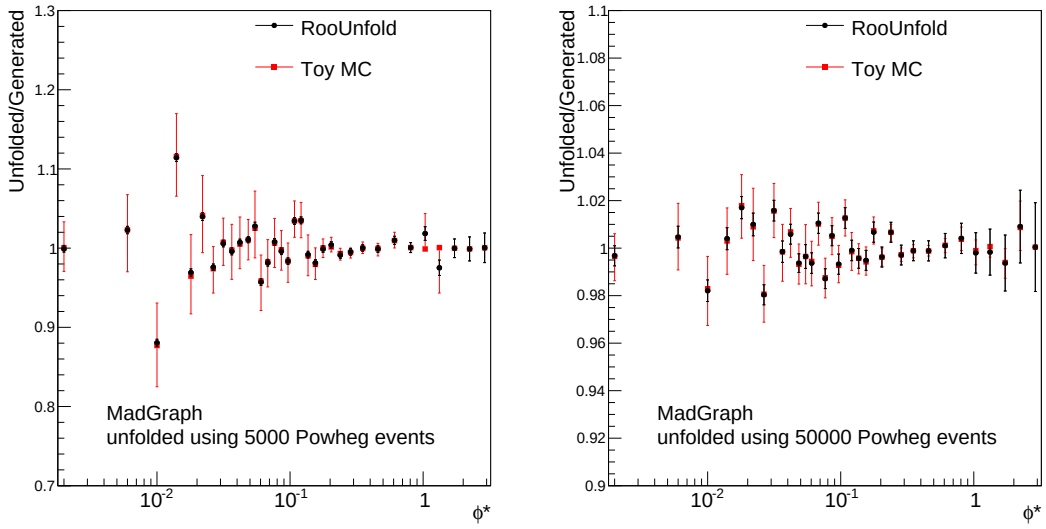

(a) (b)

Figure 8.3: 500 samples created using a central MADGRAPH where each bin was fluctuated independently based on its statistical uncertainty. These samples were unfolded using two POWHEG subsamples, with the left plot unfolded using a POWHEG sample with 5000 events and the right with a sample containing 50000 events. The black points are the central Monte Carlo sample and the black bars show the propagated uncertainty using RooUnfold, while the red points are the average value of the toys and the red error bars are the standard deviation of the unfolded toys.

8.1.3 Normalized Statistical Uncertainty

Statistical uncertainty decreases in the normalized data distributions. The uncertainty of the ith bin in a normalized distribution is calculated using the equation:

$$(\epsilon_i^{norm})^2 = (\epsilon_i^{abs} \times (\frac{1}{\sigma} - \frac{\sigma_i}{\sigma^2}))^2 + \sum_{i \neq j} (\epsilon_j^{abs} \times \frac{\sigma_i}{\sigma^2})^2; \tag{8.1}$$

ϵ_j^{abs} is the statistical uncertainty of bin j for the absolute distribution, σ_i is a particular bin's cross-section, and σ is the overall cross-section given by the integral of the distribution.

8.2 Unfolding and Monte Carlo Statistical Uncertainty

Although a Z simulation sample was used to unfold the data, according to Ref [61] it is not necessary for the distribution that is used to unfold the data to be correct. Only the relationship between generated and reconstructed bins is required to be accurate. This was tested by placing events of a POWHEG sample into a histogram of bin width $\Delta\phi^* = 0.001$. The weight for each of these bins was set to be inversely proportional to the number of events in the bin, creating a flattened distribution. This new flattened distribution was used to unfold the MADGRAPH sample. As can be seen in Fig. 8.4, there is no significant deviation. Therefore our, uncertainty due to unfolding is calculated only using the uncertainty due to simulation statistics.

The uncertainty due to the statistics of the simulation sample used to create the unfolding matrix is not included by RooUnfold's covariance matrix. In order to calculate the uncertainty of the unfolded data due to the statistical uncertainty of the sample used to unfold the data, a method similar to the one used for checking the propagation of statistical uncertainty was used. Five hundred Monte Carlo samples were created using the same method as above, and used to unfold the data. An example is shown in Fig. 8.5. The standard deviation of this plot is used as the unfolding uncertainty, and is around 0.5% for the majority of the bins, though at high ϕ^* values it increases to around 1%.

8.3 Additional Uncertainties

In addition to statistical uncertainties, there are also systematic uncertainties. These uncertainties, such as those from theory, include the cross-section of backgrounds, as

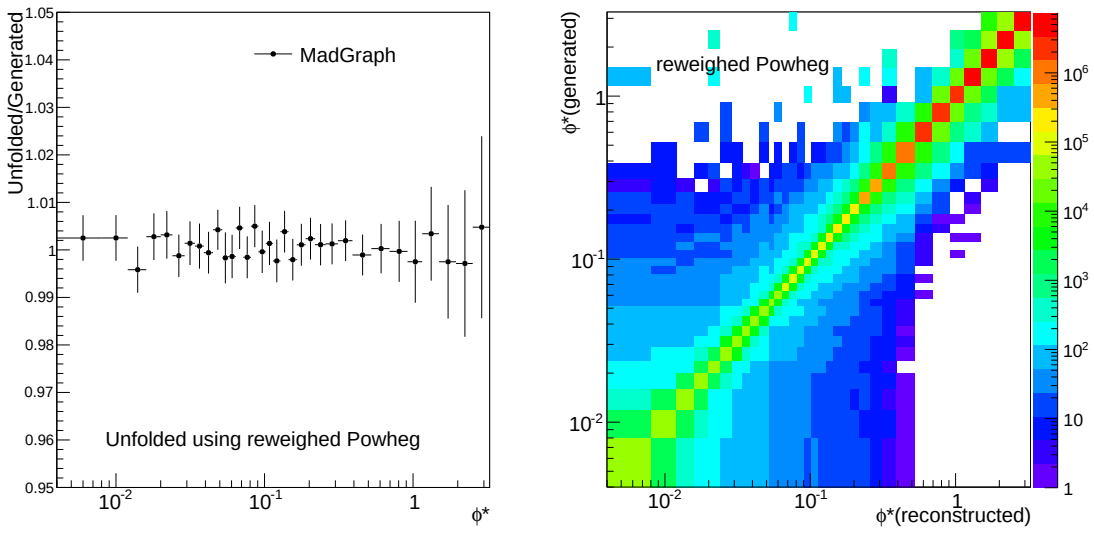

(a) (b)

Figure 8.4: Left: A ratio of unfolded reconstructed ϕ^* distribution of a MadGraph $Z \to e^+e^-$ sample over the generated distribution for the same sample. The sample was unfolded with a flattened $Z \to e^+e^-$ powheg sample. Right: The bin migration matrix produced using the flattened powheg distribution.

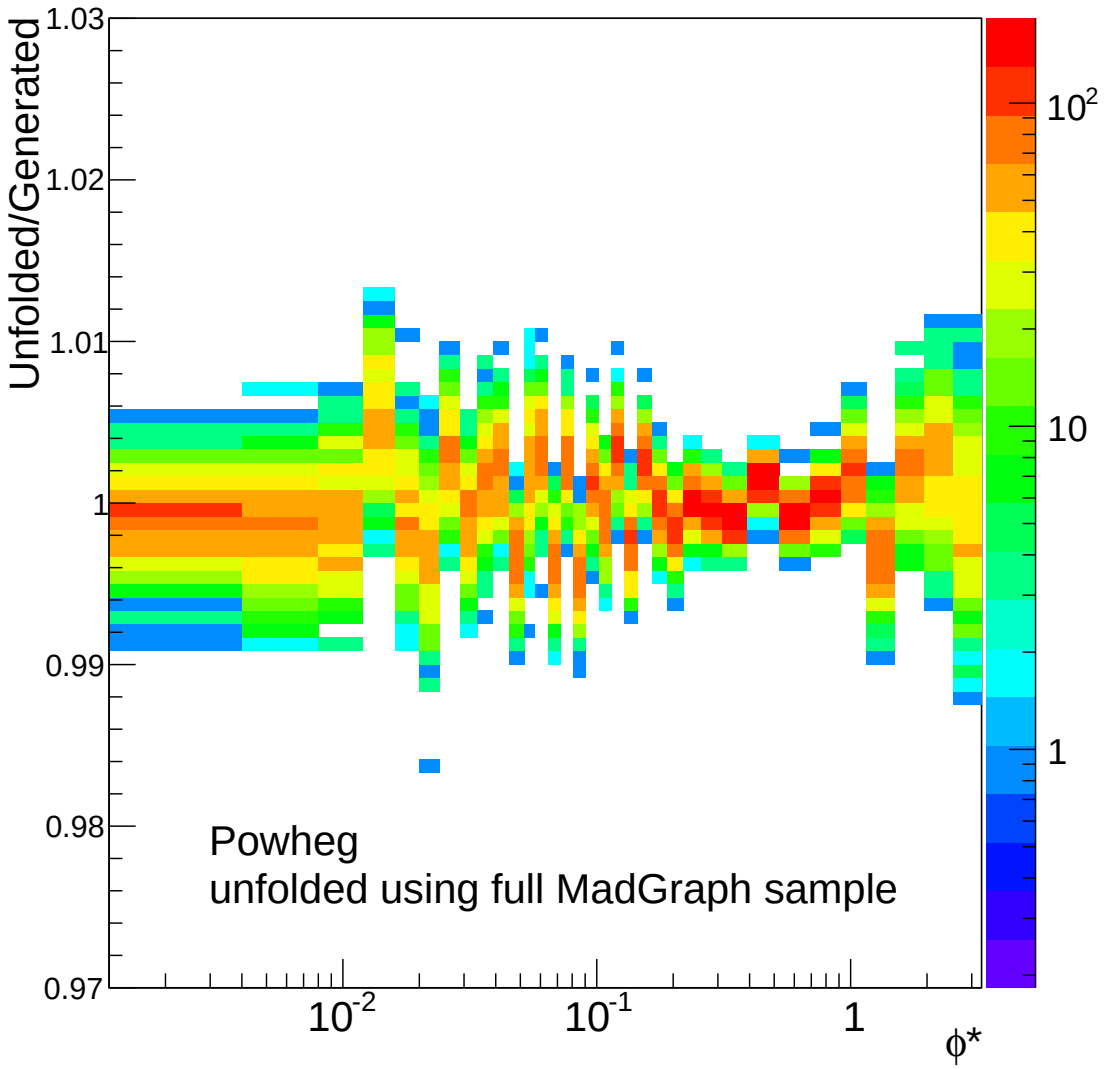

Figure 8.5: An example showing the unfolding results of a POWHEG sample after being unfolded by 500 MADGRAPH samples.

well as rates of FSR. Another source of uncertainty comes from the detector. This includes luminosity, as well as the reconstruction and measurement of the electron, such as its momentum and its direction.

8.3.1 Luminosity

All measurements of the absolute rates, or the cross-section, must be normalized to the exposure of the detector which is called the integrated luminosity of the data sample. In order to measure the integrated luminosity, CMS uses the number of charged particles produced in all interactions. The majority of interactions do not produce anything of interest; the ever-present QCD interactions create a spray of charged particles. The luminosity is calculated by measuring the occupancy of the pixel tracker [62][63]. The integrated luminosity of the data sample of CMS has a 2.6% uncertainty. This uncertainty dominates the absolute ϕ^* distribution, being larger then all other uncertainties by more than a factor of two, except in the last few bins. Fortunately this uncertainty is fully correlated between all ϕ^* bins, so normalizing cancels out the the uncertainty, and is only involved slightly in the background subtraction. Due to the small backgrounds and large uncertainties in the cross sections used in the background subtraction, the luminosity uncertainty has trivial effect on the normalized distribution.

8.3.2 Trigger, Reconstruction, and Identification Scale Factors

As mentioned in Sec 6.2, scale factors are used to compensate for differences between the simulated detector and the real one. The uncertainty is calculated by creating 500 toy Monte Carlo samples for each type of scale factor. For each toy, a new scale factor is chosen from a Gaussian centered at the nominal scale factor with the width being the uncertainty of the scale factor. The uncertainty is taken from the central 68.2% of results from the toys. This is done independently for all scale types of scale factors, and then the final uncertainties are added in quadrature.

8.3.3 Background Uncertainty

The background uncertainties are estimated by varying the theoretical cross sections of the different backgrounds. Due to the very small size of the backgrounds for this study,

it was decided to overestimate their uncertainty to remove doubt of their unimportance. The uncertainty due to $t\bar{t}$ is calculated by varying the theoretical cross section by 10%. The WZ and ZZ cross-sections are varied by 20% and the QCD and W+jets are varied by 100%. The new distributions are used in the background subtraction to create two new data distributions that are then unfolded. The uncertainty is defined as the difference between this new unfolded result and the original. The resulting uncertainties are added in quadrature. All other uncertainties due to background are negligible.

8.3.4 Pileup Uncertainty

As discussed in Sec 4.4 additional soft pp interactions are added to events in order to simulate the normal bunch crossing where multiple protons interact. These events are then reweighted so that this can match the actual experimental data. The uncertainty due to this re-weighting is calculated by varying the inelastic proton-proton cross-section up and down by 5%. The full unfolding process is then performed using these two new samples, with the pileup uncertainty defined as the largest difference between the new unfolded distributions compared to the original.

8.3.5 Lepton p_{T} Scale Uncertainty

The variable ϕ^* was chosen due to it not being dependent on the p_{T} measurement of either lepton. Despite this, mismeasurements of the p_{T} can effect the overall distribution of ϕ^*. This is due to the acceptance requirements, since it includes p_{T} requirements. To study the effect of this, we vary the p_{T} of all electrons up and down by 0.3%, which is a conservative estimate of the uncertainty of p_{T} scale. The largest difference for each bin between these new distributions and the nominal distribution is taken as the uncertainty. This leads to a p_{T} scale uncertainty between 0.07% to 0.17% for the absolute cross section, while the corresponding uncertainty on the normalized cross section is less than 0.1% for all bins.

8.3.6 Final State Radiation Uncertainty

As mentioned in Section 2.3.4 FSR occurs when one of the leptons emits a photon. Although unfolding the distribution accounts for this, the unfolding matrix is dependent

on the simulation model. Therefore, uncertainties in how well the simulation models FSR must be propagated. The uncertainties are calculated using FSRWeightProducer which weights events in an attempt to compensate for missing QED calculations in Pythia. A new ϕ^* distribution is created using these weighted events and then compared to the original distribution. The difference between the distributions is taken as the FSR uncertainty. The FSR uncertainty was found to be $< 0.013\%$ for the absolute distribution and $< 0.011\%$ for the normalized distribution.

8.4 Uncertainty Plots

Each of the uncertainties described is combined in quadrature to show the total uncertainty. Plots showing the scales of uncertainties are shown in Fig 8.6. As can be seen from these plots for the absolute case, the luminosity uncertainty dominates, with all other uncertainties having an effect on the absolute total uncertainty of less than 20% . For the normalized case, the uncertainty is mostly dominated by statistics, either directly, or in the case of unfolding indirectly, though in higher ϕ^* other uncertainties start to rise.

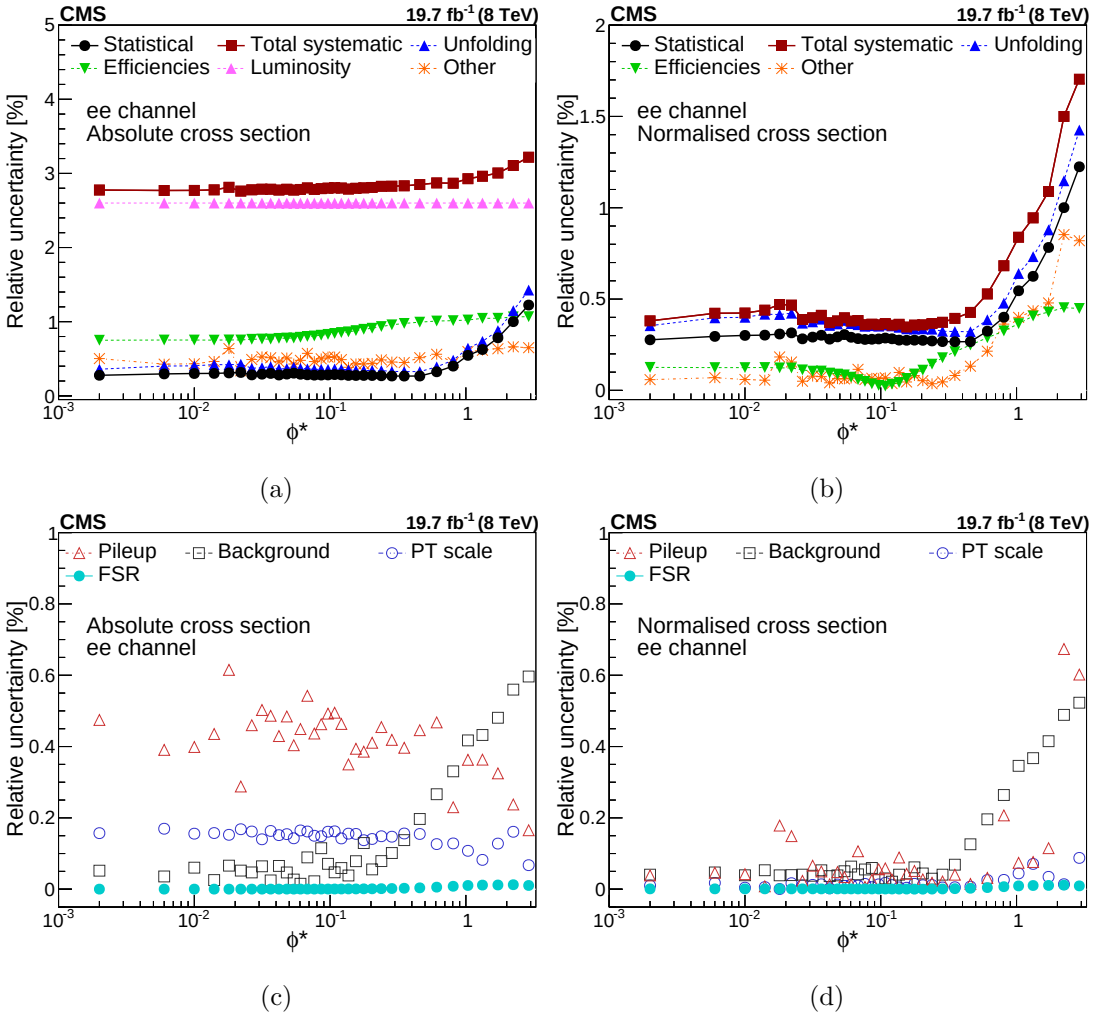

Figure 8.6: The top figures show the variation of the statistical and systematic uncertainties with ϕ^*. The uncertainties from background, pileup, electron energy scale, and from QED-FSR modeling are combined under the label "Other". The bottom plot shows each of these "Other" uncertainties.

9

Results

"Everything not saved will be lost"

– Nintendo 'Quit Screen' message

The final measured ϕ^* distribution and ϕ^* y double differential distribution for both the absolute and normalized cross-sections are presented in this chapter. Data is compared to five centrally produced distributions, POWHEG + PYTHIA6, POWHEG + PYTHIA8, MADGRAPH + PYTHIA6, aMC@NLO + PYTHIA8, and RESBOS. For this comparison the best precision of the final measurement is obtained by combining the $Z \to e^+e^-$ and $Z \to \mu^+\mu^-$ measurements. The individual $Z \to e^+e^-$ results is given in the appendix.

9.1 BLUE

It is possible to lower the uncertainty of the data distribution by combining the results of the ϕ^* measured using $Z \to e^+e^-$ and $Z \to \mu^+\mu^-$ because of lepton universality. For this analysis the combination is done using the method of Best Linear Unbiased Estimate(BLUE)[64, 65]. The uncertainties with low correlation are overall decreased to roughly $\left(\frac{1}{\epsilon_{\mu^+\mu^-}} + \frac{1}{\epsilon_{e^+e^-}}\right)^{-1}$, though uncertainties with high correlation are less-significantly affected. When combining the two distributions, a full covariance matrix is required.

This covariance matrix should ideally include all uncertainties, however if there is

too much correlation between bins, a feedback loop can lead to a nonsensical result, which Fig. 9.1 exemplifies. This example includes the uncertainty due to luminosity, which is 100% correlated between bins as well as being the largest. Although for the most part, the muon and electron result are all within roughly 1% of each other, the combined result is less than both by roughly 4% for the majority of the bins. In order to avoid this feedback loop the final covariance matrix that is used as an input to BLUE does not include the luminosity or efficiency components.

The results for both 1D and 2D are shown in Fig 9.2, 9.3 and 9.4. As expected both the electron and the muon measurements are close to each other, and the BLUE output falls between the electron and the muon results. This also succeeded in lowering the overall uncertainty.

9.2 Direct Measurements Compared to Simulation Results

With the exception of RESBOS the integrated cross sections of all the tested simulations are lower than the expected values. This is shown in Fig 9.5. Infact all simulations with the exception of RESBOS are closer to each other than to the measured result.

Figure 9.6 shows direct measurements compared to simulation. These measurements are not unfolded. As can easily be seen the data cross-section is almost consistently larger in all bins of both plots. Also, although the cross-section of data is larger than the simulation for the majority of Q_{T}, it is very consistent for the majority of bins with small statistical uncertainty; however, in the lowest Q_{T} ($< 20\,\mathrm{GeV}$) this no longer holds true. As mentioned in Sec 2.3.5, this is the area in which ϕ^* is most useful since it is capable of testing the accuracy of Q_{T}. Figure 9.6a also shows that, similar to Q_{T}, all bins of ϕ^* have a have a larger measured ϕ^* cross-section than the simulation. However, unlike the Q_{T} measurement, the ϕ^* distributions shape based on data is quite different from the simulation.

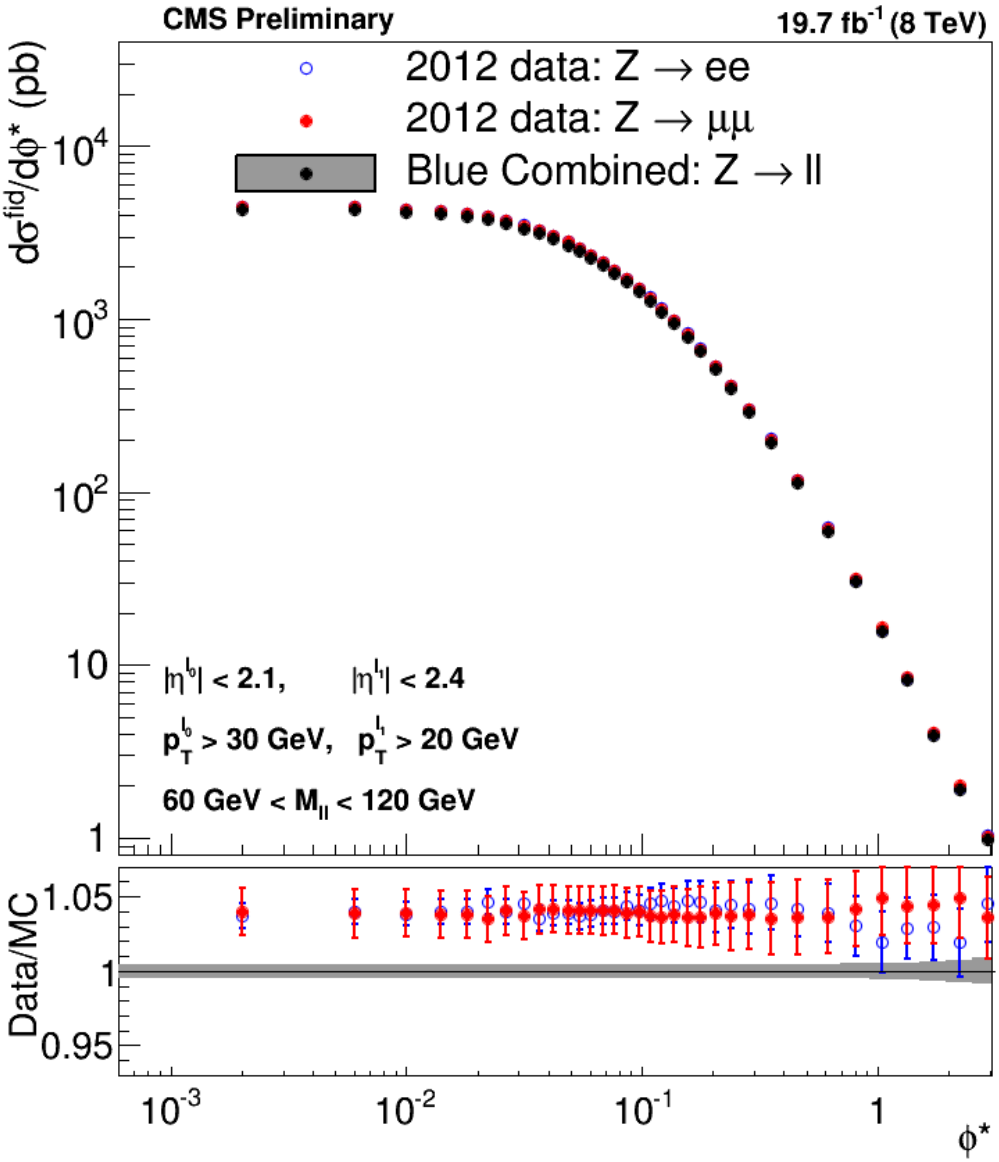

Figure 9.1: This shows the comparison between the BLUE result and the electron and muon results when there is a high input bin correlation. As can be seen the BLUE results, due to numerical effects, are roughly 3% below either the electron or muon results

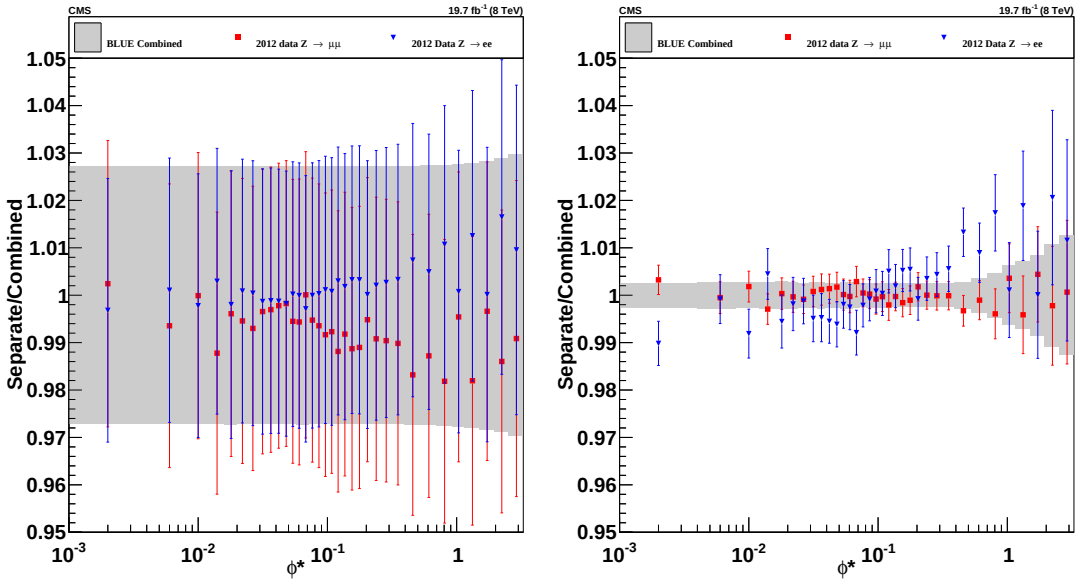

Figure 9.2: Blue one dimensional results. The left shows the case of the absolute results and the right shows the normalized combined result.

9.3 Unfolded Results Compared to Simulation

When comparing the unfolded results to multiple different simulation samples none of them match the unfolded results as can be seen in Fig 9.7, with even the sample that fits best, MadGraph, being over one standard deviation from the data in the majority of bins. These differences imply an intrinsic issue with the simulation generators production of Z Q_{T}.

Similar to the 1D distribution, the unfolded 2D distribution is compared to the same simulation samples. The normalized results are shown in Fig 9.8. As can be seen, the shape of the distributions is relatively uniform over most y bins. However, the MadGraph sample shows a visible difference in scale, with there being a deficit in almost all of the ϕ^* bins in the low rapidity plot, and an excess in the higher rapidity plots. Therefore, even though MadGraph appears to create relatively good agreement with data for the ϕ^* distribution, it is unable to create agreement with rapidity distribution. The study of the potential implication of this is described in Chapter 10.

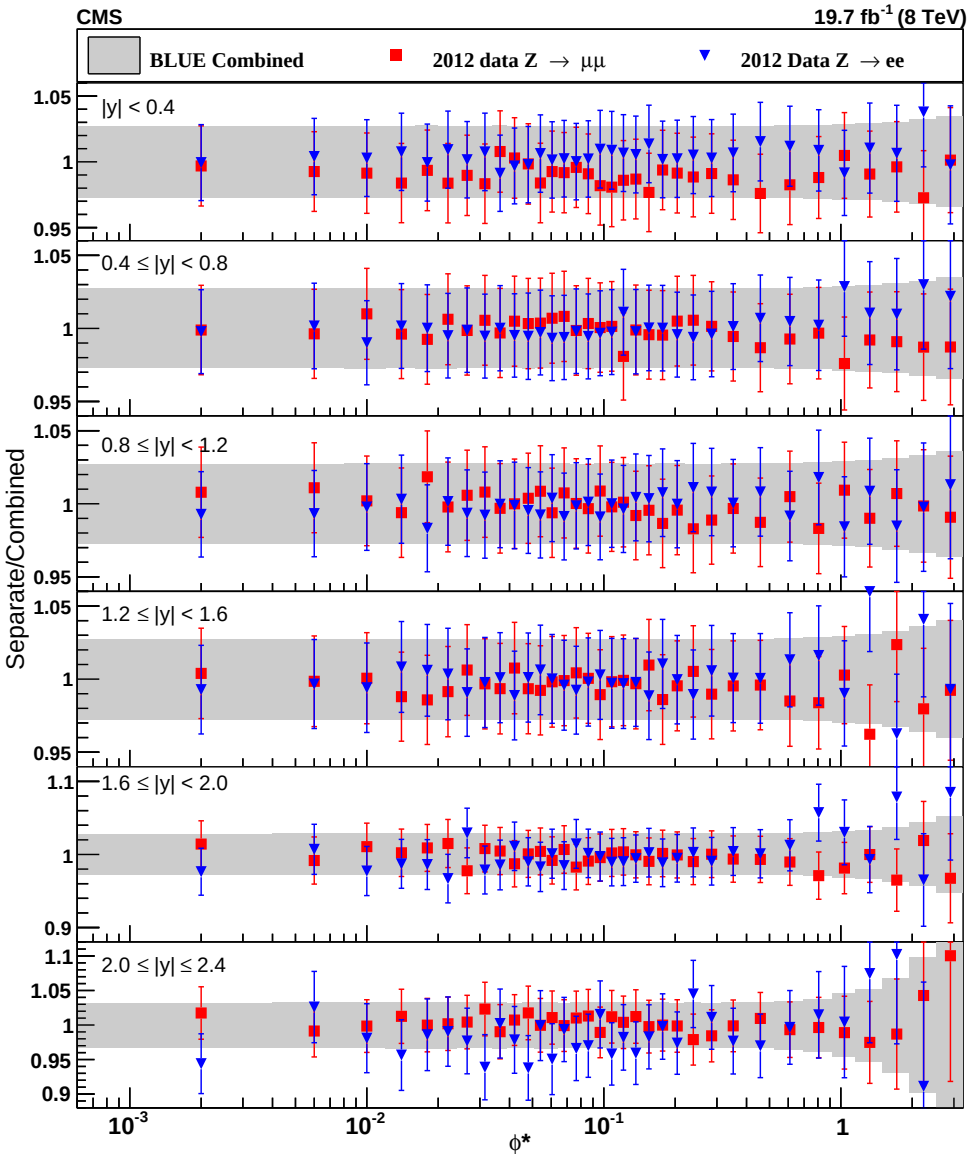

Figure 9.3: A plot comparing the ratio of the ϕ^* distributions separated by rapidity of the electron and muon studies to the BLUE combined result of the absolute distribution

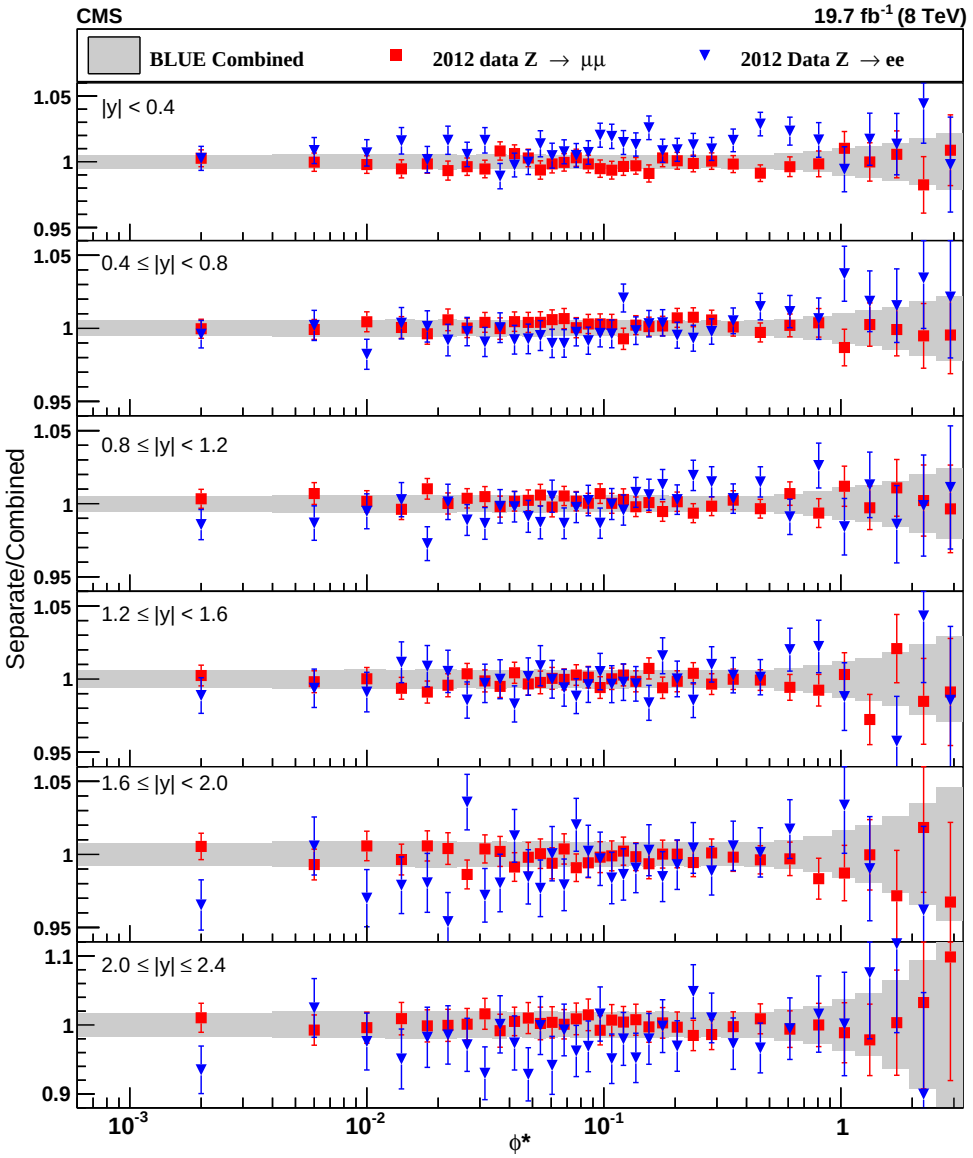

Figure 9.4: A plot comparing the ratio of the ϕ^* distributions separated by rapidity of the electron and muon studies to the BLUE combined result of the normalized distribution

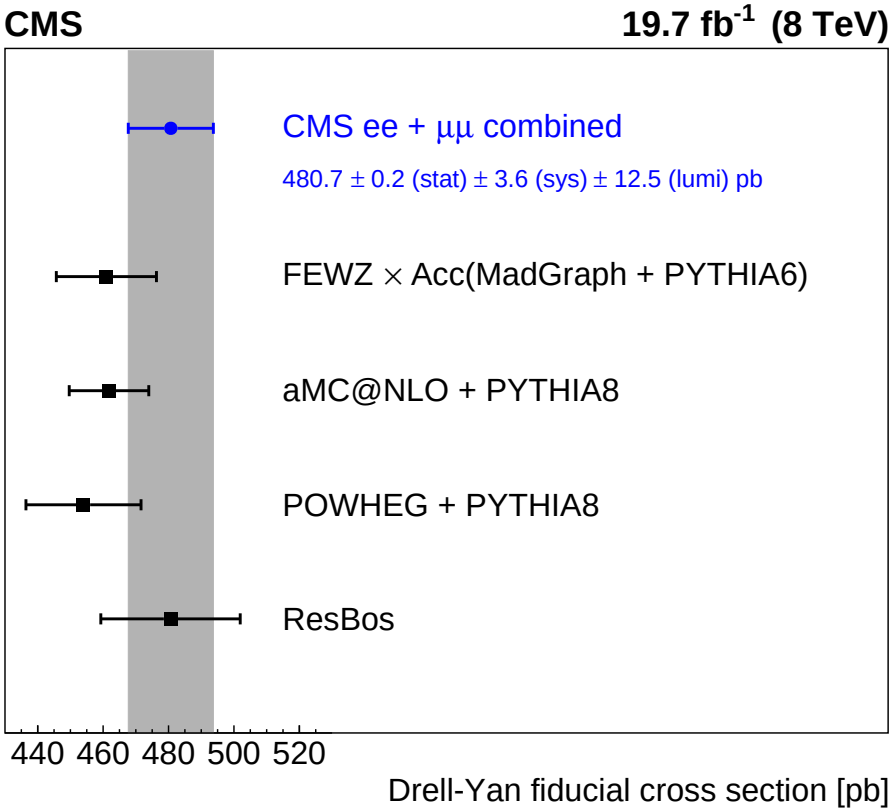

Figure 9.5: Comparison between the integrated cross-section of data compared with the used simulations. This shows that with the exception of RESBOS all simulation have cross sections lower than the measured one

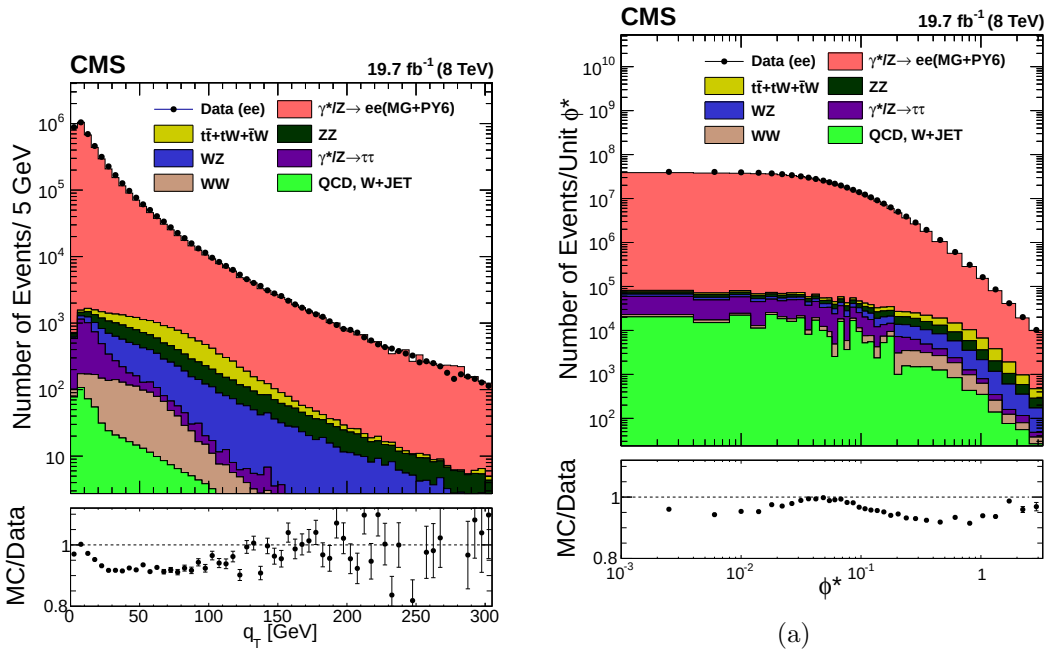

(a)

Figure 9.6: Direct measurements compared to simulation samples. The Z $\rightarrow$ e^+e^- sample used was Madgraph. The left figure makes the comparison as a function of the measured Q_{T} while the right compares as a function of ϕ^*

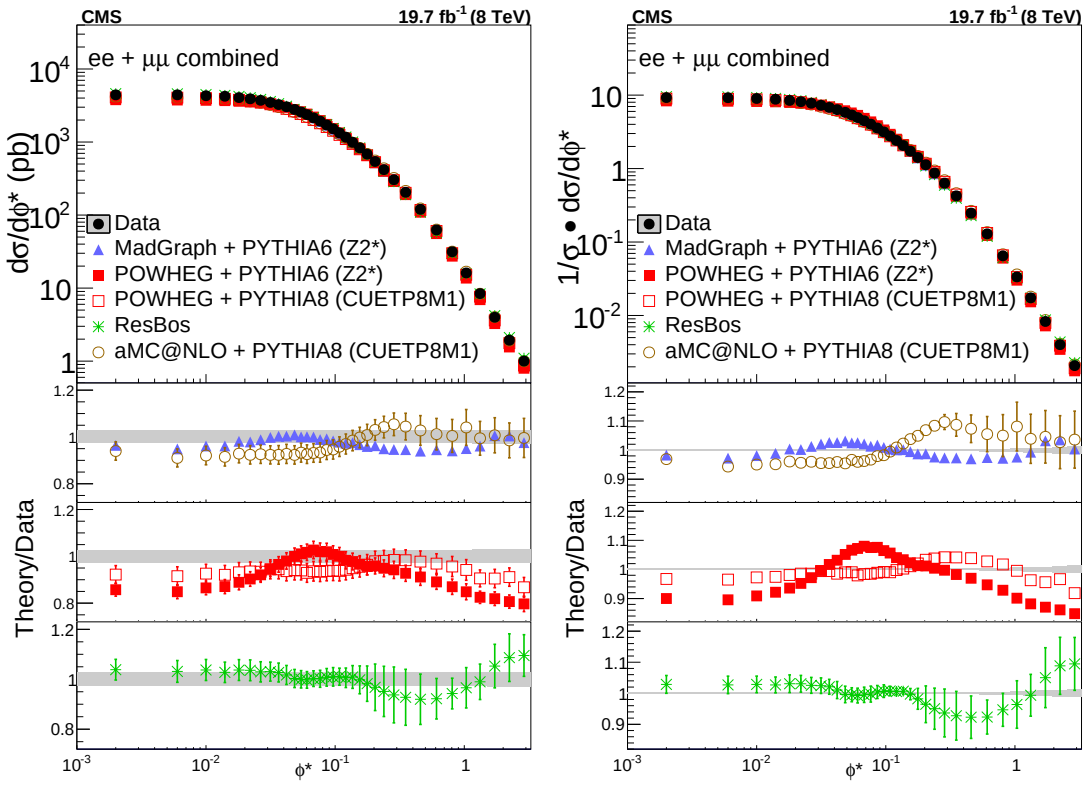

Figure 9.7: The left figure shows the absolute ϕ^* distribution compared to five separate simulation samples while the right compares the same distributions after they have been normalized.

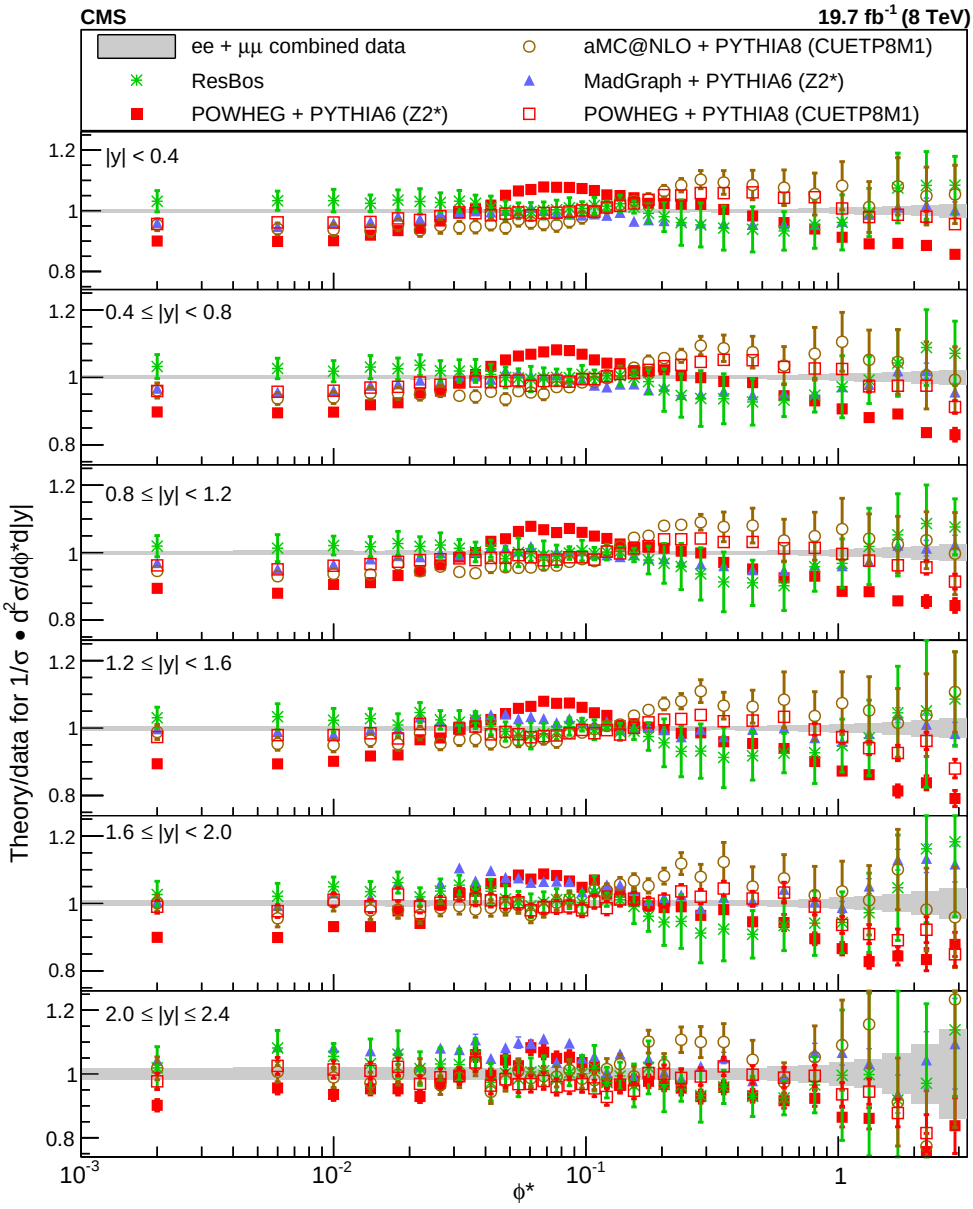

Figure 9.8: Normalized 2D results. As was seen in the 1D study none of the simulations fit the data. However, unlike the 1D results the MadGraph changes the most when comparing y bins.

10

Analysis

"I hate when the real world ignores a perfectly logical rational assumption."
– — Jim Butcher, White Knight

10.1 Interpretation of Discrepancies

As was shown in the previous chapter, no simulation model matches the data for the normalized distributions within uncertainty. This disagreement implies that the simulation does not accurately simulate the Q_{T} of the Z. Due to the similarities in the production of a Z and a W, there is most likely a similar disagreement between the simulated and actual Q_{T} distribution of the W boson. As was mentioned in Chapter 2, the measurement of the W mass is calculated based on the distribution of the leptons p_{T} distribution, which would be effected by the Q_{T} of the W. As was described in the same chapter there is currently a tension between the measured and theoretical mass measurement of the W. However, with the high uncertainty of the W mass it is not possible to tell if this tension is real. For this reason it is important to attempt to lower the uncertainty of the measured W mass. By finding a method to increase the agreement between the theoretical and measured ϕ^* distribution of the Z, the uncertainty of the W mass measurement may be lowered allowing to find if the tension between the theoretical and measured W mass is real, and in turn, if there is a flaw with the standard model.

The inconsistency of the ϕ^* measurement between POWHEG +PYTHIA6 and POWHEG +PYTHIA8 implies that part of the disagreement between simulation and data may be due to the hadronizer. PYTHIA8 contains many variables that can be changed that would effect the ϕ^* distribution. If a set of these variables could be found that fixed the ϕ^* distribution and that did not reduce the accuracy of the hadronizer for other types of simulations, it would be possible to create a new W boson simulation that was more accurate. This would allow for a W mass measurement to be made more accurately.

10.2 Pythia6 to Pythia8 comparison

Due to the large difference between the results of POWHEG hadronized by PYTHIA6 compared to PYTHIA8, some of the basic changes between parameters used for each of the hadronizers were investigated. These parameters were σ_{B}, which is the width of the Gaussian used to calculate the p_{x} and p_{y} of the partons used by the hadronizer, and the PDF used by the hadronizer. The test was done by comparing a POWHEG +PYTHIA6 sample to four POWHEG +PYTHIA8 samples. These POWHEG +PYTHIA8 samples were created using different combinations of the default PYTHIA6 and PYTHIA8 values of the σ_{B} and PDF.

The variable σ_{B} is of particular interest to the ϕ^* measurement since a larger σ_{B} results in partons with a larger p_{T}, which can create a Z with a higher Q_{T}. PYTHIA8 calculates the value of σ_{B} on a particle-by-particle basis using Eq. 4.3, while PYTHIA6 keeps σ_{B} constant, with the Z2* tune having $\sigma_{\mathrm{B}} = 2\,\mathrm{GeV}$. A second change between the two was the PDF used by the hadronizers, with the PYTHIA6 sample using the PDF CTEW6L, and PYTHIA8 sample using the PDF NNPDF2.3 QCD+QED LO, along with a change in the α_{s}, with $\alpha_{\mathrm{s}}(M_{\mathrm{Z}}) = 0.1180$ and $\alpha_{\mathrm{s}}(M_{\mathrm{Z}}) = 0.130$ for PYTHIA6 and PYTHIA8 sample respectively.

The result of these simulations are shown in Fig. 10.1. For high ϕ^* (> 0.15) none of the changes had a large effect on the overall shape of the distribution. Although all of the modified POWHEG +PYTHIA8 distributions have slightly better agreement in the high ϕ^* region than the nominal distribution, the changes are of the order of the statistical uncertainty of the bins. Therefore the large difference between POWHEG +PYTHIA6 and POWHEG +PYTHIA8 at high ϕ^* must be due to a much more intrinsic difference

between the two programs, such as the conditions that result in gluon emission.

I contrast, for low and medium ϕ^* there is a noticeable change depending on the parameters used. At low ϕ^* (< 0.03) changing σ_{B} to the PYTHIA6 settings result in decreased relative differential cross-section in low ϕ^*, which is relatively intuitive, since PYTHIA6 had a larger value, which would lead to larger boost to the Z overall, which in turn would cause a deficit of low Q_{T} Z bosons, and therefore a deficit in the low ϕ^* region. These changes also lead to an excess in the mid ϕ^* region($0.03 < \phi^* < 0.15$), similar to the excess in the PYTHIA6 sample, though noticeably smaller.

There was also a small improvement in the agreement of both the mid and low ϕ^* range by changing to the PYTHIA6 PDF, though this improvement was near the statistical uncertainty. This improvement, though intriguing, is complicated to explore due to the inherent coupling between the PDF used by the generator and the hadronizer. For this reason, it would be useful to create a dedicated study to the effect of the PDF that is used. However, because of the small effect of the PDF on the ϕ^* distribution, it was chosen to use the default PYTHIA8 PDF for the rest of the study.

These results are intuitive, since the variables that were changed would only affect the Q_{T} of the Z by a few GeV at most. High ϕ^* is correlated with Z bosons with a Q_{T} on the order of 100 GeV and would therefore have a very small fractional change due to changes in either the hadronizer's PDF or σ_{B}, but is of the order for Z bosons with a ϕ^* measurement of $\phi^* < 0.15$. Therefore, although some of the intrinsic differences between PYTHIA6 and PYTHIA8 are the cause of disagreement between the ϕ^* distribution of POWHEG +PYTHIA6 and POWHEG +PYTHIA8, some of it can be explained by changes to the default variables used, with this thesis focusing on σ_{B}.

10.3 Tuning Results

In order to test the effectiveness of changing σ_{B} to correct the differences between the theory and the data, multiple tunes were tested by changing σ_{hard} and σ_{soft} independently. As was mentioned last section, lowering σ_{B}, in this case by lowering either σ_{soft} or σ_{hard}, lowered the disagreement in the low ϕ^* region by increasing the number of events with low Q_{T}, with four examples shown in Fig. 10.2.It is worth noting that changes to σ_{hard} and σ_{soft} have nearly the exact same effect on the overall shape of the ϕ^*

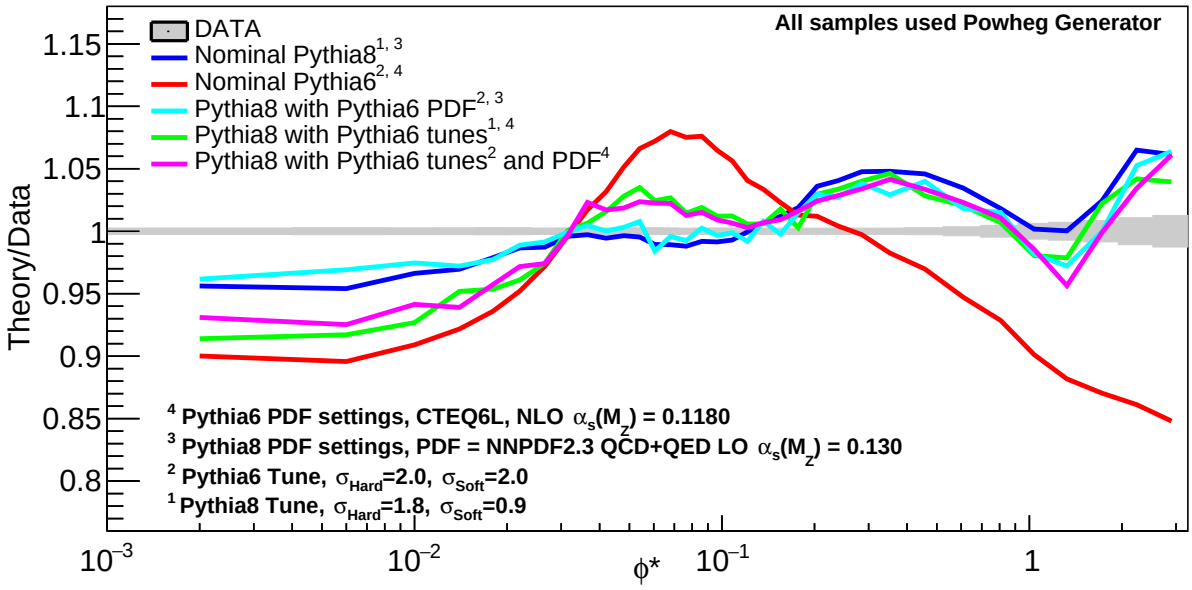

Figure 10.1: When PYTHIA8 settings were changed to settings used to create the PYTHIA6 sample, PYTHIA8 gained some characteristics of the PYTHIA6 generated sample. These include a very noticeable deficit of events in low ϕ^*, as well as an excess of events at medium ϕ^*. However, neither changes to the tune, nor changes to the PDF had much effect at high ϕ^*

distribution since lowering either lowers the σ_{B} of partons produced in the simulation, though by different amounts depending on the energy of the particular gluon involved.

Although the changes to σ_{hard} and σ_{soft} can improve the agreement between simulation and data for low ϕ^*, the same changes lead to increased disagreement in the mid ϕ^* and have no noticeable effect on the high ϕ^* region. The disagreement in very high ϕ^* (< 1) is considered acceptable in this study due to the method of which POWHEG produces events, since it inherently will limit the number of high energy jets produced which can affect the high Q_{T} distribution. However this explanation does not explain the disagreement of the simulation in the rest of ϕ^*, which contains the majority of events and is therefore vital to improving the W mass measurement uncertainty.

10.3.1 The reweighting of inherent p_{T}

In order to compare the effect of different values of σ_{hard} and σ_{soft} on the ϕ^* distribution usually multiple simulations would need to be created. The issue with this is it is very

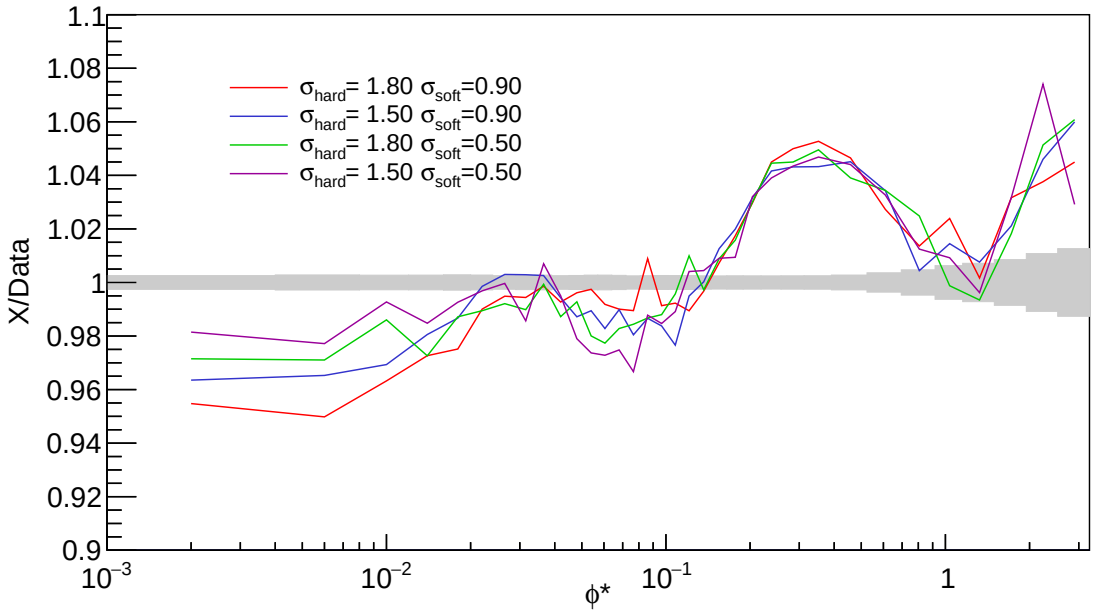

Figure 10.2: A plot comparing multiple different tunes to the data. As can be seen there is no tune that provides an improvement in all bins, nor any tune that affects the high ϕ^* region

resource intensive, both in terms of the scale of computer time to create them as well as having hard drive space to store them. This study would normally require a simulation sample for each combination of σ_{hard} and σ_{soft} that was compared. Instead only a couple simulated samples were produced and new ϕ^* distributions were created based on other σ_{hard} and using a central distribution.

In simulation, Q_{T} is affected by both the generator and the hadronizer used to produce the samples. As was mentioned in Section 4.2.2, the p_{x} and p_{y} of each parton of the initial state, as well as the particles that were created in their evolution, such as radiated gluons, are chosen using a Gaussian distribution whose width is determined using Eq. 4.3, leading to a probability density function of the form:

$$G(p_{\text{x}}, p_{\text{y}}, \sigma_{\text{B}}) = P(p_{\text{x}}, \sigma_{\text{B}}) * P(p_{\text{y}}, \sigma_{\text{B}}) \tag{10.1}$$

$$= \frac{1}{\sqrt{2\pi}\sigma_{\text{B}}} e^{\frac{-p_{\text{x}}^2}{2\sigma_{\text{B}}}} * \frac{1}{\sqrt{2\pi}\sigma_{\text{B}}} e^{\frac{-p_{\text{y}}^2}{2\sigma_{\text{B}}^2}} \tag{10.2}$$

$$= \frac{1}{2\pi\sigma_{\mathrm{B}}^2} e^{\frac{-p_t^2}{2\sigma_{\mathrm{B}}^2}}. \tag{10.3}$$

Because changes to σ_{soft} and σ_{hard} do not change any inherent function of the hadronizers, but rather the probability distribution of p_{x} and p_{y}, any interaction that happens with one set of values has an easily calculated probability to have happened with a different value of σ_{B}. This allows for the sample to be weighted on an event by event basis to simulate a sample created using different set of tuning parameters. This new event weight is calculated by multiplying the weight due to each separate parton together, i, as shown in:

$$W_{event} = \prod_i \frac{Prob(p_{\mathrm{x}i}, p_{\mathrm{y}i}, \sigma_{i,new})}{Prob(p_{\mathrm{x}i}, p_{\mathrm{y}i}, \sigma_{i,old})} = \prod_i \frac{\sigma_{old}^2}{\sigma_{new}^2} e^{\frac{-p_t^2}{2} * (\frac{1}{\sigma_{i,new}^2} - \frac{1}{\sigma_{i,old}^2})}. \tag{10.4}$$

This saves a large amount of time and space by not requiring each tune to be created individually. An example demonstrating this reweighting is shown in Fig 10.3, which compares a generated sample using $\sigma_{\mathrm{hard}} = 1.5$ to a sample generated using $\sigma_{\mathrm{hard}} = 1.8$ that had been reweighted to $\sigma_{\mathrm{hard}} = 1.5$. The reweighted $\sigma_{\mathrm{hard}} = 1.8$ matches well to $\sigma_{\mathrm{hard}} = 1.5$, with the majority of bin disagreements being near the size of the uncertainty.

However, as the tunes get farther from the central tune that was produced, some weights become extremely large, leading to a larger statistical error. This limits how far from the central value this method can function effectively. This can be seen in Fig 10.4, where the events that are far from the central tune ($\sigma_{\mathrm{hard}} = 1.8$, $\sigma_{\mathrm{soft}} = 0.9$), the uncertainty increases greatly. Events with similar weights to the central weight have very similar uncertainties. However, due to events with very high weights($> 1,000$), the uncertainties grow quickly, increasing by over a factor 10 for most bins of the sample farthest from the central tune.

Figure 10.5 shows the parton weights used when converting from a central tune($\sigma_{\mathrm{hard}} = 1.8$ and $\sigma_{\mathrm{soft}} = 0.9$), to others. As the tunes get further from the central tune, the peak widens and moves to a larger value, though all distributions drop quickly after the peak. These weights are relatively small, with no events with weights larger than 3.

Despite these small weights, due to the multiplicative nature of the weights of each parton, the total weight covers a wide range of possible values, as shown in Fig. 10.6. As

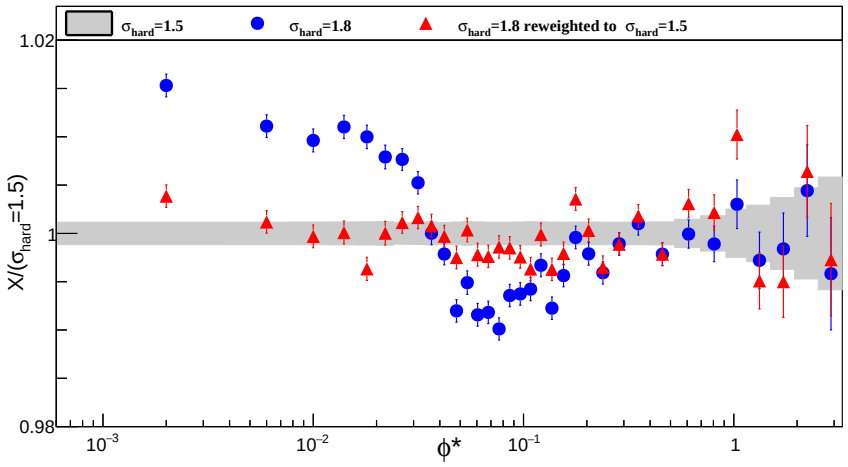

Figure 10.3: The ratio of a generated ϕ^* distribution using $\sigma_{\text{hard}} = 1.5$, $\sigma_{\text{hard}} = 1.8$, as well at $\sigma_{\text{hard}} = 1.8$ that has been reweighted to create a $\sigma_{\text{hard}} = 1.5$ distribution. As can be seen, after reweighting $\sigma_{\text{hard}} = 1.8$ the distribution fits within 0.5% of the $\sigma_{\text{hard}} = 1.5$ distribution for low ϕ^*

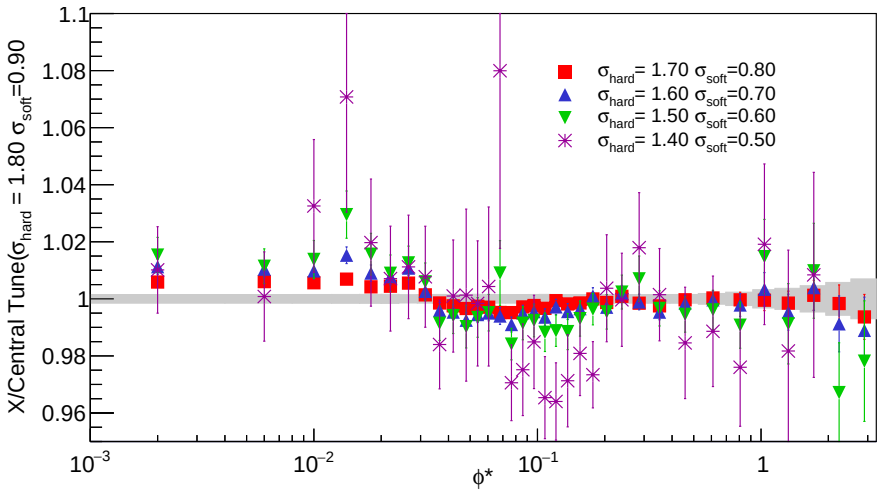

Figure 10.4: A plot showing different ϕ^* distributions over the a central tune. All these distributions are retunes of a single data set with $\sigma_{\text{hard}} = 1.8$ and $\sigma_{\text{soft}} = 0.9$. As can be seen for the tunes closest to the central tune have very small statistical fluctuations, but the tunes farthest from the central tune have large fluctuations from bin to bin.

is demonstrated by $\sigma_{\text{hard}} = 1.4$ and $\sigma_{\text{soft}} = 0.5$, when a sample is changed to a drastically different tune weights can become extremely large, with some events of having weights

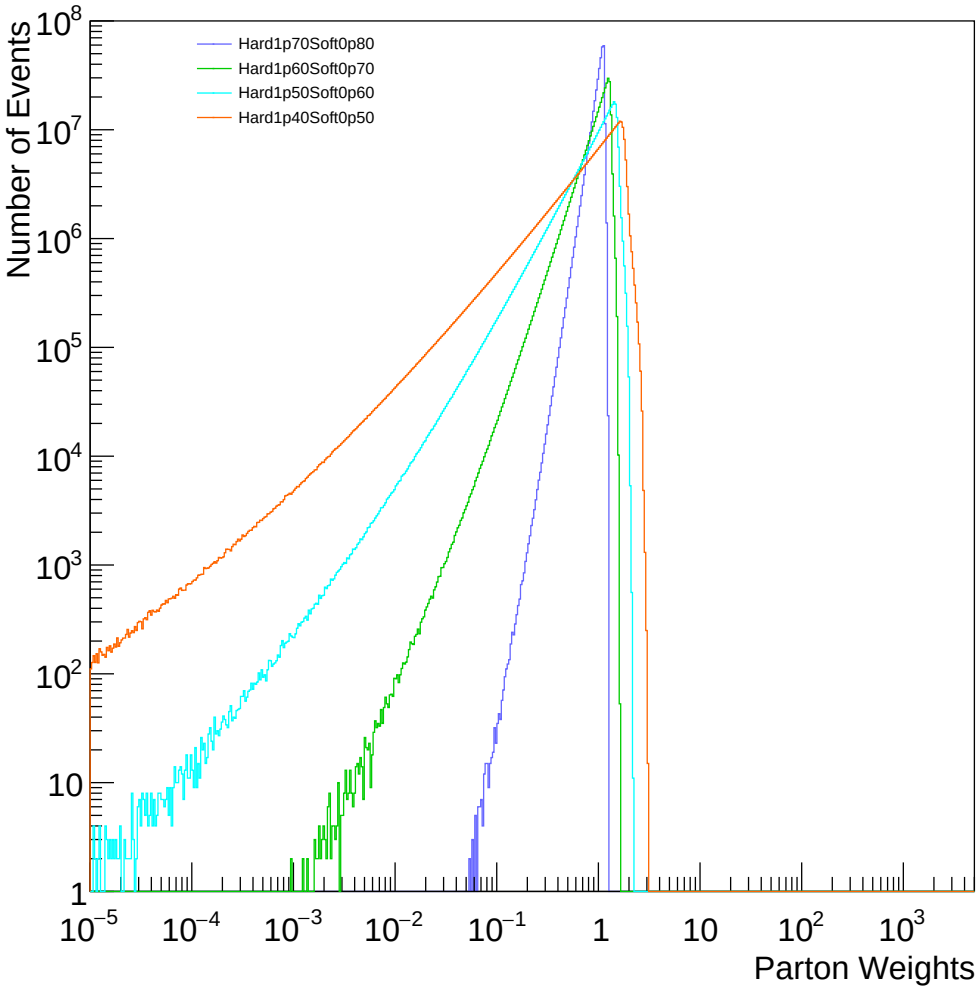

Figure 10.5: Although many of the partons weights are < 1, there are almost no partons with weights more than a factor of 3.

of the order of ten thousand. Because all bins, excluding the high ϕ^* tail, contain $\approx$ four hundred thousand events, each of these high weighted events can change the binned value by a couple of percentage points, leading to an unacceptably high fluctuation of the bin value. To remove this issue, this reweighting method is limited to changing the

tune by requiring that:

$$0.25 > \sqrt{\left(\frac{\sigma^*_{\text{hard}} - \sigma_{\text{hard}}}{\sigma_{\text{hard}}}\right)^2 + \left(\frac{\sigma^*_{\text{soft}} - \sigma_{\text{soft}}}{\sigma_{\text{soft}}}\right)^2}. \tag{10.5}$$

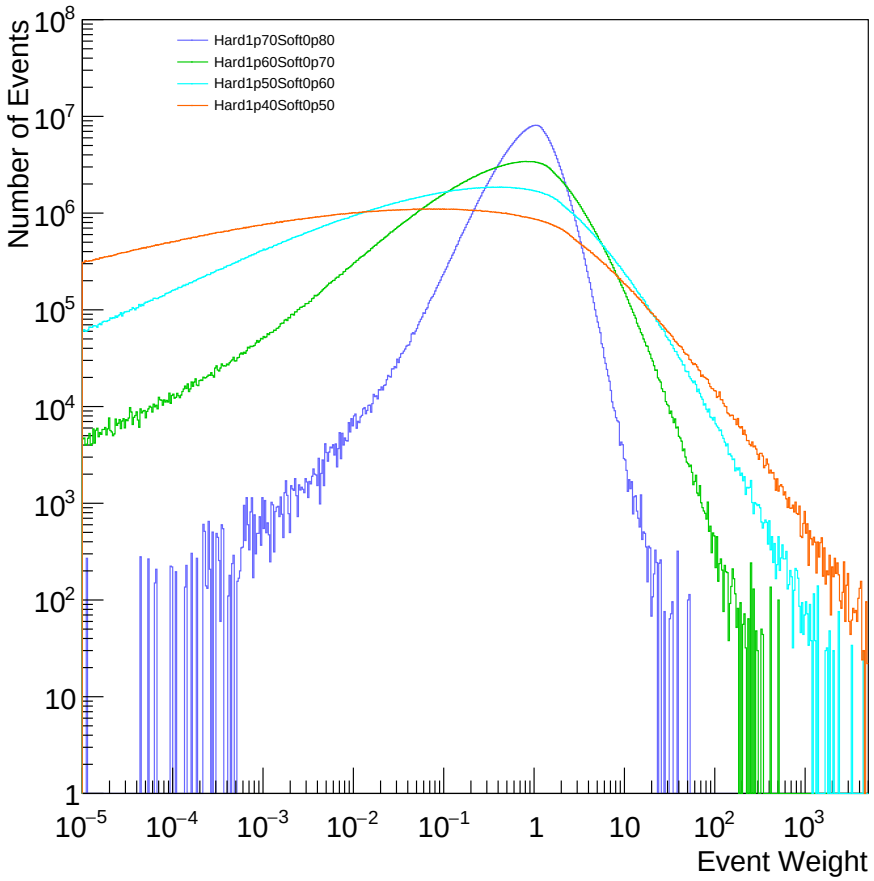

Figure 10.6: Event weights for changing the tunes. As can be seen as the tune gets further from the central tune of $\sigma_{\text{hard}} = 1.8$ and $\sigma_{\text{soft}} = 0.9$, the distributions get wider, with the $\sigma_{\text{hard}} = 1.4$ and $\sigma_{\text{soft}} = 0.5$ having multiple events of the order of 10,000.

Despite limitations of this reweighting, being unable to drastically change σ_{hard} and σ_{soft}, this reweighting method allows for distributions to be created fast and efficiently

using a central distribution.

11

Conclusion and Discussion

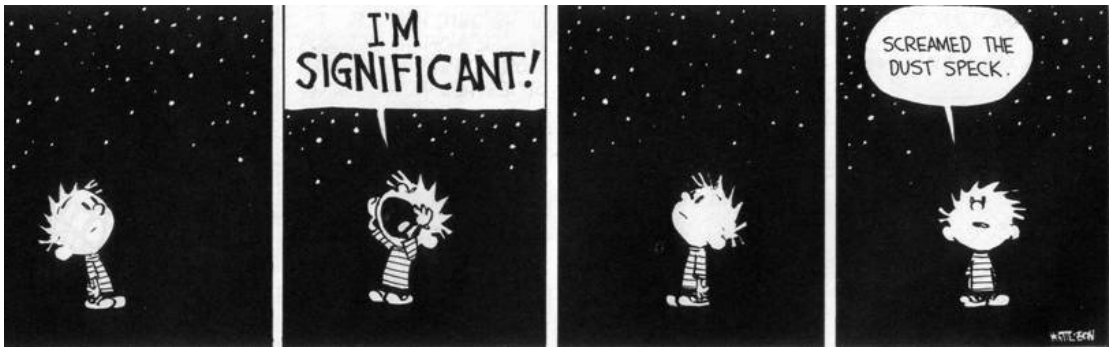

Figure 11.1: Calvin from Calvin and Hobbes tries to deal with his feeling of self worth compared with the scale of the universe[66]

The cross-section of the variable ϕ^* of the Z boson decay to lepton pairs was measured using 19.7 fb^{-1} of $\sqrt{s} = 8$ TeV data collected with the CMS detector. This data was then unfolded using a MadGraph sample and compared to powheg + Pythia8 samples, using different "tunes".

All powheg + Pythia8 tunes match unfolded data within 5% for $\phi^* < 0.2$ and are practically identical for higher ϕ^*. For $\phi^* < 0.03$, smaller values of either σ_{hard} or σ_{soft} decreased the disagreement between data and theory. This was expected since lowering either variable results in a smaller Q_{T} of the Z and reduces the deficit of low Q_{T} Z bosons. However, major changes of the tune, e.g. decreasing both σ_{hard} and σ_{soft} by a factor of two, were unable to completely remove the disagreement. It therefore does

not appear to be possible to remove the disagreement between theory and data at low ϕ^* by making a reasonable change in either σ_{hard} or σ_{soft}. It also appeared that the for medium ϕ^* region($0.03 < \phi^* < 0.15$) lowering σ_{hard} or σ_{soft} increased the disagreement. For high ϕ^* the tune has a trivial effect with all tunes overestimating the cross-section by the same amount within uncertainty. Therefore it does not appear that the variables σ_{hard} or σ_{soft} are responsible for the disagreement between data and theory. There are however many other free parameters used by PYTHIA8 that could possibly be partially responsible for the disagreements between data and theory, such as the PDF used which could be studied by another analysis in the future. Attempting to find settings in the hadronizer that remove the disagreement between data and theory of ϕ^* are important in lowering the uncertainty of the W mass measurement. Overall it is important to study this disagreement since if the hadronizer is not at fault it could imply a problem with the Standard Model. Therefore, in the future it is important that studies attempt to find the reason for the difference between theory and data, and if possible if it.

References

[1] Serguei Chatrchyan et al. Measurement of pseudorapidity distributions of charged particles in proton-proton collisions at $\sqrt{s} = 8$ TeV by the CMS and TOTEM experiments. *Eur. Phys. J.*, C74(10):3053, 2014, 1405.0722.

[2] Serguei Chatrchyan et al. Measurement of the Underlying Event Activity at the LHC with $\sqrt{s} = 7$ TeV and Comparison with $\sqrt{s} = 0.9$ TeV. *JHEP*, 09:109, 2011, 1107.0330.

[3] A. Banfi, S. Redford, M. Vesterinen, P. Waller, and T. R. Wyatt. Optimisation of variables for studying dilepton transverse momentum distributions at hadron colliders. *Eur. Phys. J.*, C71:1600, 2011, 1009.1580.

[4] Randall Munroe. Fundamental forces.

[5] Sheldon L. Glashow. Partial-symmetries of weak interactions. *Nuclear Physics*, 22(4):579 – 588, 1961, http://dx.doi.org/10.1016/0029-5582(61)90469-2.

[6] Steven Weinberg. A model of leptons. *Phys. Rev. Lett.*, 19:1264–1266, November 1967, http://dx.doi.org/10.1103/PhysRevLett.19.1264.

[7] A Salam. Elementary particle physics: Relativistic groups and analyticity. In *Proceedings to the Eighth Nobel Symposium, Almquvist and Wiksell*, page 367, May 1968, http://dx.doi.org/10.1126/science.168.3936.1196-a.

[8] Peter W. Higgs. Broken symmetries and the masses of gauge bosons. *Phys. Rev. Lett.*, 13:508–509, October 1964, http://dx.doi.org/10.1103/PhysRevLett.13.508.

[9] E. Rutherford. LXXIX. The scattering of α and β particles by matter and the structure of the atom. *Philosophical Magazine Series 6*, 21(125):669–688, May 1911, http://dx.doi.org/10.1080/14786440508637080.

[10]

[11] Max Planck. Ueber das gesetz der energieverteilung im normalspectrum. *Annalen der Physik*, 309(3):553–563, 1901.

[12] Martin L. Perl. The Discovery of the tau lepton. In *The Rise of the standard model: Particle physics in the 1960s and 1970s. Proceedings, Conference, Stanford, USA, June 24-27, 1992*, pages 79–100, 1992.

[13] John Ellis. The Discovery of the Gluon. *Int. J. Mod. Phys.*, A29(31):1430072, 2014, 1409.4232. [,189(2015)].

[14] K. Kodama et al. Observation of tau neutrino interactions. *Phys. Lett.*, B504:218–224, 2001, hep-ex/0012035.

[15] P. Bagnaia et al. Evidence for Z0 —¿ e+ e- at the CERN anti-p p Collider. *Phys. Lett.*, B129:130–140, 1983. [,7.69(1983)].

[16] M. Banner et al. Observation of Single Isolated Electrons of High Transverse Momentum in Events with Missing Transverse Energy at the CERN anti-p p Collider. *Phys. Lett.*, B122:476–485, 1983. [,7.45(1983)].

[17] G. Arnison et al. Experimental Observation of Isolated Large Transverse Energy Electrons with Associated Missing Energy at s**(1/2) = 540-GeV. *Phys. Lett.*, B122:103–116, 1983. [,611(1983)].

[18] Claudio Campagnari and Melissa Franklin. The Discovery of the top quark. *Rev. Mod. Phys.*, 69:137–212, 1997, hep-ex/9608003.

[19] Serguei Chatrchyan et al. Observation of a new boson at a mass of 125 GeV with the CMS experiment at the LHC. *Phys. Lett.*, B716:30–61, 2012, 1207.7235.

[20] V. N. Gribov and L. N. Lipatov. Deep inelastic e p scattering in perturbation theory. *Sov. J. Nucl. Phys.*, 15:438–450, 1972. [Yad. Fiz.15,781(1972)].

[21] L. N. Lipatov. The parton model and perturbation theory. *Sov. J. Nucl. Phys.*, 20:94–102, 1975. [Yad. Fiz.20,181(1974)].

[22] Guido Altarelli and G. Parisi. Asymptotic Freedom in Parton Language. *Nucl. Phys.*, B126:298–318, 1977.

[23] Yuri L. Dokshitzer. Calculation of the Structure Functions for Deep Inelastic Scattering and e+ e- Annihilation by Perturbation Theory in Quantum Chromodynamics. *Sov. Phys. JETP*, 46:641–653, 1977. [Zh. Eksp. Teor. Fiz.73,1216(1977)].

[24] A. D. Martin, W. J. Stirling, R. S. Thorne, and G. Watt. Parton distributions for the LHC. *Eur. Phys. J.*, C63:189–285, 2009, 0901.0002.

[25] Albert M Sirunyan et al. Measurement of differential cross sections in the kinematic angular variable ϕ^* for inclusive Z boson production in pp collisions at $\sqrt{s} = 8$ TeV. *JHEP*, 03:172, 2018, 1710.07955.

[26] Georges Aad et al. Measurement of angular correlations in Drell-Yan lepton pairs to probe Z/gamma* boson transverse momentum at sqrt(s)=7 TeV with the ATLAS detector. *Phys. Lett.*, B720:32–51, 2013, 1211.6899.

[27] Victor Mukhamedovich Abazov et al. Precise study of the Z/γ^* boson transverse momentum distribution in $p\bar{p}$ collisions using a novel technique. *Phys. Rev. Lett.*, 106:122001, 2011, 1010.0262.

[28] Victor Mukhamedovich Abazov et al. Measurement of the ϕ^*_η distribution of muon pairs with masses between 30 and 500 GeV in 10.4 fb^{-1} of $p\bar{p}$ collisions. *Phys. Rev.*, D91(7):072002, 2015, 1410.8052.

[29] Adam Lee. Cathedrals, february 2010.

[30] Oliver Sim Brning, Paul Collier, P Lebrun, Stephen Myers, Ranko Ostojic, John Poole, and Paul Proudlock. *LHC Design Report*. CERN Yellow Reports: Monographs. CERN, Geneva, 2004.

[31] Vardan Khachatryan et al. Transverse-momentum and pseudorapidity distributions of charged hadrons in pp collisions at $\sqrt{s} = 7$ TeV. *Phys. Rev. Lett.*, 105:022002, 2010, 1005.3299.

[32] Serguei Chatrchyan et al. Measurement of the Rapidity and Transverse Momentum Distributions of Z Bosons in pp Collisions at $\sqrt{s} = 7$ TeV. *Phys. Rev.*, D85:032002, 2012, 1110.4973.

[33] V Karimki, M Mannelli, P Siegrist, H Breuker, A Caner, R Castaldi, K Freudenreich, G Hall, R Horisberger, M Huhtinen, and A Cattai. *The CMS tracker system project: Technical Design Report*. Technical Design Report CMS. CERN, Geneva, 1997.

[34] *The CMS tracker: addendum to the Technical Design Report*. Technical Design Report CMS. CERN, Geneva, 2000.

[35] W Adam, R Frühwirth, A Strandlie, and T Todorov. Reconstruction of electrons with the gaussian-sum filter in the CMS tracker at the LHC. *Journal of Physics G: Nuclear and Particle Physics*, 31(9):N9, 2005, http://stacks.iop.org/0954-3899/31/i=9/a=N01.

[36] Kalman.R.E. A new approach to linear filtering and prediction problems. *Journal of Basic Engineering*, pages 35–45, 1960.

[37] Y. Chen, E. DiMarco, M. Spiropulu, S. Xie, B. Mangano, G. Petrucciani, V. Sharma, and A. Vartak. Electron energy reconstruction using a multivariate regression. CMS Note 2012/327, CERN, 2012.

[38] CMS Collaboration. Measurements of the new Higgs-like boson at 125 GeV in the two photon decay channel. CMS Note 2013/253, CERN, 2013.

[39] M. Oreglia. *A Study of the Reactions* $\psi' \to \gamma\gamma\psi$. PhD thesis, Stanford University, December 1980, http://www.slac.stanford.edu/cgi-wrap/getdoc/slac-r-236.pdf.

[40] M. Tanabashi, K. Hagiwara, K. Hikasa, K. Nakamura, Y. Sumino, F. Takahashi, J. Tanaka, K. Agashe, G. Aielli, C. Amsler, M. Antonelli, D. M. Asner, H. Baer, Sw. Banerjee, R. M. Barnett, T. Basaglia, C. W. Bauer, J. J. Beatty, V. I. Belousov, J. Beringer, S. Bethke, A. Bettini, H. Bichsel, O. Biebel, K. M. Black, E. Blucher, O. Buchmuller, V. Burkert, M. A. Bychkov, R. N. Cahn, M. Carena, A. Ceccucci, A. Cerri, D. Chakraborty, M.-C. Chen, R. S. Chivukula, G. Cowan, O. Dahl,

G. D'Ambrosio, T. Damour, D. de Florian, A. de Gouvêa, T. DeGrand, P. de Jong, G. Dissertori, B. A. Dobrescu, M. D'Onofrio, M. Doser, M. Drees, H. K. Dreiner, D. A. Dwyer, P. Eerola, S. Eidelman, J. Ellis, J. Erler, V. V. Ezhela, W. Fetscher, B. D. Fields, R. Firestone, B. Foster, A. Freitas, H. Gallagher, L. Garren, H.-J. Gerber, G. Gerbier, T. Gershon, Y. Gershtein, T. Gherghetta, A. A. Godizov, M. Goodman, C. Grab, A. V. Gritsan, C. Grojean, D. E. Groom, M. Grünewald, A. Gurtu, T. Gutsche, H. E. Haber, C. Hanhart, S. Hashimoto, Y. Hayato, K. G. Hayes, A. Hebecker, S. Heinemeyer, B. Heltsley, J. J. Hernández-Rey, J. Hisano, A. Höcker, J. Holder, A. Holtkamp, T. Hyodo, K. D. Irwin, K. F. Johnson, M. Kado, M. Karliner, U. F. Katz, S. R. Klein, E. Klempt, R. V. Kowalewski, F. Krauss, M. Kreps, B. Krusche, Yu. V. Kuyanov, Y. Kwon, O. Lahav, J. Laiho, J. Lesgourgues, A. Liddle, Z. Ligeti, C.-J. Lin, C. Lippmann, T. M. Liss, L. Littenberg, K. S. Lugovsky, S. B. Lugovsky, A. Lusiani, Y. Makida, F. Maltoni, T. Mannel, A. V. Manohar, W. J. Marciano, A. D. Martin, A. Masoni, J. Matthews, U.-G. Meißner, D. Milstead, R. E. Mitchell, K. Mönig, P. Molaro, F. Moortgat, M. Moskovic, H. Murayama, M. Narain, P. Nason, S. Navas, M. Neubert, P. Nevski, Y. Nir, K. A. Olive, S. Pagan Griso, J. Parsons, C. Patrignani, J. A. Peacock, M. Pennington, S. T. Petcov, V. A. Petrov, E. Pianori, A. Piepke, A. Pomarol, A. Quadt, J. Rademacker, G. Raffelt, B. N. Ratcliff, P. Richardson, A. Ringwald, S. Roesler, S. Rolli, A. Romaniouk, L. J. Rosenberg, J. L. Rosner, G. Rybka, R. A. Ryutin, C. T. Sachrajda, Y. Sakai, G. P. Salam, S. Sarkar, F. Sauli, O. Schneider, K. Scholberg, A. J. Schwartz, D. Scott, V. Sharma, S. R. Sharpe, T. Shutt, M. Silari, T. Sjöstrand, P. Skands, T. Skwarnicki, J. G. Smith, G. F. Smoot, S. Spanier, H. Spieler, C. Spiering, A. Stahl, S. L. Stone, T. Sumiyoshi, M. J. Syphers, K. Terashi, J. Terning, U. Thoma, R. S. Thorne, L. Tiator, M. Titov, N. P. Tkachenko, N. A. Törnqvist, D. R. Tovey, G. Valencia, R. Van de Water, N. Varelas, G. Venanzoni, L. Verde, M. G. Vincter, P. Vogel, A. Vogt, S. P. Wakely, W. Walkowiak, C. W. Walter, D. Wands, D. R. Ward, M. O. Wascko, G. Weiglein, D. H. Weinberg, E. J. Weinberg, M. White, L. R. Wiencke, S. Willocq, C. G. Wohl, J. Womersley, C. L. Woody, R. L. Workman, W.-M. Yao, G. P. Zeller, O. V. Zenin, R.-Y. Zhu, S.-L. Zhu, F. Zimmermann, P. A. Zyla, J. Anderson, L. Fuller, V. S. Lugovsky, and P. Schaffner. Review of particle physics. *Phys. Rev. D*, 98:030001,

Aug 2018.

[41] G. Bonneau and F. Martin. Hard-photon emission in e $^{+}$e $^{-}$ reactions. *Nuclear Physics B*, 27:381–397, 1971.

[42] Johan Alwall, Michel Herquet, Fabio Maltoni, Olivier Mattelaer, and Tim Stelzer. MadGraph 5: going beyond. *JHEP*, 06:128, 2011, 1106.0522.

[43] Torbjörn Sjöstrand, Stephen Mrenna, and Peter Z. Skands. PYTHIA 6.4 physics and manual. *JHEP*, 05:026, 2006, hep-ph/0603175.

[44] J. Pumplin, D. R. Stump, J. Huston, H. L. Lai, Pavel M. Nadolsky, and W. K. Tung. New generation of parton distributions with uncertainties from global QCD analysis. *JHEP*, 07:012, 2002, hep-ph/0201195.

[45] Johan Alwall et al. Comparative study of various algorithms for the merging of parton showers and matrix elements in hadronic collisions. *Eur. Phys. J. C*, 53:473, 2008, 0706.2569.

[46] Serguei Chatrchyan et al. Study of the underlying event at forward rapidity in pp collisions at $\sqrt{s} = 0.9$, 2.76, and 7 TeV. *JHEP*, 04:072, 2013, 1302.2394.

[47] Vardan Khachatryan et al. Event generator tunes obtained from underlying event and multiparton scattering measurements. *Eur. Phys. J. C*, 76:155, 2016, 1512.00815.

[48] J. Alwall, R. Frederix, S. Frixione, V. Hirschi, F. Maltoni, O. Mattelaer, H. S. Shao, T. Stelzer, P. Torrielli, and M. Zaro. The automated computation of tree-level and next-to-leading order differential cross sections, and their matching to parton shower simulations. *JHEP*, 07:079, 2014, 1405.0301.

[49] Richard D. Ball, Luigi Del Debbio, Stefano Forte, Alberto Guffanti, Jose I. Latorre, Juan Rojo, and Maria Ubiali. A first unbiased global NLO determination of parton distributions and their uncertainties. *Nucl. Phys. B*, 838:136, 2010, 1002.4407.

[50] Richard D. Ball, Valerio Bertone, Francesco Cerutti, Luigi Del Debbio, Stefano Forte, Alberto Guffanti, Jose I. Latorre, Juan Rojo, and Maria Ubiali. Impact of

heavy quark masses on parton distributions and LHC phenomenology. *Nucl. Phys. B*, 849:296, 2011, 1101.1300.

[51] Paolo Nason. A new method for combining NLO QCD with shower Monte Carlo algorithms. *JHEP*, 11:040, 2004, hep-ph/0409146.

[52] Simone Alioli, Paolo Nason, Carlo Oleari, and Emanuele Re. A general framework for implementing NLO calculations in shower Monte Carlo programs: the POWHEG BOX. *JHEP*, 06:043, 2010, 1002.2581.

[53] Simone Alioli, Paolo Nason, Carlo Oleari, and Emanuele Re. Vector boson plus one jet production in POWHEG. *JHEP*, 01:095, 2011, 1009.5594.

[54] Stefano Frixione, Paolo Nason, and Carlo Oleari. Matching NLO QCD computations with parton shower simulations: the POWHEG method. *JHEP*, 11:070, 2007, 0709.2092.

[55] Jun Gao, Marco Guzzi, Joey Huston, Hung-Liang Lai, Zhao Li, Pavel Nadolsky, Jon Pumplin, Daniel Stump, and C.-P. Yuan. CT10 next-to-next-to-leading order global analysis of QCD. *Phys. Rev. D*, 89:033009, 2014, 1302.6246.

[56] G. A. Ladinsky and C. P. Yuan. The nonperturbative regime in QCD resummation for gauge boson production at hadron colliders. *Phys. Rev. D*, 50:4239, 1994, hep-ph/9311341.

[57] C. Balazs and C. P. Yuan. Soft gluon effects on lepton pairs at hadron colliders. *Phys. Rev. D*, 56:5558, 1997, hep-ph/9704258.

[58] F. Landry, R. Brock, Pavel M. Nadolsky, and C. P. Yuan. Tevatron Run-1 Z boson data and Collins-Soper-Sterman resummation formalism. *Phys. Rev. D*, 67:073016, 2003, hep-ph/0212159.

[59] S. Agostinelli et al. Geant4–a simulation toolkit. *Nuclear Instruments and Methods in Physics Research Section A: Accelerators, Spectrometers, Detectors and Associated Equipment*, 506(3):250–303, 2003, http://dx.doi.org/10.1016/S0168-9002(03)01368-8.

[60] CMS Collaboration. E/gamma commissioning and physics deliverables: Electron reconstruction efficiency with 2012 data, 2013. [Online; accessed 2015-01-30].

[61] G. D'Agostini. A multidimensional unfolding method based on Bayes' theorem. *Nuclear Instruments and Methods in Physics Research Section A: Accelerators, Spectrometers, Detectors and Associated Equipment*, 362(23):487 – 498, 1995.

[62] CMS Collaboration. CMS Luminosity Based on Pixel Cluster Counting - Summer 2013 Update. *CERN*, 2013, https://cds.cern.ch/record/1598864.

[63] S. van der Meer. Calibration of the effective beam height in the ISR. Technical Report CERN-ISR-PO-68-31. ISR-PO-68-31, CERN, Geneva, June 1968, https://cds.cern.ch/record/296752.

[64] R. Nisius. Blue: a software package to combine correlated estimates of physics observables within root using the best linear unbiased estimate method - program manual, version 2.1.0. http://blue.hepforge.org.

[65] Richard Nisius. On the combination of correlated estimates of a physics observable. *Eur. Phys. J.*, C74(8):3004, 2014, 1402.4016.

[66] Bill Watterson. Calvin and hobs.

Appendix A

Electron Results

The results of the ϕ^* measurement using only $e\overline{e}$ data are shown in the following plots. The $e\overline{e}$ is the sample that was combined with the $\mu\overline{\mu}$ for the results shown in Sec. 9.1. Both the normalized and absolute 1D results are shown in Fig. A.1, while the 2D results are all normalized.

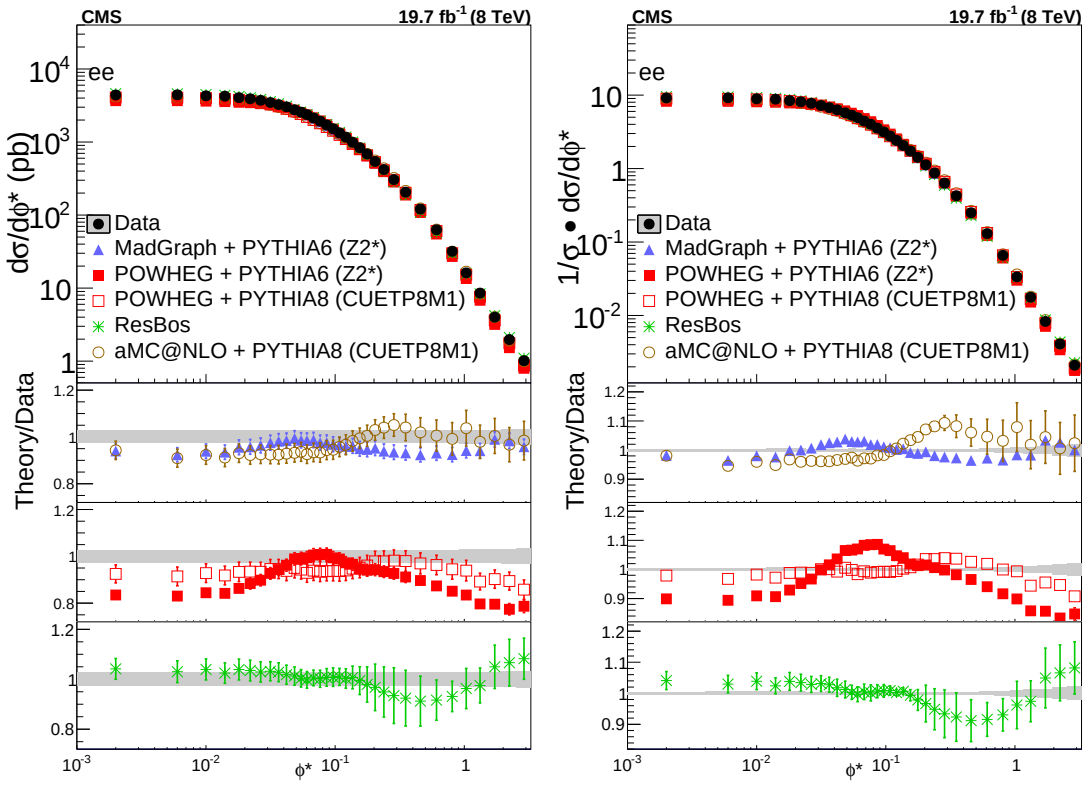

Figure A.1: $e\bar{e}$ 1D results. The left figure shows the absolute ϕ^* distribution compared to five separate simulation samples while the right compares the same distributions after they have been normalized.

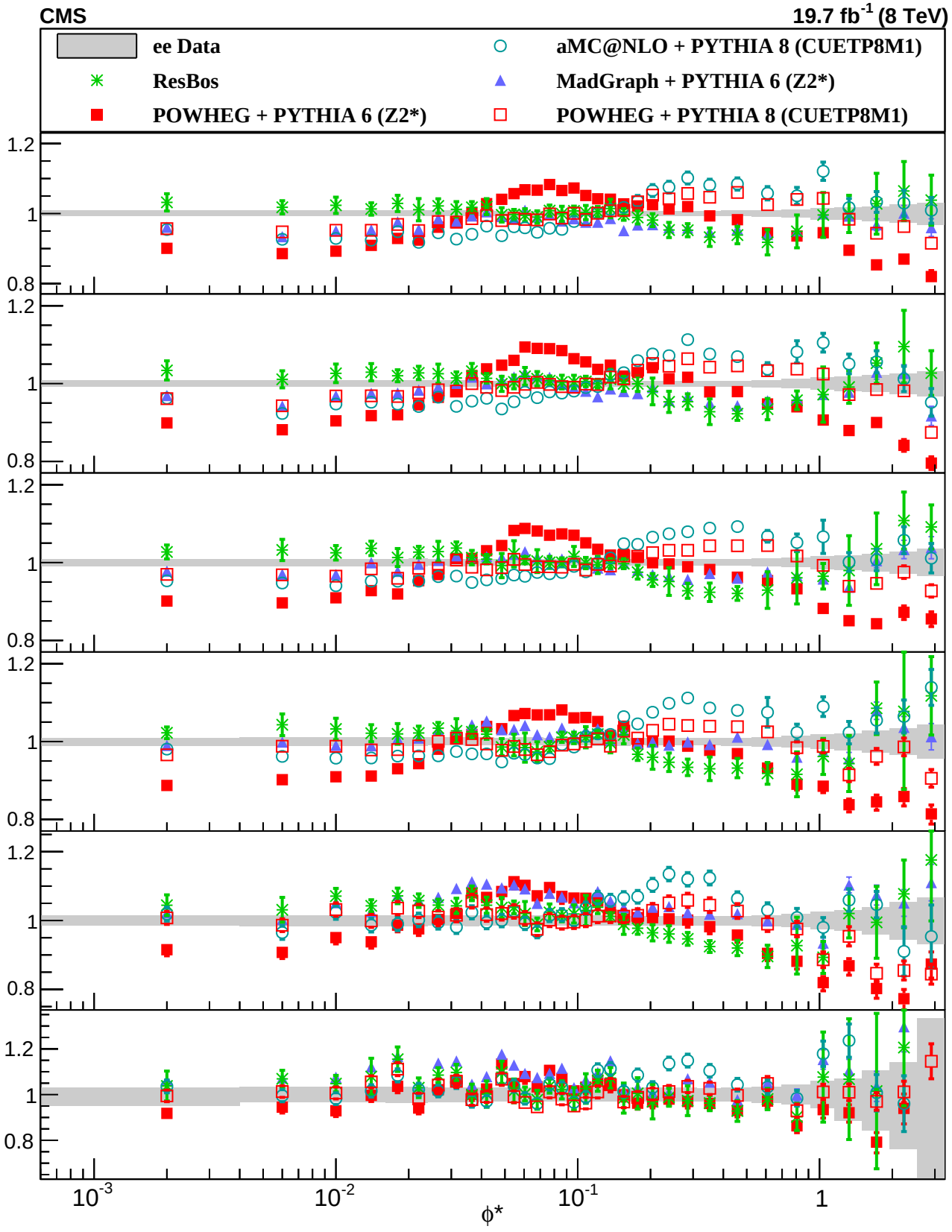

Figure A.2: Normalized $e\bar{e}$ 2D results.

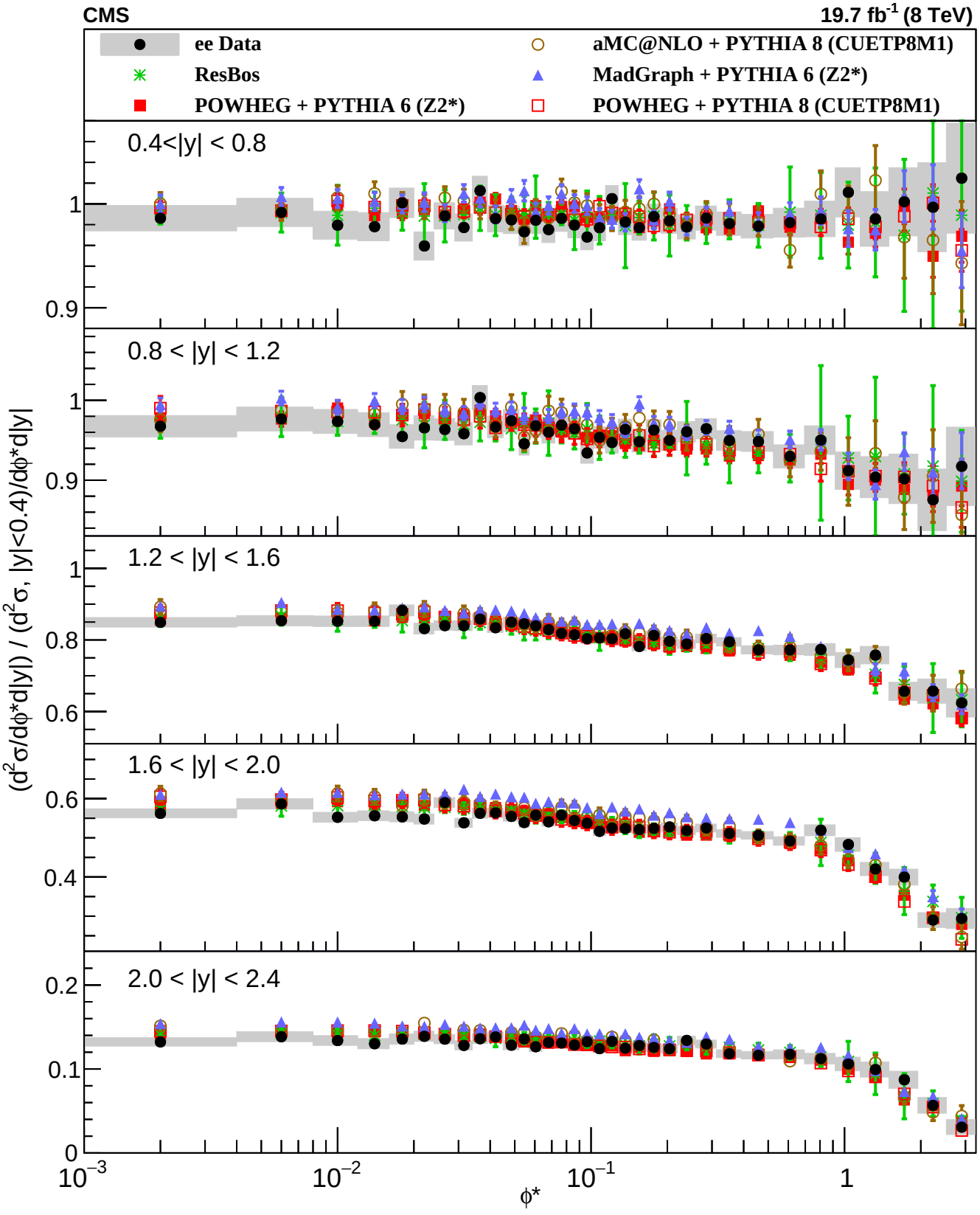

Figure A.3: This shows the ratio of all other ϕ^* distributions at all rapidity regions to the region $|y| < 0.4$

Appendix B

Tables: combination

This appendix shows the cross-sections in numrical form. The total integrated cross-section of this study is 481.2 $\pm$0.2(stat) $\pm$4.6(syst) $\pm$12.5(lumi) pb in the electron channel, 477.4 $\pm$0.2(stat) $\pm$7.1(syst) $\pm$12.4(lumi) pb in the muon channel and the cross-section is 480.7 $\pm$0.2(stat) $\pm$3.6(syst) $\pm$12.5(lumi) pb in the combined results. The 1D bin by bin results are shown in table form in Tables, with the Absolute results shown in Table B.2, while the normalized results are shown in Table B.2.

For the 2D results the integrate cross-section for each with y bin is shown table B.3, while the normalized cross-section for each bin is shown in table B.4. Table B.5 to B.16 list the double differential results. The uncertainty is given by the statistical uncertainty followed by the systematic uncertainty.

Table B.1: This table contains the normalized differential cross-sections of the measured ϕ^* variable, of both the combined result as well at the electron and muon results. The uncertainty is separated into the statistical component followed by the systematic.

ϕ^* range	Combined	Electron channel	Muon Channel
0.000-0.004	9.23±0.02 ±0.02	9.17±0.03 ±0.03	9.29±0.02 ±0.02
0.004-0.008	9.18±0.02 ±0.02	9.21±0.03 ±0.04	9.22±0.02 ±0.02
0.008-0.012	8.97±0.02 ±0.02	8.93±0.03 ±0.04	9.02±0.02 ±0.02
0.012-0.016	8.75±0.02 ±0.02	8.83±0.03 ±0.04	8.76±0.02 ±0.02
0.016-0.020	8.44±0.02 ±0.02	8.42±0.03 ±0.04	8.47±0.02 ±0.02
0.020-0.024	8.11±0.02 ±0.02	8.12±0.03 ±0.04	8.13±0.02 ±0.02
0.024-0.029	7.72±0.01 ±0.01	7.74±0.02 ±0.03	7.74±0.02 ±0.02
0.029-0.034	7.24±0.01 ±0.01	7.23±0.02 ±0.03	7.27±0.02 ±0.02
0.034-0.039	6.77±0.01 ±0.01	6.76±0.02 ±0.03	6.81±0.02 ±0.02
0.039-0.045	6.32±0.01 ±0.01	6.31±0.02 ±0.02	6.35±0.01 ±0.01
0.045-0.051	5.79±0.01 ±0.01	5.79±0.02 ±0.02	5.84±0.01 ±0.01
0.051-0.057	5.345±0.010 ±0.011	5.36±0.02 ±0.02	5.37±0.01 ±0.01
0.057-0.064	4.930±0.009 ±0.010	4.94±0.01 ±0.02	4.95±0.01 ±0.01
0.064-0.072	4.460±0.008 ±0.009	4.44±0.01 ±0.02	4.488±0.010 ±0.010
0.072-0.081	4.012±0.007 ±0.007	4.01±0.01 ±0.01	4.025±0.009 ±0.008
0.081-0.091	3.555±0.006 ±0.006	3.561±0.010 ±0.013	3.564±0.008 ±0.008
0.091-0.102	3.148±0.006 ±0.006	3.158±0.009 ±0.011	3.153±0.007 ±0.007
0.102-0.114	2.768±0.005 ±0.005	2.776±0.008 ±0.010	2.774±0.006 ±0.006
0.114-0.128	2.412±0.004 ±0.005	2.427±0.007 ±0.009	2.410±0.005 ±0.006
0.128-0.145	2.058±0.004 ±0.004	2.064±0.006 ±0.007	2.059±0.005 ±0.004
0.145-0.165	1.726±0.003 ±0.003	1.736±0.005 ±0.006	1.725±0.004 ±0.003
0.165-0.189	1.416±0.002 ±0.003	1.424±0.004 ±0.005	1.415±0.003 ±0.003
0.189-0.219	1.128±0.002 ±0.002	1.126±0.003 ±0.004	1.129±0.002 ±0.002
0.219-0.258	0.871±0.001 ±0.002	0.872±0.002 ±0.003	0.869±0.002 ±0.002
0.258-0.312	0.635±0.001 ±0.001	0.636±0.002 ±0.002	0.633±0.001 ±0.001
0.312-0.391	0.4278±0.0007±0.0007	0.428±0.001 ±0.002	0.4254±0.0009±0.0009
0.391-0.524	0.2501±0.0004±0.0005	0.2511±0.0007±0.0011	0.2470±0.0005±0.0006
0.524-0.695	0.1314±0.0003±0.0003	0.1306±0.0004±0.0007	0.1293±0.0003±0.0004
0.695-0.918	(6.64±0.02 ±0.02)$\times10^{-2}$	(6.60±0.03 ±0.05)$\times10^{-2}$	(6.46±0.02 ±0.03)$\times10^{-2}$
0.918-1.153	(3.45±0.01 ±0.01)$\times10^{-2}$	(3.36±0.02 ±0.03)$\times10^{-2}$	(3.37±0.01 ±0.02)$\times10^{-2}$
1.153-1.496	(1.792±0.007 ±0.008)$\times10^{-2}$	(1.77±0.01 ±0.02)$\times10^{-2}$	(1.730±0.009 ±0.011)$\times10^{-2}$
1.496-1.947	(8.54±0.04 ±0.04)$\times10^{-3}$	(8.29±0.06 ±0.09)$\times10^{-3}$	(8.32±0.05 ±0.06)$\times10^{-3}$
1.947-2.522	(4.13±0.03 ±0.03)$\times10^{-3}$	(4.09±0.04 ±0.06)$\times10^{-3}$	(4.00±0.03 ±0.04)$\times10^{-3}$
2.522-3.277	(2.13±0.02 ±0.02)$\times10^{-3}$	(2.10±0.03 ±0.04)$\times10^{-3}$	(2.08±0.02 ±0.02)$\times10^{-3}$

Table B.2: This table contains the absolute differential cross-sections of the measured ϕ^* variable in pb, of both the combined result as well at the electron and muon results. The uncertainty is separated into the statistical component followed by the systematic.

ϕ^* range	Combined	Electron channel	Muon channel
0.000-0.004	$(4.426\pm0.008\pm0.034\pm0.115)\times10^3$	$(4.41\pm0.01\ \pm0.04\ \pm0.11)\times10^3$	$(4.437\pm0.010\pm0.067\pm0.115)\times10^3$
0.004-0.008	$(4.429\pm0.008\pm0.033\pm0.115)\times10^3$	$(4.43\pm0.01\ \pm0.04\ \pm0.12)\times10^3$	$(4.400\pm0.010\pm0.066\pm0.114)\times10^3$
0.008-0.012	$(4.306\pm0.008\pm0.033\pm0.112)\times10^3$	$(4.30\pm0.01\ \pm0.04\ \pm0.11)\times10^3$	$(4.306\pm0.010\pm0.065\pm0.112)\times10^3$
0.012-0.016	$(4.235\pm0.008\pm0.032\pm0.110)\times10^3$	$(4.25\pm0.01\ \pm0.04\ \pm0.11)\times10^3$	$(4.183\pm0.010\pm0.063\pm0.109)\times10^3$
0.016-0.020	$(4.061\pm0.008\pm0.032\pm0.106)\times10^3$	$(4.05\pm0.01\ \pm0.04\ \pm0.11)\times10^3$	$(4.045\pm0.009\pm0.062\pm0.105)\times10^3$
0.020-0.024	$(3.905\pm0.007\pm0.030\pm0.102)\times10^3$	$(3.91\pm0.01\ \pm0.04\ \pm0.10)\times10^3$	$(3.884\pm0.009\pm0.059\pm0.101)\times10^3$
0.024-0.029	$(3.723\pm0.006\pm0.029\pm0.097)\times10^3$	$(3.72\pm0.01\ \pm0.04\ \pm0.10)\times10^3$	$(3.697\pm0.008\pm0.056\pm0.096)\times10^3$
0.029-0.034	$(3.482\pm0.006\pm0.027\pm0.091)\times10^3$	$(3.48\pm0.01\ \pm0.03\ \pm0.09)\times10^3$	$(3.470\pm0.008\pm0.052\pm0.090)\times10^3$
0.034-0.039	$(3.259\pm0.006\pm0.025\pm0.085)\times10^3$	$(3.255\pm0.010\pm0.033\pm0.085)\times10^3$	$(3.249\pm0.007\pm0.049\pm0.084)\times10^3$
0.039-0.045	$(3.039\pm0.005\pm0.023\pm0.079)\times10^3$	$(3.036\pm0.009\pm0.029\pm0.079)\times10^3$	$(3.033\pm0.007\pm0.046\pm0.079)\times10^3$
0.045-0.051	$(2.793\pm0.005\pm0.022\pm0.073)\times10^3$	$(2.788\pm0.008\pm0.028\pm0.072)\times10^3$	$(2.788\pm0.006\pm0.042\pm0.072)\times10^3$
0.051-0.057	$(2.577\pm0.005\pm0.019\pm0.067)\times10^3$	$(2.578\pm0.008\pm0.025\pm0.067)\times10^3$	$(2.563\pm0.006\pm0.038\pm0.067)\times10^3$
0.057-0.064	$(2.375\pm0.004\pm0.019\pm0.062)\times10^3$	$(2.375\pm0.007\pm0.024\pm0.062)\times10^3$	$(2.362\pm0.005\pm0.036\pm0.061)\times10^3$
0.064-0.072	$(2.143\pm0.004\pm0.017\pm0.056)\times10^3$	$(2.136\pm0.006\pm0.022\pm0.056)\times10^3$	$(2.143\pm0.005\pm0.033\pm0.056)\times10^3$
0.072-0.081	$(1.932\pm0.003\pm0.015\pm0.050)\times10^3$	$(1.932\pm0.005\pm0.019\pm0.050)\times10^3$	$(1.922\pm0.004\pm0.029\pm0.050)\times10^3$
0.081-0.091	$(1.713\pm0.003\pm0.013\pm0.045)\times10^3$	$(1.713\pm0.005\pm0.018\pm0.045)\times10^3$	$(1.702\pm0.004\pm0.026\pm0.044)\times10^3$
0.091-0.102	$(1.518\pm0.003\pm0.012\pm0.039)\times10^3$	$(1.520\pm0.004\pm0.016\pm0.040)\times10^3$	$(1.505\pm0.003\pm0.023\pm0.039)\times10^3$
0.102-0.114	$(1.335\pm0.002\pm0.010\pm0.035)\times10^3$	$(1.336\pm0.004\pm0.014\pm0.035)\times10^3$	$(1.324\pm0.003\pm0.020\pm0.034)\times10^3$
0.114-0.128	$(1.165\pm0.002\pm0.009\pm0.030)\times10^3$	$(1.168\pm0.003\pm0.012\pm0.030)\times10^3$	$(1.151\pm0.003\pm0.017\pm0.030)\times10^3$
0.128-0.145	$(9.91\pm0.02\ \pm0.08\ \pm0.26)\times10^2$	$(9.93\pm0.03\ \pm0.10\ \pm0.26)\times10^2$	$(9.83\pm0.02\ \pm0.15\ \pm0.26)\times10^2$
0.145-0.165	$(8.33\pm0.01\ \pm0.06\ \pm0.22)\times10^2$	$(8.36\pm0.02\ \pm0.09\ \pm0.22)\times10^2$	$(8.23\pm0.02\ \pm0.12\ \pm0.21)\times10^2$
0.165-0.189	$(6.83\pm0.01\ \pm0.05\ \pm0.18)\times10^2$	$(6.85\pm0.02\ \pm0.07\ \pm0.18)\times10^2$	$(6.75\pm0.01\ \pm0.10\ \pm0.18)\times10^2$
0.189-0.219	$(5.419\pm0.009\pm0.042\pm0.141)\times10^2$	$(5.42\pm0.01\ \pm0.06\ \pm0.14)\times10^2$	$(5.39\pm0.01\ \pm0.08\ \pm0.14)\times10^2$
0.219-0.258	$(4.190\pm0.007\pm0.033\pm0.109)\times10^2$	$(4.20\pm0.01\ \pm0.05\ \pm0.11)\times10^2$	$(4.151\pm0.009\pm0.063\pm0.108)\times10^2$
0.258-0.312	$(3.052\pm0.005\pm0.024\pm0.079)\times10^2$	$(3.060\pm0.008\pm0.034\pm0.080)\times10^2$	$(3.023\pm0.007\pm0.045\pm0.079)\times10^2$
0.312-0.391	$(2.052\pm0.003\pm0.016\pm0.053)\times10^2$	$(2.059\pm0.005\pm0.023\pm0.054)\times10^2$	$(2.031\pm0.004\pm0.031\pm0.053)\times10^2$
0.391-0.524	$(1.199\pm0.002\pm0.009\pm0.031)\times10^2$	$(1.208\pm0.003\pm0.014\pm0.031)\times10^2$	$(1.179\pm0.003\pm0.018\pm0.031)\times10^2$
0.524-0.695	$62.5\pm0.1\ \ \pm0.5\ \ \pm1.6$	$62.8\pm0.2\ \ \pm0.8\ \ \pm1.6$	$61.7\pm0.2\ \ \pm0.9\ \ \pm1.6$
0.695-0.918	$31.44\pm0.08\ \pm0.26\ \pm0.82$	$31.8\pm0.1\ \ \pm0.4\ \ \pm0.8$	$30.9\pm0.1\ \ \pm0.5\ \ \pm0.8$
0.918-1.153	$16.14\pm0.06\ \pm0.14\ \pm0.42$	$16.15\pm0.09\ \pm0.22\ \pm0.42$	$16.07\pm0.07\ \pm0.25\ \pm0.42$
1.153-1.496	$8.41\pm0.03\ \pm0.08\ \pm0.22$	$8.52\pm0.05\ \pm0.12\ \pm0.22$	$8.26\pm0.04\ \pm0.13\ \pm0.21$
1.496-1.947	$3.99\pm0.02\ \pm0.04\ \pm0.10$	$3.99\pm0.03\ \pm0.06\ \pm0.10$	$3.97\pm0.03\ \pm0.07\ \pm0.10$
1.947-2.522	$1.94\pm0.01\ \pm0.02\ \pm0.05$	$1.97\pm0.02\ \pm0.03\ \pm0.05$	$1.91\pm0.02\ \pm0.03\ \pm0.05$
2.522-3.277	$1.002\pm0.008\pm0.012\pm0.026$	$1.01\pm0.01\ \pm0.02\ \pm0.03$	$0.992\pm0.010\pm0.019\pm0.026$

Table B.3: This table contains the absolute cross-sections of each y bin in pb, of both the combined result as well at the electron and muon results. The uncertainty is separated into the statistical component followed by the systematic.

$\|y\|$-bin	Combined	ee	$\mu\mu$
Total	479.1±0.1 ±3.2 ±12.5	478.7±0.2 ±4.6 ±12.4	477.5±0.2 ±7.2 ±12.4
0.0-0.4	107.59±0.07±0.71±2.80	108.05±0.10±1.08±2.81	106.48±0.09±1.58±2.77
0.4-0.8	106.43±0.07±0.70±2.77	106.29±0.10±0.99±2.76	106.36±0.09±1.57±2.77
0.8-1.2	103.79±0.07±0.69±2.70	103.67±0.11±1.03±2.70	103.73±0.09±1.53±2.70
1.2-1.6	88.69±0.06±0.61±2.31	88.63±0.11±0.92±2.30	88.39±0.08±1.34±2.30
1.6-2.0	58.39±0.06±0.43±1.52	58.15±0.10±0.66±1.51	58.27±0.07±0.93±1.51
2.0-2.4	14.18±0.03±0.12±0.37	13.92±0.05±0.21±0.36	14.22±0.04±0.25±0.37

Table B.4: This table contains the measured normalized cross-sections of each y bin in pb, of both the combined result as well at the electron and muon results. The uncertainty is separated into the statistical component followed by the systematic.

$\|y\|$-bin	Combined	ee	$\mu\mu$
0.0-0.4	0.22337±0.00014±0.00021	0.22572±0.00021±0.00079	0.22301±0.00018±0.00023
0.4-0.8	0.22230±0.00014±0.00019	0.22203±0.00022±0.00054	0.22277±0.00019±0.00025
0.8-1.2	0.21694±0.00014±0.00018	0.21656±0.00023±0.00051	0.21726±0.00018±0.00023
1.2-1.6	0.18533±0.00014±0.00016	0.18513±0.00023±0.00054	0.18513±0.00017±0.00018
1.6-2.0	0.12229±0.00012±0.00021	0.12148±0.00020±0.00063	0.12204±0.00014±0.00032
2.0-2.4	0.02974±0.00006±0.00011	0.02908±0.00010±0.00027	0.02979±0.00007±0.00017

Table B.5: This table contains the measured normalized differential cross-section of ϕ^* of events where the rapidity of the Z falls in the range $|y| < 0.4$. The uncertainty is separated into the statistical component followed by the systematic.

ϕ^* range	Combined	Electron channel	Muon channel
0.000-0.004	5.08±0.02 ±0.02	5.09±0.03 ±0.04	5.09±0.02 ±0.02
0.004-0.008	5.02±0.02 ±0.02	5.07±0.03 ±0.04	5.02±0.02 ±0.03
0.008-0.012	4.93±0.02 ±0.02	4.96±0.03 ±0.04	4.92±0.02 ±0.02
0.012-0.016	4.83±0.02 ±0.02	4.91±0.03 ±0.04	4.81±0.02 ±0.02
0.016-0.020	4.64±0.02 ±0.02	4.65±0.03 ±0.04	4.63±0.02 ±0.02
0.020-0.024	4.49±0.02 ±0.02	4.56±0.03 ±0.04	4.46±0.02 ±0.02
0.024-0.029	4.26±0.01 ±0.02	4.29±0.02 ±0.03	4.25±0.02 ±0.02
0.029-0.034	3.99±0.01 ±0.02	4.05±0.02 ±0.03	3.97±0.02 ±0.02
0.034-0.039	3.74±0.01 ±0.02	3.70±0.02 ±0.03	3.77±0.02 ±0.02
0.039-0.045	3.52±0.01 ±0.01	3.51±0.02 ±0.03	3.54±0.02 ±0.02
0.045-0.051	3.22±0.01 ±0.01	3.22±0.02 ±0.02	3.23±0.02 ±0.01
0.051-0.057	2.97±0.01 ±0.01	3.02±0.02 ±0.02	2.96±0.01 ±0.01
0.057-0.064	2.745±0.010 ±0.011	2.76±0.02 ±0.02	2.74±0.01 ±0.01
0.064-0.072	2.483±0.009 ±0.009	2.50±0.01 ±0.02	2.48±0.01 ±0.01
0.072-0.081	2.240±0.008 ±0.008	2.25±0.01 ±0.02	2.25±0.01 ±0.01
0.081-0.091	1.994±0.007 ±0.008	2.01±0.01 ±0.01	1.991±0.009 ±0.010
0.091-0.102	1.770±0.006 ±0.007	1.806±0.010 ±0.013	1.761±0.008 ±0.008
0.102-0.114	1.554±0.006 ±0.006	1.584±0.009 ±0.012	1.544±0.007 ±0.007
0.114-0.128	1.353±0.005 ±0.005	1.373±0.007 ±0.010	1.348±0.006 ±0.006
0.128-0.145	1.154±0.004 ±0.004	1.169±0.006 ±0.008	1.151±0.005 ±0.005
0.145-0.165	0.971±0.003 ±0.004	0.996±0.005 ±0.007	0.962±0.004 ±0.004
0.165-0.189	0.801±0.003 ±0.003	0.808±0.004 ±0.006	0.803±0.004 ±0.004
0.189-0.219	0.637±0.002 ±0.002	0.643±0.003 ±0.004	0.638±0.003 ±0.003
0.219-0.258	0.493±0.002 ±0.002	0.499±0.003 ±0.003	0.492±0.002 ±0.002
0.258-0.312	0.358±0.001 ±0.001	0.361±0.002 ±0.003	0.358±0.002 ±0.002
0.312-0.391	0.2418±0.0008±0.0009	0.246±0.001 ±0.002	0.241±0.001 ±0.001
0.391-0.524	0.1412±0.0005±0.0005	0.1452±0.0007±0.0010	0.1400±0.0006±0.0006
0.524-0.695	(7.44±0.03 ±0.03)$\times 10^{-2}$	(7.61±0.05 ±0.06)$\times 10^{-2}$	(7.41±0.04 ±0.04)$\times 10^{-2}$
0.695-0.918	(3.76±0.02 ±0.02)$\times 10^{-2}$	(3.82±0.03 ±0.04)$\times 10^{-2}$	(3.76±0.03 ±0.03)$\times 10^{-2}$
0.918-1.153	(2.00±0.01 ±0.02)$\times 10^{-2}$	(1.98±0.02 ±0.03)$\times 10^{-2}$	(2.02±0.02 ±0.02)$\times 10^{-2}$
1.153-1.496	(1.050±0.008 ±0.009)$\times 10^{-2}$	(1.07±0.01 ±0.02)$\times 10^{-2}$	(1.05±0.01 ±0.01)$\times 10^{-2}$
1.496-1.947	(5.08±0.05 ±0.05)$\times 10^{-3}$	(5.15±0.08 ±0.09)$\times 10^{-3}$	(5.11±0.07 ±0.06)$\times 10^{-3}$
1.947-2.522	(2.54±0.03 ±0.03)$\times 10^{-3}$	(2.65±0.05 ±0.06)$\times 10^{-3}$	(2.49±0.04 ±0.04)$\times 10^{-3}$
2.522-3.277	(1.36±0.02 ±0.02)$\times 10^{-3}$	(1.36±0.03 ±0.04)$\times 10^{-3}$	(1.37±0.03 ±0.03)$\times 10^{-3}$

Table B.6: This table contains the measured normalized differential cross-section of ϕ^* of events where the rapidity of the Z falls in the range $0.4 < |y| < 0.8$. The uncertainty is separated into the statistical component followed by the systematic.

ϕ^* range	Combined	Electron channel	Muon channel
0.000-0.004	5.04±0.02 ±0.02	5.02±0.03 ±0.04	5.04±0.02 ±0.02
0.004-0.008	5.01±0.02 ±0.02	5.02±0.03 ±0.04	5.01±0.02 ±0.02
0.008-0.012	4.95±0.02 ±0.02	4.86±0.03 ±0.04	4.97±0.02 ±0.02
0.012-0.016	4.79±0.02 ±0.02	4.80±0.03 ±0.04	4.79±0.02 ±0.03
0.016-0.020	4.65±0.02 ±0.02	4.65±0.03 ±0.04	4.63±0.02 ±0.02
0.020-0.024	4.41±0.02 ±0.02	4.38±0.03 ±0.04	4.44±0.02 ±0.02
0.024-0.029	4.25±0.02 ±0.02	4.24±0.02 ±0.03	4.25±0.02 ±0.02
0.029-0.034	4.00±0.01 ±0.02	3.96±0.02 ±0.03	4.02±0.02 ±0.02
0.034-0.039	3.74±0.01 ±0.02	3.74±0.02 ±0.03	3.74±0.02 ±0.02
0.039-0.045	3.49±0.01 ±0.01	3.46±0.02 ±0.03	3.50±0.02 ±0.02
0.045-0.051	3.20±0.01 ±0.01	3.17±0.02 ±0.03	3.21±0.02 ±0.02
0.051-0.057	2.95±0.01 ±0.01	2.93±0.02 ±0.02	2.96±0.01 ±0.02
0.057-0.064	2.74±0.01 ±0.01	2.71±0.02 ±0.02	2.76±0.01 ±0.01
0.064-0.072	2.465±0.009 ±0.010	2.44±0.01 ±0.02	2.48±0.01 ±0.01
0.072-0.081	2.225±0.008 ±0.009	2.22±0.01 ±0.02	2.23±0.01 ±0.01
0.081-0.091	1.984±0.007 ±0.008	1.97±0.01 ±0.01	1.990±0.009 ±0.009
0.091-0.102	1.754±0.006 ±0.007	1.748±0.010 ±0.013	1.760±0.008 ±0.009
0.102-0.114	1.554±0.006 ±0.006	1.548±0.009 ±0.012	1.558±0.008 ±0.008
0.114-0.128	1.352±0.005 ±0.006	1.380±0.008 ±0.010	1.342±0.006 ±0.007
0.128-0.145	1.151±0.004 ±0.004	1.149±0.006 ±0.009	1.153±0.005 ±0.005
0.145-0.165	0.970±0.003 ±0.004	0.973±0.005 ±0.007	0.971±0.005 ±0.004
0.165-0.189	0.795±0.003 ±0.003	0.798±0.004 ±0.006	0.796±0.004 ±0.004
0.189-0.219	0.636±0.002 ±0.002	0.633±0.003 ±0.004	0.640±0.003 ±0.003
0.219-0.258	0.491±0.002 ±0.002	0.488±0.003 ±0.003	0.495±0.002 ±0.002
0.258-0.312	0.357±0.001 ±0.001	0.356±0.002 ±0.002	0.359±0.002 ±0.002
0.312-0.391	0.2398±0.0008±0.0009	0.241±0.001 ±0.002	0.240±0.001 ±0.001
0.391-0.524	0.1400±0.0005±0.0005	0.1421±0.0008±0.0010	0.1396±0.0006±0.0006
0.524-0.695	(7.39±0.03 ±0.04)$\times10^{-2}$	(7.48±0.05 ±0.07)$\times10^{-2}$	(7.41±0.04 ±0.04)$\times10^{-2}$
0.695-0.918	(3.74±0.02 ±0.02)$\times10^{-2}$	(3.77±0.03 ±0.04)$\times10^{-2}$	(3.76±0.03 ±0.03)$\times10^{-2}$
0.918-1.153	(1.93±0.01 ±0.02)$\times10^{-2}$	(2.01±0.02 ±0.03)$\times10^{-2}$	(1.91±0.02 ±0.02)$\times10^{-2}$
1.153-1.496	(1.034±0.008 ±0.009)$\times10^{-2}$	(1.05±0.01 ±0.02)$\times10^{-2}$	(1.04±0.01 ±0.01)$\times10^{-2}$
1.496-1.947	(5.08±0.05 ±0.05)$\times10^{-3}$	(5.16±0.08 ±0.10)$\times10^{-3}$	(5.07±0.07 ±0.06)$\times10^{-3}$
1.947-2.522	(2.55±0.03 ±0.03)$\times10^{-3}$	(2.64±0.05 ±0.07)$\times10^{-3}$	(2.54±0.04 ±0.04)$\times10^{-3}$
2.522-3.277	(1.36±0.02 ±0.02)$\times10^{-3}$	(1.39±0.03 ±0.05)$\times10^{-3}$	(1.35±0.03 ±0.02)$\times10^{-3}$

Table B.7: This table contains the measured normalized differential cross-section of ϕ^* of events where the rapidity of the Z falls in the range $0.8 < |y| < 1.2$. The uncertainty is separated into the statistical component followed by the systematic.

ϕ^* range	Combined	Electron channel	Muon channel
0.000-0.004	5.00±0.02 ±0.02	4.93±0.03 ±0.04	5.01±0.02 ±0.02
0.004-0.008	5.01±0.02 ±0.02	4.95±0.03 ±0.05	5.05±0.02 ±0.03
0.008-0.012	4.86±0.02 ±0.02	4.83±0.03 ±0.05	4.87±0.02 ±0.03
0.012-0.016	4.75±0.02 ±0.02	4.76±0.03 ±0.05	4.73±0.02 ±0.02
0.016-0.020	4.56±0.02 ±0.02	4.44±0.03 ±0.04	4.61±0.02 ±0.02
0.020-0.024	4.40±0.02 ±0.02	4.41±0.03 ±0.04	4.40±0.02 ±0.02
0.024-0.029	4.18±0.02 ±0.02	4.13±0.03 ±0.04	4.19±0.02 ±0.02
0.029-0.034	3.94±0.02 ±0.02	3.89±0.03 ±0.03	3.96±0.02 ±0.02
0.034-0.039	3.72±0.01 ±0.02	3.71±0.02 ±0.03	3.71±0.02 ±0.02
0.039-0.045	3.40±0.01 ±0.01	3.39±0.02 ±0.03	3.41±0.02 ±0.02
0.045-0.051	3.17±0.01 ±0.01	3.14±0.02 ±0.03	3.17±0.02 ±0.02
0.051-0.057	2.89±0.01 ±0.01	2.85±0.02 ±0.03	2.91±0.01 ±0.02
0.057-0.064	2.66±0.01 ±0.01	2.67±0.02 ±0.02	2.65±0.01 ±0.01
0.064-0.072	2.435±0.009 ±0.010	2.40±0.02 ±0.02	2.45±0.01 ±0.01
0.072-0.081	2.186±0.008 ±0.009	2.18±0.01 ±0.02	2.19±0.01 ±0.01
0.081-0.091	1.933±0.007 ±0.008	1.94±0.01 ±0.02	1.934±0.009 ±0.009
0.091-0.102	1.710±0.007 ±0.007	1.69±0.01 ±0.01	1.722±0.008 ±0.008
0.102-0.114	1.511±0.006 ±0.006	1.511±0.010 ±0.013	1.511±0.007 ±0.007
0.114-0.128	1.306±0.005 ±0.006	1.300±0.008 ±0.011	1.310±0.006 ±0.007
0.128-0.145	1.118±0.004 ±0.004	1.127±0.007 ±0.009	1.116±0.005 ±0.005
0.145-0.165	0.938±0.004 ±0.004	0.944±0.006 ±0.008	0.939±0.004 ±0.004
0.165-0.189	0.768±0.003 ±0.003	0.778±0.005 ±0.006	0.763±0.004 ±0.004
0.189-0.219	0.609±0.002 ±0.002	0.611±0.004 ±0.005	0.610±0.003 ±0.003
0.219-0.258	0.470±0.002 ±0.002	0.479±0.003 ±0.004	0.467±0.002 ±0.002
0.258-0.312	0.343±0.001 ±0.001	0.348±0.002 ±0.003	0.342±0.002 ±0.002
0.312-0.391	0.2325±0.0009±0.0009	0.233±0.001 ±0.002	0.233±0.001 ±0.001
0.391-0.524	0.1357±0.0005±0.0005	0.1378±0.0008±0.0011	0.1353±0.0006±0.0006
0.524-0.695	(7.14±0.03 ±0.04)×10^{-2}	(7.08±0.05 ±0.07)×10^{-2}	(7.19±0.04 ±0.04)×10^{-2}
0.695-0.918	(3.54±0.02 ±0.02)×10^{-2}	(3.63±0.03 ±0.04)×10^{-2}	(3.52±0.02 ±0.02)×10^{-2}
0.918-1.153	(1.84±0.01 ±0.02)×10^{-2}	(1.81±0.02 ±0.03)×10^{-2}	(1.86±0.02 ±0.02)×10^{-2}
1.153-1.496	(9.53±0.08 ±0.09)×10^{-3}	(9.7±0.1 ±0.2)×10^{-3}	(9.5±0.1 ±0.1)×10^{-3}
1.496-1.947	(4.71±0.05 ±0.05)×10^{-3}	(4.64±0.08 ±0.10)×10^{-3}	(4.76±0.06 ±0.07)×10^{-3}
1.947-2.522	(2.32±0.03 ±0.03)×10^{-3}	(2.32±0.05 ±0.06)×10^{-3}	(2.33±0.04 ±0.04)×10^{-3}
2.522-3.277	(1.23±0.02 ±0.02)×10^{-3}	(1.24±0.03 ±0.04)×10^{-3}	(1.23±0.03 ±0.03)×10^{-3}

Table B.8: This table contains the measured normalized differential cross-section of ϕ^* of events where the rapidity of the Z falls in the range $1.2 < |y| < 1.6$. The uncertainty is separated into the statistical component followed by the systematic.

ϕ^* range	Combined	Electron channel	Muon channel
0.000-0.004	4.37±0.02 ±0.02	4.32±0.03 ±0.04	4.38±0.02 ±0.02
0.004-0.008	4.35±0.02 ±0.02	4.32±0.03 ±0.05	4.34±0.02 ±0.02
0.008-0.012	4.27±0.02 ±0.02	4.23±0.03 ±0.05	4.27±0.02 ±0.02
0.012-0.016	4.14±0.02 ±0.02	4.19±0.03 ±0.05	4.11±0.02 ±0.02
0.016-0.020	4.07±0.02 ±0.02	4.10±0.03 ±0.05	4.03±0.02 ±0.02
0.020-0.024	3.78±0.02 ±0.02	3.80±0.03 ±0.05	3.76±0.02 ±0.02
0.024-0.029	3.65±0.01 ±0.02	3.60±0.03 ±0.04	3.67±0.02 ±0.02
0.029-0.034	3.42±0.01 ±0.02	3.40±0.03 ±0.04	3.41±0.02 ±0.02
0.034-0.039	3.17±0.01 ±0.02	3.17±0.02 ±0.03	3.16±0.02 ±0.02
0.039-0.045	2.98±0.01 ±0.01	2.93±0.02 ±0.03	2.99±0.01 ±0.02
0.045-0.051	2.73±0.01 ±0.01	2.74±0.02 ±0.03	2.72±0.01 ±0.02
0.051-0.057	2.53±0.01 ±0.01	2.55±0.02 ±0.03	2.52±0.01 ±0.01
0.057-0.064	2.316±0.010 ±0.011	2.32±0.02 ±0.02	2.32±0.01 ±0.01
0.064-0.072	2.086±0.009 ±0.009	2.07±0.02 ±0.02	2.09±0.01 ±0.01
0.072-0.081	1.864±0.008 ±0.008	1.84±0.01 ±0.02	1.869±0.010 ±0.009
0.081-0.091	1.642±0.007 ±0.007	1.64±0.01 ±0.02	1.644±0.009 ±0.009
0.091-0.102	1.444±0.006 ±0.007	1.45±0.01 ±0.01	1.435±0.008 ±0.008
0.102-0.114	1.281±0.006 ±0.006	1.276±0.009 ±0.013	1.281±0.007 ±0.006
0.114-0.128	1.105±0.005 ±0.005	1.103±0.008 ±0.011	1.108±0.006 ±0.006
0.128-0.145	0.959±0.004 ±0.004	0.956±0.007 ±0.009	0.957±0.005 ±0.005
0.145-0.165	0.791±0.003 ±0.003	0.778±0.006 ±0.008	0.797±0.004 ±0.004
0.165-0.189	0.646±0.003 ±0.003	0.656±0.005 ±0.006	0.642±0.003 ±0.003
0.189-0.219	0.512±0.002 ±0.002	0.512±0.004 ±0.005	0.511±0.003 ±0.003
0.219-0.258	0.399±0.002 ±0.002	0.393±0.003 ±0.004	0.401±0.002 ±0.002
0.258-0.312	0.287±0.001 ±0.001	0.290±0.002 ±0.003	0.286±0.001 ±0.001
0.312-0.391	0.1947±0.0008±0.0008	0.195±0.001 ±0.002	0.195±0.001 ±0.001
0.391-0.524	0.1120±0.0005±0.0005	0.1122±0.0008±0.0011	0.1120±0.0006±0.0005
0.524-0.695	(5.76±0.03 ±0.03)$\times10^{-2}$	(5.88±0.05 ±0.07)$\times10^{-2}$	(5.73±0.04 ±0.04)$\times10^{-2}$
0.695-0.918	(2.89±0.02 ±0.02)$\times10^{-2}$	(2.96±0.03 ±0.04)$\times10^{-2}$	(2.87±0.02 ±0.02)$\times10^{-2}$
0.918-1.153	(1.49±0.01 ±0.01)$\times10^{-2}$	(1.48±0.02 ±0.03)$\times10^{-2}$	(1.50±0.02 ±0.02)$\times10^{-2}$
1.153-1.496	(7.58±0.07 ±0.08)$\times10^{-3}$	(8.1±0.1 ±0.2)$\times10^{-3}$	(7.37±0.09 ±0.09)$\times10^{-3}$
1.496-1.947	(3.53±0.04 ±0.05)$\times10^{-3}$	(3.38±0.07 ±0.08)$\times10^{-3}$	(3.60±0.06 ±0.06)$\times10^{-3}$
1.947-2.522	(1.67±0.03 ±0.03)$\times10^{-3}$	(1.74±0.05 ±0.06)$\times10^{-3}$	(1.64±0.03 ±0.04)$\times10^{-3}$
2.522-3.277	(8.6±0.2 ±0.2)$\times10^{-4}$	(8.5±0.3 ±0.3)$\times10^{-4}$	(8.5±0.2 ±0.2)$\times10^{-4}$

Table B.9: This table contains the measured normalized differential cross-section of ϕ^* of events where the rapidity of the Z falls in the range $0.4 < |y| < 0.8$. The uncertainty is separated into the statistical component followed by the systematic.

ϕ^* range	Combined	Electron channel	Muon channel
0.000-0.004	2.97±0.02 ±0.02	2.86±0.03 ±0.04	2.98±0.02 ±0.02
0.004-0.008	2.95±0.02 ±0.02	2.97±0.03 ±0.05	2.93±0.02 ±0.02
0.008-0.012	2.83±0.02 ±0.02	2.74±0.03 ±0.05	2.84±0.02 ±0.02
0.012-0.016	2.79±0.02 ±0.02	2.73±0.03 ±0.05	2.78±0.02 ±0.02
0.016-0.020	2.62±0.02 ±0.02	2.57±0.03 ±0.04	2.64±0.02 ±0.02
0.020-0.024	2.62±0.02 ±0.02	2.50±0.03 ±0.04	2.63±0.02 ±0.02
0.024-0.029	2.44±0.01 ±0.02	2.53±0.03 ±0.04	2.41±0.02 ±0.02
0.029-0.034	2.25±0.01 ±0.01	2.18±0.02 ±0.03	2.25±0.01 ±0.02
0.034-0.039	2.12±0.01 ±0.01	2.08±0.02 ±0.03	2.13±0.01 ±0.02
0.039-0.045	1.95±0.01 ±0.01	1.98±0.02 ±0.03	1.94±0.01 ±0.01
0.045-0.051	1.81±0.01 ±0.01	1.79±0.02 ±0.03	1.81±0.01 ±0.01
0.051-0.057	1.664±0.010 ±0.011	1.63±0.02 ±0.03	1.66±0.01 ±0.01
0.057-0.064	1.537±0.009 ±0.010	1.54±0.02 ±0.02	1.53±0.01 ±0.01
0.064-0.072	1.382±0.008 ±0.009	1.35±0.01 ±0.02	1.387±0.009 ±0.011
0.072-0.081	1.231±0.007 ±0.007	1.26±0.01 ±0.02	1.220±0.008 ±0.008
0.081-0.091	1.091±0.006 ±0.007	1.09±0.01 ±0.02	1.084±0.007 ±0.009
0.091-0.102	0.973±0.005 ±0.007	0.971±0.010±0.015	0.972±0.006 ±0.008
0.102-0.114	0.832±0.005 ±0.005	0.818±0.009±0.012	0.831±0.006 ±0.006
0.114-0.128	0.731±0.004 ±0.004	0.721±0.007±0.011	0.733±0.005 ±0.005
0.128-0.145	0.618±0.003 ±0.004	0.613±0.006±0.008	0.617±0.004 ±0.004
0.145-0.165	0.517±0.003 ±0.003	0.519±0.005±0.007	0.514±0.003 ±0.004
0.165-0.189	0.430±0.002 ±0.003	0.423±0.004±0.006	0.430±0.003 ±0.003
0.189-0.219	0.342±0.002 ±0.002	0.339±0.003±0.005	0.342±0.002 ±0.002
0.219-0.258	0.257±0.001 ±0.002	0.259±0.003±0.004	0.256±0.002 ±0.002
0.258-0.312	0.192±0.001 ±0.001	0.190±0.002±0.003	0.192±0.001 ±0.001
0.312-0.391	0.1248±0.0007±0.0008	0.126±0.001±0.002	0.1246±0.0008±0.0009
0.391-0.524	(7.34±0.04 ±0.05)$\times10^{-2}$	(7.35±0.07 ±0.10)$\times10^{-2}$	(7.32±0.05 ±0.05)$\times10^{-2}$
0.524-0.695	(3.68±0.02 ±0.03)$\times10^{-2}$	(3.74±0.04 ±0.06)$\times10^{-2}$	(3.67±0.03 ±0.03)$\times10^{-2}$
0.695-0.918	(1.86±0.02 ±0.02)$\times10^{-2}$	(1.99±0.03 ±0.04)$\times10^{-2}$	(1.83±0.02 ±0.02)$\times10^{-2}$
0.918-1.153	(9.3±0.1 ±0.1)$\times10^{-3}$	(9.6±0.2 ±0.2)$\times10^{-3}$	(9.2±0.1 ±0.1)$\times10^{-3}$
1.153-1.496	(4.54±0.06 ±0.07)$\times10^{-3}$	(4.49±0.10 ±0.13)$\times10^{-3}$	(4.53±0.07 ±0.08)$\times10^{-3}$
1.496-1.947	(1.90±0.03 ±0.04)$\times10^{-3}$	(2.06±0.06 ±0.08)$\times10^{-3}$	(1.85±0.04 ±0.04)$\times10^{-3}$
1.947-2.522	(8.0±0.2 ±0.2)$\times10^{-4}$	(7.7±0.3 ±0.3)$\times10^{-4}$	(8.1±0.2 ±0.3)$\times10^{-4}$
2.522-3.277	(3.7±0.1 ±0.1)$\times10^{-4}$	(4.0±0.2 ±0.3)$\times10^{-4}$	(3.6±0.1 ±0.1)$\times10^{-4}$

Table B.10: This table contains the measured normalized differential cross-section of ϕ^* of events where the rapidity of the Z falls in the range $2.0 < |y| < 2.4$. The uncertainty is separated into the statistical component followed by the systematic.

ϕ^* range	Combined	Electron channel	Muon channel
0.000-0.004	0.720±0.008±0.009	0.67±0.01 ±0.02	0.728±0.010±0.012
0.004-0.008	0.685±0.008±0.010	0.70±0.02 ±0.02	0.680±0.010±0.012
0.008-0.012	0.681±0.008±0.010	0.66±0.01 ±0.02	0.678±0.010±0.012
0.012-0.016	0.672±0.008±0.011	0.64±0.02 ±0.02	0.678±0.010±0.012
0.016-0.020	0.642±0.008±0.010	0.63±0.02 ±0.02	0.641±0.010±0.011
0.020-0.024	0.644±0.008±0.010	0.63±0.02 ±0.02	0.643±0.010±0.011
0.024-0.029	0.598±0.007±0.009	0.58±0.01 ±0.02	0.599±0.008±0.011
0.029-0.034	0.559±0.007±0.008	0.52±0.01 ±0.02	0.568±0.008±0.010
0.034-0.039	0.503±0.006±0.008	0.50±0.01 ±0.02	0.499±0.007±0.009
0.039-0.045	0.498±0.006±0.007	0.49±0.01 ±0.02	0.501±0.007±0.008
0.045-0.051	0.445±0.005±0.006	0.414±0.010±0.014	0.450±0.006±0.008
0.051-0.057	0.410±0.005±0.006	0.409±0.010±0.014	0.411±0.006±0.007
0.057-0.064	0.371±0.005±0.006	0.349±0.008±0.013	0.372±0.005±0.006
0.064-0.072	0.332±0.004±0.004	0.329±0.007±0.010	0.332±0.005±0.005
0.072-0.081	0.306±0.004±0.004	0.295±0.006±0.009	0.309±0.004±0.006
0.081-0.091	0.266±0.003±0.004	0.258±0.006±0.008	0.270±0.004±0.005
0.091-0.102	0.236±0.003±0.003	0.239±0.005±0.008	0.234±0.003±0.004
0.102-0.114	0.207±0.003±0.003	0.197±0.004±0.006	0.208±0.003±0.004
0.114-0.128	0.186±0.002±0.003	0.182±0.004±0.006	0.187±0.003±0.003
0.128-0.145	0.153±0.002±0.002	0.146±0.003±0.004	0.154±0.002±0.003
0.145-0.165	0.130±0.002±0.002	0.127±0.003±0.004	0.130±0.002±0.002
0.165-0.189	0.102±0.001±0.001	0.101±0.002±0.003	0.102±0.001±0.002
0.189-0.219	$(8.23\pm0.10\ \pm0.11)\times10^{-2}$	$(8.0\pm0.2\ \ \pm0.2)\times10^{-2}$	$(8.2\pm0.1\ \ \pm0.1)\times10^{-2}$
0.219-0.258	$(6.38\pm0.08\ \pm0.09)\times10^{-2}$	$(6.7\pm0.1\ \ \pm0.2)\times10^{-2}$	$(6.28\pm0.09\ \pm0.11)\times10^{-2}$
0.258-0.312	$(4.64\pm0.05\ \pm0.06)\times10^{-2}$	$(4.68\pm0.10\ \pm0.14)\times10^{-2}$	$(4.57\pm0.06\ \pm0.08)\times10^{-2}$
0.312-0.391	$(2.99\pm0.04\ \pm0.04)\times10^{-2}$	$(2.90\pm0.06\ \pm0.09)\times10^{-2}$	$(2.98\pm0.04\ \pm0.05)\times10^{-2}$
0.391-0.524	$(1.75\pm0.02\ \pm0.02)\times10^{-2}$	$(1.69\pm0.04\ \pm0.05)\times10^{-2}$	$(1.76\pm0.03\ \pm0.03)\times10^{-2}$
0.524-0.695	$(9.0\pm0.1\ \ \pm0.2)\times10^{-3}$	$(8.9\pm0.2\ \ \pm0.3)\times10^{-3}$	$(8.9\pm0.2\ \ \pm0.2)\times10^{-3}$
0.695-0.918	$(4.23\pm0.08\ \pm0.09)\times10^{-3}$	$(4.3\pm0.1\ \ \pm0.2)\times10^{-3}$	$(4.23\pm0.09\ \pm0.10)\times10^{-3}$
0.918-1.153	$(2.10\pm0.05\ \pm0.06)\times10^{-3}$	$(2.10\pm0.09\ \pm0.13)\times10^{-3}$	$(2.08\pm0.06\ \pm0.07)\times10^{-3}$
1.153-1.496	$(9.9\pm0.3\ \ \pm0.3)\times10^{-4}$	$(1.06\pm0.06\ \pm0.08)\times10^{-3}$	$(9.7\pm0.4\ \ \pm0.4)\times10^{-4}$
1.496-1.947	$(4.0\pm0.2\ \ \pm0.2)\times10^{-4}$	$(4.5\pm0.3\ \ \pm0.4)\times10^{-4}$	$(4.0\pm0.2\ \ \pm0.2)\times10^{-4}$
1.947-2.522	$(1.67\pm0.10\ \pm0.12)\times10^{-4}$	$(1.5\pm0.2\ \ \pm0.2)\times10^{-4}$	$(1.7\pm0.1\ \ \pm0.2)\times10^{-4}$
2.522-3.277	$(5.1\pm0.5\ \ \pm0.5)\times10^{-5}$	$(4.2\pm0.8\ \ \pm0.9)\times10^{-5}$	$(5.6\pm0.6\ \ \pm0.7)\times10^{-5}$

Table B.11: This table contains the measured absolute differential cross-section of ϕ^* of events where the rapidity of the Z falls in the range $|y| < 0.4$. The uncertainty is separated into the statistical component followed by the systematic.

ϕ^* range	Combined	Electron channel	Muon channel
0.000-0.004	$(2.439\pm0.008\pm0.018\pm0.063)\times10^3$	$(2.44\pm0.01\ \pm0.03\ \pm0.06)\times10^3$	$(2.43\pm0.01\ \pm0.04\ \pm0.06)\times10^3$
0.004-0.008	$(2.415\pm0.009\pm0.018\pm0.063)\times10^3$	$(2.42\pm0.01\ \pm0.03\ \pm0.06)\times10^3$	$(2.40\pm0.01\ \pm0.04\ \pm0.06)\times10^3$
0.008-0.012	$(2.369\pm0.009\pm0.018\pm0.062)\times10^3$	$(2.38\pm0.01\ \pm0.03\ \pm0.06)\times10^3$	$(2.35\pm0.01\ \pm0.04\ \pm0.06)\times10^3$
0.012-0.016	$(2.333\pm0.009\pm0.018\pm0.061)\times10^3$	$(2.35\pm0.01\ \pm0.03\ \pm0.06)\times10^3$	$(2.30\pm0.01\ \pm0.04\ \pm0.06)\times10^3$
0.016-0.020	$(2.226\pm0.008\pm0.017\pm0.058)\times10^3$	$(2.23\pm0.01\ \pm0.03\ \pm0.06)\times10^3$	$(2.21\pm0.01\ \pm0.04\ \pm0.06)\times10^3$
0.020-0.024	$(2.165\pm0.008\pm0.016\pm0.056)\times10^3$	$(2.18\pm0.01\ \pm0.03\ \pm0.06)\times10^3$	$(2.13\pm0.01\ \pm0.03\ \pm0.06)\times10^3$
0.024-0.029	$(2.049\pm0.007\pm0.016\pm0.053)\times10^3$	$(2.05\pm0.01\ \pm0.02\ \pm0.05)\times10^3$	$(2.028\pm0.009\pm0.032\pm0.053)\times10^3$
0.029-0.034	$(1.926\pm0.007\pm0.015\pm0.050)\times10^3$	$(1.94\pm0.01\ \pm0.02\ \pm0.05)\times10^3$	$(1.894\pm0.009\pm0.030\pm0.049)\times10^3$
0.034-0.039	$(1.786\pm0.007\pm0.014\pm0.046)\times10^3$	$(1.77\pm0.01\ \pm0.02\ \pm0.05)\times10^3$	$(1.800\pm0.009\pm0.028\pm0.047)\times10^3$
0.039-0.045	$(1.686\pm0.006\pm0.013\pm0.044)\times10^3$	$(1.681\pm0.009\pm0.019\pm0.044)\times10^3$	$(1.691\pm0.008\pm0.026\pm0.044)\times10^3$
0.045-0.051	$(1.546\pm0.006\pm0.012\pm0.040)\times10^3$	$(1.542\pm0.008\pm0.018\pm0.040)\times10^3$	$(1.543\pm0.007\pm0.024\pm0.040)\times10^3$
0.051-0.057	$(1.434\pm0.005\pm0.011\pm0.037)\times10^3$	$(1.443\pm0.008\pm0.017\pm0.038)\times10^3$	$(1.411\pm0.007\pm0.022\pm0.037)\times10^3$
0.057-0.064	$(1.318\pm0.005\pm0.010\pm0.034)\times10^3$	$(1.320\pm0.007\pm0.015\pm0.034)\times10^3$	$(1.308\pm0.006\pm0.021\pm0.034)\times10^3$
0.064-0.072	$(1.195\pm0.004\pm0.009\pm0.031)\times10^3$	$(1.198\pm0.006\pm0.014\pm0.031)\times10^3$	$(1.185\pm0.006\pm0.019\pm0.031)\times10^3$
0.072-0.081	$(1.077\pm0.004\pm0.008\pm0.028)\times10^3$	$(1.078\pm0.006\pm0.013\pm0.028)\times10^3$	$(1.073\pm0.005\pm0.017\pm0.028)\times10^3$
0.081-0.091	$(9.59\pm0.03\ \pm0.07\ \pm0.25)\times10^2$	$(9.61\pm0.05\ \pm0.11\ \pm0.25)\times10^2$	$(9.51\pm0.04\ \pm0.15\ \pm0.25)\times10^2$
0.091-0.102	$(8.56\pm0.03\ \pm0.06\ \pm0.22)\times10^2$	$(8.65\pm0.05\ \pm0.11\ \pm0.22)\times10^2$	$(8.41\pm0.04\ \pm0.13\ \pm0.22)\times10^2$
0.102-0.114	$(7.52\pm0.03\ \pm0.06\ \pm0.20)\times10^2$	$(7.58\pm0.04\ \pm0.09\ \pm0.20)\times10^2$	$(7.37\pm0.04\ \pm0.11\ \pm0.19)\times10^2$
0.114-0.128	$(6.53\pm0.02\ \pm0.05\ \pm0.17)\times10^2$	$(6.57\pm0.03\ \pm0.08\ \pm0.17)\times10^2$	$(6.44\pm0.03\ \pm0.10\ \pm0.17)\times10^2$
0.128-0.145	$(5.57\pm0.02\ \pm0.04\ \pm0.14)\times10^2$	$(5.60\pm0.03\ \pm0.07\ \pm0.15)\times10^2$	$(5.49\pm0.03\ \pm0.09\ \pm0.14)\times10^2$
0.145-0.165	$(4.70\pm0.02\ \pm0.03\ \pm0.12)\times10^2$	$(4.77\pm0.02\ \pm0.06\ \pm0.12)\times10^2$	$(4.59\pm0.02\ \pm0.07\ \pm0.12)\times10^2$
0.165-0.189	$(3.86\pm0.01\ \pm0.03\ \pm0.10)\times10^2$	$(3.87\pm0.02\ \pm0.05\ \pm0.10)\times10^2$	$(3.84\pm0.02\ \pm0.06\ \pm0.10)\times10^2$
0.189-0.219	$(3.07\pm0.01\ \pm0.02\ \pm0.08)\times10^2$	$(3.08\pm0.02\ \pm0.04\ \pm0.08)\times10^2$	$(3.04\pm0.01\ \pm0.05\ \pm0.08)\times10^2$
0.219-0.258	$(2.376\pm0.008\pm0.018\pm0.062)\times10^2$	$(2.39\pm0.01\ \pm0.03\ \pm0.06)\times10^2$	$(2.35\pm0.01\ \pm0.04\ \pm0.06)\times10^2$
0.258-0.312	$(1.723\pm0.006\pm0.013\pm0.045)\times10^2$	$(1.728\pm0.009\pm0.021\pm0.045)\times10^2$	$(1.708\pm0.008\pm0.026\pm0.044)\times10^2$
0.312-0.391	$(1.168\pm0.004\pm0.009\pm0.030)\times10^2$	$(1.176\pm0.006\pm0.015\pm0.031)\times10^2$	$(1.152\pm0.005\pm0.018\pm0.030)\times10^2$
0.391-0.524	$68.5\pm0.2\ \ \pm0.5\ \ \pm1.8$	$69.5\pm0.4\ \ \pm0.9\ \ \pm1.8$	$66.8\pm0.3\ \ \pm1.0\ \ \pm1.7$
0.524-0.695	$36.0\pm0.1\ \ \pm0.3\ \ \pm0.9$	$36.4\pm0.2\ \ \pm0.5\ \ \pm0.9$	$35.4\pm0.2\ \ \pm0.6\ \ \pm0.9$
0.695-0.918	$18.15\pm0.09\ \pm0.16\ \pm0.47$	$18.3\pm0.1\ \ \pm0.3\ \ \pm0.5$	$17.9\pm0.1\ \ \pm0.3\ \ \pm0.5$
0.918-1.153	$9.58\pm0.07\ \pm0.10\ \pm0.25$	$9.5\pm0.1\ \ \pm0.2\ \ \pm0.2$	$9.63\pm0.09\ \pm0.17\ \pm0.25$
1.153-1.496	$5.06\pm0.04\ \pm0.06\ \pm0.13$	$5.11\pm0.06\ \pm0.09\ \pm0.13$	$5.01\pm0.05\ \pm0.09\ \pm0.13$
1.496-1.947	$2.45\pm0.02\ \pm0.03\ \pm0.06$	$2.46\pm0.04\ \pm0.05\ \pm0.06$	$2.44\pm0.03\ \pm0.05\ \pm0.06$
1.947-2.522	$1.22\pm0.01\ \pm0.02\ \pm0.03$	$1.27\pm0.02\ \pm0.03\ \pm0.03$	$1.19\pm0.02\ \pm0.02\ \pm0.03$
2.522-3.277	$0.651\pm0.010\pm0.011\pm0.017$	$0.65\pm0.01\ \pm0.02\ \pm0.02$	$0.65\pm0.01\ \pm0.02\ \pm0.02$

Table B.12: This table contains the measured absolute differential cross-section of ϕ^* of events where the rapidity of the Z falls in the range $0.4 < |y| < 0.8$. The uncertainty is separated into the statistical component followed by the systematic.

ϕ^* range	Combined	Electron channel	Muon channel
0.000-0.004	$(2.409\pm0.009\pm0.018\pm0.063)\times10^3$	$(2.40\pm0.01\ \pm0.03\ \pm0.06)\times10^3$	$(2.41\pm0.01\ \pm0.04\ \pm0.06)\times10^3$
0.004-0.008	$(2.401\pm0.009\pm0.018\pm0.062)\times10^3$	$(2.40\pm0.01\ \pm0.03\ \pm0.06)\times10^3$	$(2.39\pm0.01\ \pm0.04\ \pm0.06)\times10^3$
0.008-0.012	$(2.350\pm0.009\pm0.018\pm0.061)\times10^3$	$(2.33\pm0.01\ \pm0.03\ \pm0.06)\times10^3$	$(2.37\pm0.01\ \pm0.04\ \pm0.06)\times10^3$
0.012-0.016	$(2.296\pm0.009\pm0.017\pm0.060)\times10^3$	$(2.30\pm0.01\ \pm0.03\ \pm0.06)\times10^3$	$(2.29\pm0.01\ \pm0.03\ \pm0.06)\times10^3$
0.016-0.020	$(2.227\pm0.009\pm0.018\pm0.058)\times10^3$	$(2.23\pm0.01\ \pm0.03\ \pm0.06)\times10^3$	$(2.21\pm0.01\ \pm0.04\ \pm0.06)\times10^3$
0.020-0.024	$(2.107\pm0.008\pm0.016\pm0.055)\times10^3$	$(2.10\pm0.01\ \pm0.02\ \pm0.05)\times10^3$	$(2.12\pm0.01\ \pm0.03\ \pm0.06)\times10^3$
0.024-0.029	$(2.031\pm0.007\pm0.015\pm0.053)\times10^3$	$(2.03\pm0.01\ \pm0.02\ \pm0.05)\times10^3$	$(2.028\pm0.009\pm0.031\pm0.053)\times10^3$
0.029-0.034	$(1.907\pm0.007\pm0.014\pm0.050)\times10^3$	$(1.90\pm0.01\ \pm0.02\ \pm0.05)\times10^3$	$(1.917\pm0.009\pm0.029\pm0.050)\times10^3$
0.034-0.039	$(1.792\pm0.007\pm0.014\pm0.047)\times10^3$	$(1.79\pm0.01\ \pm0.02\ \pm0.05)\times10^3$	$(1.787\pm0.009\pm0.027\pm0.046)\times10^3$
0.039-0.045	$(1.665\pm0.006\pm0.012\pm0.043)\times10^3$	$(1.657\pm0.009\pm0.018\pm0.043)\times10^3$	$(1.673\pm0.008\pm0.026\pm0.043)\times10^3$
0.045-0.051	$(1.527\pm0.006\pm0.012\pm0.040)\times10^3$	$(1.519\pm0.009\pm0.020\pm0.039)\times10^3$	$(1.532\pm0.007\pm0.024\pm0.040)\times10^3$
0.051-0.057	$(1.409\pm0.005\pm0.011\pm0.037)\times10^3$	$(1.405\pm0.009\pm0.016\pm0.037)\times10^3$	$(1.414\pm0.007\pm0.022\pm0.037)\times10^3$
0.057-0.064	$(1.308\pm0.005\pm0.010\pm0.034)\times10^3$	$(1.299\pm0.008\pm0.016\pm0.034)\times10^3$	$(1.317\pm0.006\pm0.020\pm0.034)\times10^3$
0.064-0.072	$(1.175\pm0.004\pm0.009\pm0.031)\times10^3$	$(1.168\pm0.007\pm0.013\pm0.030)\times10^3$	$(1.185\pm0.006\pm0.018\pm0.031)\times10^3$
0.072-0.081	$(1.064\pm0.004\pm0.008\pm0.028)\times10^3$	$(1.062\pm0.006\pm0.012\pm0.028)\times10^3$	$(1.063\pm0.005\pm0.017\pm0.028)\times10^3$
0.081-0.091	$(9.47\pm0.03\ \pm0.07\ \pm0.25)\times10^2$	$(9.42\pm0.05\ \pm0.11\ \pm0.24)\times10^2$	$(9.50\pm0.04\ \pm0.15\ \pm0.25)\times10^2$
0.091-0.102	$(8.40\pm0.03\ \pm0.06\ \pm0.22)\times10^2$	$(8.37\pm0.05\ \pm0.10\ \pm0.22)\times10^2$	$(8.40\pm0.04\ \pm0.13\ \pm0.22)\times10^2$
0.102-0.114	$(7.43\pm0.03\ \pm0.06\ \pm0.19)\times10^2$	$(7.41\pm0.04\ \pm0.09\ \pm0.19)\times10^2$	$(7.44\pm0.04\ \pm0.11\ \pm0.19)\times10^2$
0.114-0.128	$(6.53\pm0.02\ \pm0.05\ \pm0.17)\times10^2$	$(6.60\pm0.04\ \pm0.08\ \pm0.17)\times10^2$	$(6.41\pm0.03\ \pm0.10\ \pm0.17)\times10^2$
0.128-0.145	$(5.51\pm0.02\ \pm0.04\ \pm0.14)\times10^2$	$(5.50\pm0.03\ \pm0.06\ \pm0.14)\times10^2$	$(5.51\pm0.03\ \pm0.09\ \pm0.14)\times10^2$
0.145-0.165	$(4.66\pm0.02\ \pm0.04\ \pm0.12)\times10^2$	$(4.66\pm0.03\ \pm0.06\ \pm0.12)\times10^2$	$(4.64\pm0.02\ \pm0.07\ \pm0.12)\times10^2$
0.165-0.189	$(3.82\pm0.01\ \pm0.03\ \pm0.10)\times10^2$	$(3.82\pm0.02\ \pm0.05\ \pm0.10)\times10^2$	$(3.80\pm0.02\ \pm0.06\ \pm0.10)\times10^2$
0.189-0.219	$(3.04\pm0.01\ \pm0.02\ \pm0.08)\times10^2$	$(3.03\pm0.02\ \pm0.04\ \pm0.08)\times10^2$	$(3.06\pm0.01\ \pm0.05\ \pm0.08)\times10^2$
0.219-0.258	$(2.350\pm0.008\pm0.018\pm0.061)\times10^2$	$(2.34\pm0.01\ \pm0.03\ \pm0.06)\times10^2$	$(2.36\pm0.01\ \pm0.04\ \pm0.06)\times10^2$
0.258-0.312	$(1.711\pm0.006\pm0.013\pm0.044)\times10^2$	$(1.705\pm0.009\pm0.021\pm0.044)\times10^2$	$(1.714\pm0.008\pm0.026\pm0.045)\times10^2$
0.312-0.391	$(1.152\pm0.004\pm0.009\pm0.030)\times10^2$	$(1.154\pm0.006\pm0.014\pm0.030)\times10^2$	$(1.146\pm0.005\pm0.018\pm0.030)\times10^2$
0.391-0.524	$67.6\pm0.2\ \ \pm0.5\ \ \pm1.8$	$68.0\pm0.4\ \ \pm0.9\ \ \pm1.8$	$66.7\pm0.3\ \ \pm1.0\ \ \pm1.7$
0.524-0.695	$35.6\pm0.2\ \ \pm0.3\ \ \pm0.9$	$35.8\pm0.2\ \ \pm0.5\ \ \pm0.9$	$35.4\pm0.2\ \ \pm0.6\ \ \pm0.9$
0.695-0.918	$18.00\pm0.09\ \pm0.16\ \pm0.47$	$18.0\pm0.1\ \ \pm0.3\ \ \pm0.5$	$17.9\pm0.1\ \ \pm0.3\ \ \pm0.5$
0.918-1.153	$9.34\pm0.07\ \pm0.10\ \pm0.24$	$9.6\pm0.1\ \ \pm0.2\ \ \pm0.2$	$9.11\pm0.08\ \pm0.16\ \pm0.24$
1.153-1.496	$4.99\pm0.04\ \pm0.06\ \pm0.13$	$5.04\pm0.06\ \pm0.10\ \pm0.13$	$4.95\pm0.05\ \pm0.09\ \pm0.13$
1.496-1.947	$2.44\pm0.02\ \pm0.03\ \pm0.06$	$2.47\pm0.04\ \pm0.06\ \pm0.06$	$2.42\pm0.03\ \pm0.05\ \pm0.06$
1.947-2.522	$1.23\pm0.02\ \pm0.02\ \pm0.03$	$1.26\pm0.03\ \pm0.03\ \pm0.03$	$1.21\pm0.02\ \pm0.02\ \pm0.03$
2.522-3.277	$0.651\pm0.010\pm0.011\pm0.017$	$0.67\pm0.02\ \pm0.02\ \pm0.02$	$0.64\pm0.01\ \pm0.02\ \pm0.02$

Table B.13: This table contains the measured absolute differential cross-section of ϕ^* of events where the rapidity of the Z falls in the range $0.8 < |y| < 1.2$. The uncertainty is separated into the statistical component followed by the systematic.

ϕ^* range	Combined	Electron channel	Muon channel
0.000-0.004	(2.375±0.009±0.018±0.062)×10^3	(2.36±0.01 ±0.03 ±0.06)×10^3	(2.39±0.01 ±0.04 ±0.06)×10^3
0.004-0.008	(2.384±0.009±0.018±0.062)×10^3	(2.37±0.02 ±0.03 ±0.06)×10^3	(2.41±0.01 ±0.04 ±0.06)×10^3
0.008-0.012	(2.318±0.009±0.018±0.060)×10^3	(2.31±0.02 ±0.03 ±0.06)×10^3	(2.32±0.01 ±0.04 ±0.06)×10^3
0.012-0.016	(2.272±0.009±0.018±0.059)×10^3	(2.28±0.02 ±0.03 ±0.06)×10^3	(2.26±0.01 ±0.04 ±0.06)×10^3
0.016-0.020	(2.161±0.009±0.017±0.056)×10^3	(2.12±0.01 ±0.03 ±0.06)×10^3	(2.20±0.01 ±0.03 ±0.06)×10^3
0.020-0.024	(2.107±0.009±0.016±0.055)×10^3	(2.11±0.01 ±0.03 ±0.05)×10^3	(2.10±0.01 ±0.03 ±0.05)×10^3
0.024-0.029	(1.990±0.007±0.016±0.052)×10^3	(1.98±0.01 ±0.03 ±0.05)×10^3	(2.002±0.009±0.031±0.052)×10^3
0.029-0.034	(1.875±0.007±0.015±0.049)×10^3	(1.86±0.01 ±0.02 ±0.05)×10^3	(1.890±0.009±0.030±0.049)×10^3
0.034-0.039	(1.777±0.007±0.014±0.046)×10^3	(1.78±0.01 ±0.02 ±0.05)×10^3	(1.771±0.009±0.028±0.046)×10^3
0.039-0.045	(1.626±0.006±0.013±0.042)×10^3	(1.62±0.01 ±0.02 ±0.04)×10^3	(1.626±0.008±0.025±0.042)×10^3
0.045-0.051	(1.510±0.006±0.012±0.039)×10^3	(1.503±0.010±0.019±0.039)×10^3	(1.516±0.007±0.024±0.039)×10^3
0.051-0.057	(1.375±0.006±0.011±0.036)×10^3	(1.365±0.009±0.017±0.035)×10^3	(1.387±0.007±0.022±0.036)×10^3
0.057-0.064	(1.273±0.005±0.010±0.033)×10^3	(1.278±0.008±0.016±0.033)×10^3	(1.265±0.006±0.020±0.033)×10^3
0.064-0.072	(1.160±0.004±0.009±0.030)×10^3	(1.150±0.007±0.016±0.030)×10^3	(1.169±0.006±0.018±0.030)×10^3
0.072-0.081	(1.045±0.004±0.008±0.027)×10^3	(1.044±0.006±0.013±0.027)×10^3	(1.046±0.005±0.016±0.027)×10^3
0.081-0.091	(9.26±0.04 ±0.07 ±0.24)×10^2	(9.27±0.06 ±0.12 ±0.24)×10^2	(9.23±0.04 ±0.14 ±0.24)×10^2
0.091-0.102	(8.15±0.03 ±0.06 ±0.21)×10^2	(8.08±0.05 ±0.10 ±0.21)×10^2	(8.22±0.04 ±0.13 ±0.21)×10^2
0.102-0.114	(7.23±0.03 ±0.06 ±0.19)×10^2	(7.23±0.05 ±0.10 ±0.19)×10^2	(7.22±0.04 ±0.11 ±0.19)×10^2
0.114-0.128	(6.25±0.02 ±0.05 ±0.16)×10^2	(6.23±0.04 ±0.08 ±0.16)×10^2	(6.25±0.03 ±0.10 ±0.16)×10^2
0.128-0.145	(5.37±0.02 ±0.04 ±0.14)×10^2	(5.39±0.03 ±0.07 ±0.14)×10^2	(5.33±0.03 ±0.08 ±0.14)×10^2
0.145-0.165	(4.50±0.02 ±0.03 ±0.12)×10^2	(4.52±0.03 ±0.06 ±0.12)×10^2	(4.48±0.02 ±0.07 ±0.12)×10^2
0.165-0.189	(3.69±0.01 ±0.03 ±0.10)×10^2	(3.72±0.02 ±0.05 ±0.10)×10^2	(3.65±0.02 ±0.06 ±0.09)×10^2
0.189-0.219	(2.93±0.01 ±0.02 ±0.08)×10^2	(2.92±0.02 ±0.04 ±0.08)×10^2	(2.91±0.01 ±0.05 ±0.08)×10^2
0.219-0.258	(2.269±0.008±0.017±0.059)×10^2	(2.29±0.01 ±0.03 ±0.06)×10^2	(2.23±0.01 ±0.03 ±0.06)×10^2
0.258-0.312	(1.654±0.006±0.013±0.043)×10^2	(1.667±0.010±0.022±0.043)×10^2	(1.635±0.008±0.025±0.043)×10^2
0.312-0.391	(1.116±0.004±0.009±0.029)×10^2	(1.117±0.007±0.015±0.029)×10^2	(1.113±0.005±0.017±0.029)×10^2
0.391-0.524	65.4±0.2 ±0.5 ±1.7	65.9±0.4 ±0.9 ±1.7	64.6±0.3 ±1.0 ±1.7
0.524-0.695	34.2±0.2 ±0.3 ±0.9	33.9±0.2 ±0.5 ±0.9	34.3±0.2 ±0.5 ±0.9
0.695-0.918	17.09±0.09 ±0.16 ±0.44	17.4±0.2 ±0.3 ±0.5	16.8±0.1 ±0.3 ±0.4
0.918-1.153	8.80±0.07 ±0.09 ±0.23	8.7±0.1 ±0.2 ±0.2	8.88±0.08 ±0.15 ±0.23
1.153-1.496	4.58±0.04 ±0.05 ±0.12	4.62±0.06 ±0.10 ±0.12	4.54±0.05 ±0.08 ±0.12
1.496-1.947	2.26±0.02 ±0.03 ±0.06	2.22±0.04 ±0.05 ±0.06	2.27±0.03 ±0.05 ±0.06
1.947-2.522	1.11±0.01 ±0.02 ±0.03	1.11±0.02 ±0.03 ±0.03	1.11±0.02 ±0.03 ±0.03
2.522-3.277	0.588±0.010±0.011±0.015	0.60±0.02 ±0.02 ±0.02	0.58±0.01 ±0.02 ±0.02

Table B.14: This table contains the measured absolute differential cross-section of ϕ^* of events where the rapidity of the Z falls in the range $1.2 < |y| < 1.6$. The uncertainty is separated into the statistical component followed by the systematic.

ϕ^* range	Combined	Electron channel	Muon channel
0.000-0.004	$(2.085\pm0.008\pm0.017\pm0.054)\times10^3$	$(2.07\pm0.01\ \pm0.03\ \pm0.05)\times10^3$	$(2.09\pm0.01\ \pm0.03\ \pm0.05)\times10^3$
0.004-0.008	$(2.077\pm0.009\pm0.017\pm0.054)\times10^3$	$(2.07\pm0.02\ \pm0.03\ \pm0.05)\times10^3$	$(2.07\pm0.01\ \pm0.03\ \pm0.05)\times10^3$
0.008-0.012	$(2.037\pm0.009\pm0.017\pm0.053)\times10^3$	$(2.02\pm0.02\ \pm0.03\ \pm0.05)\times10^3$	$(2.04\pm0.01\ \pm0.03\ \pm0.05)\times10^3$
0.012-0.016	$(1.987\pm0.009\pm0.016\pm0.052)\times10^3$	$(2.00\pm0.02\ \pm0.03\ \pm0.05)\times10^3$	$(1.96\pm0.01\ \pm0.03\ \pm0.05)\times10^3$
0.016-0.020	$(1.952\pm0.009\pm0.016\pm0.051)\times10^3$	$(1.96\pm0.02\ \pm0.03\ \pm0.05)\times10^3$	$(1.92\pm0.01\ \pm0.03\ \pm0.05)\times10^3$
0.020-0.024	$(1.811\pm0.008\pm0.015\pm0.047)\times10^3$	$(1.82\pm0.01\ \pm0.03\ \pm0.05)\times10^3$	$(1.796\pm0.010\pm0.029\pm0.047)\times10^3$
0.024-0.029	$(1.740\pm0.007\pm0.014\pm0.045)\times10^3$	$(1.72\pm0.01\ \pm0.02\ \pm0.04)\times10^3$	$(1.751\pm0.009\pm0.028\pm0.046)\times10^3$
0.029-0.034	$(1.634\pm0.007\pm0.014\pm0.042)\times10^3$	$(1.63\pm0.01\ \pm0.02\ \pm0.04)\times10^3$	$(1.628\pm0.008\pm0.026\pm0.042)\times10^3$
0.034-0.039	$(1.518\pm0.007\pm0.013\pm0.039)\times10^3$	$(1.52\pm0.01\ \pm0.02\ \pm0.04)\times10^3$	$(1.508\pm0.008\pm0.025\pm0.039)\times10^3$
0.039-0.045	$(1.418\pm0.006\pm0.012\pm0.037)\times10^3$	$(1.40\pm0.01\ \pm0.02\ \pm0.04)\times10^3$	$(1.429\pm0.007\pm0.023\pm0.037)\times10^3$
0.045-0.051	$(1.309\pm0.006\pm0.011\pm0.034)\times10^3$	$(1.310\pm0.010\pm0.018\pm0.034)\times10^3$	$(1.300\pm0.007\pm0.021\pm0.034)\times10^3$
0.051-0.057	$(1.212\pm0.005\pm0.010\pm0.032)\times10^3$	$(1.220\pm0.010\pm0.017\pm0.032)\times10^3$	$(1.203\pm0.007\pm0.019\pm0.031)\times10^3$
0.057-0.064	$(1.108\pm0.005\pm0.009\pm0.029)\times10^3$	$(1.108\pm0.008\pm0.015\pm0.029)\times10^3$	$(1.106\pm0.006\pm0.018\pm0.029)\times10^3$
0.064-0.072	$(9.97\pm0.04\ \pm0.08\ \pm0.26)\times10^2$	$(9.93\pm0.07\ \pm0.15\ \pm0.26)\times10^2$	$(9.96\pm0.05\ \pm0.16\ \pm0.26)\times10^2$
0.072-0.081	$(8.89\pm0.04\ \pm0.07\ \pm0.23)\times10^2$	$(8.82\pm0.06\ \pm0.12\ \pm0.23)\times10^2$	$(8.93\pm0.05\ \pm0.14\ \pm0.23)\times10^2$
0.081-0.091	$(7.85\pm0.03\ \pm0.06\ \pm0.20)\times10^2$	$(7.83\pm0.06\ \pm0.11\ \pm0.20)\times10^2$	$(7.85\pm0.04\ \pm0.12\ \pm0.20)\times10^2$
0.091-0.102	$(6.93\pm0.03\ \pm0.06\ \pm0.18)\times10^2$	$(6.95\pm0.05\ \pm0.10\ \pm0.18)\times10^2$	$(6.85\pm0.04\ \pm0.11\ \pm0.18)\times10^2$
0.102-0.114	$(6.13\pm0.03\ \pm0.05\ \pm0.16)\times10^2$	$(6.11\pm0.05\ \pm0.09\ \pm0.16)\times10^2$	$(6.12\pm0.03\ \pm0.10\ \pm0.16)\times10^2$
0.114-0.128	$(5.30\pm0.02\ \pm0.04\ \pm0.14)\times10^2$	$(5.28\pm0.04\ \pm0.08\ \pm0.14)\times10^2$	$(5.29\pm0.03\ \pm0.09\ \pm0.14)\times10^2$
0.128-0.145	$(4.59\pm0.02\ \pm0.04\ \pm0.12)\times10^2$	$(4.58\pm0.03\ \pm0.06\ \pm0.12)\times10^2$	$(4.57\pm0.02\ \pm0.07\ \pm0.12)\times10^2$
0.145-0.165	$(3.77\pm0.02\ \pm0.03\ \pm0.10)\times10^2$	$(3.73\pm0.03\ \pm0.05\ \pm0.10)\times10^2$	$(3.81\pm0.02\ \pm0.06\ \pm0.10)\times10^2$
0.165-0.189	$(3.11\pm0.01\ \pm0.03\ \pm0.08)\times10^2$	$(3.14\pm0.02\ \pm0.04\ \pm0.08)\times10^2$	$(3.07\pm0.02\ \pm0.05\ \pm0.08)\times10^2$
0.189-0.219	$(2.45\pm0.01\ \pm0.02\ \pm0.06)\times10^2$	$(2.45\pm0.02\ \pm0.03\ \pm0.06)\times10^2$	$(2.44\pm0.01\ \pm0.04\ \pm0.06)\times10^2$
0.219-0.258	$(1.904\pm0.008\pm0.016\pm0.049)\times10^2$	$(1.88\pm0.01\ \pm0.03\ \pm0.05)\times10^2$	$(1.914\pm0.010\pm0.031\pm0.050)\times10^2$
0.258-0.312	$(1.382\pm0.006\pm0.011\pm0.036)\times10^2$	$(1.390\pm0.010\pm0.021\pm0.036)\times10^2$	$(1.368\pm0.007\pm0.022\pm0.036)\times10^2$
0.312-0.391	$93.4\pm0.4\ \ \pm0.8\ \ \pm2.4$	$93.5\pm0.6\ \ \pm1.3\ \ \pm2.4$	$93.0\pm0.5\ \ \pm1.5\ \ \pm2.4$
0.391-0.524	$53.7\pm0.2\ \ \pm0.4\ \ \pm1.4$	$53.7\pm0.4\ \ \pm0.8\ \ \pm1.4$	$53.5\pm0.3\ \ \pm0.8\ \ \pm1.4$
0.524-0.695	$27.8\pm0.1\ \ \pm0.2\ \ \pm0.7$	$28.1\pm0.2\ \ \pm0.5\ \ \pm0.7$	$27.4\pm0.2\ \ \pm0.5\ \ \pm0.7$
0.695-0.918	$13.93\pm0.09\ \pm0.14\ \pm0.36$	$14.2\pm0.1\ \ \pm0.3\ \ \pm0.4$	$13.7\pm0.1\ \ \pm0.2\ \ \pm0.4$
0.918-1.153	$7.14\pm0.06\ \pm0.08\ \pm0.19$	$7.07\pm0.10\ \pm0.15\ \pm0.18$	$7.16\pm0.08\ \pm0.13\ \pm0.19$
1.153-1.496	$3.66\pm0.04\ \pm0.05\ \pm0.10$	$3.87\pm0.06\ \pm0.09\ \pm0.10$	$3.52\pm0.04\ \pm0.07\ \pm0.09$
1.496-1.947	$1.68\pm0.02\ \pm0.03\ \pm0.04$	$1.62\pm0.03\ \pm0.04\ \pm0.04$	$1.72\pm0.03\ \pm0.04\ \pm0.04$
1.947-2.522	$0.80\pm0.01\ \pm0.02\ \pm0.02$	$0.83\pm0.02\ \pm0.03\ \pm0.02$	$0.78\pm0.02\ \pm0.02\ \pm0.02$
2.522-3.277	$0.408\pm0.008\pm0.009\pm0.011$	$0.41\pm0.01\ \pm0.02\ \pm0.01$	$0.41\pm0.01\ \pm0.01\ \pm0.01$

Table B.15: This table contains the measured absolute differential cross-section of ϕ^* of events where the rapidity of the Z falls in the range $1.6 < |y| < 2.0$. The uncertainty is separated into the statistical component followed by the systematic.

ϕ^* range	Combined	Electron channel	Muon channel
0.000-0.004	$(1.404\pm0.007\pm0.013\pm0.036)\times10^3$	$(1.37\pm0.01\ \pm0.02\ \pm0.04)\times10^3$	$(1.424\pm0.009\pm0.023\pm0.037)\times10^3$
0.004-0.008	$(1.412\pm0.008\pm0.014\pm0.037)\times10^3$	$(1.42\pm0.01\ \pm0.03\ \pm0.04)\times10^3$	$(1.401\pm0.009\pm0.026\pm0.036)\times10^3$
0.008-0.012	$(1.343\pm0.008\pm0.013\pm0.035)\times10^3$	$(1.31\pm0.01\ \pm0.03\ \pm0.03)\times10^3$	$(1.357\pm0.009\pm0.023\pm0.035)\times10^3$
0.012-0.016	$(1.325\pm0.008\pm0.013\pm0.034)\times10^3$	$(1.31\pm0.01\ \pm0.02\ \pm0.03)\times10^3$	$(1.328\pm0.009\pm0.024\pm0.035)\times10^3$
0.016-0.020	$(1.249\pm0.007\pm0.012\pm0.032)\times10^3$	$(1.23\pm0.01\ \pm0.02\ \pm0.03)\times10^3$	$(1.260\pm0.009\pm0.021\pm0.033)\times10^3$
0.020-0.024	$(1.238\pm0.007\pm0.012\pm0.032)\times10^3$	$(1.20\pm0.01\ \pm0.02\ \pm0.03)\times10^3$	$(1.257\pm0.009\pm0.023\pm0.033)\times10^3$
0.024-0.029	$(1.176\pm0.006\pm0.011\pm0.031)\times10^3$	$(1.21\pm0.01\ \pm0.02\ \pm0.03)\times10^3$	$(1.150\pm0.007\pm0.020\pm0.030)\times10^3$
0.029-0.034	$(1.068\pm0.006\pm0.010\pm0.028)\times10^3$	$(1.04\pm0.01\ \pm0.02\ \pm0.03)\times10^3$	$(1.076\pm0.007\pm0.018\pm0.028)\times10^3$
0.034-0.039	$(1.011\pm0.006\pm0.010\pm0.026)\times10^3$	$(10.0\pm0.1\ \ \pm0.2\ \ \pm0.3)\times10^2$	$(1.015\pm0.007\pm0.018\pm0.026)\times10^3$
0.039-0.045	$(9.37\pm0.05\ \pm0.09\ \pm0.24)\times10^2$	$(9.47\pm0.09\ \pm0.16\ \pm0.25)\times10^2$	$(9.25\pm0.06\ \pm0.16\ \pm0.24)\times10^2$
0.045-0.051	$(8.64\pm0.05\ \pm0.08\ \pm0.22)\times10^2$	$(8.55\pm0.09\ \pm0.15\ \pm0.22)\times10^2$	$(8.65\pm0.06\ \pm0.15\ \pm0.22)\times10^2$
0.051-0.057	$(7.92\pm0.05\ \pm0.08\ \pm0.21)\times10^2$	$(7.78\pm0.09\ \pm0.15\ \pm0.20)\times10^2$	$(7.95\pm0.06\ \pm0.14\ \pm0.21)\times10^2$
0.057-0.064	$(7.35\pm0.04\ \pm0.07\ \pm0.19)\times10^2$	$(7.36\pm0.08\ \pm0.14\ \pm0.19)\times10^2$	$(7.30\pm0.05\ \pm0.13\ \pm0.19)\times10^2$
0.064-0.072	$(6.58\pm0.04\ \pm0.06\ \pm0.17)\times10^2$	$(6.48\pm0.07\ \pm0.12\ \pm0.17)\times10^2$	$(6.62\pm0.04\ \pm0.12\ \pm0.17)\times10^2$
0.072-0.081	$(5.93\pm0.03\ \pm0.05\ \pm0.15)\times10^2$	$(6.01\pm0.06\ \pm0.11\ \pm0.16)\times10^2$	$(5.82\pm0.04\ \pm0.10\ \pm0.15)\times10^2$
0.081-0.091	$(5.22\pm0.03\ \pm0.05\ \pm0.14)\times10^2$	$(5.23\pm0.05\ \pm0.09\ \pm0.14)\times10^2$	$(5.18\pm0.03\ \pm0.09\ \pm0.13)\times10^2$
0.091-0.102	$(4.66\pm0.03\ \pm0.05\ \pm0.12)\times10^2$	$(4.65\pm0.05\ \pm0.09\ \pm0.12)\times10^2$	$(4.64\pm0.03\ \pm0.08\ \pm0.12)\times10^2$
0.102-0.114	$(3.96\pm0.02\ \pm0.04\ \pm0.10)\times10^2$	$(3.92\pm0.04\ \pm0.07\ \pm0.10)\times10^2$	$(3.97\pm0.03\ \pm0.07\ \pm0.10)\times10^2$
0.114-0.128	$(3.49\pm0.02\ \pm0.03\ \pm0.09)\times10^2$	$(3.45\pm0.04\ \pm0.06\ \pm0.09)\times10^2$	$(3.50\pm0.02\ \pm0.06\ \pm0.09)\times10^2$
0.128-0.145	$(2.95\pm0.02\ \pm0.03\ \pm0.08)\times10^2$	$(2.93\pm0.03\ \pm0.05\ \pm0.08)\times10^2$	$(2.95\pm0.02\ \pm0.05\ \pm0.08)\times10^2$
0.145-0.165	$(2.48\pm0.01\ \pm0.02\ \pm0.06)\times10^2$	$(2.48\pm0.02\ \pm0.05\ \pm0.06)\times10^2$	$(2.45\pm0.02\ \pm0.04\ \pm0.06)\times10^2$
0.165-0.189	$(2.05\pm0.01\ \pm0.02\ \pm0.05)\times10^2$	$(2.03\pm0.02\ \pm0.04\ \pm0.05)\times10^2$	$(2.05\pm0.01\ \pm0.04\ \pm0.05)\times10^2$
0.189-0.219	$(1.633\pm0.009\pm0.015\pm0.042)\times10^2$	$(1.62\pm0.02\ \pm0.03\ \pm0.04)\times10^2$	$(1.63\pm0.01\ \pm0.03\ \pm0.04)\times10^2$
0.219-0.258	$(1.235\pm0.007\pm0.012\pm0.032)\times10^2$	$(1.24\pm0.01\ \pm0.02\ \pm0.03)\times10^2$	$(1.222\pm0.008\pm0.021\pm0.032)\times10^2$
0.258-0.312	$91.6\pm0.5\ \ \pm0.9\ \ \pm2.4$	$90.7\pm0.9\ \ \pm1.6\ \ \pm2.4$	$91.6\pm0.6\ \ \pm1.6\ \ \pm2.4$
0.312-0.391	$59.9\pm0.3\ \ \pm0.6\ \ \pm1.6$	$60.1\pm0.6\ \ \pm1.0\ \ \pm1.6$	$59.5\pm0.4\ \ \pm1.0\ \ \pm1.5$
0.391-0.524	$35.2\pm0.2\ \ \pm0.3\ \ \pm0.9$	$35.2\pm0.3\ \ \pm0.6\ \ \pm0.9$	$34.9\pm0.2\ \ \pm0.6\ \ \pm0.9$
0.524-0.695	$17.7\pm0.1\ \ \pm0.2\ \ \pm0.5$	$17.9\pm0.2\ \ \pm0.4\ \ \pm0.5$	$17.5\pm0.1\ \ \pm0.3\ \ \pm0.5$
0.695-0.918	$8.99\pm0.07\ \pm0.10\ \pm0.23$	$9.5\pm0.1\ \ \pm0.2\ \ \pm0.2$	$8.73\pm0.09\ \pm0.16\ \pm0.23$
0.918-1.153	$4.45\pm0.05\ \pm0.06\ \pm0.12$	$4.59\pm0.09\ \pm0.13\ \pm0.12$	$4.37\pm0.06\ \pm0.09\ \pm0.11$
1.153-1.496	$2.16\pm0.03\ \pm0.03\ \pm0.06$	$2.15\pm0.05\ \pm0.07\ \pm0.06$	$2.16\pm0.04\ \pm0.05\ \pm0.06$
1.496-1.947	$0.91\pm0.02\ \pm0.02\ \pm0.02$	$0.98\pm0.03\ \pm0.04\ \pm0.03$	$0.88\pm0.02\ \pm0.02\ \pm0.02$
1.947-2.522	$0.381\pm0.009\pm0.010\pm0.010$	$0.37\pm0.01\ \pm0.02\ \pm0.01$	$0.39\pm0.01\ \pm0.01\ \pm0.01$
2.522-3.277	$0.176\pm0.005\pm0.006\pm0.005$	$0.191\pm0.010\pm0.012\pm0.005$	$0.170\pm0.007\pm0.007\pm0.004$

Table B.16: This table contains the measured absolute differential cross-section of ϕ^* of events where the rapidity of the Z falls in the range $2.0 < |y| < 2.4$. The uncertainty is separated into the statistical component followed by the systematic.

ϕ^* range	Combined	Electron channel	Muon channel
0.000-0.004	$(3.42\pm0.04\ \pm0.05\ \pm0.09)\times10^2$	$(3.22\pm0.07\pm0.10\pm0.08)\times10^2$	$(3.47\pm0.05\ \pm0.08\ \pm0.09)\times10^2$
0.004-0.008	$(3.27\pm0.04\ \pm0.05\ \pm0.09)\times10^2$	$(3.36\pm0.08\pm0.12\pm0.09)\times10^2$	$(3.24\pm0.05\ \pm0.08\ \pm0.08)\times10^2$
0.008-0.012	$(3.24\pm0.04\ \pm0.05\ \pm0.08)\times10^2$	$(3.18\pm0.07\pm0.12\pm0.08)\times10^2$	$(3.24\pm0.05\ \pm0.08\ \pm0.08)\times10^2$
0.012-0.016	$(3.20\pm0.04\ \pm0.06\ \pm0.08)\times10^2$	$(3.06\pm0.07\pm0.12\pm0.08)\times10^2$	$(3.24\pm0.05\ \pm0.08\ \pm0.08)\times10^2$
0.016-0.020	$(3.06\pm0.04\ \pm0.05\ \pm0.08)\times10^2$	$(3.02\pm0.07\pm0.12\pm0.08)\times10^2$	$(3.06\pm0.05\ \pm0.08\ \pm0.08)\times10^2$
0.020-0.024	$(3.07\pm0.04\ \pm0.05\ \pm0.08)\times10^2$	$(3.04\pm0.07\pm0.11\pm0.08)\times10^2$	$(3.07\pm0.05\ \pm0.07\ \pm0.08)\times10^2$
0.024-0.029	$(2.85\pm0.03\ \pm0.05\ \pm0.07)\times10^2$	$(2.78\pm0.06\pm0.10\pm0.07)\times10^2$	$(2.86\pm0.04\ \pm0.07\ \pm0.07)\times10^2$
0.029-0.034	$(2.65\pm0.03\ \pm0.04\ \pm0.07)\times10^2$	$(2.49\pm0.06\pm0.09\pm0.06)\times10^2$	$(2.71\pm0.04\ \pm0.06\ \pm0.07)\times10^2$
0.034-0.039	$(2.40\pm0.03\ \pm0.04\ \pm0.06)\times10^2$	$(2.41\pm0.06\pm0.09\pm0.06)\times10^2$	$(2.38\pm0.04\ \pm0.06\ \pm0.06)\times10^2$
0.039-0.045	$(2.37\pm0.03\ \pm0.04\ \pm0.06)\times10^2$	$(2.32\pm0.05\pm0.08\pm0.06)\times10^2$	$(2.39\pm0.03\ \pm0.05\ \pm0.06)\times10^2$
0.045-0.051	$(2.11\pm0.03\ \pm0.03\ \pm0.05)\times10^2$	$(1.98\pm0.05\pm0.07\pm0.05)\times10^2$	$(2.15\pm0.03\ \pm0.05\ \pm0.06)\times10^2$
0.051-0.057	$(1.96\pm0.02\ \pm0.03\ \pm0.05)\times10^2$	$(1.96\pm0.05\pm0.07\pm0.05)\times10^2$	$(1.96\pm0.03\ \pm0.05\ \pm0.05)\times10^2$
0.057-0.064	$(1.76\pm0.02\ \pm0.03\ \pm0.05)\times10^2$	$(1.67\pm0.04\pm0.07\pm0.04)\times10^2$	$(1.78\pm0.03\ \pm0.04\ \pm0.05)\times10^2$
0.064-0.072	$(1.59\pm0.02\ \pm0.02\ \pm0.04)\times10^2$	$(1.58\pm0.03\pm0.05\pm0.04)\times10^2$	$(1.58\pm0.02\ \pm0.04\ \pm0.04)\times10^2$
0.072-0.081	$(1.46\pm0.02\ \pm0.02\ \pm0.04)\times10^2$	$(1.41\pm0.03\pm0.05\pm0.04)\times10^2$	$(1.48\pm0.02\ \pm0.04\ \pm0.04)\times10^2$
0.081-0.091	$(1.27\pm0.02\ \pm0.02\ \pm0.03)\times10^2$	$(1.24\pm0.03\pm0.04\pm0.03)\times10^2$	$(1.29\pm0.02\ \pm0.03\ \pm0.03)\times10^2$
0.091-0.102	$(1.13\pm0.01\ \pm0.02\ \pm0.03)\times10^2$	$(1.15\pm0.03\pm0.04\pm0.03)\times10^2$	$(1.12\pm0.02\ \pm0.02\ \pm0.03)\times10^2$
0.102-0.114	$98\pm1\ \ \pm2\ \ \pm3$	$94\pm2\ \ \pm3\ \ \pm2$	$100\pm1\ \ \pm2\ \ \pm3$
0.114-0.128	$89\pm1\ \ \pm1\ \ \pm2$	$87\pm2\ \ \pm3\ \ \pm2$	$89\pm1\ \ \pm2\ \ \pm2$
0.128-0.145	$72.8\pm0.9\ \ \pm1.2\ \ \pm1.9$	$70\pm2\ \ \pm2\ \ \pm2$	$74\pm1\ \ \pm2\ \ \pm2$
0.145-0.165	$62.1\pm0.7\ \ \pm1.0\ \ \pm1.6$	$61\pm1\ \ \pm2\ \ \pm2$	$61.9\pm0.9\ \ \pm1.5\ \ \pm1.6$
0.165-0.189	$48.7\pm0.6\ \ \pm0.8\ \ \pm1.3$	$49\pm1\ \ \pm2\ \ \pm1$	$48.7\pm0.7\ \ \pm1.1\ \ \pm1.3$
0.189-0.219	$39.2\pm0.5\ \ \pm0.6\ \ \pm1.0$	$38.2\pm0.8\ \pm1.2\ \pm1.0$	$39.2\pm0.6\ \ \pm0.9\ \ \pm1.0$
0.219-0.258	$30.6\pm0.4\ \ \pm0.5\ \ \pm0.8$	$32.0\pm0.7\ \pm1.0\ \pm0.8$	$30.0\pm0.4\ \ \pm0.7\ \ \pm0.8$
0.258-0.312	$22.2\pm0.3\ \ \pm0.4\ \ \pm0.6$	$22.4\pm0.5\ \pm0.7\ \pm0.6$	$21.8\pm0.3\ \ \pm0.5\ \ \pm0.6$
0.312-0.391	$14.2\pm0.2\ \ \pm0.2\ \ \pm0.4$	$13.9\pm0.3\ \pm0.5\ \pm0.4$	$14.2\pm0.2\ \ \pm0.3\ \ \pm0.4$
0.391-0.524	$8.35\pm0.10\ \pm0.13\ \pm0.22$	$8.1\pm0.2\ \pm0.3\ \pm0.2$	$8.4\pm0.1\ \ \pm0.2\ \ \pm0.2$
0.524-0.695	$4.30\pm0.06\ \pm0.08\ \pm0.11$	$4.3\pm0.1\ \pm0.2\ \pm0.1$	$4.27\pm0.08\ \pm0.11\ \pm0.11$
0.695-0.918	$2.03\pm0.04\ \pm0.04\ \pm0.05$	$2.06\pm0.07\pm0.10\pm0.05$	$2.02\pm0.04\ \pm0.06\ \pm0.05$
0.918-1.153	$1.00\pm0.03\ \pm0.03\ \pm0.03$	$1.01\pm0.04\pm0.06\pm0.03$	$0.99\pm0.03\ \pm0.03\ \pm0.03$
1.153-1.496	$0.47\pm0.01\ \pm0.02\ \pm0.01$	$0.51\pm0.03\pm0.04\pm0.01$	$0.46\pm0.02\ \pm0.02\ \pm0.01$
1.496-1.947	$0.195\pm0.008\pm0.010\pm0.005$	$0.21\pm0.01\pm0.02\pm0.01$	$0.192\pm0.010\pm0.011\pm0.005$
1.947-2.522	$(7.9\pm0.5\ \ \pm0.6\ \ \pm0.2)\times10^{-2}$	$(7.2\pm0.7\ \pm0.9\ \pm0.2)\times10^{-2}$	$(8.2\pm0.6\ \ \pm0.8\ \ \pm0.2)\times10^{-2}$
2.522-3.277	$(2.4\pm0.2\ \ \pm0.3\ \ \pm0.1)\times10^{-2}$	$(2.0\pm0.4\ \pm0.4\ \pm0.1)\times10^{-2}$	$(2.7\pm0.3\ \ \pm0.3\ \ \pm0.1)\times10^{-2}$